



# Active Sensing of CO<sub>2</sub> Emissions over Nights, Days, and Seasons (ASCENDS) Mission

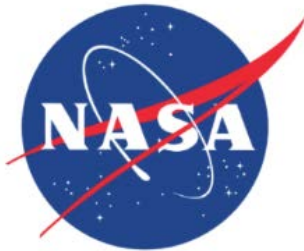
## Science Mission Definition Study

Draft

### ASCENDS Ad Hoc Science Definition Team:

Kenneth W. Jucks,<sup>1</sup> Steven Neeck,<sup>2</sup> James B. Abshire,<sup>3</sup> David F. Baker,<sup>4</sup> Edward V. Browell,<sup>5</sup> Abhishek Chatterjee,<sup>6</sup> David Crisp,<sup>7</sup> Sean M. Crowell,<sup>8</sup> Scott Denning,<sup>9</sup> Dorit Hammerling,<sup>10</sup> Fenton Harrison,<sup>11</sup> Jason J. Hyon,<sup>12</sup> Stephan R. Kawa,<sup>13</sup> Bing Lin,<sup>14</sup> Byron L. Meadows,<sup>15</sup> Robert T. Menzies,<sup>16</sup> Anna Michalak,<sup>17</sup> Berrien Moore,<sup>18</sup> Keith E. Murray,<sup>19</sup> Lesley E. Ott,<sup>20</sup> Peter Rayner,<sup>21</sup> Otilia I. Rodriguez,<sup>22</sup> Andrew Schuh,<sup>23</sup> Yoichi Shiga,<sup>24</sup> Gary D. Spiers,<sup>25</sup> James Shih Wang,<sup>26</sup> and T. Scott Zaccheo.<sup>27</sup>

April 15, 2015



**Revision History:**

<b>Version</b>	<b>Date</b>	<b>Description/Comments</b>
1.0	4/15/2014	ASCENDS NASA Science Definition Study

**Edited By:**

Emily A. Greene, Raytheon  
Autumn M. Burdick, Raytheon  
Felicia M. Vlnrotter, Raytheon

## TABLE OF CONTENTS

<b>EXECUTIVE SUMMARY .....</b>	<b>1</b>
<b>1. INTRODUCTION.....</b>	<b>3</b>
1.1 JUSTIFICATION AND KEY SCIENCE QUESTIONS .....	3
1.2 CO <sub>2</sub> MEASUREMENTS NEAR THE SURFACE.....	3
1.3 SPACE MISSIONS USING PASSIVE REMOTE SENSING.....	4
1.4 POTENTIAL BENEFITS OF ACTIVE (LASER-BASED) CO <sub>2</sub> MEASUREMENTS .....	4
1.5 OBJECTIVES FOR ASCENDS .....	5
1.6 THE ASCENDS APPROACH.....	5
1.7 THE BENEFITS OF THE ASCENDS APPROACH.....	6
1.8 OVERVIEW OF NASA’S DEVELOPMENT OF ASCENDS MISSION .....	7
1.9 REMAINDER OF REPORT .....	8
<b>2. SCIENCE OF ATMOSPHERIC CO<sub>2</sub> AND MEASUREMENT HISTORY .....</b>	<b>9</b>
2.1 INTRODUCTION .....	9
2.2 HISTORY OF CO <sub>2</sub> MEASUREMENTS FROM SPACE .....	12
<b>3. IMPACT TO CARBON SCIENCE AND MODELING .....</b>	<b>14</b>
3.1 INTRODUCTION .....	14
3.2 DETECTION OF CHANGES IN COLUMN CO <sub>2</sub> AND FLUX BY ASCENDS .....	14
3.2.1 <i>Arctic Permafrost Thawing Emissions</i> .....	16
3.2.2 <i>Fossil Fuel Emission Shift</i> .....	19
3.2.3 <i>Flux Changes in the Southern Oceans</i> .....	22
3.2.4 <i>Enhanced Sink Due to Carbon Fertilization</i> .....	25
3.3 IMPROVED FLUX ESTIMATES AT GLOBAL AND REGIONAL SCALES .....	28
3.3.1 <i>North American Regional Flux Estimates</i> .....	30
3.3.2 <i>Regional Fossil Fuel Emissions</i> .....	31
3.3.3 <i>Global Flux Estimation with ASCENDS</i> .....	32
3.3.3.1 Impact of Random Observational Errors .....	33
3.3.3.2 Impact of Systematic Measurement Errors .....	35
3.4 ASCENDS IN THE CONTEXT OF OTHER CO <sub>2</sub> OBSERVING SYSTEMS.....	37
3.4.1 <i>Comparison in Terms of Random Errors</i> .....	37
3.4.2 <i>Comparison Considering Systematic Errors</i> .....	38
3.5 SUMMARY.....	41
<b>4. IMPACT OF UNCERTAINTIES IN ATMOSPHERIC STATE ON ASCENDS MEASUREMENTS .....</b>	<b>42</b>
4.1 INTRODUCTION .....	42
4.2 UNCERTAINTIES IN OBSERVED ATMOSPHERIC STATE.....	43
4.2.1 <i>Uncertainties in Surface Pressure</i> .....	43
4.2.1.1 Comparison of Surface Pressure Model Values and Observations.....	44
4.2.1.2 Inter-model Comparison of Surface Pressure Differences.....	46
4.2.1.3 Spatial Interpolation Errors in Surface Pressure .....	47
4.2.2 <i>Uncertainties in Temperature and Water Vapor Profiles</i> .....	48

4.3	IMPACT OF UNCERTAINTY IN KNOWLEDGE OF ATMOSPHERIC STATE ON RETRIEVED XCO <sub>2</sub> .....	48
4.4	SUMMARY.....	53
<b>5.</b>	<b>TECHNICAL FEASIBILITY.....</b>	<b>54</b>
5.1	INTRODUCTION – LIDAR MEASUREMENTS FOR THE ASCENDS MISSION.....	54
5.1.1	<i>Overview of Measurement Approach.....</i>	54
5.1.2	<i>General Measurement Principle.....</i>	56
5.1.3	<i>Measurement Section Overview.....</i>	58
5.2	ASCENDS LIDAR MEASUREMENT REQUIREMENTS.....	58
5.2.1	<i>Why Are Ranging Measurements Important?.....</i>	60
5.2.2	<i>Discussion of Requirement Elements.....</i>	60
5.3	LIDAR DEVELOPMENT AND MEASUREMENT DEMONSTRATIONS.....	68
5.3.1	<i>CO<sub>2</sub> Sounder Approach and Lidar.....</i>	69
5.3.1.1	CO <sub>2</sub> Sounder Measurement Approach and Lidar Description.....	70
5.3.1.2	Airborne Measurements of CO <sub>2</sub> Column Concentration and Range:.....	71
5.3.1.3	Near Term Plans for the CO <sub>2</sub> Sounder.....	74
5.3.2	<i>Pulsed IPDA Lidar for Measurements of Atmospheric Density Using the Oxygen A-Band.....</i>	75
5.3.2.1	Airborne Campaigns and Data Analysis.....	77
5.3.2.2	Summary.....	79
5.3.2.3	Near-Term Plans for O <sub>2</sub> Lidar.....	79
5.3.3	<i>Overview of the IM-CW Measurement Approach.....</i>	80
5.3.3.1	Basic Characteristics of IM-CW LAS System.....	80
5.3.3.2	Approach for Determining CO <sub>2</sub> Column Differential Absorption Optical Depth.....	84
5.3.3.3	Airborne CO <sub>2</sub> Column Measurements.....	85
5.3.3.4	Surface Reflectance, Thin Cloud Discrimination, and Range Measurements.....	86
5.3.3.5	Airborne O <sub>2</sub> Column Measurements.....	87
5.3.3.6	Laboratory and Ground-Based Measurements.....	90
5.3.3.7	Near-term Plans.....	91
5.3.4	<i>CO<sub>2</sub> Laser Absorption Spectrometer (LAS).....</i>	91
5.3.4.1	JPL CO <sub>2</sub> LAS Instrument Description and Data Processing.....	92
5.3.4.2	Signal Processing and Data Analysis.....	93
5.3.4.3	Cloud Detection and Filtering.....	95
5.3.4.4	Observation of CO <sub>2</sub> Drawdown.....	95
5.3.4.5	Observation of Power Plant CO <sub>2</sub> Plume and CO <sub>2</sub> Emission Rate Calculation.....	97
5.3.4.6	CO <sub>2</sub> Retrievals over Snow-Covered Surfaces: Evidence of Plumes from Developments.....	98
5.3.4.7	Near-term Plans for the LAS.....	100
5.4	DEVELOPMENT OF ADDITIONAL LIDAR MEASUREMENT APPROACHES.....	100
5.4.1	<i>Broad Band Lidar Approach.....</i>	100
5.4.1.1	BBL Fabry-Perot Interferometer and Detector.....	101
5.4.1.2	BBL Receiver Design.....	102
5.4.1.3	Laser for BBL:.....	103
5.4.2	<i>Pulsed 2-<math>\mu</math>m Differential Absorption Lidar (DIAL)/IPDA Lidar.....</i>	104
5.4.2.1	Single-Pulsed 2- $\mu$ m CO <sub>2</sub> DIAL Demonstration.....	104
5.4.2.2	Double-Pulsed CO <sub>2</sub> IPDA Lidar for Aircraft.....	105
5.4.2.3	Laser and Receiver Development.....	106
5.4.2.4	Plans for Ground and Aircraft Testing.....	107

5.5	PLANS FOR DEMONSTRATION OF NEW CAPABILITIES AND MEASUREMENTS .....	107
5.5.1	<i>Additional Measurements Over Snow</i> .....	108
5.5.2	<i>Measurements Over Forests</i> .....	108
5.5.3	<i>Demonstrating CO<sub>2</sub> Flux Measurements with Airborne Lidar</i> .....	109
5.5.4	<i>Comparisons with Satellite Measurements Made with Passive Spectrometers</i> .....	109
5.5.5	<i>Improvements in Numerical Simulations of the ASCENDS Mission</i> .....	109
5.6	NEEDED TECHNOLOGY DEVELOPMENTS FOR THE ASCENDS SPACE LIDAR.....	109
5.6.1	<i>Generic Needs for Up-scaling Existing Airborne Lidar as “Bridge” to Space</i> .....	110
5.6.1.1	Scaling the CO <sub>2</sub> Sounder to Space .....	110
5.6.1.1.1	Space Lidar Technology for the CO <sub>2</sub> Sounder .....	112
5.6.1.2	Advancing Airborne IM-CW instruments to Space .....	114
5.6.1.2.1	Model and Simulations for MFL Space Lidar .....	115
5.6.1.3	Scaling the BBL Lidar to Space.....	117
5.6.1.4	Scaling the Pulsed 2- $\mu$ m CO <sub>2</sub> IPDA Lidar to Space .....	118
5.7	ONGOING TECHNOLOGY DEVELOPMENT ACTIVITIES AND PLANNED FOR RESULTS .....	119
5.7.1	<i>Technology Developments Needed for ASCENDS</i> .....	120
<b>6.</b>	<b>MISSION DESIGN</b> .....	<b>121</b>
6.1	INTRODUCTION .....	121
6.2	SUMMARY OF ASSESSMENT .....	125
6.2.1	<i>Summary</i> .....	125
6.2.2	<i>Recommendations for Future Studies</i> .....	125
6.2.3	<i>Recommendation for an Implementation Schedule</i> .....	125
<b>7.</b>	<b>SUMMARY</b> .....	<b>127</b>
7.1	SUMMARY.....	127
7.2	ONGOING WORK AND PLANS .....	128
7.2.1	<i>Activities Planned for the Modeling Group Include:</i> .....	128
7.2.2	<i>Activities Planned for Atmospheric Analysis Include:</i> .....	128
7.2.3	<i>Activities Planned and Needed for the Measurement Group Include Further Demonstrating Capabilities and Measurements from Aircraft. Some Ongoing Needs are:</i> .....	129
7.2.4	<i>Activities are Needed to Further Develop Lidar Technology</i> .....	129
7.2.5	<i>Activities Needed for the ASCENDS Mission Planning and Development Include:</i> 129	
	<b>APPENDICES</b> .....	<b>131</b>
<b>A.</b>	<b>REFERENCES</b> .....	<b>131</b>
<b>B.</b>	<b>ACRONYMS</b> .....	<b>153</b>
<b>C.</b>	<b>DETAILED COMPARISON OF MODELING APPROACHES</b> .....	<b>159</b>

**LIST OF FIGURES**

Figure 1-1 One approach for an Integrated Path Differential Absorption (IPDA) measurement from space to.....	6
Figure 2-1 Simulated surface (top) and column average (bottom) CO <sub>2</sub> fields for July from the Goddard Earth.....	11
Figure 3-1 Monthly (RMS) ASCENDS random measurement errors for January 2007 computed using Equation .....	16
Figure 3-2 Perturbation flux and column average CO <sub>2</sub> mixing ratio for carbon release experiment (a) 3-month.....	16
Figure 3-3 Results from the permafrost carbon release experiment (a) 3-month (May-July) ASCENDS-mapped CO <sub>2</sub> .....	17
Figure 3-4 Regional inversion results from the permafrost carbon release experiment. Flux error is the RMSE of the.....	18
Figure 3-5 Perturbation flux and column CO <sub>2</sub> mixing ratio for the fossil fuel experiments. First row: Yearly average.....	20
Figure 3-6 Significance results for the fossil fuel experiments for ASCENDS. Using nominal measurement noise at 1 .....	20
Figure 3-7 Regional flux errors for the 20% European fossil fuel emission shift scenario as in Figure 3-4. The prior.....	21
Figure 3-8 Southern Ocean experiment flux difference and column average CO <sub>2</sub> mixing ratio perturbation using the .....	22
Figure 3-9 Significance results for Southern Ocean experiment for medium measurement noise (1 ppmv, 1.57 μm.....	23
Figure 3-10 Inversion results from the Southern Ocean interannual variability experiment. Colors represent the .....	24
Figure 3-11 The simulated net CO <sub>2</sub> flux anomalies that arise from the GPP and ocean flux perturbations used in the .....	25
Figure 3-12 Simulated perturbation signal-to-noise for XCO <sub>2</sub> with 2.05 μm weighting function (See Box 3-1 and.....	26
Figure 3-13 Comparison of ‘truth’ and model annual Net Ecosystem Exchange (NEE, gC m <sup>-2</sup> yr <sup>-1</sup> ) (a) the ‘truth’ .....	27
Figure 3-14 Regional integrated annual NEE for atmospheric inversion test. The blue shaded area can be interpreted .....	28
Figure 3-15 Weekly flux uncertainty reduction (RMS over the 4 months) over North America for a) Case 1 (1.57 μm.....	30
Figure 3-16 Results aggregated to biomes and continent, and compared with other studies a) A priori and a posteriori.....	31

Figure 3-17 The regions where fossil fuel CO <sub>2</sub> emissions are detected for January (in orange) using ASCENDS.....	32
Figure 3-18 Fractional error reduction in weekly flux at 4.5°x6° resolution (lat/long) for four cases: using the 2.05 μm .....	33
Figure 3-19 Seasonal RMS shift or bias cases compared to a priori and a posteriori errors b) The RMS of the shift or .....	36
Figure 3-20 The annual-mean measurement bias [ppm] derived from a comparison of raw ACOS B2.10 GOSAT.....	39
Figure 3-21 Uncertainty reductions for weekly 4.5x6° fluxes aggregated to TRANSCOM regions produced by.....	39
Figure 3-22 The shift in the weekly flux estimates caused by the addition of measurement biases of three different .....	40
Figure 4-1 Estimated surface pressure biases and RMS errors for the U.S. and Europe. Estimated surface pressure.....	45
Figure 4-2 RMS differences in surface pressure observations vs fraction of stations with annual RMSE less than.....	45
Figure 4-3 Model comparison between reanalysis surface pressure estimates for dry air. Comparison provides .....	47
Figure 4-4 Effects of grid scale on surface pressure errors. Errors induced when relatively coarse resolution.....	48
Figure 4-5 Ensemble RMS differences for radiosonde soundings in upper air observations for 5000 randomly .....	48
Figure 4-6 Representative signal/noise for 20 km nadir sensor to ground path length. Plots show values (left) and.....	50
Figure 4-7 Two-dimensional representation of noise equivalent signal for CO <sub>2</sub> line at 1.5711 μm and 20 km.....	51
Figure 4-8 Equivalent noise signal errors for sample CO <sub>2</sub> line at 1.5711 μm. Minimum equivalent noise for on-line .....	52
Figure 4-9 Sample set of minimum equivalent noise errors for CO <sub>2</sub> lines between 1.57 and 2.05 CO <sub>2</sub> lines centered.....	52
Figure 5-1 Illustration of one approach for an Integrated Path Differential Absorption (IPDA) measurement from .....	54
Figure 5-2 Absorption cross section and relative weight by pressure for an example CO <sub>2</sub> line. (Left) Example of.....	57
Figure 5-3 The CO <sub>2</sub> Laser Sounder measures column CO <sub>2</sub> & O <sub>2</sub> absorption and range to surface. (Left) Nominal .....	69
Figure 5-4 Airborne CO <sub>2</sub> Sounder lidar installation, line sampling approach and parameters. (Top) Photos of the .....	70

Figure 5-5 Results from CO <sub>2</sub> Sounder lidar measurements over a flat Central Valley CA. Data taken with a .....	71
Figure 5-6 Detection of power plant plumes using the CO <sub>2</sub> Sounder lidar. In this flight segment over Four Corners, .....	72
Figure 5-7 Measurements from the 2011 flight over Railroad Valley NV. This area is a flat playa surrounded by.....	72
Figure 5-8 CO <sub>2</sub> Measurements made to the tops of marine stratus clouds. (Left) The ground track of a flight made .....	73
Figure 5-9 Measurements made to the ground through thin cirrus and gaps in cumulus clouds. Data was taken on .....	73
Figure 5-10 Comparison of single column average retrievals from airborne lidar versus altitude. Comparison .....	74
Figure 5-11 An initial example of a two-altitude level retrieval from the 2011 flight over Iowa. This demonstrated.....	75
Figure 5-12 Atmospheric transmittance calculated from a 10 km altitude to the surface showing the Oxygen A-.....	76
Figure 5-13 Block diagram (left) and the timing sequence (right) of the O <sub>2</sub> IPDA Lidar. The optical pulses from.....	77
Figure 5-14 Plots of the results from the O <sub>2</sub> IPDA lidar flights for 2011. Flight 6 (left) and Flight 7 (right). The plots .....	78
Figure 5-15 Results for the O <sub>2</sub> laser from the 2013 flight 2 over California's Central Valley. (Left) Plot of .....	79
Figure 5-16 Architecture of the airborne prototype MFL lidar.....	80
Figure 5-17 The wavelength sampling approach for the airborne MFL lidar and the altitude dependence of the .....	81
Figure 5-18 Sample laser signals detected by the airborne MFL lidar.....	82
Figure 5-19 Photograph of the MFL lidar mounted inside the NASA DC-8 aircraft. ....	83
Figure 5-20 Comparison of airborne measured and modeled CO <sub>2</sub> DAODs. The figure shows flights over .....	85
Figure 5-21 Range discrimination of cloud returns from ground returns using the swept frequency IM-CW.....	87
Figure 5-22 Calculated spectral profile of the O <sub>2</sub> absorption line doublet at 1262.52195 and 1262.5416 nm (c.f.,.....	88
Figure 5-23 A lidar spectral sweep across the O <sub>2</sub> doublet from 6 km altitude on 7 August 2011.....	89
Figure 5-24 Variation of SNR in the measurements of O <sub>2</sub> SNR <sub>DAOD</sub> with range from the DC-8 on 27 July and 3 .....	90
Figure 5-25 Comparison of measured and in-situ derived O <sub>2</sub> DAOD from the DC-8 on 27 July 2011. Measured.....	90

Figure 5-26 LAS with optical bench horizontal, telescope side up, base plate in background. ...	93
Figure 5-27 LAS transceiver in hermetically sealed enclosure. ....	94
Figure 5-28 LAS weighted column CO <sub>2</sub> mole fraction retrievals during flight over Central US. The segment from .....	96
Figure 5-29 Four-Corners Power Plant, New Mexico, U.S showing 3 main clusters of stacks. From left to right, .....	97
Figure 5-30 Weighted column CO <sub>2</sub> retrievals during flyby of the Four-Corners Power Plant at 15 kft pressure.....	98
Figure 5-31 LAS measured surface reflectance during a portion of the “snowline out” flight segment over the .....	99
Figure 5-32 CO <sub>2</sub> retrieval in vicinity of Kirksville, Missouri on March 7, 2013 (Left) JPL nadir camera image of.....	100
Figure 5-33 BBL measurements made shortly after takeoff on August 10 test flight. The anti- correlation of total.....	101
Figure 5-34 Image and plot of the four signals represented in the InGaAs camera focal plane.	102
Figure 5-35 Drawing showing light path in instrument to reach 3 FPs and reference channel. Light reflecting from.....	103
Figure 5-36 Two possible ways that the Multiple FP detector can investigate CO <sub>2</sub> absorptions. The approach on.....	103
Figure 5-37 A Q-switched fiber laser architecture is used to generate multi-line broadband wavelengths near 2.05.....	104
Figure 5-38 Schematic of the 2- $\mu$ m, double-pulsed, CO <sub>2</sub> IPDA lidar. Given an estimate of the O <sub>2</sub> column, a.....	105
Figure 5-39 Comparison of the CO <sub>2</sub> and H <sub>2</sub> O integrated optical depths. (Left) Comparison derived using the.....	106
Figure 5-40 Illustration of 2- $\mu$ m, double-pulsed IPDA lidar for airborne CO <sub>2</sub> measurements. (Left) Integrated, 2-.....	107
Figure 5-41 Block diagram of the space lidar instrument and wavelength-stepped pulse-train. (Left) Simultaneous .....	111
Figure 5-42 Modeled and measured SNR for efficient pulse modulation technique. ( <i>Left top</i> ) Calculations of SNR .....	112
Figure 5-43 Schematic of a stepped wavelength locked source as shown in (Numata et al., 2012). ( <i>Left</i> ) The .....	113
Figure 5-44 The highly sensitive 4x4 element HgCdTe APD array inside a mini- dewar/cryocooler assembly.....	114
Figure 5-45 Concept for a space-based LAS lidar.....	115
Figure 5-46 Comparison of simulated results of DAODs with observations for RRV. The Railroad Valley playa .....	116

Figure 5-47 Simulated 0.1-s  $SNR_{DAOD}$  for the space IM-CW LAS instrument for a range of surface reflectance ..... 116

Figure 5-48 Simulated 0.1-s results for a spaceborne lidar under thin cirrus cloud conditions. The  $CO_2$   $SNR_{DAOD}$  ..... 117

Figure 6-1 Hosted payload mounted to the side of the spacecraft bus. .... 124

**LIST OF TABLES**

Table 1-1 Unique capabilities of the ASCENDS approach .....	7
Table 3-1 ASCENDS Inverse Models Summary.....	19
Table 3-2 Flux Inversion Fractional Error Reduction*.....	34
Table 3-3 ASCENDS Bias Cases .....	35
Table 4-1 Regional differences mean bias and RMSE, and inter-modal range RMSE thresholds (in mb) for GFS analysis.....	46
Table 5-1 Unique capabilities of the ASCENDS Lidar .....	55
Table 5-2 Summary of Measurement Requirements needed for ASCENDS .....	59
Table 5-3 Return Signal Dynamic Range for 1570-nm CO <sub>2</sub> lidar.....	62
Table 5-4 Return Signal Dynamic Range for 2051-nm CO <sub>2</sub> Lidar .....	63
Table 5-5 Return Signal Dynamic Range for 765-nm O <sub>2</sub> Lidar .....	63
Table 5-6 Return Signal Dynamic Range for 1262-nm O <sub>2</sub> Lidar .....	64
Table 5-7 O <sub>2</sub> Sounder Lidar Parameters .....	77
Table 5-8 Airborne MFL Lidar Parameters.....	84
Table 5-9 Line parameters of the O <sub>2</sub> absorption lines .....	88
Table 5-10 JPL airborne LAS instrument parameters .....	94
Table 5-11 Space-based Broad Band Lidar Parameters .....	118
Table 5-12 Comparison of CO <sub>2</sub> state-of-the-art 2- $\mu$ m current and proposed technology with space requirement .....	119
Table 6-1 ASCENDS Generic Instrument Parameters .....	121
Table 6-2 Notional schedule of mission implementation .....	126
Table C-1 Detailed Comparison of Modeling Approaches .....	159

**LIST OF BOXES**

Box 3-1 Simulation of Random Errors ..... 15  
Box 3-2 Flux Estimation Techniques ..... 29  
Box 3-3 Simulation of Systematic Errors ..... 38  
Box C-1 Calculation of Model-Data Mismatch Errors ..... 161

## 1 **Executive Summary**

2 Improved remote sensing observations of atmospheric CO<sub>2</sub> are critically needed to quantify,  
3 monitor, and understand the Earth's carbon cycle and its evolution in a changing climate. The  
4 processes governing ocean and terrestrial carbon uptake remain poorly understood, especially in  
5 dynamic regions with large carbon stocks and strong vulnerability to climate change, for example,  
6 the tropical land biosphere, the northern hemisphere high latitudes, and the Southern Ocean.  
7 Because the passive spectrometers used by GOSAT and OCO-2 require sunlit and cloud-free  
8 conditions, current observations over these regions remain infrequent and are subject to biases.  
9 These shortcomings limit our ability to understand the processes controlling the carbon cycle on  
10 regional to global scales.

11 In contrast, active CO<sub>2</sub> remote-sensing techniques allow accurate measurements to be taken day  
12 and night, over ocean and land surfaces, in the presence of thin or scattered clouds, and at all  
13 times of year. Because of these benefits, the National Research Council recommended the NASA  
14 Active Sensing of CO<sub>2</sub> Emissions over Nights, Days, and Seasons (ASCENDS) mission in the  
15 2007 report Earth Science and Applications from Space: National Imperatives for the Next  
16 Decade and Beyond. The ability of ASCENDS to collect low-bias observations in these key  
17 regions is expected to address important gaps in our knowledge of the contemporary carbon cycle.

18 The ASCENDS ad hoc Science Definition Team (SDT), comprised of carbon cycle modeling and  
19 active remote sensing instrument teams throughout the U.S., has worked to develop the mission's  
20 requirements and advance its readiness since 2008. Numerous scientific investigations have been  
21 carried out to identify the benefit of active CO<sub>2</sub> remote sensing measurements for improving our  
22 understanding of CO<sub>2</sub> sources and sinks. This report summarizes their findings and  
23 recommendations to date, based on mission modeling studies, analysis of ancillary meteorological  
24 data products, development and demonstration of candidate technologies, and design studies of  
25 the ASCENDS mission concept.

26 To date, the ASCENDS modeling studies have demonstrated that:

- 27 1. ASCENDS will resolve statistically significant differences in total column CO<sub>2</sub>  
28 concentrations, resulting from foreseeable changes in surface flux over the entire globe.  
29 These flux changes could include identifying CO<sub>2</sub> emissions from permafrost thaw at high  
30 latitudes, shifting patterns in regional fossil fuel emissions, the evolving nature of the  
31 Southern Ocean carbon flux, and/or changes to tropical and mid-latitude terrestrial sinks.
- 32 2. ASCENDS will substantially advance our understanding of the carbon cycle through  
33 improved flux estimates with reduced uncertainty at global to regional scales. Reduced  
34 flux uncertainties at regional scales are necessary for improved understanding of the  
35 processes controlling long-term carbon sinks.
- 36 3. ASCENDS measurements also have the potential to reduce biases due primarily to lower  
37 susceptibility to errors from atmospheric scattering and changes in illumination geometry.  
38 This can contribute significantly towards improving constraints on surface fluxes beyond  
39 passive sensors such as GOSAT and OCO-2.

40 During the past decade, NASA has invested in the development of several different Integrated  
41 Path Differential Absorption (IPDA) lidar approaches and associated technologies that are  
42 candidates for ASCENDS. The IPDA approach measures the range to the scattering surface, and  
43 the column abundance and average mixing ratio of atmospheric CO<sub>2</sub> with increased sensitivity

44 throughout the mid- and lower troposphere. Several aircraft field campaigns have already  
45 demonstrated that:

- 46 1. Accurate CO<sub>2</sub> column mixing ratios can be retrieved from airborne lidar data.
- 47 2. Evaluation against in situ aircraft observations show that CO<sub>2</sub> column absorption  
48 measurements can be made with high precision and low bias over a wide range of surface  
49 types and between scattered clouds.
- 50 3. High-quality observations can be made to cloud tops and through thin clouds and aerosol  
51 layers.

52 In addition, evaluation of the magnitude of errors in present atmospheric models has helped to  
53 clarify the need for ancillary measurements and to define the error budget for the ASCENDS  
54 measurements. Statistical analysis of meteorological products from three different atmospheric  
55 modeling centers shows that uncertainty in current surface pressure estimates from models is  
56 typically less than 0.1% except in high latitudes regions. These findings will be used to evaluate  
57 the need and required performance for a coincident oxygen lidar measurement to meet the desired  
58 CO<sub>2</sub> mixing ratio accuracy for ASCENDS.

59 These studies and field activities have greatly improved our understanding of the space-based  
60 capabilities required for ASCENDS, and represent significant progress toward meeting the  
61 demands of an active remote-sensing mission. Integrating results from the measurement  
62 campaigns and modeling studies, the ASCENDS SDT has developed a preliminary set of  
63 measurement requirements as well as a study of the ASCENDS mission that demonstrates the  
64 feasibility of deploying the observatory. The results of this study show that multiple  
65 commercially-available spacecraft buses should be able to accommodate an ASCENDS  
66 instrument with minor mission-specific modifications. In addition, the Falcon 9 or Atlas V  
67 (EELV) launch vehicles can accommodate an ASCENDS observatory with the parameters used in  
68 this study.

69 Finally, this report outlines areas where further research is needed. These include but are not  
70 limited to:

- 71 1. Modeling studies that incorporate error statistics from the OCO-2 mission, assess the  
72 impact of errors in meteorological parameters on flux estimates, and evaluate the impact  
73 of different orbit choices and vertical information on flux inference.
- 74 2. Aircraft campaigns targeting observations over high latitudes and forested areas, and also  
75 performed to coincide with OCO-2 overpasses.
- 76 3. Technology development focused on demonstrating the required laser power for space,  
77 and further improving O<sub>2</sub> lidar capabilities.

78 Such studies are needed to improve traceability from science questions to measurement  
79 requirements. The ASCENDS SDT plans to continue working on these activities to advance  
80 mission readiness in coordination with the carbon cycle research community.

## 81 **1. Introduction**

### 82 **1.1 Justification and Key Science Questions**

83 The fourth and fifth Assessment Reports of the Intergovernmental Panel on Climate Change  
84 (IPCC) conclude that warming of the global climate system is unequivocal, and anthropogenic  
85 emissions of greenhouse gases are responsible for most of the increase (IPCC, 2007 and IPCC,  
86 2013). Additionally, the reports state that the interaction between the global carbon cycle and the  
87 physical climate system is still a substantial source of uncertainty in climate projections.

88 The difference between observed increases in atmospheric CO<sub>2</sub> concentrations and anthropogenic  
89 CO<sub>2</sub> emissions indicate that the natural terrestrial and oceanic sinks have absorbed approximately  
90 55% of the CO<sub>2</sub> generated by human activities. There are, however, significant year to-year  
91 variations. Although these variations are attributed to changes in the terrestrial and oceanic sinks,  
92 the processes governing sink strengths and the relative partitioning of CO<sub>2</sub> between terrestrial,  
93 oceanic, and atmospheric reservoirs are poorly understood.

94 Errors in the representation of these processes in existing coupled carbon-climate models lead to  
95 large uncertainties in long-term climate projections. Therefore improving our understanding of  
96 carbon sink processes is critical to improving projections of atmospheric CO<sub>2</sub> levels and Earth's  
97 climate.

98 In order to address the gaps in our current understanding of atmospheric CO<sub>2</sub> and its relationship  
99 to climate change, three overarching needs have been defined (NASA, 2008). They are to:

- 100 • *Improve our understanding of the current magnitude and distribution of terrestrial and*  
101 *oceanic sources and sinks, distinguishing between natural and anthropogenic sources*  
102 *and sinks,*
- 103 • *Improve our understanding of the time scales of natural sources and sinks, from short*  
104 *(e.g. diurnal) to medium (seasonal/annual) to extended (climatological) time scales,*  
105 *including processes resulting from ecosystem/biosphere disturbances, and*
- 106 • *Improve our ability to predict/model long-term changes in the climate system due to*  
107 *natural variability of carbon sources and sinks, as well as the transport of carbon*  
108 *through the atmosphere.*

109 Globally distributed atmospheric CO<sub>2</sub> measurements are critical to address these needs. The  
110 fluxes of CO<sub>2</sub> from the surface vary in both space and time. The resulting gradients in  
111 concentration caused by the fluxes are small and are mixed and integrated by atmospheric  
112 transport. Sampling atmospheric CO<sub>2</sub> in time and space can be used, along with appropriate  
113 transport and inversion models, to quantify the surface fluxes. The remote sensing challenge is to  
114 provide the atmospheric CO<sub>2</sub> measurements with sufficient global coverage, accuracy and  
115 sampling frequency to allow inferring the locations and magnitudes of the sources and sinks.

### 116 **1.2 CO<sub>2</sub> Measurements Near the Surface**

117 The modern atmospheric CO<sub>2</sub> measurement record began in 1957 with flask measurements taken  
118 atop Mauna Loa. These provided samples of the global background concentration of atmospheric  
119 CO<sub>2</sub>. Over the years, our understanding of the spatial and temporal variations in atmospheric CO<sub>2</sub>  
120 concentrations has improved via the establishment of additional ground measurement sites  
121 providing both surface and tower measurements, aircraft campaigns and routine airborne  
122 observations, and most recently, contributions from space-based remote sensing. Yet there remain

123 significant gaps in our understanding that result from limited measurements, particularly related  
124 to the distribution and variability of terrestrial and oceanic sinks and the processes controlling this  
125 variability.

### 126 **1.3 Space Missions Using Passive Remote Sensing**

127 The important first steps toward measuring greenhouse gases globally from space were  
128 demonstrated using spectrometers that viewed the Earth's thermal emission or reflected sunlight.  
129 The initial passive radiometer and spectrometer missions for GHG observations included  
130 SCIAMACHY on ENVISAT, AIRS, and IASI. Their observations have been critical in  
131 demonstrating using space-based spectrometers to address questions about atmospheric  
132 composition. However, all these early multi-purpose instruments had relatively coarse spectral  
133 resolution and large measurement footprints that limited their coverage and the precisions and  
134 accuracies of their retrievals.

135 Subsequently two satellite missions have been developed specifically for measuring atmospheric  
136 CO<sub>2</sub> and CH<sub>4</sub> using higher resolution passive spectrometers. The Japanese Greenhouse gas  
137 Observing Satellite (GOSAT) was launched in 2009. The precision of GOSAT's XCO<sub>2</sub> and XCH<sub>4</sub>  
138 measurements has been assessed by comparing its measurements to those from ground-based  
139 spectrometers, in particular those of the Total Column Concentration Observing Network  
140 (TCCON).

141 In order to extend CO<sub>2</sub> observations from space, NASA's OCO-2 mission was launched during  
142 July 2014. While it does not measure CH<sub>4</sub>, the OCO-2 mission uses optical spectrometers with  
143 higher sensitivity detectors, and it views the Earth in smaller footprints. Preliminary OCO-2 data  
144 show higher precision XCO<sub>2</sub> observations from space, and it is hoped these will improve  
145 knowledge of CO<sub>2</sub> sources and sinks [5]. More details on these missions are in Chapter 2.

### 146 **1.4 Potential Benefits of Active (Laser-Based) CO<sub>2</sub> Measurements**

147 To date, observations of CO<sub>2</sub> from space have used passive remote sensing techniques. While  
148 their contributions to understanding the global carbon cycle are significant, passive measurement  
149 techniques have some inherent limitations. When conditions are favorable, these approaches  
150 allow accurate measurements of the atmospheric gases. However favorable conditions require  
151 sunlit scenes, cloud-free conditions, and accurate estimates of surface elevation within the spatial  
152 resolution elements.

153 The Earth's atmosphere is complex and optical scattering by clouds and aerosols is common. For  
154 passive sensors, this scattering causes variability in the optical path length and hence it  
155 contributes to spatially and temporally varying biases. There are also wide variations in surface  
156 elevation, due to topography and trees, which change the length of the measurement path and the  
157 CO<sub>2</sub> column. The accuracy of measurements at large solar zenith angles is also limited due to this  
158 scattering and by variability in surface reflectance. The resulting sparse coverage of passive  
159 spectrometers at high latitudes is a serious limitation, particularly for the Northern Hemisphere,  
160 since these regions exhibit substantial emissions during the winter as well as other times of year.

161 In contrast, an active (laser) remote sensing mission carries its illumination source whose  
162 characteristics have been carefully optimized for these measurements. It involves a simpler fixed  
163 observational geometry, with a common vertical illumination and observation path. The range -  
164 resolved laser measurements eliminate errors from atmospheric scattering. This approach allows  
165 measurements to be taken day and night, over ocean and land surfaces, at all latitudes, and at all

166 times of year. Active CO<sub>2</sub> remote sensing also enables enhanced sensitivity to CO<sub>2</sub> in the lower  
167 troposphere, where the atmospheric concentrations respond most strongly to surface fluxes. Over  
168 oceans, a lidar enables more frequent observations of the southern ocean, especially in the  
169 wintertime, where dark oceans are virtually inaccessible to passive systems.

170 The ability of active CO<sub>2</sub> sensors to measure during day and night provides for at least twice the  
171 coverage of passive systems that rely on reflected sunlight. Nocturnal measurements with  
172 atmospheric weighting toward the surface are desired for investigations of respiration and urban  
173 areas. Since lidar can make effective measurements regardless of local observation time, various  
174 non-Sun synchronous orbits also can be considered to provide additional information about  
175 diurnal cycles on different time scales.

176 Depending on the approach chosen, there are other potential benefits from lidar measurements.  
177 Higher spatial sampling, for example, would allow detection of strong, localized gradients in CO<sub>2</sub>  
178 concentration to facilitate investigations in complex terrain. It could also enable measurements  
179 through smaller gaps in clouds and to cloud tops, significantly improving the measurement  
180 density and coverage under these conditions.

## 181 **1.5 Objectives for ASCENDS**

182 To address these unmet needs, more accurate remote sensing measurements of atmospheric CO<sub>2</sub>  
183 are required with more complete global coverage. In the US, the NRC's 2007 Decadal Survey  
184 (NAP, 2007) recommended the Active Sensing of CO<sub>2</sub> Emissions over Nights, Days, and Seasons  
185 (ASCENDS) mission (NASA, n.d.). The objectives of ASCENDS are to:

- 186 1) Quantify the global spatial distribution of atmospheric CO<sub>2</sub> on scales of weather  
187 models in the 2010-2020 era;
- 188 2) Quantify the current global spatial distribution of terrestrial and oceanic sources and  
189 sinks of CO<sub>2</sub> on 1-degree grids at weekly resolution; and
- 190 3) Provide a scientific basis for future projections of CO<sub>2</sub> sources and sinks through data-  
191 driven enhancements of the Earth-system process modeling.

192 An important consideration for this mission is that the CO<sub>2</sub> fluxes from the surface cause only  
193 small changes in the spatial distributions of CO<sub>2</sub> concentrations in the lower troposphere. Hence  
194 the remote sensing challenge is to accurately measure these small changes in in CO<sub>2</sub>  
195 concentrations globally. The required levels of measurement uncertainty that must be attained  
196 over a wide range of atmospheric and surface conditions are typically <0.25% (< 1 ppm).

## 197 **1.6 The ASCENDS Approach**

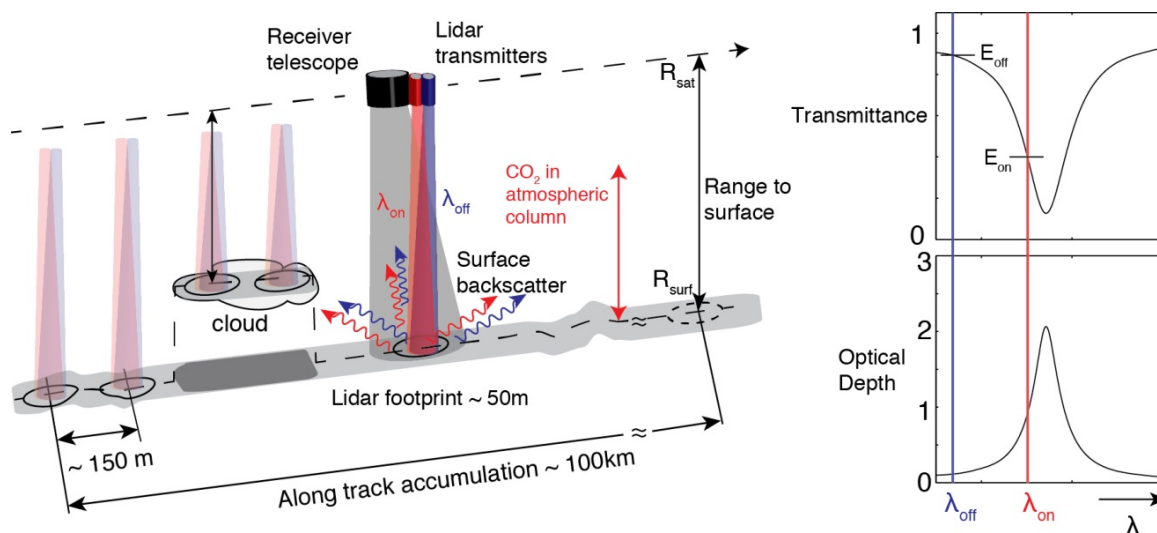
198 A lidar utilizes its own specialized light source and use a common illumination and observation  
199 path. Greenhouse gas measurements can be made using a range-resolved integrated path  
200 differential absorption (IPDA) lidar approach. These measurements are independent of solar angle  
201 and of prior knowledge of scattering surface elevation. Measurements with high precision and  
202 low bias can be made under a wide variety of atmospheric and topographic conditions thus  
203 allowing extended spatial coverage. The lidar can sample a selected gas absorption line, measure  
204 the surface elevation, and retrieve the gas mixing ratio. The range resolving capability of the lidar  
205 enables accurate measurement of scattering surface elevation and atmospheric path length, as well  
206 as excluding biases due to the optical scatter by clouds and aerosols.

207 The basic approach for the ASCENDS measurements of CO<sub>2</sub> is shown in Figure 1.1. This  
208 example depicts a pulsed approach using the minimum of two wavelengths to sample the

209 absorption line. The figure shows two beams (red and blue) directed at nadir, corresponding to  
 210 the laser pulses tuned on and off the absorption line. They pass through the atmospheric column  
 211 containing an unknown concentration of  $\text{CO}_2$  and illuminate nearly the same area on the  
 212 scattering surface, either the Earth's surface or cloud top. The light reflected by the surface passes  
 213 back through the atmosphere and a small fraction is collected by the receiver telescope. The lidar  
 214 receiver measures the energies of the on- and off-line pulses ( $E_{on}$  and  $E_{off}$ ) and the range to the  
 215 surface.

216 The insert shows a sketch of the shape of the  $\text{CO}_2$  line's transmission (top) and optical depth  
 217 when measured from space. The maximum  $\text{CO}_2$  absorption occurs for laser wavelengths tuned to  
 218 the line's center. The wavelength of the laser's "on-line" pulse is usually selected to be offset  
 219 from the peak of the  $\text{CO}_2$  absorption line and is indicated by the red vertical line. The wavelength  
 220 of the laser's "off-line" pulse, that undergoes negligible  $\text{CO}_2$  absorption, is indicated by the blue  
 221 line.

222



223

224 **Figure 1-1** One approach for an Integrated Path Differential Absorption (IPDA) measurement from space to  
 225 scattering surfaces on or near the Earth's surface. While there are several different IPDA measurement approaches,  
 226 this drawing is for the two-wavelength pulsed approach that was considered for the ESA A-SCOPE Mission [8]  
 227 Several IPDA approaches use more than two wavelengths to sample the absorption line shape to provide additional  
 228 information.

229 The  $\text{CO}_2$  column abundance is calculated from the lidar's measurement of range to the scattering  
 230 surface and ratio of the energies in the on- and off-line echo pulse signals. The column integrated  
 231 mixing ratio  $X_{\text{CO}_2}$  is calculated using additional information about the density of dry air in the  
 232 same measurement column. In the present baseline approach for ASCENDS, a simultaneous  $\text{O}_2$   
 233 lidar measurement is being considered as an additional capability of the instrument. Another  
 234 option may be to use a numerical weather prediction model's estimate of surface pressure at the  
 235 location and time of the  $\text{CO}_2$  lidar measurement to calculate the  $\text{CO}_2$  mixing ratio.

## 236 1.7 The Benefits of the ASCENDS Approach

237 The IPDA lidar approach offers a number of unique and important capabilities for ASCENDS,  
 238 allowing accurate column measurements of  $\text{CO}_2$  with extended coverage. These are summarized  
 239 in Table 1.

240 For these reasons the ASCENDS approach, using an orbital IPDA lidar, will allow accurate  
 241 measurements of greenhouse gas concentrations over a much wider variety of conditions than is  
 242 possible with passive sensors. These more accurate measurements, with wider spatial coverage,  
 243 are key to address important questions about the locations, strengths and evolution of the regional  
 244 CO<sub>2</sub> fluxes needed for climate models.

245 **Table 1-1 Unique capabilities of the ASCENDS approach**

1. The lidar measurements work well in darkness and are independent of sun angle.
2. It measures in a single vertical column, using a common illumination and observation path.
3. The same nadir-zenith viewing geometry is also the “glint mode” for the ocean and water surfaces. This allows ocean and land measurements to be made continuously using the same spacecraft orientation.
4. The laser line-width is much smaller than the gas absorption line, and so the absorption lines measured are fully resolved. Using on-line measurements on the side of the gas line allows weighting of the column measurements preferentially in the lower troposphere, which contains a stronger signature from the surface fluxes. On-line measurements near the peak of the line also allow additional measurements weighted toward the upper atmosphere.
5. The laser can utilize gas absorption lines to minimize temperature sensitivity and contamination from other gases. The spectroscopic knowledge needed for accurate retrievals involves only the region around the single gas line sampled by the lidar, and is independent of the solar spectrum.
6. The small (typically 100m) lidar spot size also enables utilizing small gaps in clouds to obtain gas column measurements to the surface in partially cloudy scenes and through broken cloud fields.
7. The lidar measures range to the scattering surface simultaneously with column gas absorption. This provides accurate determination of the scattering surface elevation and column length. This also allows simple range gating to eliminate signals scattered by thin clouds and aerosols. The range measurements are particularly important when measuring over regions with varying topography and tree cover that cause the range to vary significantly.
8. The ranging information also enables accurate column measurements to the tops of some clouds, providing some vertical resolution in the column concentrations.

246

## 247 **1.8 Overview of NASA’s Development of ASCENDS Mission**

248 Over the past decade NASA has been supporting the development of several lidar concepts and  
 249 their associated technologies for its planned ASCENDS mission, as described in the 2007 US  
 250 National Research Council’s Decadal Survey for Earth Science [10]. The approaches all use the  
 251 IPDA technique. An ASCENDS ad hoc science definition team leads the mission definition  
 252 activities. Team members are from NASA Goddard, NASA Langley (LaRC) and NASA Jet  
 253 Propulsion Laboratory (JPL) as well as the University of Oklahoma, Colorado State University,  
 254 and others. Their work has focused on four areas, including developing the mission’s science  
 255 objectives and requirements, conducting science mission modeling studies (Observing System  
 256 Simulation Experiments) for various parameters of the space mission, and carrying out initial  
 257 engineering studies of potential lidar and spacecraft. NASA’s Earth Science Technology Office  
 258 has supported the development of the key lidar technologies used by the investigators.

259 A large fraction of the ASCENDS work has been directed at developing and demonstrating  
260 candidate lidar approaches from aircraft. Candidate lidar techniques that include two direct  
261 detection lidar approaches have been demonstrated that measure both range and a selected CO<sub>2</sub>  
262 lines near 1571 and 1572 nm. One uses sine-wave laser intensity modulation that is swept in  
263 modulation frequency. The other uses pulsed laser modulation that samples the absorption line at  
264 multiple wavelengths and uses a time resolved receiver to measure the laser backscatter profile  
265 and range to the surface. Two approaches have demonstrated measurements of the CO<sub>2</sub> line near  
266 2051 nm. A CW heterodyne approach measures this line at two wavelengths, and a pulsed direct  
267 detection approach that measures both range and CO<sub>2</sub> absorption using the same line.

268 In parallel with the technique development and system-level demonstrations, Observing System  
269 Simulation Experiment (OSSE) studies are being conducted to assess the characteristics of the  
270 CO<sub>2</sub> fluxes that can be inferred from space-based lidar measurements with various levels of  
271 measurement precision and accuracy. The mission simulations have used a lidar measurement  
272 model with surface reflectivity maps from MODIS and information on cloud and aerosol heights  
273 and extinctions from the Calipso Mission [11]. OSSE analysis has identified some mission  
274 science tradeoffs and the formulation of an initial set of ASCENDS measurement requirements.  
275 Preliminary instrument and space mission engineering studies also have been conducted on lidar  
276 candidates that are suitable for the mission. The payload parameters are consistent with a  
277 medium-sized spacecraft bus to be flown in a polar ~400 km altitude orbit.

## 278 **1.9 Remainder of Report**

279 The remaining chapters of this report expand on the topics briefly introduced here. Chapter 2  
280 summarizes the science of CO<sub>2</sub> and history of atmospheric CO<sub>2</sub> measurements. Chapter 3  
281 summarizes present studies on the impact of Ascends Mission on carbon cycle science and  
282 Modeling. Chapter 4 assesses the influence from uncertainties in the atmospheric state on the  
283 space-based measurements. Chapter 5 provides a summary of the mission measurement  
284 requirements, along with an overview of the various lidar techniques that may be candidates for  
285 the mission. Several have demonstrated promising measurements during airborne campaigns.  
286 This chapter also has a brief overview of ongoing work and discusses scaling the approaches to  
287 space. Chapter 6 summarizes the result from an initial space mission engineering study. Finally  
288 Chapter 7 summarizes the report and discusses next steps.

289

## 290 **2. Science of Atmospheric CO<sub>2</sub> and Measurement History**

### 291 **2.1 Introduction**

292 At the beginning of the industrial era in the late 18<sup>th</sup> century, the atmospheric carbon dioxide  
293 (CO<sub>2</sub>) concentration (or “dry air mole fraction”) was about 280 parts per million (e.g. Etheridge et  
294 al., 1996). Since that time, fossil fuel combustion, deforestation, and other human activities have  
295 emitted more carbon dioxide (CO<sub>2</sub>) into the atmosphere each decade, driving the weekly average  
296 atmospheric CO<sub>2</sub> mole fraction past the 400 ppm mark in May 2013. Recent estimates of fossil  
297 fuel emissions derived from fossil fuel inventories (Marland et al., 2009; Guan et al., 2012;  
298 Andres et al. 2012) show that this source alone was adding more than 36 billion tons (Gigatons or  
299 Gt) of CO<sub>2</sub> to the atmosphere each year (Peters et al., 2012; Le Quéré et al., 2013).

300 The CO<sub>2</sub> emissions from burning fossil fuels are superimposed on an active, global carbon cycle  
301 that regulates the exchange of carbon among reservoirs in the ocean, land biosphere, and  
302 atmosphere (SOCCR (State of the Carbon Cycle Report), 2008). Each year, the land biosphere  
303 absorbs and then re-emits over 440 Gt of CO<sub>2</sub> into the atmosphere through photosynthesis and  
304 respiration, respectively. The ocean is also a massive reservoir of carbon, exchanging about 330  
305 Gt of CO<sub>2</sub> with the atmosphere each year, as CO<sub>2</sub> is exchanged across the air-sea interface.  
306 Because these natural fluxes of CO<sub>2</sub> are roughly balanced, ice core records show they have  
307 maintained atmospheric CO<sub>2</sub> mole fractions between ~180 and 300 ppm for at least the past  
308 several hundred thousand years (cf. Archer et al., 2009). The CO<sub>2</sub> emissions associated with  
309 human activities are still only about 1/20<sup>th</sup> as large as these natural fluxes, but they are not  
310 balanced, and are now pushing the atmospheric CO<sub>2</sub> mole fractions to levels not seen throughout  
311 the 800,000 year ice core record (Lüthi et al., 2008) and perhaps for as long ago as 3-4 million  
312 years (cf. Badger et al., 2013).

313 A precise, continuous, record of direct atmospheric CO<sub>2</sub> measurements was started in 1958, when  
314 Charles Keeling of Scripps Institute of Oceanography installed a CO<sub>2</sub> monitoring station on the  
315 flanks of the Mauna Loa volcano in Hawaii (Keeling, 1960). The initial measurements showed  
316 CO<sub>2</sub> mole fractions near 315 ppm, about 35 ppm above the pre-industrial values of ~280 ppm.  
317 Within a couple of years, his measurements clearly documented the global atmospheric signature  
318 of photosynthesis and respiration by land plants. They showed a ~7 ppm CO<sub>2</sub> drawdown during  
319 the northern hemisphere spring and summer, when forests and grasslands were growing rapidly  
320 and a comparable CO<sub>2</sub> buildup during fall and winter when these plants dropped their leaves and  
321 went dormant or died. As this measurement record continued through the 1960’s and 1970’s, a  
322 clear trend emerged, revealing an increase in the background CO<sub>2</sub> mole fraction of over 1 ppm per  
323 year.

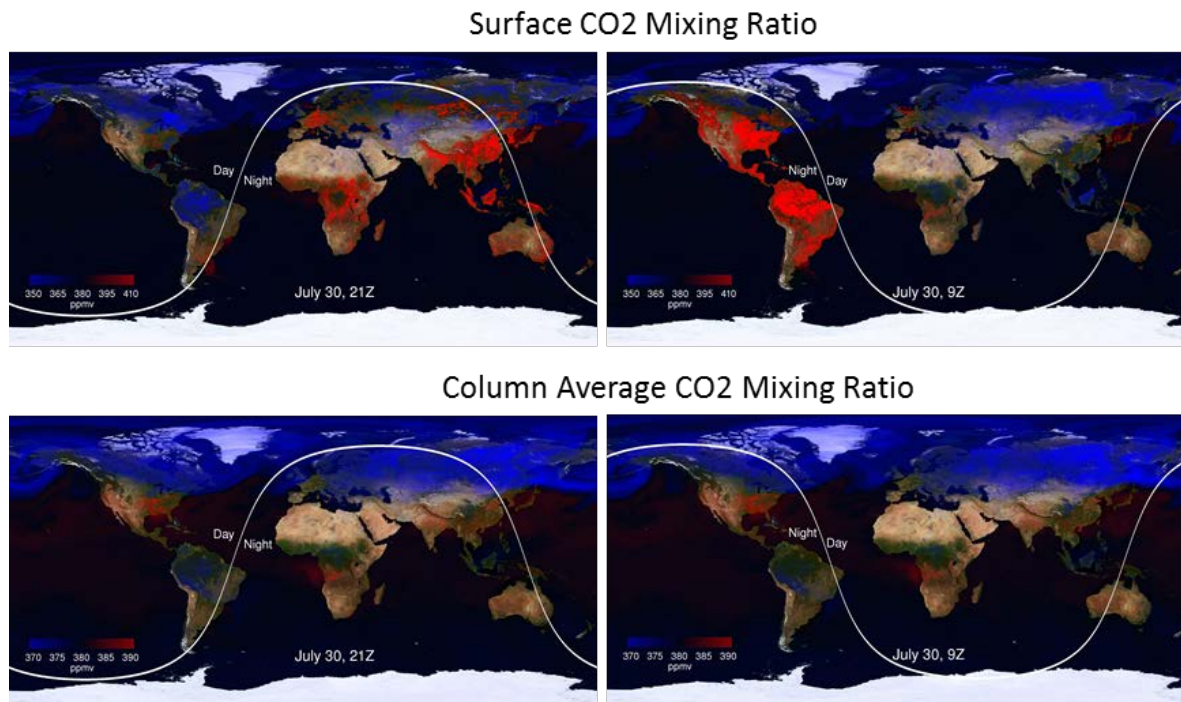
324 The National Oceanic and Atmospheric Administration (NOAA) joined the atmospheric CO<sub>2</sub>  
325 monitoring effort in 1974. The NOAA Earth System Research Laboratory Global Monitoring  
326 Division (ESRL GMD) now operates the Carbon Cycle Greenhouse Gas (CCGG) Cooperative  
327 Air Sampling Network, which currently includes 71 surface stations and 17 vertical profiling  
328 sites. This network has been incorporated into the World Meteorological Organization (WMO)  
329 Global Atmospheric Watch (GAW) Program, which now includes over 150 surface stations that  
330 report CO<sub>2</sub> mole fraction measurements on time scales varying from minutes to one week. These  
331 data are collected and distributed by the World Data Centre for Greenhouse Gases (WDCGG) at  
332 the Japan Meteorological Agency. Stringent quality control procedures and frequent, rigorous  
333 calibration efforts ensure that these measurements from these stations are not only extremely

334 precise, but also highly accurate, through comparisons to standards with accuracies of ~0.2 ppm  
335 (cf. Conway et al., 2009; Conway et al., 1994; Zhao and Tans, 2006; Dlugokencky et al. 2013;  
336 Tans and Keeling, n.d.).

337 Recent measurements from this surface-based greenhouse gas network show that the annual  
338 growth rate of CO<sub>2</sub> has increased by about a factor of two since the 1960's, and now exceeds 2  
339 ppm (0.5%) each year. Comparisons of these measurements with CO<sub>2</sub> emission inventories  
340 reveal an intriguing puzzle. If all of the CO<sub>2</sub> emitted by human activities remains in the  
341 atmosphere, the atmospheric CO<sub>2</sub> abundance should be increasing at twice this rate. This  
342 apparent discrepancy was initially somewhat surprising because CO<sub>2</sub> is also a chemically stable  
343 atmospheric constituent, with an estimated atmospheric half-life of almost 900 years. The  
344 accuracies of both the CO<sub>2</sub> emissions estimated from fossil fuel inventory and the atmospheric  
345 measurements are more than adequate to resolve a deficit this large. Apparently, since the  
346 beginning of the industrial age, natural "sinks" in the ocean and land biosphere have kept pace  
347 with the rapidly growing emission rates, and are now absorbing slightly over half of the CO<sub>2</sub>  
348 emitted by human activities (cf. Le Quéré et al., 2013).

349 As atmospheric CO<sub>2</sub> is absorbed by the ocean, it produces carbonic acid, and recent  
350 measurements of increases in the ocean acidity indicate that the ocean has been absorbing about  
351 half of the "missing" CO<sub>2</sub>. The rest (~ 9.6 Gt CO<sub>2</sub> / year) is apparently being absorbed by sinks in  
352 the terrestrial biosphere, whose identity, location, and driving mechanisms are still very poorly  
353 understood. While they absorb about half of the CO<sub>2</sub> emitted by human activities, when averaged  
354 over decadal time scales, their efficiency appears to vary dramatically from year to year. In some  
355 years, they absorb almost all of CO<sub>2</sub> emitted by human activities, while in others they absorb  
356 almost none (Dlugokencky et al. 2013; Tans and Keeling, n.d.). The processes responsible for  
357 modulating the efficiency of these sinks from year to year are largely unknown. There are also  
358 large uncertainties in the response of these natural sinks to climate change. Will they continue to  
359 absorb roughly half of all the CO<sub>2</sub> emitted by human activities, or will they eventually saturate, or  
360 perhaps even become sources as the climate changes in response to greenhouse-gas-induced  
361 warming? An improved understanding of these natural sinks and the processes that control them  
362 is therefore critical for predictions of future atmospheric CO<sub>2</sub> increases and their impact on the  
363 climate.

364 An improved understanding of CO<sub>2</sub> emissions from human activities is also needed to predict  
365 future CO<sub>2</sub> growth rates. Until recently, these emissions were dominated by fossil fuel  
366 combustion in the developed world. The inventory-based CO<sub>2</sub> emission estimates have grown  
367 progressively more accurate for this particular source, with uncertainties as small as ~5% in  
368 Europe and North America (cf. EPA, 2010; Boden et al. 2013). However, since the turn of the 21<sup>st</sup>  
369 century, fossil fuel CO<sub>2</sub> emissions from China, India, the Russian Federation, and other  
370 developing nations have grown rapidly, and now account for more than 57% of all emissions  
371 from fossil fuel combustion (cf. Le Quéré et al., 2013). The uncertainties in these emissions are  
372 much higher than those for Europe and North America, and their future rate of increase (currently  
373 5.9%/year for China) is difficult to predict. CO<sub>2</sub> emissions from other sources in the developing  
374 world, including biomass burning and other land use practices, are also less well known. When  
375 these uncertainties in CO<sub>2</sub> emission sources are combined with those associated with possible  
376 changes in natural CO<sub>2</sub> sinks, predictions of the atmospheric CO<sub>2</sub> concentration at the end of this  
377 century are uncertain by amounts exceeding the current atmospheric CO<sub>2</sub> abundance.



378  
379 **Figure 2-1** Simulated surface (top) and column average (bottom) CO<sub>2</sub> fields for July from the Goddard Earth  
380 Observing System Model, Version 5 (GEOS-5; Ott et al., 2014) illustrate the effects of diurnal variations in surface  
381 sources. The white line indicates the position of the terminator.

382 The quantity and accuracy of the measurements of CO<sub>2</sub> and other greenhouse gases from the  
383 surface-based greenhouse gas monitoring network have improved progressively since 1957, and  
384 now produce a highly accurate integral constraint on the global abundance of CO<sub>2</sub> and its rate of  
385 change. These precise atmospheric measurements have been augmented by CO<sub>2</sub> flux networks,  
386 that quantify the exchange of CO<sub>2</sub> between the surface and atmosphere associated with natural  
387 processes. Ground-based remote sensing measurements of the column-average dry air mole  
388 fraction of CO<sub>2</sub>, CH<sub>4</sub> (Methane), and other gases by the 21-station Total Carbon Column  
389 Observing Network (TCCON) are providing additional insight into the emission, absorption, and  
390 transport of the species (cf. Keppel-Aleks et al., 2012; Geibel et al., 2012; Wennberg et al., 2012;  
391 Messerschmidt et al., 2013; Wunch et al., 2013).

392 The existing ground based greenhouse gas network was not designed to quantify emissions from  
393 large point sources, such as cities or power plants. In fact, most of its stations were deployed  
394 away from large point sources, to record large-scale global trends. The simulation of the  
395 atmospheric CO<sub>2</sub> distribution shown in Figure 2.1 illustrates another reason why it has been  
396 impossible to identify and study these sinks with the existing ground-based network. As CO<sub>2</sub> is  
397 emitted into the atmosphere or absorbed by surface processes, the resulting CO<sub>2</sub>-rich or CO<sub>2</sub>-poor  
398 air is transported by the prevailing winds, mixing the CO<sub>2</sub> with the ambient air mass. To track  
399 these air masses, the measurement system must be able to resolve the wind field as well as the  
400 spatial scales of the sources and sinks. This is challenging because the atmosphere already  
401 contains a substantial amount of CO<sub>2</sub> (~400 ppm), such that even the largest sources rarely  
402 produce CO<sub>2</sub> perturbations larger than 10% near the surface, where their amplitudes are largest.  
403 The amplitude of these CO<sub>2</sub> anomalies decays rapidly with altitude, yielding column-integrated

404 variations in the background CO<sub>2</sub> distribution that are almost always less than 2%, and typically  
405 no larger than a few tenths of a percent on local to regional scales.

## 406 **2.2 History of CO<sub>2</sub> Measurements From Space**

407 The ground based greenhouse gas monitoring network is reasonably dense in some areas (e.g.  
408 North America, Europe), but far more sparse elsewhere, especially over tropical and polar land  
409 masses and the ocean basins. A dramatic expansion of this network would be needed to identify  
410 and quantify sources and sinks of CO<sub>2</sub> on local to regional scales over the globe. One way to  
411 expand the spatial and temporal resolution and sampling of CO<sub>2</sub> observations is to acquire global  
412 measurements at high spatial resolution from space (Rayner and O'Brien 2001; O'Brien and  
413 Rayner, 2002; Rayner et al., 2002; Houweling et al., 2004; Chevallier et al., 2007; Hungershoefer  
414 et al., 2010). The principle challenge to this approach has been the need for precise  
415 measurements of CO<sub>2</sub> near the surface, where most sources and sinks are located. Thermal  
416 infrared (5 to 15 micron) temperature sounders such as the NASA Atmospheric Infrared Sounder  
417 (AIRS) and the CNES (Centre National d'Etudes Spatiales (French Space Agency)) Infrared  
418 Atmospheric Sounding Interferometer (IASI) routinely acquire measurements within atmospheric  
419 CO<sub>2</sub> bands, where CO<sub>2</sub> absorbs and emits thermal radiation. These measurements typically yield  
420 CO<sub>2</sub> mixing ratios with accuracies of ~1% at altitudes in the middle troposphere (~5 km), but  
421 have little or no sensitivity near the surface (Chevallier et al., 2009).

422 Estimates of the column averaged CO<sub>2</sub> dry air mole fraction, XCO<sub>2</sub>, can be retrieved from space-  
423 based observations of reflected sunlight in near infrared CO<sub>2</sub> and O<sub>2</sub> bands. The European Space  
424 Agency's (ESA) EnvisAT (Environmental SATellite) SCIAMACHY (SCanning Imaging  
425 Absorption Spectrometer for Atmospheric Cartography) and Japanese Greenhouse gases  
426 Observing SATellite (GOSAT) TANSO-FTS (Thermal And Near infrared Sensor for carbon  
427 Observation-Fourier Transform Spectrometer) were the first two satellite instruments designed to  
428 use this approach. SCIAMACHY returned global maps of XCO<sub>2</sub> and XCH<sub>4</sub> from 2002 – 2012.  
429 The precision of its measurements over land eventually approached ~1 to 2 percent. However, the  
430 instrument's low sensitivity over dark surfaces precluded useful observations over the ocean and  
431 its large (30 km by 60 km) sounding footprints were often contaminated by clouds.

432 GOSAT was launched in January, 2009, and flies in a 666 km altitude, sun synchronous orbit  
433 with a 12:47 PM equator crossing time and a 3-day ground track repeat cycle. Its Thermal And  
434 Near infrared Sensor for carbon Observation (TANSO) Fourier Transform Spectrometer (FTS)  
435 has returns high resolution spectra of reflected sunlight in the CO<sub>2</sub> bands near 1.57, 1.61, and 2.06  
436 microns, the CH<sub>4</sub> band near 1.67 microns, and O<sub>2</sub> A-band near 0.765 microns since April 2009.  
437 Groups in Japan, the U.S. and Europe are using these spectra to estimate XCO<sub>2</sub> and XCH<sub>4</sub>. Due to  
438 strong collaboration among these groups on retrieval algorithms, validation techniques, and data  
439 screening methods the observational biases are being reduced. Random errors that are typically  
440 less than 0.5% (2 ppm) on regional scales over much of the Earth (cf. Yoshida et al., 2012; Inoue  
441 et al., 2013; Crisp et al., 2013).

442 As the biases and random errors have been reduced, the principal limitation of the GOSAT data  
443 set has been its coverage and resolution. The TANSO-FTS acquires about 10,000 soundings over  
444 the sunlit hemisphere each day. Over land, the ~10.5 km diameter surface footprints of these  
445 soundings are separated by ~253 km. With its relatively large sounding footprint (85 km<sup>2</sup>), up to  
446 90% of these soundings are too contaminated by clouds or optically-thick aerosols to yield  
447 accurate estimates of XCO<sub>2</sub> with the current retrieval algorithms. Persistent cloudiness over the

448 tropics, south Asia (monsoons), and at high latitudes in the winter hemisphere further reduces the  
449 coverage there. Over the ocean, the TANSO-FTS coverage is restricted to  $\pm 20^\circ$  of the sub-solar  
450 latitude, where its pointing mechanism can target the bright “glint spot,” in which sunlight is  
451 specularly reflected from the surface. So, while GOSAT extends the coverage of the ground  
452 based network, it still leaves large regions with little or no sampling. In spite of these limitations  
453 in coverage and resolution, XCO<sub>2</sub> estimates from GOSAT TANSO-FTS are being used in flux  
454 inversion models and are beginning to improve our understanding of CO<sub>2</sub> sources and sinks in  
455 data poor regions, such as Africa and central Asia (Basu et al. 2013; Belikov et al., 2014; Guerlet  
456 et al. 2013).

457 The Orbiting Carbon Observatory-2 (OCO-2) is NASA’s first satellite designed to retrieve  
458 estimates of XCO<sub>2</sub> over the sunlit hemisphere. OCO-2 was launched from Vandenberg Air Force  
459 Base in California in July 2014. It flies at the head of the 705-km Afternoon Constellation (“A-  
460 Train”), in an orbit tailored to yield nadir observations that overlap with those from CALIPSO  
461 (Cloud-Aerosol Lidar and Infrared Pathfinder Satellite Observations) and CloudSat. This sun-  
462 synchronous orbit has a 1:30 PM equatorial crossing time and a 16-day repeat cycle.

463 The OCO-2 spacecraft carries single instrument that incorporates three, co-bore-sighted high-  
464 resolution, imaging, grating spectrometers designed to measure reflected sunlight in the O<sub>2</sub> A-  
465 band, and within the CO<sub>2</sub> bands near 1.61 and 2.06 microns. Each spectrometer collects 24 XCO<sub>2</sub>  
466 soundings per second along a narrow (< 10.6 km), ground track, yielding up to one million  
467 soundings over the sunlit hemisphere each day. To yield more useful data in partially cloudy  
468 regions, the surface footprint of each OCO-2 sounding has an area of less than 3 km<sup>2</sup>. With this  
469 small footprint, cloud screening studies indicate that 20 to 30% of these soundings should be  
470 sufficiently cloud free to yield full-column estimates of XCO<sub>2</sub>. To detect CO<sub>2</sub> variations over  
471 dark, ocean or ice-covered surfaces, OCO-2 can point the instrument’s field of view toward the  
472 bright ocean glint spot over almost 90% of the range of latitudes on the sunlit hemisphere. The  
473 baseline plan is to alternate between glint and nadir observations on alternate, 16-day ground-  
474 track repeat cycles, to optimize the coverage of the sunlit hemisphere at monthly intervals. With  
475 these capabilities, OCO-2 provides substantially better coverage than previous missions.

### 476 **3. Impact to Carbon Science and Modeling**

#### 477 **3.1 Introduction**

478 The overarching science goal of the ASCENDS Mission, as outlined above, is to establish  
479 quantitative constraints on terrestrial and oceanic CO<sub>2</sub> surface fluxes at both global and regional  
480 scales from measurements of CO<sub>2</sub> column concentration. In order to achieve this goal, it is critical  
481 to thoroughly understand the impact of measurement accuracy and precision on the flux  
482 estimates. Even the largest sources and sinks produce local perturbations in the background  
483 concentration of CO<sub>2</sub> no larger than a few percent. In addition, biases in the data are particularly  
484 problematic since their impact cannot be reduced via averaging.

485 This chapter outlines the ongoing modeling efforts undertaken by the ASCENDS ad hoc science  
486 definition team to assess the ability of expected ASCENDS measurements to constrain flux  
487 estimates. Under reasonable assumptions for ASCENDS technical performance, the modeling  
488 efforts consistently demonstrate the following major points:

- 489 • ASCENDS will resolve statistically-significant differences in total column CO<sub>2</sub>  
490 concentrations, resulting from foreseeable changes in surface flux, over the entire globe  
491 including high latitudes throughout the year.
- 492 • ASCENDS will substantially advance our understanding of the global carbon budget  
493 through improved flux estimates with reduced uncertainty at global to regional scales.
- 494 • ASCENDS measurements have the potential for lesser bias and greater representation that  
495 can contribute significantly to improved constraints on surface fluxes beyond what passive  
496 sensors such as GOSAT and OCO-2 can provide.

497 In this chapter, we elaborate on these points in detail through the use of three common,  
498 overlapping modeling approaches or Observing System Simulation Experiment (OSSE)  
499 frameworks. These approaches are: 1) Signal detection simulations that test the global  
500 measurement significance for perturbation flux scenarios of interest; 2) Inverse modeling OSSEs  
501 that quantify the reduction in flux uncertainty provided by the ASCENDS data at global and  
502 regional scales, and 3) OSSEs that compare the impact of ASCENDS data to that of current  
503 passive measurements from GOSAT and that expected from OCO-2 at the global scale. Most of  
504 the modeling is performed using a range of possible technology implementations and  
505 performance specifications for ASCENDS to bracket projected measurement error levels and  
506 ultimately to help guide requirements for the mission formulation.

#### 507 **3.2 Detection of Changes in Column CO<sub>2</sub> and Flux by ASCENDS**

508 The ability of ASCENDS to detect changes in total column CO<sub>2</sub> resulting from variations in  
509 underlying fluxes is tested in the two-step methodology of Hammerling et al. (2015). First, a  
510 realistic baseline set of CO<sub>2</sub> sources and sinks is perturbed to generate a simulated atmosphere,  
511 which represents the science hypothesis in question. Second, the control and perturbed CO<sub>2</sub> fields  
512 are sampled according to the projected ASCENDS sampling and error characteristics, and the  
513 'observed' differences are evaluated statistically. This procedure is carried out for three  
514 hypothetical flux scenarios (Hammerling et al., 2015): emissions from thawing permafrost  
515 (Section 3.2.1), a shift in fossil fuel emissions from Europe to China (Section 3.2.2), and  
516 simulated interannual variability in the Southern Oceans (Section 3.2.3). These scenarios are then

517 introduced into an inversion model framework to calculate the fluxes and uncertainties inferred  
518 from the pseudo data.

519 **Box 3-1** Simulation of Random Errors

Prospective ASCENDS sampling and measurement error characteristics are derived in a realistic scheme from observations and model output using the Cloud-Aerosol Lidar and Infrared Pathfinder Satellite Observations (CALIPSO) orbital track for the ASCENDS orbit (Kawa et al., 2010, Kiemle et al., 2014). CALIPSO optical depth (OD) data are reported every 5 km along track and this forms our basic ASCENDS sample set. We have also tested sample error calculated using OD derived for a subset of single-shot 20-Hz CALIPSO data and found that the global statistics are very similar to those using the 5-km data.

Since ASCENDS laser measurements of atmospheric CO<sub>2</sub> (and O<sub>2</sub>) will be made using the integrated path differential absorption (IPDA) technique, the dominant random error source is likely to be the shot noise in the signal, i.e., the statistical variability in the number of detected signal photons. Hence the measured signal to noise ratio (SNR) of the optical depth of the gas absorption depends on the square root of the received signal energy. In general, the SNR of an individual measurement of 2-way optical depth (SNR<sub>i</sub>), can be related to that measured under reference conditions (SNR<sub>0</sub>) by:

$$SNR_i = SNR_0 \left[ \frac{\beta_i T_i^2}{\beta_0 T_0^2} \right]^{1/2} \quad (3-1)$$

Where  $\beta_i$  is the average backscatter factor (sr-1) of the measured surface,  $\beta_0$  is the backscatter for the reference surface,  $T_i$  is the one-way atmospheric transmission to the surface due to aerosols and clouds for measurement  $i$ , and  $T_0$  is the transmission for the reference measurement. For the reference conditions, we have chosen clear air with the high reflectivity of a desert like Railroad Valley, NV in summer and a 10-s sample integration time. The measurement at this reference location is assumed to be aerosol and cloud free, thus  $T_0 = 1$ . Using Equation (3-1), we estimate the random relative error ( $= 1/SNR_i$ ) globally from an estimate of the error under the reference conditions.

The transmission for each ASCENDS pseudo data sample is taken directly from the CALIPSO OD data: where  $\tau_i$  is the one-way integrated aerosol and cloud OD to the surface reported by CALIPSO. The aerosol OD is taken from the 1064-nm channel and the cloud OD from the 532-nm, and these values are assumed to apply equally at each of the possible ASCENDS measurement wavelengths (i.e., 1.57 and 2.05  $\mu\text{m}$ ). Samples are excluded where CALIPSO cannot see to the surface due to thick clouds. Global backscatter estimates over land have been assembled for wavelength bands at 1.57 and 2.05  $\mu\text{m}$  for CO<sub>2</sub>, and 0.76 and 1.26  $\mu\text{m}$  for O<sub>2</sub> measurement using MODIS bands 6, 7, 2, and 5, respectively, which are then interpolated to the CALIPSO-based sampling points. The details vary slightly from band to band. Backscatter over water is calculated according to Hu et al. (2008) using surface wind speeds from GEOS-5.

For the modeling studies, a range of nominal reference random error levels ( $1/SNR_0$ ) is considered (0.5, 1.0, 2.0 ppmv) to represent a range of possible instrument precision levels. Global median errors scaled from these ideal/desert-like nominal values are 1.7, 3.3, 6.7 ppmv, respectively for the 1.57  $\mu\text{m}$  case when screened for samples with optical depth less than 1.0. All of the models use the same sample distribution and measurement error scaling described here, however, different modeling teams employ somewhat different techniques to aggregate the pseudo data and determine the model-data mismatch errors that are ultimately used in the flux estimation experiments (Appendix C).

520

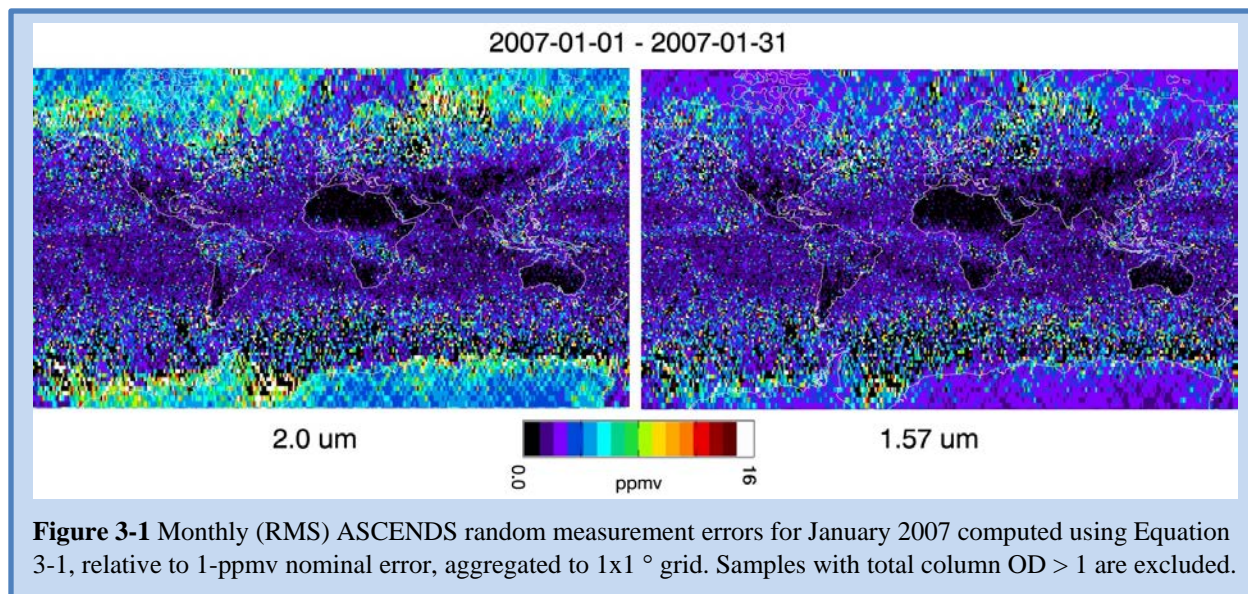
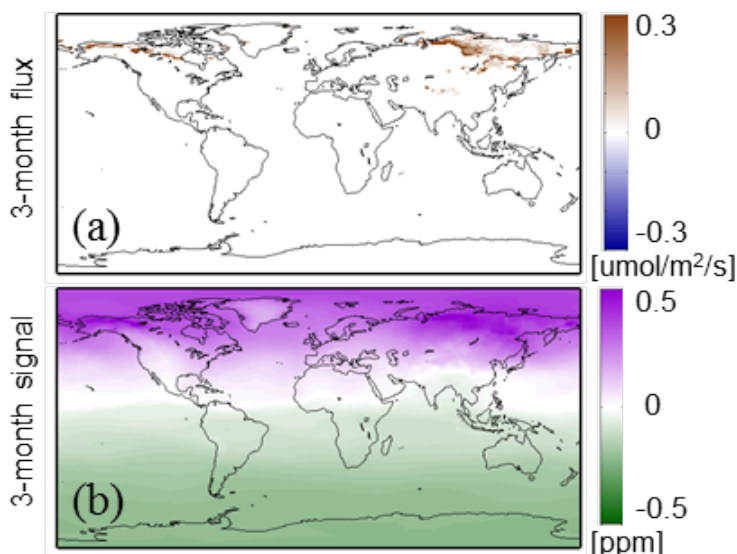


**Figure 3-1** Monthly (RMS) ASCENDS random measurement errors for January 2007 computed using Equation 3-1, relative to 1-ppmv nominal error, aggregated to 1x1 ° grid. Samples with total column OD > 1 are excluded.

521

522 **3.2.1 Arctic Permafrost Thawing Emissions**

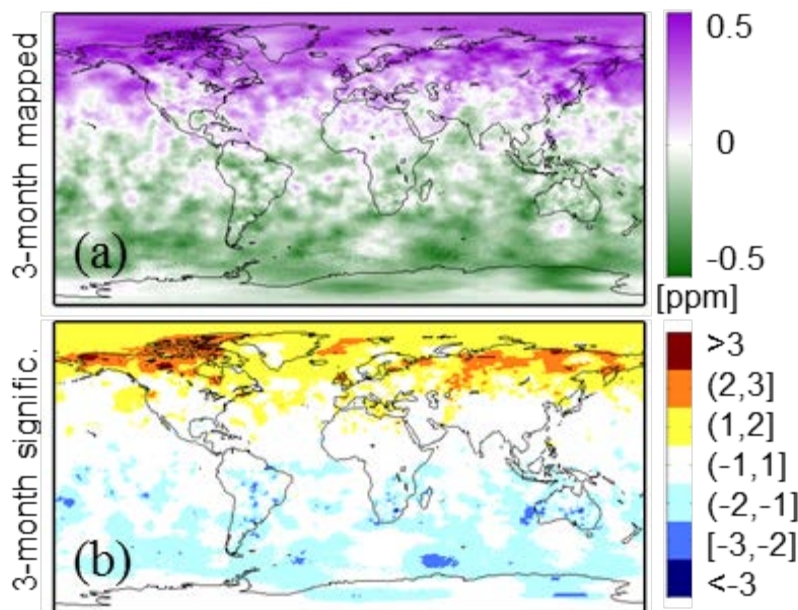
523 Permafrost soils occupy about 24% of the exposed land area in the high latitude Northern  
 524 Hemisphere (Zhang et al., 1999) and contain approximately 1700 Gt of carbon in the form of  
 525 frozen organic matter (Tarnocai et al., 2009). As temperatures increase and the permafrost thaws,  
 526 the organic material begins to decay, releasing CO<sub>2</sub> and methane into the atmosphere, resulting in  
 527 enhanced atmospheric concentrations of these greenhouse gases and further warming. The rate of  
 528 this feedback is highly uncertain, however, prompting calls for enhanced pan-Arctic greenhouse  
 529 gas monitoring including satellite observations (NRC, 2013). Measurements at high latitudes  
 530 with required sensitivity near the surface are particularly difficult, if not often impossible, for  
 531 passive sensors making this a unique area of contribution for the ASCENDS lidar approach.



532

533 **Figure 3-2** Perturbation flux and column average CO<sub>2</sub> mixing ratio for carbon release experiment (a) 3-month  
 534 average (May – July) CO<sub>2</sub> flux for 2022 and (b) resulting 3-month average CO<sub>2</sub> perturbation. Negative mixing ratio  
 535 values in the Southern hemisphere are a result of the global mean adjustment to create an overall flux neutral scenario  
 536 (Hammerling et al., 2015).

537 The permafrost carbon emission scenario tested here derives from the simulations of Schaefer et  
 538 al. (2011). Emission distributions are formed from the ensemble mean of CO<sub>2</sub> flux projections  
 539 calculated in the Simple Biosphere/Carnegie-Ames-Stanford Approach (SiB-CASA) land  
 540 biosphere model, driven by output from several General Circulation Models for the A1B scenario  
 541 from the Intergovernmental Panel on Climate Change (IPCC) Fourth Assessment report (Lemke  
 542 et al., 2007). The 2020 and 2021 fluxes were used to spin up the Parameterized Chemistry and  
 543 Transport Model (PCTM, Kawa et al., 2004) and create corresponding atmospheric CO<sub>2</sub>  
 544 concentrations. The atmosphere resulting from the 2022 fluxes was taken as the perturbation field.  
 545 The 2022 permafrost fluxes and CO<sub>2</sub> perturbation are shown in Figure 3-2.



546  
 547 **Figure 3-3** Results from the permafrost carbon release experiment (a) 3-month (May-July) ASCENDS-mapped CO<sub>2</sub>  
 548 signal (perturbation minus baseline) and (b) significance level of the 3-month mapped signal. Significance is the  
 549 mapped signal divided by the uncertainty of the mapped signal in units of standard deviations. The values are  
 550 discretized for improved visualization. Yellow, orange and dark red (light, medium and dark blue) represent areas  
 551 where the mapped CO<sub>2</sub> perturbation is larger (smaller) than the mapped baseline CO<sub>2</sub> concentration by more than  
 552 one, two or three standard deviations, respectively, of the uncertainty of the mapped signal. This example uses the  
 553 ASCENDS medium measurement noise (1 ppmv random error), 1.57 μm case (See Box 3-1 and Hammerling et al.,  
 554 2015).

### 555 *Signal Detection Significance*

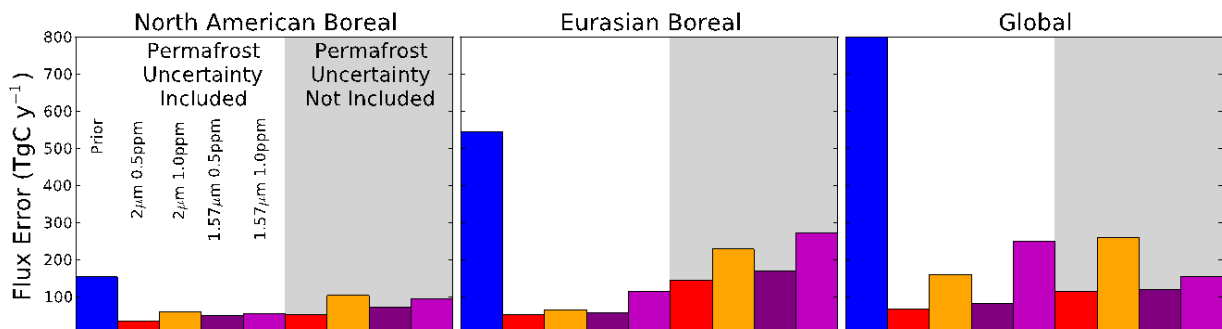
556 The detectability of a significant signal is relatively straightforward in the case of the anticipated  
 557 permafrost carbon emissions (Figure 3-3). The challenge is in capturing longitudinal and  
 558 latitudinal gradients, which can better attribute the increase to the permafrost thawing process.  
 559 Because of the seasonality of the permafrost fluxes, the gradients in the atmospheric CO<sub>2</sub>  
 560 distribution are most evident in the months following the start of the spring thaw. By August,  
 561 atmospheric mixing, which occurs rapidly in the Arctic, spreads the spatial signature of the tundra  
 562 thawing into a near-uniform zonal increase. While the concentration signal is highest around  
 563 September, or even later in the year, when most of the seasonal melting has occurred, the  
 564 diagnostic concentration signals are mostly indicative of the spatial pattern of the tundra thawing  
 565 fluxes that occur in the late spring/early summer before the effects of atmospheric mixing take  
 566 over. This phenomenon is caused by the specific combination of the temporal pattern of the

567 permafrost carbon release and rapid atmospheric mixing in the High Northern Latitudes. Overall,  
568 the permafrost thawing signal is readily detectable (i.e., SNR > 2-3) for either level of ASCENDS  
569 measurement noise considered (0.5, 1.0 ppmv, see Box 3-1), and spatial gradients are best  
570 detected using two to three month aggregation periods in the late spring/early summer.

### 571 *Flux Estimation*

572 Flux estimation experiments were conducted using the transport model TM5 (Krol et al, 2005)  
573 together with a 4DVAR inversion system (see Table 3-1, Box 3-2, and Basu et al, 2013). The  
574 prior (first guess) emissions are taken to be the baseline fluxes (with no permafrost thaw  
575 included), while the “true” fluxes are the prior plus the permafrost emissions described above, for  
576 the model year 2022. These true fluxes are used to drive TM5, whose output is sampled with the  
577 ASCENDS weighting functions for the two instrument wavelengths considered. The observation  
578 errors are as detailed in Appendix C. Two different prior error covariance assumptions were  
579 made. The first is that we would have no knowledge of the permafrost thaw, and so the prior  
580 covariance is taken to be the difference between two biosphere and ocean flux estimates, as  
581 described below in Section 3.3.3. The second assumption is that the community has some  
582 knowledge of the spatial pattern of the permafrost, but that its flux magnitude is uncertain. This is  
583 modeled by taking a prior covariance that is the sum of the general background covariance in the  
584 first experiment together with the permafrost emissions themselves. The spatial pattern is  
585 important to the 4DVAR assimilation system, because the optimization makes the largest  
586 corrections where the prior uncertainty is largest. In general including this uncertainty in the  
587 spatial pattern improved posterior errors.

588



589

590 **Figure 3-4** Regional inversion results from the permafrost carbon release experiment. Flux error is the RMSE of the  
591 monthly fluxes aggregated across each region scaled to an annual amount. The blue bar represents the prior and the  
592 red and orange bars represent the posterior fluxes using ASCENDS pseudo-data derived with the 2.05 μm weighting  
593 function and 0.5 ppm (red) and 1.0 ppm (orange) nominal errors (see Box 3-1). The purple and magenta bars  
594 represent the posterior flux error using the 1.57 μm weighting function and 0.5 ppm (purple) and 1.0 ppm (magenta)  
595 errors. The bars under the grey shaded background represent experiments in which the permafrost distribution  
596 uncertainty was not included in the prior covariance, while the other four bars represent the case in which the  
597 permafrost uncertainty was included.

598 The results are depicted in Figure 3-4. The optimized fluxes are found at the monthly time scale,  
599 at a global resolution of 6° longitude by 4° latitude, and the resulting fluxes are aggregated to  
600 regions that contain the permafrost flux signal of interest. The global value is also shown. For the  
601 boreal regions, ASCENDS reduces the monthly aggregate error significantly (40 to 90%) in all  
602 experiments. The cases with greater measurement precision resulted in greater uncertainty  
603 reductions. Especially for the 0.5 ppm nominal measurement precision, the high latitude monthly

604 fluxes are recoverable with relatively low error (10 to 30%) using ASCENDS. These results  
 605 reinforce the signal detection experiment conclusions, which show detectability after a few  
 606 months of observations. The lesser measurement time requirement in the inversion is expected,  
 607 since the transport model and its adjoint provide source information in the identification problem,  
 608 reducing the need for the temporal averaging in the signal detection.

609 **Table 3-1 ASCENDS Inverse Models Summary**  
 610

Modeling Approaches					
	4DVAR-TM5	4DVAR-PCTM	EnKF-GEOS-Chem	Bayesian	GIM
<b>Team</b>	OU/Melbourne	CSU-CIRA	CSU-CIRA	GSFC/AER	Stanford-Carnegie
<b>Inversion Method</b>	Four-dimensional variational data assimilation	Four-dimensional variational data assimilation	Ensemble Kalman filter	Batch Bayesian synthesis inversion	Batch geostatistical synthesis inversion
<b>Transport Model</b>	TM5 (Eulerian), ECMWF winds	PCTM (Eulerian), MERRA winds	GEOS-Chem (Eulerian), MERRA winds	STILT (Lagrangian), WRF winds	STILT (Lagrangian), WRF winds
<b>Domain and Flux Resolution</b>	Global, 6°x4°, monthly	Global, 6°x4.5°, weekly	Global, 2°x2.5°, two weeks	North America, 1°x1°, weekly	North America, 1°x1°, 3-hourly
<b>Chapter Sections</b>	3.2.1-3.2.3	3.3.3, 3.4.1-3.4.2	3.2.4	3.3.2	3.3.1
<b>Reference</b>	Basu et al. (2013); Krol et al. (2005)	Baker et al. (2006); Kawa et al. (2004)	Tippet et al. (2003); Bey et al. (2001)	Wang et al. (2014)	Shiga et al. (2014)

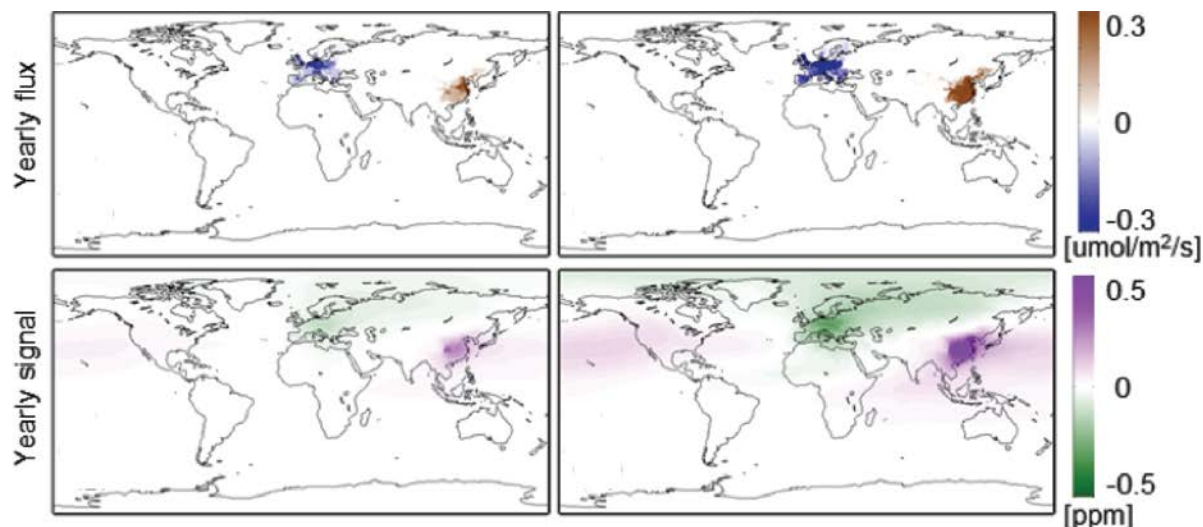
611

**ASCENDS data will readily enable detection of realizable permafrost thawing CO<sub>2</sub> emissions at high latitudes on a monthly to seasonal time scale.**

612

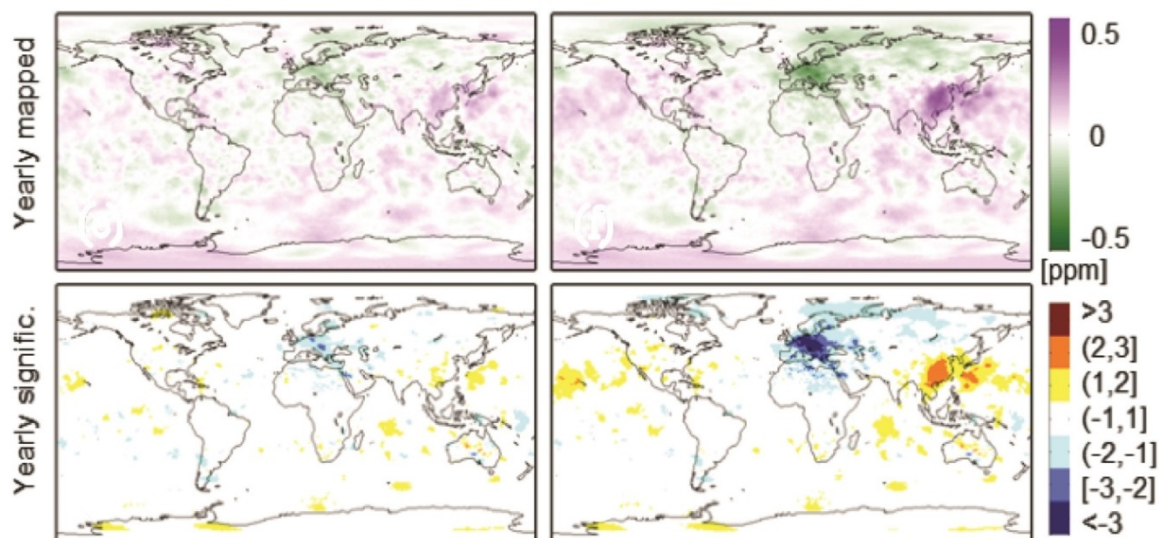
### 613 3.2.2 Fossil Fuel Emission Shift

614 As fossil fuel burning increases rapidly in the developing world and potentially decreases as a  
 615 result of policy implementation in industrialized countries, more accurate and better-resolved  
 616 emissions information is needed (Duren and Miller, 2012). Fossil fuel emissions from China have  
 617 increased rapidly over the last decades (Olivier et al., 2012; Peters et al., 2011), while those from  
 618 Europe decreased by 3% in 2011 relative to 2010 with an overall decline over the last two  
 619 decades (Olivier et al., 2012). Satellite data, such as those available from the ASCENDS mission,  
 620 increasingly play a role in both validating bottom-up estimates (e.g., Bovensman et al., 2010) and  
 621 directly inferring fossil fuel emissions. In this section, we describe results from experiments to  
 622 test the capability of the ASCENDS data to constrain fossil fuel distributions.



623  
624 **Figure 3-5** Perturbation flux and column CO<sub>2</sub> mixing ratio for the fossil fuel experiments. First row: Yearly average  
625 CO<sub>2</sub> flux shift. Second row: Yearly average column CO<sub>2</sub> concentration perturbation. Left (right) panels show the  
626 lower (higher) emission change case.

627 Two “flux neutral” emission scenarios valid around the year 2022 were derived to test ASCENDS  
628 ability to detect potential fossil fuel emissions changes (Hammerling et al., 2015). The emissions  
629 scenarios and corresponding CO<sub>2</sub> column average mixing ratio perturbation are depicted in Figure  
630 3-5. The lower emission change scenario represents a 20% decrease (compared to 2007 Carbon  
631 Dioxide Information Analysis Center (CDIAC) levels (Andres et al., 2011)) of European  
632 emissions, with a corresponding 12% increase in China. The higher signal case includes a 50%  
633 decrease of emissions in Europe with a corresponding 30% increase in China, and is used for  
634 illustration purposes; a decrease of this size is not expected in Europe within a decade.

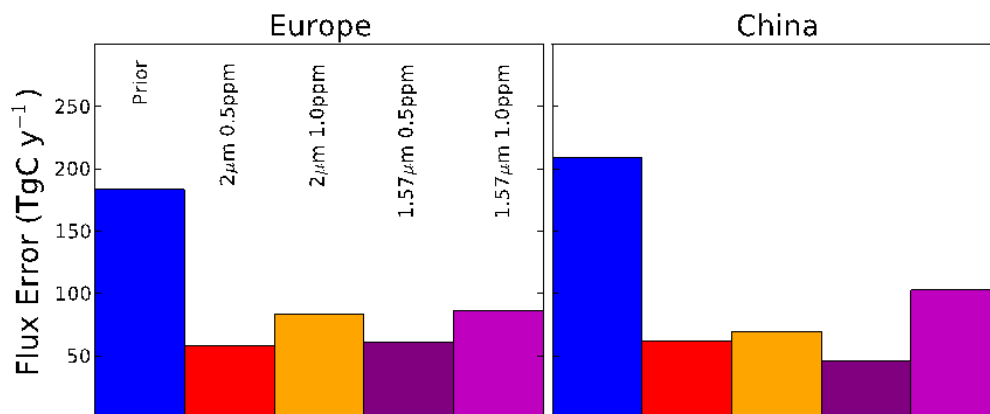


635  
636 **Figure 3-6** Significance results for the fossil fuel experiments for ASCENDS. Using nominal measurement noise at 1  
637 ppmv and the 1.57  $\mu\text{m}$  case (Box 3-1). First row: yearly mapped CO<sub>2</sub> signal. Second row: significance of the yearly  
638 mapped CO<sub>2</sub> signal. The mapped signal is calculated and plotted as described in Figure 3-3. Left (right) panels show  
639 the lower (higher) emission change case.

640 *Signal Detection Significance*

641 The imposed fossil fuel emissions perturbations lead to a pronounced CO<sub>2</sub> spatial signature that is  
 642 localized over Europe and China (Figure 3-6). This is in contrast to other experiments at mid-to-  
 643 high latitude, where the spatial signatures are largely diffused and the signals in atmospheric CO<sub>2</sub>  
 644 are seen primarily as zonal increases. The magnitude of the lower fossil fuel perturbation signal,  
 645 however, is very small, and likely to be difficult to detect

646 Given the relative lack of seasonality in the imposed fossil fuel perturbation scenarios, averaging  
 647 over longer periods of time leads to better detectability, i.e., the annual signals are greater than  
 648 those aggregated for 3 months. Although the diffusive nature of the atmospheric transport clearly  
 649 plays a role, the atmospheric signal still localizes the source region of the perturbation flux  
 650 throughout all the seasons. The effect of varying measurement noise levels on the detectability is  
 651 as expected: increasing measurement noise leads to decreased significance in the results and  
 652 requires in turn longer averaging periods. For the higher signal case, however, all three  
 653 considered instrument noise levels (0.5, 1.0, 2.0 ppmv, Box 3-1) capture the signal in the annual  
 654 results. Overall, these findings imply that ASCENDS can detect changes in fossil fuel emissions,  
 655 but depending on the strength of the signal, detection may require multiple years of observations.

656 *Flux Estimation*

657  
 658 **Figure 3-7** Regional flux errors for the 20% European fossil fuel emission shift scenario as in Figure 3-4. The prior  
 659 errors for each region are about 200 TgC, and each of the ASCENDS instruments reduces that significantly. The flux  
 660 errors are monthly RMSE, scaled to an annual amount.

661 For the TM5-4DVAR inverse experiment, the true fluxes are the baseline emissions together with  
 662 the low fossil fuel shift scenario pictured in the left panels of Figure 3-5. The perturbation adds  
 663 about 0.2 PgC for Europe and subtracts the same from China. The prior uncertainty was taken to  
 664 be the biospheric uncertainty described in Section 3.3.4 together with 20% of the CDIAC  
 665 emissions for 2010. This small value for the fossil fuel emissions is enough to provide the  
 666 4DVAR system with some spatial information on the location of the sources. Results for the flux  
 667 estimation are shown in Figure 3-7. These figures suggest that ASCENDS is able to reduce errors  
 668 in the prior emissions by at least 50% at the monthly time scale. In addition, aggregating to annual  
 669 numbers yielded even larger reductions in the fossil fuel emissions errors. This greatly  
 670 strengthens the results of the signal detection experiment. Again, this is due to the inclusion of the  
 671 transport model adjoint, which is able to correctly trace concentration differences back to source  
 672 regions as large as Europe and China. Though not shown here, similar experiments that did not

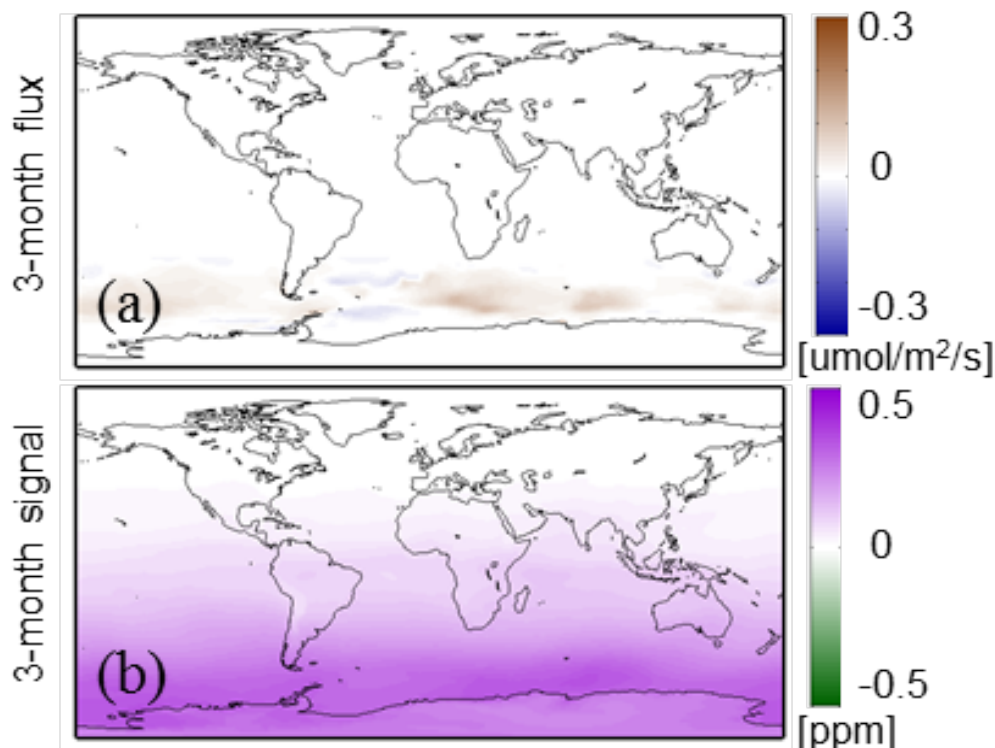
673 include a fossil fuel prior uncertainty term yielded promising results, though with smaller  
674 reductions in the posterior error.

**ASCENDS will be able to identify a foreseeable shift in monthly fossil fuel emissions at the scale of Europe and China, presuming an accurate model for transport.**

675

### 676 3.2.3 Flux Changes in the Southern Oceans

677 The Southern Ocean is a very sparsely sampled region that represents a key uncertainty in the  
678 carbon cycle. This region has an apparent high sensitivity to climate change (Le Quéré et al.,  
679 2009), and understanding its regional carbon-climate feedback has implications for quantifying  
680 the region's future as a carbon sink. Studies have shown that the southern oceans contributes half  
681 of the ocean uptake of anthropogenic CO<sub>2</sub> (e.g., Le Quéré et al., 2009; Meredith et al., 2012),  
682 although uncertainties on the magnitude of this uptake and its trend over time are high. Given that  
683 the Southern Ocean is also very difficult to monitor *in situ*, the ability of the ASCENDS mission  
684 to observe in this region could provide invaluable insights into changes in the ocean carbon sink.



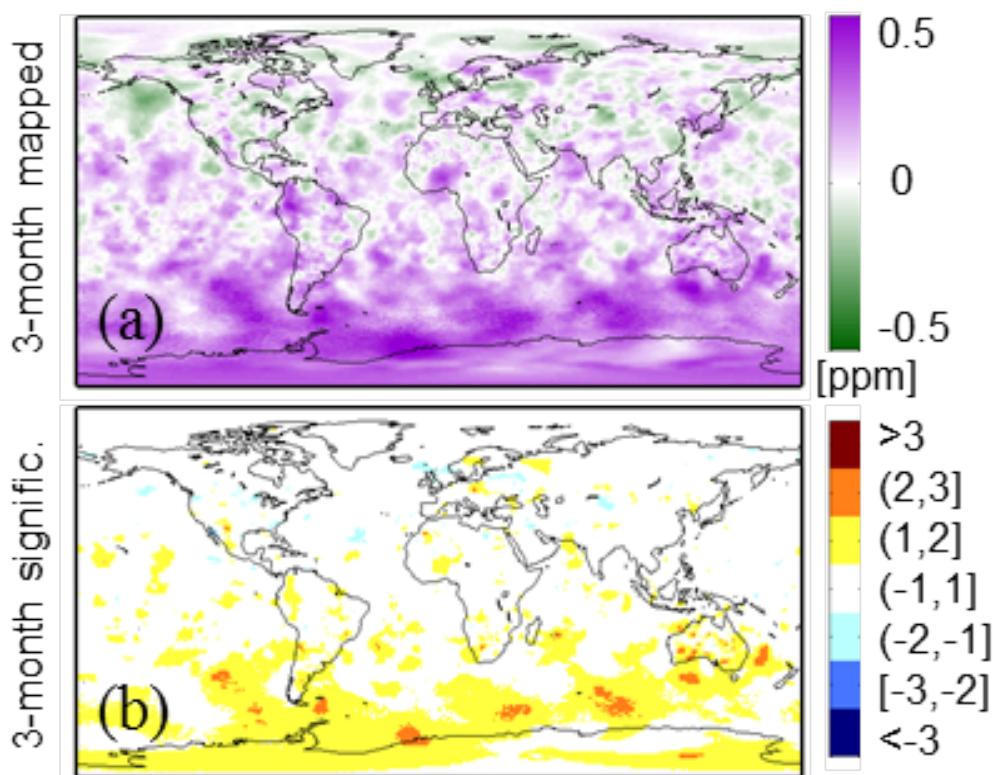
685  
686 **Figure 3-8** Southern Ocean experiment flux difference and column average CO<sub>2</sub> mixing ratio perturbation using the  
687 1-ppmv, 1.57  $\mu\text{m}$  nominal ASCENDS error case. (a) 3-month (April – June) average CO<sub>2</sub> flux and (b) 3-month  
688 average CO<sub>2</sub> concentration.

689 Variations in climatic modes, such as the El Niño-Southern Oscillation (ENSO), are key drivers  
690 of interannual variability in ocean carbon exchange. For this reason, scenarios for opposing  
691 ENSO modes were chosen to test detectability of Southern Hemisphere (SH) ocean flux changes  
692 that ASCENDS expects to encounter. The Southern ocean fluxes used for this scenario are based  
693 on a hindcast simulation of the Community Climate System Model (CCSM) Ocean

694 Biogeochemical Elemental Cycle model as described by Doney et al. (2009). Fluxes were  
 695 obtained at one degree spatial and monthly temporal resolution. The years 1977 and 1979 were  
 696 chosen as prototypical example flux patterns, as they represent large differences in ocean fluxes  
 697 due to variations in climatic modes. The simulated air-sea CO<sub>2</sub> flux in 1979 was about half of  
 698 that for 1977 averaged across the Southern ocean. The flux difference between 1977 and 1979 in  
 699 the Southern Ocean is used for the perturbation scenario. Figure 3-8 shows the average fluxes and  
 700 column mixing ratio change for April through June (from Hammerling et al. (2015)).

### 701 *Signal Detection Significance*

702 The detection of changes in the Southern Ocean source/sink characteristics is the most  
 703 challenging of the three signal detection scenarios considered for several reasons. The overall  
 704 magnitude of the CO<sub>2</sub> difference signal in the Southern Oceans is weak, with an absolute value  
 705 never exceeding 0.4 ppm in the column. In addition, this scenario contains sub-seasonal and sub-  
 706 regional-scale flux variability, superimposed on the seasonal pattern in the fluxes, which makes  
 707 the perturbation more difficult to distinguish. Atmospheric mixing also plays a role in obscuring  
 708 the longitudinal fingerprint of the Southern Ocean as the origin of the signal, similar to what was  
 709 observed in the permafrost carbon release scenario described above.



710  
 711 **Figure 3-9** Significance results for Southern Ocean experiment for medium measurement noise (1 ppmv, 1.57  $\mu$ m  
 712 case, Box 3-1). (a) 3-month mapped CO<sub>2</sub> signal, (b) Significance of the 3-month mapped CO<sub>2</sub> signal as described in  
 713 Figure 3-4.

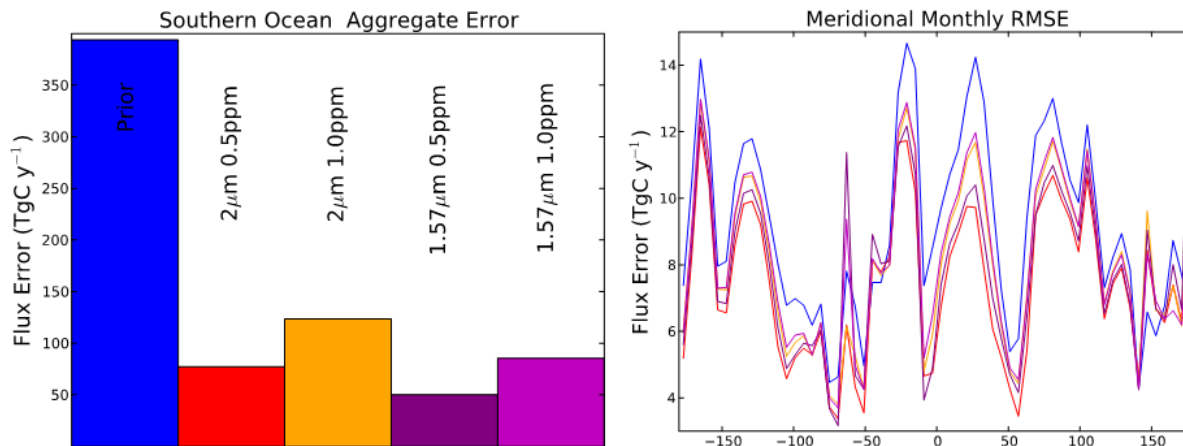
714 Figure 3-9 shows areas of the SH ocean are distinguishable at the 2 to 3 sigma level for 3-month  
 715 aggregated ASCENDS sampling with 1-ppmv nominal random error levels, but the signal is not  
 716 strong. For annually aggregated measurements (not shown), the yearly results clearly indicate a

717 zonal increase in the High Southern Latitudes, however, the pattern indicative of the Southern  
718 Ocean flux difference within the zonal band is less clear.

### 719 *Flux Estimation*

720 A surface flux estimation experiment was performed, similar to those described in Sections 3.2.1  
721 and 3.2.2, where the true flux was taken to be the ocean flux from 1979 (and zero for the rest of  
722 the globe), while the prior was the flux from 1977. The prior covariance was as described in  
723 Section 3.3.3 below, which for the Southern Ocean is the difference between the NCAR Ocean  
724 Model and Takahashi et al. (1999) for the reference year 2000.

725 The prior and posterior errors aggregated for the Southern Ocean are shown in Fig 3-10. Despite  
726 the weak signal strength, ASCENDS would be able to estimate at least 65% of the tested  
727 interannual variability in the emissions of the Southern Ocean. Furthermore, we assess the ability  
728 of ASCENDS to give information about the spatial gradient from east to west in the Southern  
729 Ocean by aggregating along lines of longitude in the Southern Ocean and plotting the resulting  
730 meridional errors (Figure 3-10). Note that ASCENDS is able to reduce the errors for nearly every  
731 longitude across the Southern Ocean by about  $1 \text{ TgC mon}^{-1} (6 \text{ deg longitude})^{-1}$ , despite the weak  
732 magnitude of the spatial gradient across the region. In addition, though the RMSE for the  $1.57 \mu\text{m}$   
733 instrument was lower for the region as a whole, the flux error for the  $2.05 \mu\text{m}$  instrument is  
734 smaller than for  $1.57 \mu\text{m}$  when the spatial dimension is considered, which is evident from the red  
735 line in Figure 3-10 being lower than the purple for most of the longitude bins. This type of spatial  
736 information would be unavailable using the current surface network, which could only provide a  
737 few pieces of information that would represent local flux variations only.



738  
739 **Figure 3-10** Inversion results from the Southern Ocean interannual variability experiment. Colors represent the  
740 different instrument concepts as described in Figure 3-4. In the left panel, the bars represent the monthly RMSE  
741 aggregated to Southern Ocean taken as a whole. In the right panel, the latitudinally averaged errors are plotted as a  
742 function of longitude, with the line color denoting the experiment as labeled in the left panel. Southern Ocean is  
743 treated here as south of 40S, and excluding landmasses.

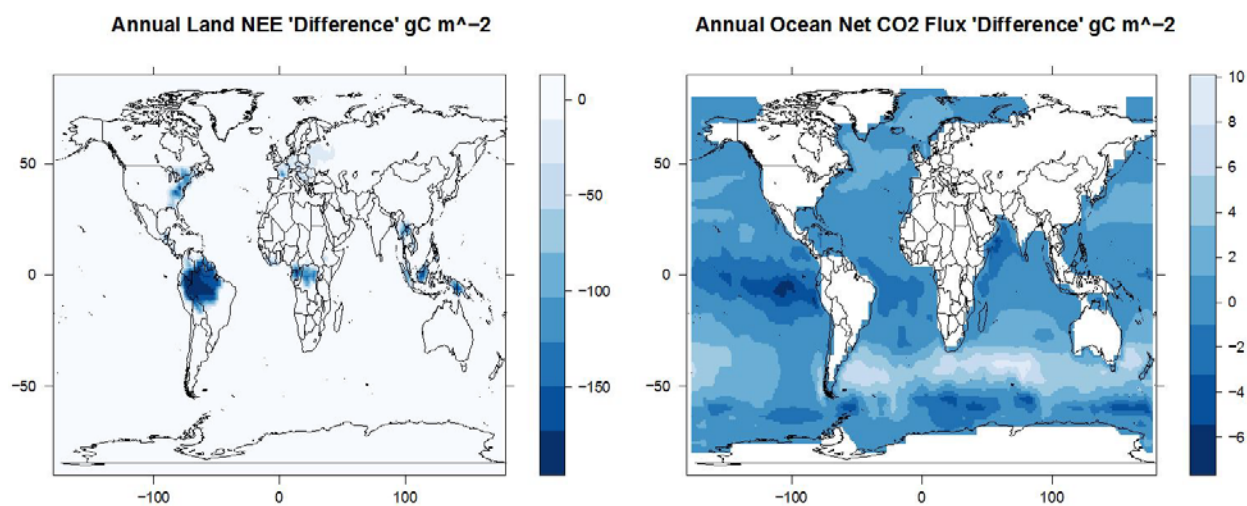
**ASCENDS observations, coupled with an accurate transport model, have potential to substantially reduce uncertainty in Southern Ocean fluxes and provide some constraint on their spatial and temporal variability.**

744

### 745 3.2.4 Enhanced Sink Due to Carbon Fertilization

746 The previous experiments examine realistic perturbations to one aspect of the carbon cycle. In  
747 reality, CO<sub>2</sub> datasets and models will be used to examine multiple possible perturbations to land  
748 and ocean fluxes occurring simultaneously. Here, we create a more complex signal detection  
749 experiment by combining several realistic perturbations to test the ability of the ASCENDS data  
750 to constrain net ecosystem carbon exchange (NEE) over different times and locations. These  
751 perturbations include:

- 752 • Respiration reduced by 5% over Northeastern U.S. forests to simulate forest regrowth  
753 after land use change. There is strong evidence (Houghton et al., 1999; SOCCR, 2007;  
754 Pan et al., 2011) to support an enhanced carbon sink as forests re-grow after centuries of  
755 clearing for agriculture.
- 756 • Forest Gross Primary Production (GPP) increased by up to 10% over regions of Western  
757 Europe and the Central U.S. as a function of nitrogen deposition, with peak effect over  
758 areas of known industrial nitrogen emissions.
- 759 • GPP amplified by 5% over tropical broadleaf forest regions between 30°S and 30°N to  
760 account for a CO<sub>2</sub> fertilization effect in tropical forests. Both basic plant physiology, as  
761 well as experimentation (Oren et al., 2001) support the idea that increased atmospheric  
762 carbon dioxide levels should lead to increased plant uptake.
- 763 • A reduction of overall atmospheric-ocean exchange (as might result from decreasing  
764 winds) imposed by providing a zonal variation to the flux, from a 5% reduction in flux  
765 over the Northern Oceans to a 15% reduction over the Tropical Oceans, to a 25%  
766 reduction over the Southern Oceans (e.g., Le Quéré et al., 2009).

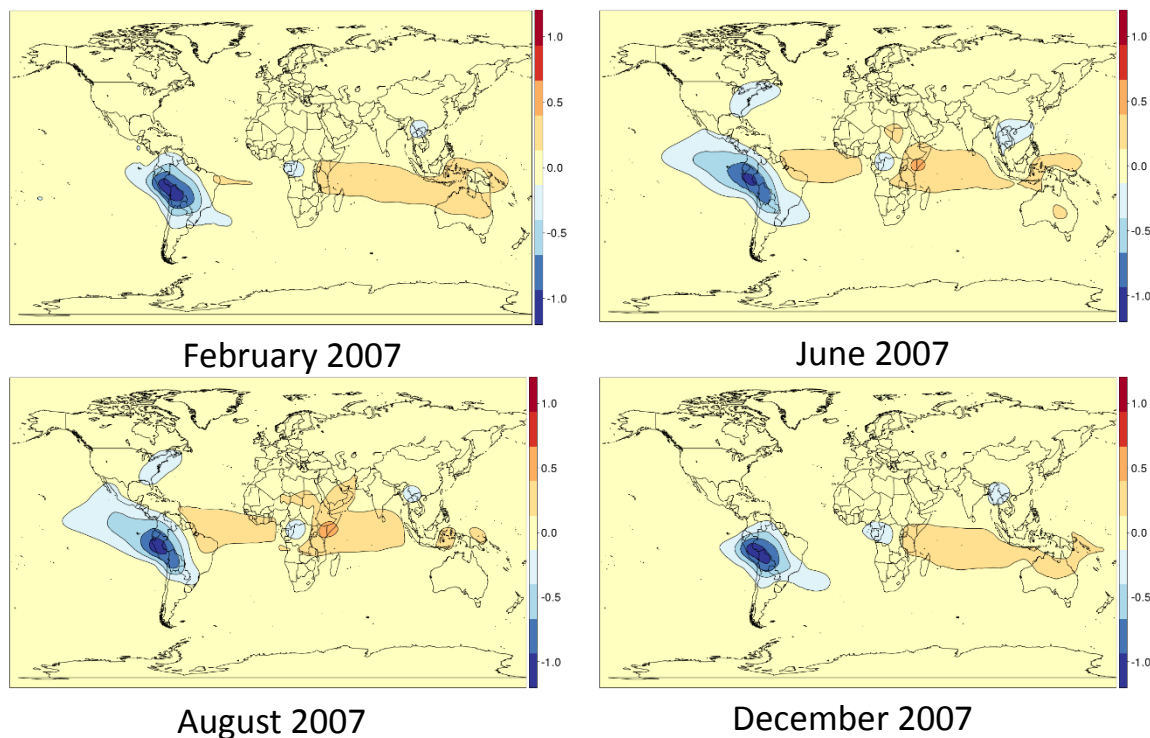


767  
768 **Figure 3-11** The simulated net CO<sub>2</sub> flux anomalies that arise from the GPP and ocean flux perturbations used in the  
769 multiple signal detection exercise and inversions. Note the dominance of Amazon GPP sink enhancement.

770 The flux perturbations shown in Figure 3-11 were used to drive GEOS-Chem for 2006 and 2007  
771 to produce 3-D CO<sub>2</sub> anomaly fields for 2007. The fields were then sampled using the ASCENDS  
772 weighting functions resulting in XCO<sub>2</sub>. The mean zonal gradient for each month was then  
773 subtracted from the monthly perturbation XCO<sub>2</sub> fields in order to isolate the local effects of sinks  
774 on XCO<sub>2</sub>. Finally, this average perturbation field was divided by the expected ASCENDS errors.

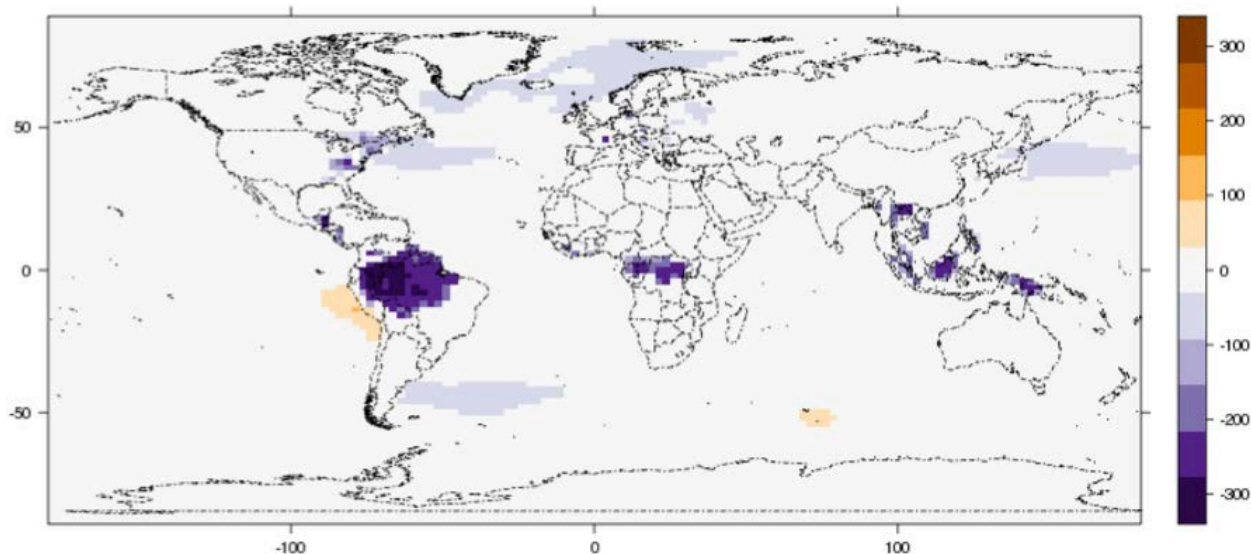
775 The absolute perturbation signal-to-noise of the ASCENDS pseudo measurements (Figure 3-12)  
 776 is often greater than 0.5 for *individual* retrievals at 1-ppmv nominal error (Box 3-1), with slightly  
 777 stronger signals during the Amazonian wet season. These results suggest that the strong Amazon  
 778 drawdown would be evident from ASCENDS by carefully aggregating individual satellite  
 779 retrievals. While the weakened surface exchange of CO<sub>2</sub> in the oceans seems unlikely to be  
 780 detectable from individual ASCENDS retrievals, the combined effect of reduced respiration and  
 781 N fertilization effects on regrowing Northeastern U.S. forests, most evident in the late spring and  
 782 summer, is evident, although at much lower signal to noise than the Amazon.

### 783 *Flux Estimation*



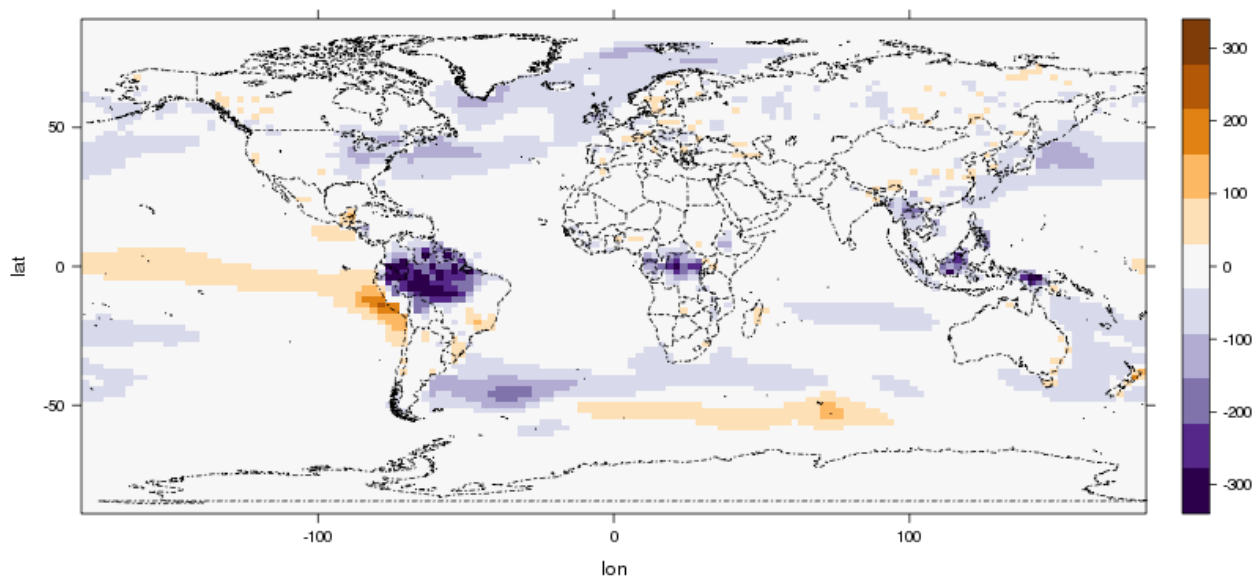
784  
 785 **Figure 3-12** Simulated perturbation signal-to-noise for XCO<sub>2</sub> with 2.05 μm weighting function (See Box 3-1 and  
 786 Figure 5-2) for the multiple flux perturbations of Figure 3-11.

787 The results above suggest the ability of individual retrievals to detect realistic flux perturbations.  
 788 An EnKF-based inversion (Table 3-1, Box 3-2, Appendix C) was run on the perturbed CO<sub>2</sub> field  
 789 to determine to what degree the true perturbed fluxes could be estimated using ASCENDS  
 790 observations. Figure 3-13 shows the true and the posterior estimated fluxes: their similarity  
 791 indicates that large perturbations in land fluxes, such as the Amazon, will be attributable via  
 792 inversions of atmospheric CO<sub>2</sub> measurements from ASCENDS. Figure 3-14 shows that the  
 793 difference between the ensemble mean CO<sub>2</sub> flux estimate for the Tropical South American region  
 794 (Transcom, Gurney et al., 2002) and the “truth” is approximately 100 TgC/year with a standard  
 795 deviation (uncertainty) of the posterior estimate at approximately the same magnitude. The  
 796 recovered sink is approximately 18 times that, indicating a strong recovery by the inversion  
 797 system.



798  
799

(a)



800  
801

(b)

802 **Figure 3-13** Comparison of ‘truth’ and model annual Net Ecosystem Exchange (NEE, gC m<sup>-2</sup> yr<sup>-1</sup>) (a) the ‘truth’  
803 representing the sum of the two sets of perturbations shown in Figure 3-11 and (b) model estimated posterior mean  
804 NEE from the atmospheric inversion. Posterior uncertainty can be seen below in Figure 3-14.

805 Weaker land signals such as those generated by regrowth of forests in the northeastern U.S. and  
806 nitrogen fertilization of Europe are also generally improved by the inversion system, although the  
807 pattern is more diffuse than that specified in the “true” fluxes. The difference between the  
808 ensemble mean CO<sub>2</sub> flux estimate for the Temperate North American region and the “truth” is  
809 approximately 38 TgC/year with the standard deviation of the estimate at approximately 40  
810 TgC/year, significantly smaller than the recovered sink (~200 TgC/year). Spatial differences of  
811 up to 100 gC/m<sup>-2</sup> within the region are seen (Figure 3-13) although the integrated average

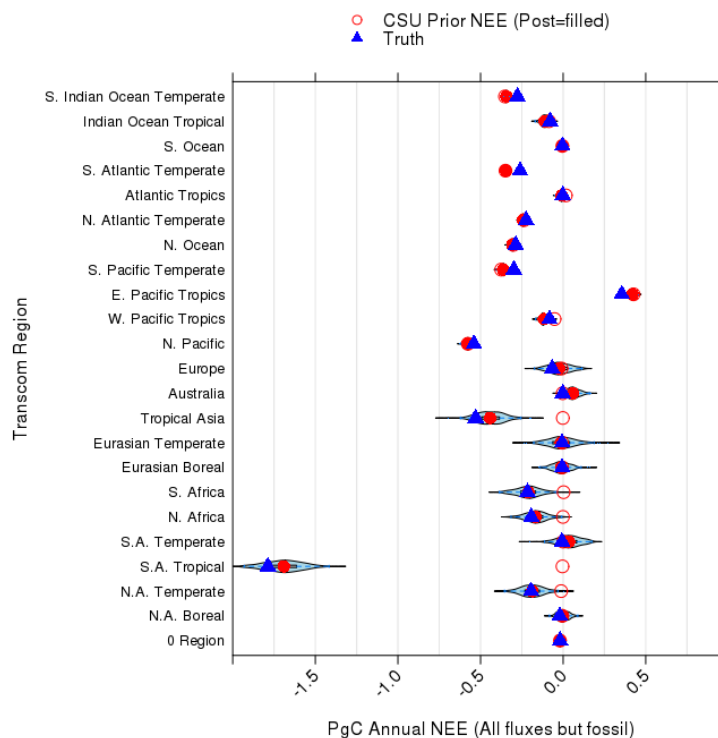
812 difference is much smaller. Ocean perturbations are not seen well by the inversion system, which  
 813 could be due to a misspecification of the prior covariance for the ocean fluxes in the simulations,  
 814 weaker magnitudes of the ocean flux perturbations, or likely some combination of the two.

815

**ASCENDS will provide data sufficient to constrain large tropical land sinks as well as some weaker Northern mid-latitude regional land sinks.**

816

817



818

819 **Figure 3-14** Regional integrated annual NEE for atmospheric inversion test. The blue shaded area can be interpreted  
 820 as the probability density function estimate for the ENKF ensemble (Hintze et al., 1998).

821 **3.3 Improved Flux Estimates at Global and Regional Scales**

822 The experiments in Section 3.2 evaluated the ability of ASCENDS measurements to address  
 823 specific science hypotheses posed as realistic perturbations to carbon fluxes. Here, we broaden  
 824 this approach to test the general impact of prospective ASCENDS data on flux inversions at both  
 825 regional and global scales. A major goal of this exercise is to test the impact of a range of  
 826 possible mission and instrument implementation options (Chapter 5) on the ability of ASCENDS  
 827 to reduce uncertainty in our knowledge of the carbon budget. Some of these parameter  
 828 explorations were already exhibited in the inversions in Sections 3.2. A variety of modeling  
 829 approaches is used in order to bolster the robustness of the findings from any individual model,  
 830 whose flux retrieval performance may well depend on model-specific methods and assumptions  
 831 (Table 3-1). The general Bayesian inverse modeling approach, and its variants, employed for  
 832 these experiments are briefly outlined in Box 3-2, and in more detail in Appendix C. The  
 833 instrument models that are tested include sampling with vertical weighting functions applicable to

834 measurement wavelengths of 1.57 and 2.05  $\mu\text{m}$  (Figure 5.2), three levels of nominal random error  
835 (0.5, 1.0, and 2.0 ppmv) scaled globally (Box 3.1), and several possible forms of bias error (in the  
836 global inverse model only).

837 **Box 3-2 Flux Estimation Techniques**

The basic premise of the inverse modeling approaches is that, given a set of atmospheric concentration observations and using a model of atmospheric transport and chemistry, it is possible to infer information on the distribution of sources and sinks at the surface of the Earth (Enting, 2002). The approach most commonly adopted in atmospheric inverse modeling of  $\text{CO}_2$  sources and sinks is based on Bayesian inverse modeling, in which one seeks the optimal flux estimate  $\hat{\mathbf{s}}$  that minimizes:

$$J(\mathbf{s}) = (\mathbf{s} - \mathbf{s}_0)^T \mathbf{B}^{-1} (\mathbf{s} - \mathbf{s}_0) + (\mathbf{h}(\mathbf{s}) - \mathbf{y})^T \mathbf{R}^{-1} (\mathbf{h}(\mathbf{s}) - \mathbf{y}) \quad (3-2)$$

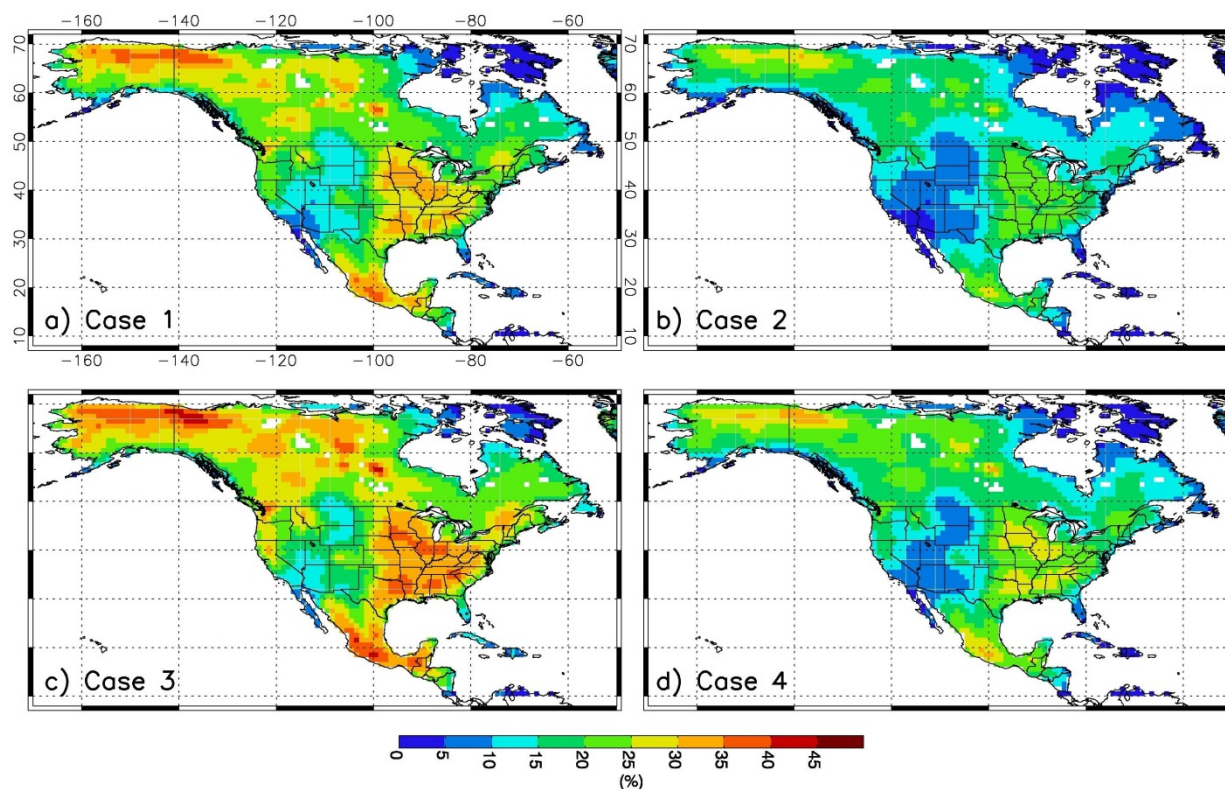
where  $\mathbf{y}$  is a vector of atmospheric  $\text{CO}_2$  observations,  $\mathbf{h}$  represents an atmospheric transport model,  $\mathbf{s}$  is a vector of the discretized unknown surface flux distribution,  $\mathbf{R}$  is the model-data mismatch covariance,  $\mathbf{s}_0$  is the prior estimate of the flux distribution  $\mathbf{s}$ , and  $\mathbf{B}$  is the covariance of errors in the prior estimate  $\mathbf{s}_0$ . The final solution in the form of a posteriori means and covariances is given by:

$$\hat{\mathbf{s}} = \mathbf{s}_0 + \mathbf{B}\mathbf{H}^T (\mathbf{H}\mathbf{B}\mathbf{H}^T + \mathbf{R})^{-1} (\mathbf{y} - \mathbf{H}\mathbf{s}_0) \quad (3-3)$$

$$\mathbf{V}_{\hat{\mathbf{s}}} = \mathbf{B} - \mathbf{B}\mathbf{H}^T (\mathbf{H}\mathbf{B}\mathbf{H}^T + \mathbf{R})^{-1} \mathbf{H}\mathbf{B} \quad (3-4)$$

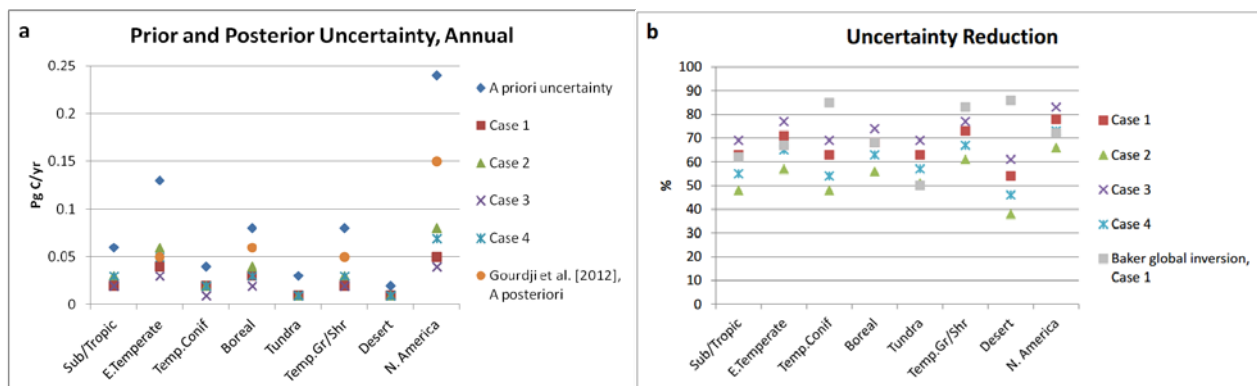
where  $\hat{\mathbf{s}}$  is the posterior best estimate of the surface flux distribution and  $\mathbf{V}_{\hat{\mathbf{s}}}$  is the a posteriori covariance of that best estimate, where the diagonal elements represent the predicted error variance ( $\sigma^2$ ) of individual elements in  $\mathbf{s}$ .  $\mathbf{H}$  (a.k.a. the sensitivity matrix) is calculated by sampling the atmospheric transport model and represents the sensitivity of the observations  $\mathbf{y}$  to the fluxes  $\mathbf{s}$  (i.e.). Participating modeling groups (Table 3-1) have employed different techniques to find the solution to the atmospheric inverse problem posed in the equations above. Further detailed information can be found in Appendix C.

838

839 **3.3.1 North American Regional Flux Estimates**

840  
841 **Figure 3-15** Weekly flux uncertainty reduction (RMS over the 4 months) over North America for a) Case 1 (1.57  $\mu\text{m}$   
842 and 0.5 ppm nominal error), b) Case 2 (1.57  $\mu\text{m}$  and 1.0 ppm), c) Case 3 (2.05  $\mu\text{m}$  and 0.5 ppm), and d) Case 4 (2.05  
843  $\mu\text{m}$  and 1.0 ppm).

844 Bayesian synthesis (batch) inversions are used to quantify the precision with which ASCENDS  
845 measurements can constrain land carbon sinks and sources at relatively high spatial resolution  
846 over a region such as North America (Wang et al., 2014). We consider four possible instrument  
847 configurations, including two weighting functions (for the 1.57  $\mu\text{m}$  and 2.05  $\mu\text{m}$  wavelengths)  
848 and two nominal random error levels (0.5 ppm and 1.0 ppm, see Box 3-1). ASCENDS  
849 observations in this modeling framework reduce flux uncertainties substantially at fine scales. At  
850  $1^\circ \times 1^\circ$  resolution, weekly uncertainty reductions up to 30-45% (averaged over the year) are  
851 achieved depending on the instrument configuration (Figure 3-15). Relatively large uncertainty  
852 reductions occur year-round in southern Mexico and the U.S. Pacific Northwest and seasonally  
853 over the southeastern and mid-western U.S. and parts of Canada and Alaska. The magnitude of  
854 uncertainty reduction is dependent on the observational coverage, the specified model-data  
855 mismatch and the prior flux errors. Uncertainty reductions at the annual, biome scale range from  
856  $\sim 40\%$  (desert) to  $\sim 75\%$  (eastern temperate forest and temperate grassland/shrubland) over the four  
857 experimental cases, and from  $\sim 65\%$  to  $\sim 85\%$  for the continent as a whole (Figure 3-16). The  
858 uncertainty reductions for the 1.57  $\mu\text{m}$  candidate wavelength are on average 8% smaller than  
859 those for 2.05  $\mu\text{m}$ , and for 0.5 ppm reference error are on average  $\sim 15\%$  larger than those for 1.0  
860 ppm error.



861  
862 **Figure 3-16** Results aggregated to biomes and continent, and compared with other studies a) A priori and a posteriori  
863 uncertainties for the year, including results from Gourdj et al. (2012). b) Fractional uncertainty reductions, including  
864 results from the CSU-PCTM OSSE described in Section 3.3.3. Gourdj et al. reported results for only the three  
865 biomes that were well constrained by their in situ observation network, along with results aggregated over the full  
866 continent; we show the approximate average of their "Simple" and "NARR" inversions. The Gourdj et al. method  
867 does not rely on prior flux estimates.

868 The uncertainty reductions in this regional OSSE are similar in magnitude on average to those of  
869 the global ASCENDS inversion detailed in Section 3.3.3.1 when aggregated to the latter's coarser  
870  $4.5^\circ \times 6^\circ$  model grid and to the biome and continent scales (Figure 3-16).

871 Based on the flux precision level suggested by Hungershoefer et al. (2010), ASCENDS  
872 observations would meet the threshold requirement (flux uncertainty of less than  $0.1 \text{ Pg C yr}^{-1}$  at  
873 the annual, biome scale) for all biomes within the range of measurement designs considered here  
874 (Figure 3-16). The observations constrain *a posteriori* flux uncertainties to a level of 0.01-0.06  
875  $\text{Pg C yr}^{-1}$ , and could thus help identify the location and magnitude of long-term carbon sinks.  
876 With regard to the more stringent target requirement (less than  $0.02 \text{ Pg C yr}^{-1}$ ), a subset of the  
877 instrument designs would meet the target for a majority of biomes.

878 These results represent a best-case scenario, as measurement biases and other sources of  
879 systematic errors not considered here (e.g., transport model, boundary condition) degrade inverse  
880 flux estimates. However, abundant concentration measurements by ASCENDS can be expected  
881 to mitigate the impact of boundary condition uncertainties on regional flux estimates (Wang et al.,  
882 2014).

**ASCENDS observations could reduce flux uncertainties substantially at biome and finer (e.g. approximately 100 km by 100 km) scales, meeting requirements for improved understanding of long-term carbon sinks.**

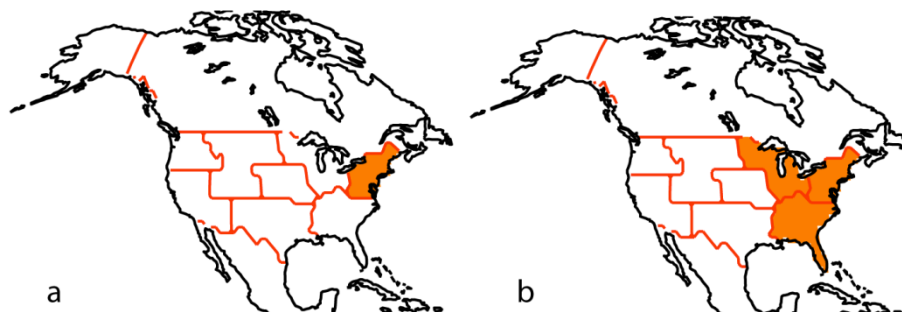
### 883 884 3.3.2 Regional Fossil Fuel Emissions

885 In this experiment, we explore the ability of ASCENDS  $\text{CO}_2$  measurements to distinguish  
886 between fossil fuel and natural biospheric fluxes. This analysis is performed with a regional  
887 geostatistical inverse modeling (GIM) framework over North America (NA) that examines fluxes  
888 at a  $1^\circ$  by  $1^\circ$  spatial and 3-hourly temporal resolution (Table 3-1). We examine the potential of  
889 ASCENDS measurements to detect and attribute variations in the spatio-temporal patterns of  
890 fossil fuel  $\text{CO}_2$  ( $\text{FFCO}_2$ ) emissions from sub-continental regions in NA during January. January is  
891 selected because it represents a time when the confounding effects of biospheric  $\text{CO}_2$  flux are at a

892 minimum. Simulated CO<sub>2</sub> observations are created using biospheric fluxes from CASA-GFEDv2  
 893 (Randerson et al., 1997), FFCO<sub>2</sub> emission from the Vulcan Project (Gurney et al., 2009) over the  
 894 continental U.S. and Open-source Data Inventory of Anthropogenic CO<sub>2</sub> emission (ODIAC) (Oda  
 895 and Maksyutov, 2011) over Alaska, Canada and Mexico, and various levels of random error.  
 896 Detection is evaluated by the ability to attribute variations in three-hourly ASCENDS CO<sub>2</sub>  
 897 observations to patterns consistent with the simulated FFCO<sub>2</sub> emissions. A more detailed  
 898 description of the FFCO<sub>2</sub> emissions pattern detection methodology can be found in Shiga et al.  
 899 (2014).

900 Four cases representing different instrument configurations are explored using the two weighting  
 901 functions (1.57 μm and 2.05 μm) and two random error levels (0.5 ppm and 1.0 ppm) as in the  
 902 previous section. For the 1 ppm nominal error cases, both 1.57 μm and 2.05 μm instrument  
 903 configurations could detect the FFCO<sub>2</sub> emissions from only one region, i.e., the Northeast US  
 904 region (Figure 3-17a). For the 1.57 μm instrument case, reducing errors to the 0.5 ppm nominal  
 905 error level did not improve detectability. However, for the 2.05 μm instrument case, when  
 906 reducing errors to the 0.5 ppm nominal error level, detection of the FFCO<sub>2</sub> emissions patterns  
 907 from the Midwest and Southeast US regions becomes possible (Figure 3-17b). This result shows  
 908 that the impact of reducing errors for the 2.05 μm instrument are greater with regards to detecting  
 909 FFCO<sub>2</sub> emissions than for the 1.57 μm instrument configuration. For all configurations, the  
 910 ASCENDS CO<sub>2</sub> observations, in the absence of in-situ observations, will be able to detect the  
 911 FFCO<sub>2</sub> emissions patterns of the largest emitting sub-continental regions over NA.

912



913

914 **Figure 3-17** The regions where fossil fuel CO<sub>2</sub> emissions are detected for January (in orange) using ASCENDS  
 915 2.05μm weighting function with (a) 1 ppm nominal error and (b) 0.5 ppm nominal error. Detection results for the  
 916 1.57 μm weighting function for both error levels mirror panel (a).

**ASCENDS will be able to discern the FFCO<sub>2</sub> emissions patterns from the largest emitting sub-continental regions over North America, particularly with the 2.05 μm weighting function.**

917

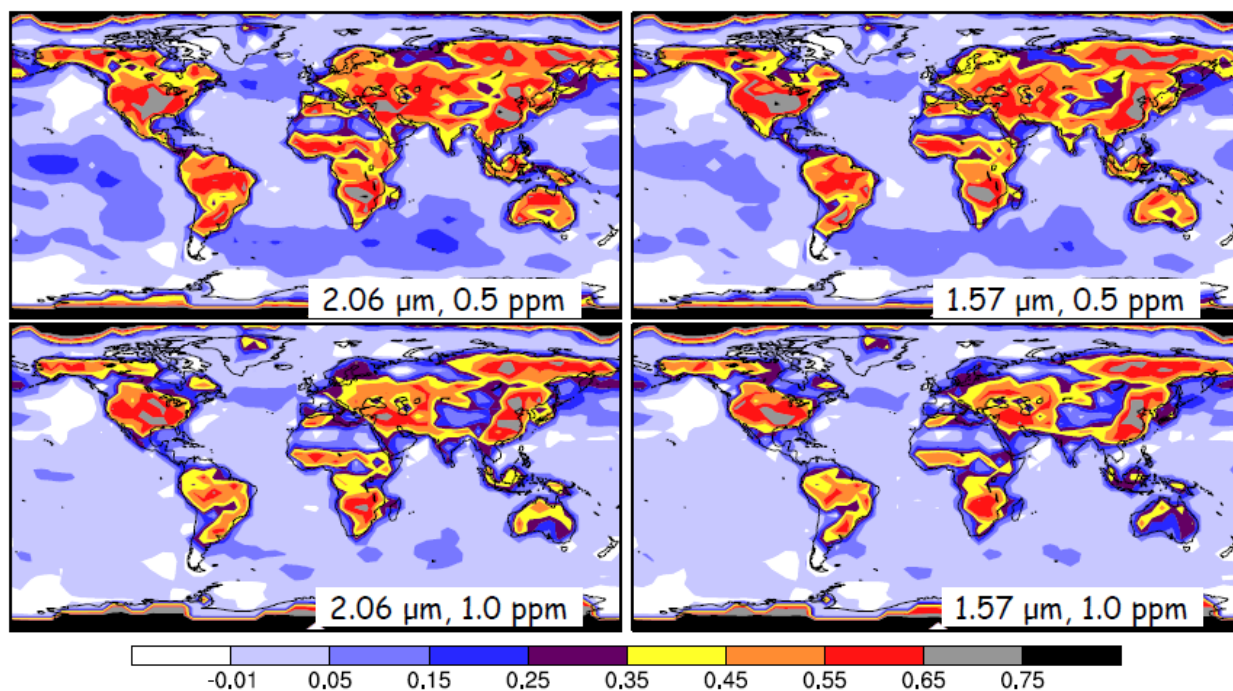
### 918 3.3.3 Global Flux Estimation with ASCENDS

919 In this section we quantify the reduction in the uncertainty in the flux estimates globally that is  
 920 possible by using CO<sub>2</sub> measurements from ASCENDS. The flux errors are constructed by  
 921 selecting two reasonable models of global land biospheric fluxes and air-sea fluxes, each set  
 922 having the seasonal variability of a representative year (Table 3-1, Box 3-2, Baker et al., 2010).  
 923 Net fluxes from the Lund–Potsdam–Jena (LPJ) land biosphere model (Sitch, et al., 2003) plus

924 ocean fluxes from a run of the National Center for Atmospheric Research (NCAR) ocean model  
 925 that captures the impact of rising anthropogenic CO<sub>2</sub> concentrations (Doney et al., 2006; Najjar et  
 926 al., 2007) are assigned the role of the “true” fluxes. Net CASA land biospheric flux from  
 927 Randerson et al. (1997) plus air-sea fluxes from Takahashi et al. (1999) are used as the prior flux  
 928 estimate. The difference between the two can be thought of as a global net CO<sub>2</sub> flux error  
 929 “signal” to be estimated in the assimilation, analogous to the sum of process-based signals like  
 930 those used in Section 3.2. The difference is that this “signal” is perhaps more representative of the  
 931 actual flux error we expect to encounter in the real world. Insofar as the inversion problem is  
 932 made more difficult by having to distinguish between large fluxes in close proximity to each  
 933 other, this simulation should provide a more general test of the ability of ASCENDS data to  
 934 constrain fluxes. Other than not having errors due to uncertainties in the fossil fuel flux  
 935 distribution (which are relatively small except over the strongest fossil emission areas), this case  
 936 should provide flux estimation errors similar to what would be obtained using real ASCENDS  
 937 data.

### 938 3.3.3.1 Impact of Random Observational Errors

939 To test the flux impact of different instrument design possibilities, weekly fluxes for a full year  
 940 were estimated at 4.5° x 6° resolution (lat/long) for four ASCENDS cases: the 2.05 and 1.57 μm  
 941 weighting functions with nominal random measurement errors at two levels, 0.5 and 1.0 ppm  
 942 (Box 3-1). In this model setup, measurement uncertainties across the globe were estimated by  
 943 multiplying the spatial patterns like those in Figure 3-1 by a given error value (e.g., 0.5 ppm) on a  
 944 monthly basis (see Appendix C).



945  
 946 **Figure 3-18** Fractional error reduction in weekly flux at 4.5°x6° resolution (lat/long) for four cases: using the 2.05 μm  
 947 and 1.57 μm vertical weighting and measurement uncertainties at 0.5 and 1.0 ppm.

948 Figure 3-18 shows the fractional error reduction with respect to the prior for the four cases.  
 949 Substantial improvements in the flux estimates are obtained in all cases (Table 3-2). At 0.5 ppm

950 nominal measurement error, flux uncertainty reductions of 50% or better are obtained over most  
 951 of the vegetated land areas. As expected, reducing the measurement error from 1.0 to 0.5 ppm,  
 952 reduces flux error over both land and ocean areas. The improvements obtained for the 2.05  $\mu\text{m}$   
 953 case, whose vertical sensitivity (Figure 5-2) peaks nearer the surface, are generally slightly larger  
 954 than for the 1.57  $\mu\text{m}$  case. This is true despite the fact that the measurement uncertainties for the  
 955 2.05  $\mu\text{m}$  case are somewhat higher over land (Figure 3-1): the stronger near-surface vertical  
 956 sensitivity outweighs the impact of the higher errors.

957 The *a posteriori* flux uncertainties obtained here should be applicable to localized fluxes from any  
 958 part of the globe, since they primarily reflect the constraint provided by the measurements rather  
 959 than the prior flux uncertainties. To compare these results to those of the signal detection  
 960 experiments in Section 3.2, we sample the grid-scale errors for the regions of interest. Fluxes  
 961 north of 65°N are retrieved here with a precision of 0.38  $\text{gC}/\text{m}^2/\text{day}$  ( $1\sigma$ ) during June-August, and  
 962 to 0.26  $\text{gC}/\text{m}^2/\text{day}$  across the full year, using ASCENDS data at the 0.5 ppm nominal  
 963 measurement uncertainty. This corresponds to a weekly flux uncertainty of  $\sim 200$  TgC/year.  
 964 Uncertainty totals for the North American and Siberian areas are  $\sim 80$  and  $\sim 180$  TgC/year,  
 965 respectively. These numbers give the precision of the estimate of net  $\text{CO}_2$  flux coming from the  
 966 permafrost region – that is, the combined impact of photosynthesis, respiration, fire, and any other  
 967 permafrost-related emissions (e.g. methane oxidized to  $\text{CO}_2$ ) – but cannot say how much is due  
 968 strictly to permafrost-related emissions. The magnitude of the permafrost emission perturbation is  
 969 613 to 752 TgC/y for 2020 to 2022 (Hammerling et al., 2015), which should be readily  
 970 attributable, consistent with the findings from Section 3.2 above.

971

**Table 3-2 Flux Inversion Fractional Error Reduction\***

Mission Sampling  Mmt Error (ppmv)	ASCENDS 1.57 $\mu\text{m}$		ASCENDS 2.05 $\mu\text{m}$		In situ + TCCON	GOSAT ACOS	OCO-2 estimated
	0.5	1.0	0.5	1.0			
Land	0.49	0.41	0.51	0.44	0.22	0.30	0.59
Ocean	0.21	0.14	0.24	0.17	0.09	0.10	0.31

972 \* Reduction is equal to (prior-posterior)/prior error where the prior error is the grid-scale RMS flux difference  
 973 between two carbon models and the posterior error is the flux difference after assimilating each data stream  
 974 separately. Values are the RMS of 52 weekly flux differences. Global prior errors are 2.84 and 0.33 ( $10^{-8} \text{kgCO}_2 \text{m}^{-2} \text{s}^{-1}$ )  
 975 for land and ocean, respectively.

976 In the Southern Ocean (taken as south of 47°S), weekly net  $\text{CO}_2$  fluxes at the scale of the  $4.5^\circ \times 6^\circ$   
 977 grid boxes used here may be retrieved with a precision of  $\sim 0.05 \text{gC}/\text{m}^2/\text{day}$  using ASCENDS data  
 978 at the 0.5 ppm measurement uncertainty. This is accurate enough to track strong local spatial and  
 979 temporal variability. In terms of the precision of the flux integrated across the full extent of the  
 980 Southern Ocean, the measurements can constrain fluxes with an uncertainty of  $\sim 300$  TgC/year, a  
 981 precision that is not sensitive to the time-scale of the solution (weekly to seasonal). The  
 982 magnitude of the flux perturbation for this case in Section 3.2 is  $\pm 180$  TgC/y (Hammerling et  
 983 al., 2015), which is near the detection limit if taken to be at signal to noise of 1, again consistent  
 984 with the prior assessments.

**Substantial flux uncertainty reductions are obtained for all tested cases of ASCENDS measurement error and vertical weighting function. Simulations with the 2.05 μm weighting function are slightly better than for 1.57 μm at the same nominal errors levels.**

985

986 **3.3.3.2 Impact of Systematic Measurement Errors**

987 In addition to the impact of random measurement errors on the uncertainty in the estimated  
 988 fluxes, systematic errors in remote sensing CO<sub>2</sub> measurements can lead to serious flux errors even  
 989 at relatively small magnitudes (Chevallier et al., 2014) because the systematic errors can be  
 990 correlated with geophysical variations related to flux, e.g., land/ocean, solar zenith, surface  
 991 reflectance, clouds, etc. For satellite CO<sub>2</sub> measurements, systematic measurement errors can be of  
 992 a similar magnitude to random measurement errors, as is thought to be the case with GOSAT data  
 993 (O’Dell et al., 2012, Kulawik et al., 2015). The impact of systematic errors on flux estimation is  
 994 assessed in the same OSSE setup as used above, where systematic errors are added to the  
 995 simulated measurements in parallel with the random errors. Although systematic errors are by  
 996 their nature hard to foresee (if we knew them, we could calibrate them out), we have derived a set  
 997 of potential bias cases for ASCENDS that can be scaled and used in flux OSSEs to help guide  
 998 bias requirements for the instrument development based on their impact in flux estimation.

999

**Table 3-3 ASCENDS Bias Cases**

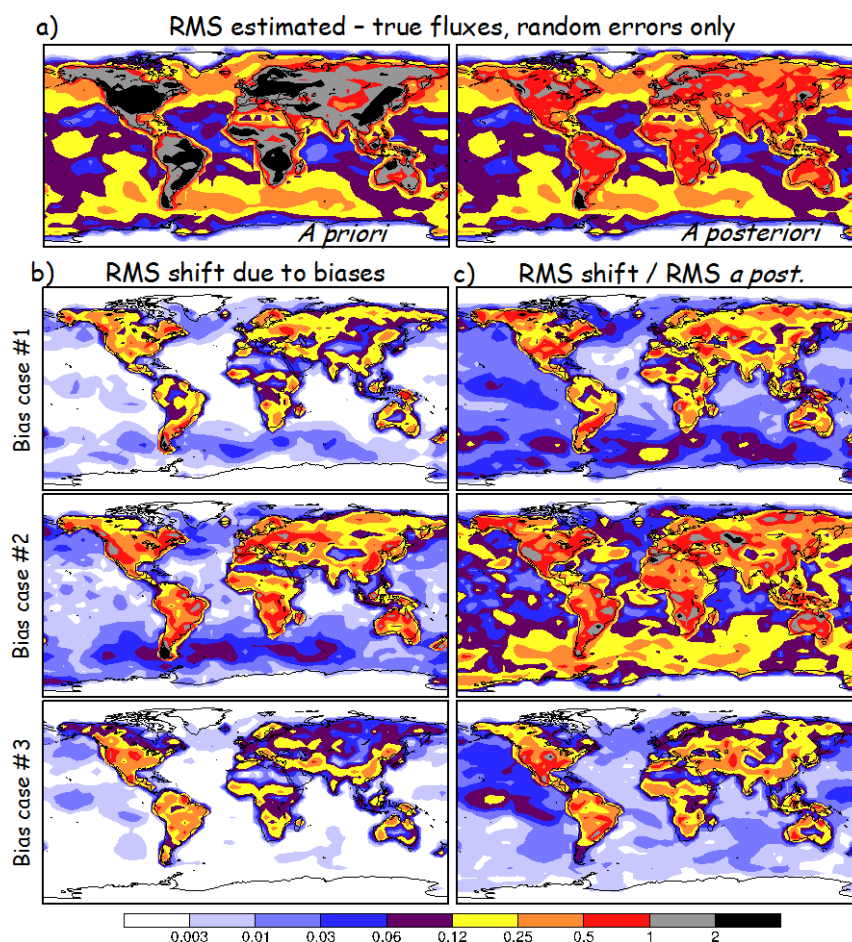
Case #	Bias Error Dependence	Rationale	Initial Error Scaling	Comments
1	Error varies with <u>Sun angle</u> on spacecraft	Instrument temperature changes can cause errors. Sun illumination is a heat source and heating usually depends on angle of the sun relative to the instrument.	Error (x) = 1 ppm * COS (solar zenith angle) for SZA < 95.	Instruments usually cool in shadow.
2	Error depends on received <u>signal strength</u>	Plausible to expect small degree of non-linear instrument response, or small offset	Error (x) = -1 ppm * ((1-r) / (1+50*r) + r <sup>2</sup> ) where r = 0.33 * signal strength (x) / nominal desert signal	Error scaling formula is for a small offset in readings.
3	Error varies with cloud backscatter (i.e., cloud optical depth)	Possible “leakage” of cloud scattered light into signal. Usually, cloud scatter has a shorter path length resulting in negative bias.	Error (x) = -1 ppm * (cloud OD(x) ) for OD cutoff < 1	Mixed cloud and ground scattering (i.e., cloud OD is not too high)

1000

1001 The ASCENDS measurement teams formulated three possible bias cases based on sources of  
 1002 systematic error that could conceivably be present in actual lidar CO<sub>2</sub> measurements on-orbit  
 1003 (Table 3-3). The maximum magnitudes of the biases were arbitrarily set at 1 ppm. The biases in  
 1004 Table 3-3 were then added to the simulated true CO<sub>2</sub> concentrations in separate OSSEs, in  
 1005 addition to the 0.5 ppm nominal random errors added above. The magnitude of the shift in the

1006 flux estimates caused by the measurement biases was then compared to the magnitude of the  
1007 random flux errors computed before.

1008 The impact of these biases on the fluxes at seasonal time scales is significant (Figure 3-19). They  
1009 cause a bias in the flux estimates that is generally 25-50% of the magnitude of the a posteriori  
1010 random errors over land, with a smaller impact over the oceans. Bias case #2 (the signal strength-  
1011 dependent bias) caused the largest impact at these longer time scales. A fourth case (not shown),  
1012 which tested snow under northern trees biasing the apparent surface height, had a much smaller  
1013 impact on the fluxes.



1014  
1015 **Figure 3-19** Seasonal RMS shift or bias cases compared to a priori and a posteriori errors b) The RMS of the shift or  
1016 bias in the seasonal fluxes caused by the three ASCENDS bias cases from 3 at the  $\pm 1$  ppm level, compared to a) the a  
1017 priori and a posteriori RMS seasonal flux errors [ $10^{-8}$  kgCO<sub>2</sub>/m<sup>2</sup>/s] caused by random errors only. c) The ratio of the  
1018 RMS flux bias to the RMS a posteriori random errors is also given according to the same color scale (unitless). All  
1019 results are for the 1.57  $\mu$ m, 0.50 ppm random error case.

1020 These experiments illustrate the importance of considering the impact of systematic errors when  
1021 assessing the scientific return of a space mission like ASCENDS. Systematic errors are thought  
1022 to be significant for CO<sub>2</sub> measurements of current satellites (e.g. GOSAT, AIRS) and will likely  
1023 play a significant role for future satellites such as OCO-2 and ASCENDS. They are considered  
1024 further below in assessing the value of ASCENDS in comparison with other measurements.

### 1025 3.4 ASCENDS in the Context of Other CO<sub>2</sub> Observing Systems

1026 In this section we compare the impact on flux estimates of using simulated ASCENDS data to  
1027 that of using current in situ plus TCCON data, GOSAT, and projected OCO-2 data. The global  
1028 flux estimation OSSEs are well-suited to answer these questions because they can be constructed  
1029 to estimate the flux uncertainty reduction provided by any hypothetical set of measurements. Two  
1030 sets of experiments were run, one using only random measurement errors, the other including  
1031 systematic errors as well. Passive sensors such as OCO-2 and GOSAT are expected to be more  
1032 susceptible to bias errors than ASCENDS due to the greater difficulty in determining the  
1033 atmospheric path length and influence of scattering, as has been seen with GOSAT (O'Dell et al.,  
1034 2012). The measurement capabilities of GOSAT are based on its current performance, while those  
1035 for OCO-2 are based on its expected performance using prelaunch calibration data and the  
1036 experience of GOSAT as a guide.

#### 1037 3.4.1 Comparison in Terms of Random Errors

1038 Together with the ASCENDS OSSE results discussed above (Section 3.3.3.1), Table 3-2 includes  
1039 aggregate flux uncertainty reductions for a case using CO<sub>2</sub> from the current NOAA *in situ*  
1040 network (flasks, observatories, tall towers, and routine light aircraft profiles) plus the TCCON  
1041 network, as well as that using the GOSAT satellite in 3-point cross-scan mode. For weekly fluxes  
1042 at the scale of (~500km<sup>2</sup>), the existing ground network provides only a weak constraint, except  
1043 over certain well-instrumented areas like Temperate North America. The GOSAT satellite  
1044 improves upon this, but due to its relatively large FOV (~100 km<sup>2</sup>) and consequent sensitivity to  
1045 clouds, the additional constraint is not great. We have assumed measurement uncertainties of 1.7,  
1046 1.5, and 1.0 ppm (1σ) for GOSAT high-gain land, medium-gain land, and ocean glint data,  
1047 respectively, based on its currently estimated capabilities (ACOS b3.4 retrieval, ACOS Level 2).  
1048 GOSAT data add the most value in areas that are poorly constrained by the ground-based  
1049 measurements. Aggregating results into TRANSCOM regions (not shown) produces rank-order  
1050 results consistent with those given for global land and ocean. ASCENDS data for any of the  
1051 tested instrument configurations provide a major improvement in flux uncertainty reduction  
1052 compared to current observations.

1053 Flux estimates have also been made using projections for random errors from OCO-2. OCO-2  
1054 nominal uncertainties in the 0.5-1.0 ppm range are obtained by multiplying the uncertainties of  
1055 Bösch et al. (2011), by a factor of two to account for errors not captured by their analysis. The  
1056 Bösch et al. measurement uncertainties and averaging kernels are computed as a function of solar  
1057 zenith angle, aerosol optical depth, and surface type. According to these simulations, OCO-2  
1058 provides a much stronger constraint than either GOSAT or the ground-based measurements  
1059 (Table 3.2). This is a result of OCO-2's much greater sampling density. The smaller OCO-2 field  
1060 of view (~3 km<sup>2</sup>), should allow more frequent cloud-free shots, improving data yield fraction by  
1061 as much as a factor of two compared to GOSAT (Miller et al., 2007). OCO-2 also has greater  
1062 measurement frequency: with roughly 24x60 possible measurements per minute, compared to ~30  
1063 for GOSAT, the OCO-2 satellite should provide substantially more CO<sub>2</sub> information than  
1064 GOSAT, even if the two satellite instruments were to have similar precision levels.

1065 Considering only random errors, ASCENDS measurements with a nominal precision equivalent  
1066 to 0.5 ppm provide a somewhat weaker constraint on the fluxes globally at weekly time scales  
1067 than expected from OCO-2 (Table 3-2). By these global metrics, the denser OCO-2 sampling  
1068 more than compensates for the extra coverage provided by ASCENDS on the night side of the

1069 orbit and at high latitudes. ASCENDS would have to push nominal random errors as low as 0.25  
1070 ppm (not shown) to equal or improve upon OCO-2 in these random error OSSE results. Random  
1071 errors of 0.25 ppm, however, are outside the current ASCENDS design envelope.

**ASCENDS data will provide a major improvement in flux uncertainty compared to current observations including in situ, TCCON, and GOSAT. Globally, flux estimates from ASCENDS will be similar to or slightly worse than those projected for OCO-2 if only random errors are considered.**

1072

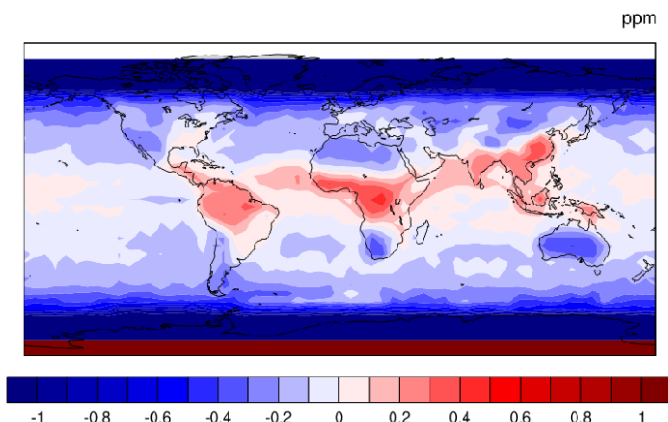
### 1073 3.4.2 Comparison Considering Systematic Errors

1074 Systematic errors can greatly degrade the flux constraints as calculated above and, based on  
1075 GOSAT experience, are suspected to have a larger impact on the flux estimates from satellite data  
1076 than random errors at this point in time (Chevallier et al., 2014). GOSAT measurements currently  
1077 suffer from significant and poorly-characterized systematic errors, up to about 0.7 ppm even after  
1078 the standard bias correction is applied (Kulawik *et al.*, 2015). OCO-2 will be subject to similar  
1079 possible systematic errors (though perhaps of a lower magnitude due to its improved ability to  
1080 avoid clouds.) ASCENDS can be expected to provide measurements with significantly lower  
1081 biases than the passive missions as a result of the laser measurement approach (Section 1.4). Flux  
1082 OSSEs are used here to demonstrate the impact of systematic errors, based on plausible  
1083 systematic error patterns added to the random measurement errors.

#### 1084 **Box 3-3** Simulation of Systematic Errors

1085 One approach to estimating the systematic errors that will affect the OCO-2 measurements is to  
1086 pattern them after the biases currently affecting the GOSAT measurements (the best source of  
1087 near-infrared (IR) CO<sub>2</sub> measurements currently available). The raw column CO<sub>2</sub> mixing ratios  
1088 retrieved by the Atmospheric CO<sub>2</sub> Observations from Space (ACOS) team for GOSAT have been  
1089 compared to column CO<sub>2</sub> measurements from the TCCON network, as well as to CO<sub>2</sub> from a  
1090 suite of atmospheric models; the differences were then correlated with a variety of parameters  
1091 used in the CO<sub>2</sub> retrieval (O'Dell et al., 2012). Assuming the differences are due to instrument  
1092 retrieval problems, an XCO<sub>2</sub> bias correction is derived by regressing the differences on a subset of  
1093 these parameters. Since it is not always clear that the parameters used in the regression are  
1094 uncorrelated with the desired XCO<sub>2</sub> values in the real atmosphere, it is unclear how aggressive a  
1095 bias correction to make. Using more parameters in the bias fit increases the likelihood that actual  
1096 flux information (or signal) will be removed instead of measurement bias. For the results  
1097 presented in Section 3.4.2 the biases are constructed by regressing the difference between actual  
1098 raw GOSAT XCO<sub>2</sub> values (ACOS B2.10 retrievals) and the XCO<sub>2</sub> values from a forward run of  
1099 the PCTM atmospheric transport model on (1) aerosol optical depth derived from CALIPSO, (2)  
1100 the ratio of the signal in the weak CO<sub>2</sub> band to that in the O<sub>2</sub> band (referred to as S31, which is  
1101 related to the albedo in the two bands as well as the signal strength in each), and (3) the solar  
1102 zenith angle. The parameters used in this bias correction curve fit are different than those used in  
1103 the official ACOS XCO<sub>2</sub> bias correction (based on O'Dell et al., 2012), in order to provide global  
1104 values outside the current GOSAT ground track. The patterns produced with this correction are  
1105 similar to those in Deng et al. (2014), though the magnitudes in Figure 3-20 are about 25% larger,  
1106 which makes them a fair prediction of the biases expected from OCO-2 retrieved XCO<sub>2</sub>. The  
1107 biases varied by month; their annual average is shown in Figure 3-20.

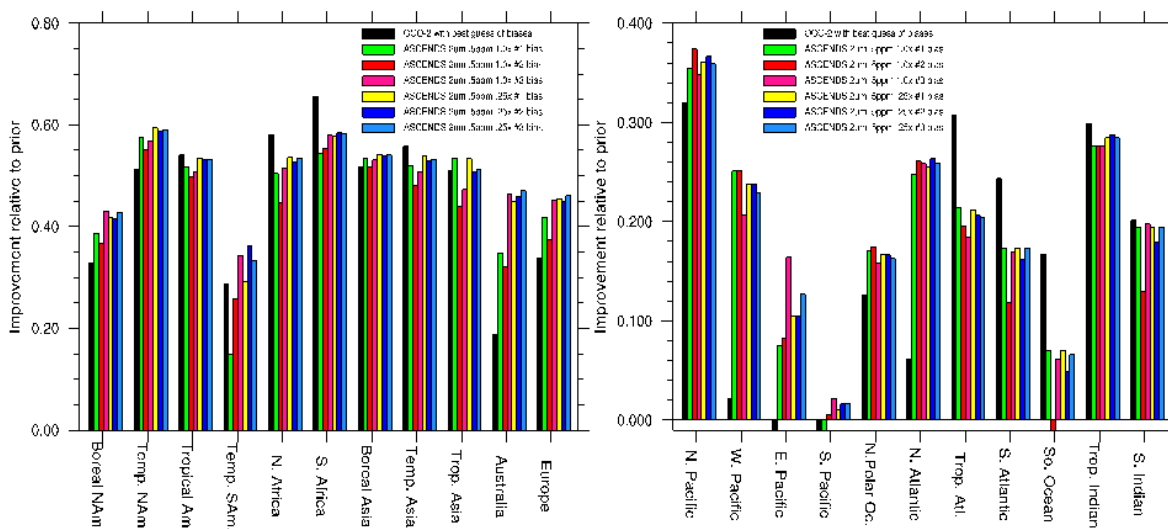
1108 Realistic bias patterns that might affect OCO-2 are obtained from estimates of such biases  
 1109 currently being calculated for GOSAT by the ACOS project (Box 3-3). These biases were then  
 1110 added on top of the OCO-2 random measurement errors assumed in Section 3.4.1. For  
 1111 ASCENDS, we added scaled multiples of the hypothetical bias distributions given by Table 3-3.



1112

1113  
1114  
1115

**Figure 3-20** The annual-mean measurement bias [ppm] derived from a comparison of raw ACOS B2.10 GOSAT XCO<sub>2</sub> values to modeled values, used to approximate OCO-2 bias.

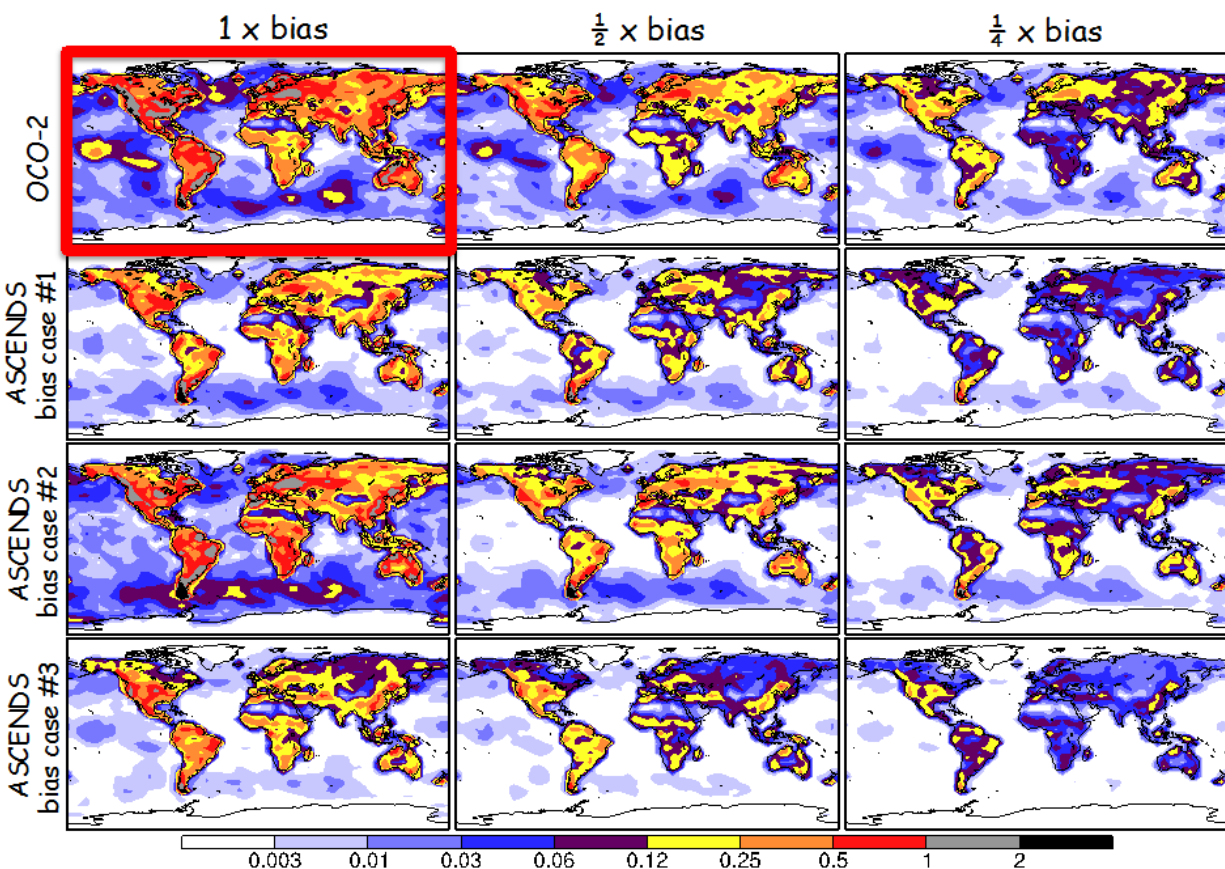


1116

1117 **Figure 3-21** Uncertainty reductions for weekly  $4.5 \times 6^9$  fluxes aggregated to TRANSCOM regions produced by  
 1118 assimilating CO<sub>2</sub> measurements from OCO-2 and ASCENDS, accounting for both random and systematic  
 1119 measurement errors of different forms and magnitudes. The biases from Figure 3-20 were applied to the OCO-2  
 1120 sampling, while the biases from Table 3-3 were applied to the ASCENDS cases at two levels of scaling (1 and 0.25).  
 1121 Random errors were as in Table 3-2 for OCO-2 and the ASCENDS 2.05  $\mu\text{m}$ , 0.5 ppmv nominal error case. Note  
 1122 different y-axis scales.

1123 Figure 3-21 shows the flux uncertainty reductions that result when biased measurements are used  
 1124 to infer fluxes. When the biases are added into the glint-mode OCO-2 OSSE, most of the  
 1125 improvement in the fluxes over the oceans seen in the random error OSSEs (c.f., Table 3-2)  
 1126 disappears: the relatively low-magnitude ocean fluxes are the first to be thrown off by the  
 1127 systematic errors. The improvements over land are also degraded to a lesser extent. When these  
 1128 degraded OCO-2 estimates are compared to the ASCENDS results, it is seen that ASCENDS can  
 1129 equal or exceed OCO-2's performance for almost all regions, if the tested systematic errors can be

1130 kept under about 1 ppmv. This is true especially over some ocean regions, even though OCO-2  
 1131 has lower random flux errors there when looking in sun glint mode. For many regions,  
 1132 ASCENDS does not even need to reduce its systematic errors below OCO-2's to achieve better  
 1133 results, e.g., Boreal NA. The benefit of not experiencing SZA-dependent biases is significant. The  
 1134 1.57  $\mu\text{m}$  case flux improvement is similar although less pronounced, especially over ocean (not  
 1135 shown).



1136  
 1137 **Figure 3-22** The shift in the weekly flux estimates caused by the addition of measurement biases of three different  
 1138 magnitudes (1x, 0.5x, & 0.25x) for OCO-2 and for the three different forms of ASCENDS bias given in Table 3-3.  
 1139 The RMS of 52 weekly flux shifts [ $10^{-8}$  kgCO<sub>2</sub>/m<sup>2</sup>/s] is shown for each case. The case in the red box is thought to be  
 1140 the most realistic guess of OCO-2 biases: ASCENDS can improve upon this by limiting biases to the  $\pm 0.5$  ppm level.

1141 The impact of the measurement biases can be seen more directly by comparing the magnitude of  
 1142 the shift in fluxes globally caused by the bias, as is done in Figure 3-22. Relatively speaking,  
 1143 ASCENDS would need to keep its systematic errors to about half of those shown in Table 3-3  
 1144 (i.e. to the  $\pm 0.50$  ppm level or better) to achieve a flux estimate with significantly lower error than  
 1145 that projected for OCO-2 (highlighted in Figure 3-22 with the red box). This is thought to be a  
 1146 realistic design goal for ASCENDS. Since biases in the CO<sub>2</sub> retrievals of passive missions such  
 1147 as GOSAT are currently thought to be the limiting factor in the usability of their data, not the  
 1148 random errors, reducing these biases is of primary interest for future CO<sub>2</sub> missions such as  
 1149 ASCENDS.

**Reducing systematic errors in ASCENDS CO<sub>2</sub> measurements compared to prior CO<sub>2</sub> missions will lead to significantly smaller errors in inferred fluxes.**

1150

1151 **3.5 Summary**

1152 A series of modeling tests is used to explore the impact of prospective ASCENDS observations in  
1153 inferring surface sources and sinks of CO<sub>2</sub>. A fairly realistic representation of expected random  
1154 and systematic measurement errors for ASCENDS has been constructed to test the impact of  
1155 instrument implementation alternatives on the models' ability to infer fluxes and, thus, to begin to  
1156 establish measurement performance requirements for the mission. A variety of modeling  
1157 approaches has been employed to bolster the findings from any individual model, given that flux  
1158 retrieval performance typically depends on model-specific methods and assumptions. The results  
1159 show: 1) ASCENDS will resolve statistically significant differences in total column CO<sub>2</sub>  
1160 concentrations, resulting from foreseeable changes in surface flux, over the entire globe including  
1161 high latitudes throughout the year; 2) it will advance our understanding of the carbon cycle  
1162 through improved flux estimates with reduced uncertainty at global to regional scales; and 3)  
1163 ASCENDS data have potential for reduced bias and improved representation that can contribute  
1164 significantly improved constraints on surface fluxes beyond passive sensors such as GOSAT and  
1165 OCO-2. In summary, the modeling tests consistently demonstrate that, under reasonable  
1166 assumptions for instrument technical performance, ASCENDS will provide accurate, precise, and  
1167 representative data to address key carbon cycle science problems and hypotheses, i.e., ASCENDS  
1168 can provide new science, better science, and continuity of global CO<sub>2</sub> observations from space.

1169 The mission formulation for ASCENDS is currently a work in progress and several modeling  
1170 exercises are planned to further explore its potential. For example, we expect to further study the  
1171 impact of including O<sub>2</sub> measurement errors in calculating CO<sub>2</sub> dry air mixing ratio versus using  
1172 surface pressure from weather analyses. We also plan to explore the impact on flux estimates of  
1173 using ASCENDS data retrieved above clouds or vertical multi-layer CO<sub>2</sub> retrievals. Simulations  
1174 using alternate orbital parameters, e.g., dawn/dusk or precessing, will be tested to see if additional  
1175 information on vegetation respiration and photosynthesis fluxes can be extracted. Finally, as the  
1176 performance of OCO-2 is now starting to come to light, we plan to further refine our random and  
1177 bias error comparisons using real OCO-2 data and to test the impact of combining active and  
1178 passive measurements in obtaining robust estimates of the carbon budget at a variety of  
1179 spatiotemporal scales.

## 1180 **4. Impact of Uncertainties in Atmospheric State on ASCENDS Measurements**

### 1181 **4.1 Introduction**

1182 This section addresses two critical elements that span mission requirements and general  
 1183 instrument design space. They are: 1) The assessment of uncertainties in ancillary knowledge of  
 1184 the atmospheric state and 2) The general impact of these uncertainties on measurement error.  
 1185 Special attention is given to the assessment of uncertainty in surface pressure estimates from  
 1186 meteorological reanalyzes to determine the necessity of an O<sub>2</sub> lidar measurement and, potentially,  
 1187 target requirements. ASCENDS provides Column XCO<sub>2</sub> amounts derived from active differential  
 1188 absorption measurements along CO<sub>2</sub> spectral features, in conjunction with collocated estimates of  
 1189 the atmospheric state provided by meteorological analyses. Understanding the propagation of  
 1190 errors in the atmospheric state into XCO<sub>2</sub> measurement errors is necessary to define a rigorous  
 1191 error budget and ensure a high quality measurement.

1192 Measurement error terms are not only driven by the instrument design, but also the ancillary  
 1193 meteorological data employed in the retrieval process, and the interplay between the two. The  
 1194 observed CO<sub>2</sub> differential optical depth,  $\Delta\tau$ , associated with a given CO<sub>2</sub> spectral feature, is given  
 1195 by

$$\Delta\tau = \int_0^{P_{sfc}} \Delta\sigma(\lambda_{on}, \lambda_{off}, T, p) \cdot \eta(T, WV, p) dp \quad (4-1)$$

1196 where  $\Delta\sigma$  is the CO<sub>2</sub> differential absorption cross section,  $\eta$  is the dry air CO<sub>2</sub> number density,  $p_{sfc}$   
 1197 is the surface pressure, and  $\lambda_{on}/\lambda_{off}$  represent the on/off-line wavelengths. XCO<sub>2</sub> is given by

$$XCO_2 = \frac{\Delta\tau}{\int_0^{P_{sfc}} \Delta\sigma(\lambda_{on}, \lambda_{off}, T, p) dp} \quad (4-2)$$

1198 Both  $\Delta\sigma$  and  $\eta$  vary as a function of pressure (P) and temperature (T). In addition, absorption due  
 1199 to other trace gas features (including water vapor), which are not considered in this simplified  
 1200 formulation, may also impact the observed  $\Delta\tau$ . As illustrated by these equations, the accuracy of  
 1201 retrieved XCO<sub>2</sub> values depends not only on the error characteristics of the observed  $\Delta\tau$ , but also  
 1202 the ability to accurately characterize the P, T, and water vapor (WV) concentration along the  
 1203 observed path. In the case of global space-based monitoring systems, retrievals typically rely on  
 1204 values derived from meteorological analyses that combine atmospheric general circulation models  
 1205 (GCMs) with assimilation of both conventional and satellite observations to estimate the  
 1206 atmospheric state globally.

1207 The work summary below provides a baseline assessment of these uncertainties in atmospheric  
 1208 state variables (vertical temperature and moisture, plus surface pressure), and their impact on a  
 1209 generic instrument implementation for a selected set of spectral lines/features. While it does not  
 1210 address the end-to-end performance of a fixed-point baseline ASCENDS solution, it does provide  
 1211 a common parametric baseline that will evolve over time as the design matures. The assessment  
 1212 will aid in instrument and mission definition, design and potential future source selection  
 1213 activities, as well as provide a systematic mechanism for comparing proposed solutions and a  
 1214 foundation for assessing end-to-end mission performance throughout the ASCENDS mission life-

1215 cycle. In addition, these analyses will help guide the mission requirements for potential additional  
1216 space-based measurements, e.g. the necessity for an O<sub>2</sub> based surface pressure measurement, and  
1217 provide a single common set of vetted sources of ancillary data that may be incorporated into the  
1218 procurement phase to aid in source selection. Section 4.2 provides a summary of the uncertainty  
1219 analysis of expected atmospheric state and Section 4.3 summarizes a baseline analysis of potential  
1220 impact due to these uncertainties on retrieved XCO<sub>2</sub> column amounts.

## 1221 **4.2 Uncertainties in Observed Atmospheric State**

1222 Current pre-phase A investigations focus on gathering current state-of-the-art model analysis and  
1223 forecast fields as a proxy for future ancillary mission data to develop a comprehensive set of  
1224 statistically-based estimates that bound the expected uncertainties in surface pressure and vertical  
1225 temperature and moisture profiles. A variety of methods are employed to develop these bounds,  
1226 including:

- 1227 1. Comparison of in situ observations and meteorological analysis data to assess model errors.
- 1228 2. Comparison of reanalysis products with independent (not assimilated) datasets, where  
1229 available.
- 1230 3. Inter-comparison of multiple reanalysis products to inform error estimates in poorly observed  
1231 regions

1232 Comparing analysis fields to prior short-term forecasts for the same period constrains the error  
1233 introduced into an operational retrieval relying on forecast fields and the temporal interpolation  
1234 error that may occur when meteorological information from a different time is assumed during the  
1235 retrieval process. Differences that arise in comparisons of fields from different modeling systems  
1236 are due in part to errors in the Numerical Weather Prediction (NWP) model physics, spatial  
1237 scales, and other implementation differences; such analysis is also valuable in estimating model  
1238 error in data poor regions. Comparisons of NWP fields to observations is challenging because the  
1239 majority of high quality, operationally available in situ data are assimilated to produce  
1240 meteorological analyses. Truly independent observations are limited in number and distribution,  
1241 and indeed often are near operational sites. Standard in situ observations also have limited  
1242 precision due to instrument limitations or through data collection procedures (Sun et al., 2010)  
1243 (U.S. DOC/NOAA Office of the Federal Coordinator for Meteorology (OFCM), Washington,  
1244 D.C., 2005; NOAA, Washington, D.C., 2003; Developmental Testbed Center (DTC), n.d.)  
1245 (Salstein et al., 2008). Despite these limitations, the collective statistics provide a semi-unbiased  
1246 assessment of expected uncertainties in atmospheric state knowledge, and a consistent set of  
1247 benchmarks that can be used to assess potential mission design solutions.

### 1248 **4.2.1 Uncertainties in Surface Pressure**

1249 ASCENDS requires both a precise knowledge of the surface pressure on a fine scale grid and a  
1250 comprehensive understanding of the associated errors. While state-of-the-art mesoscale NWP  
1251 models currently have horizontal grid spacings of at least several kilometers, with global-scale  
1252 models an order of magnitude larger, surface pressure must be characterized on a spatial scale  
1253 comparable to the measurement of interest. Space-based estimates of surface pressure normally  
1254 require a separate sensor, thereby increasing the overall size, weight, power and complexity of the  
1255 satellite payload. The use of meteorological analyses presents an alternative approach for  
1256 estimating surface pressure, but implementation depends on the quality of the analyses and the  
1257 ability to adjust relatively coarse resolution grid-based information to precise measurement

1258 locations. A comprehensive understanding of the errors associated with each of these approaches  
 1259 is a critical part of the design characterization of a remote-sensing system whose measurement  
 1260 accuracy depends on knowledge of surface pressure. Current capabilities of O<sub>2</sub> measurement  
 1261 techniques are addressed in Sections 5.2 and 5.3.3.5 while errors in surface pressure derived from  
 1262 meteorological analyses are addressed here.

#### 1263 4.2.1.1 Comparison of Surface Pressure Model Values and Observations

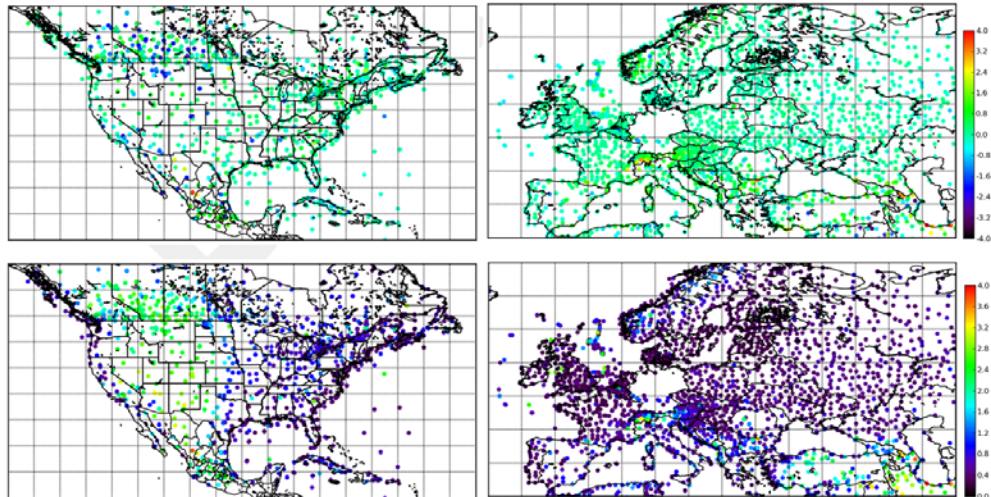
1264 In this study we compared global in situ measurements with estimates of surface pressure derived  
 1265 from the Global Forecast System (GFS) and the North American Mesoscale Model (NAM) NWP  
 1266 analyses and short-term forecast data. Surface observations were obtained from National Climatic  
 1267 Data Center (NCDC's) Integrated Surface Database (ISD) (NCDC, n.d.). In order to compare  
 1268 measured surface pressure to model fields, a correction must be applied to the surface pressure of  
 1269 the model to account for the altitude difference between the model surface height and the actual  
 1270 terrain height of the station. In this work, the standard lapse rate equation

$$P_{adj} = P_s \cdot \exp\left(\frac{-g \cdot dz}{R(T_m + L_r \cdot dZ/2)}\right) \quad (4-3)$$

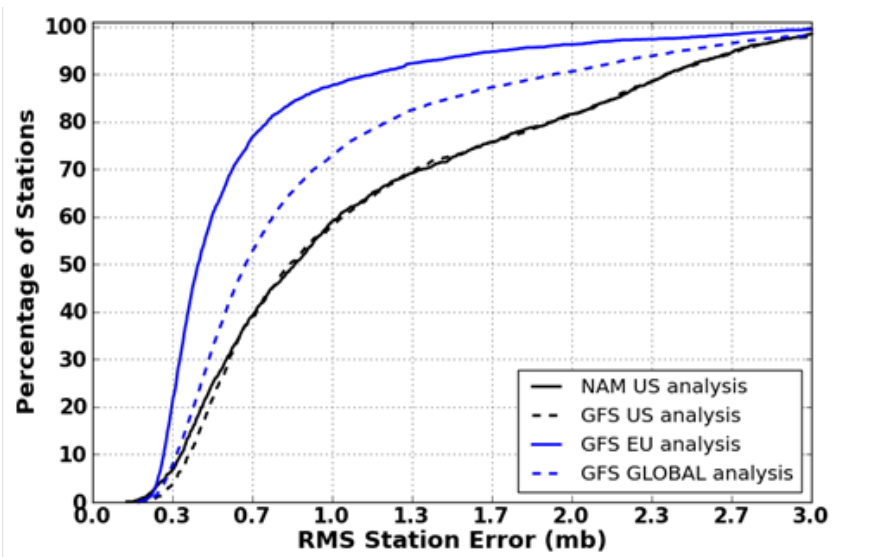
1271 where  $P_s$  is the model surface pressure,  $dZ$  is the difference between the model terrain height of  
 1272 the two resolutions,  $R$  is the dry gas constant,  $T_m$  is the model two-meter air temperature, and  $L_r$  is  
 1273 the lapse rate of 0.0065 K/m, was employed to account for these height differences. This  
 1274 adjustment was also applied, where required based on database values, to convert surface  
 1275 observations of sea-level pressure to station pressure. ISD surface pressure observations were  
 1276 converted from sea-level pressure to station pressure and co-located with model estimates that had  
 1277 been corrected for model height error. The results shown in this work are based on data retained  
 1278 every fifth day from the thirteen-month period between January 2012 and August 2013  
 1279 (inclusive). Observations in the matched pair database are comprised of observations valid at  
 1280 0000 and 1200 Coordinated Universal Time (UTC). Model data are either analyses valid at 0000  
 1281 and 1200 UTC or 6-h forecasts from the prior 1800 and 0600 UTC model cycles. The choice of a  
 1282 6-hour forecast was selected to match the time interval between typical synoptic model runs. In a  
 1283 real-time environment, surface pressure estimates would be computed from both spatially and  
 1284 temporally interpolated NWP data to match the satellite measurement. This approach requires not  
 1285 only the most recent NWP analysis, but also a forecast or set of forecasts that span the  
 1286 observation times. In non-real-time environments, where data are not required to be processed as  
 1287 they are received, one could consider temporally interpolating between analyses or data from  
 1288 alternative applications that provide non-forecast fields on a more frequent basis.

1289 Figure 4-1 illustrates the overall small bias and Root Mean Square Error (RMSE) values at most  
 1290 observing sites. Errors are typically larger in regions with complex topography or at high  
 1291 elevations as evident over the Alps. Model values in these regions are heavily influenced by the  
 1292 veracity of the underlying model initial conditions whose effects are most strongly felt at such  
 1293 short forecast lengths. It is also in these regions that the failures in the corrections using the  
 1294 standard atmospheric lapse rate are most apparent. Figure 4-2 illustrates that even at a 90%  
 1295 confidence level, the majority of stations sampled have  $1\sigma$  values below 2 mb. The cumulative  
 1296 distribution functions (CDFs) in this figure illustrate the distribution of RMSE values for selected  
 1297 sets of surface station observations. The minimum annual RMSE for all station approaches  
 1298 0.25mb and the maximum exceeds 3mb for a handful of outlier stations as illustrated in Figure 4-

1299 1. Errors for the 6-h forecasts are slightly larger (not shown). Table 4-1 shows biases binned by  
 1300 latitude band for the GFS global analysis typically are small and negative, while RMSE values for  
 1301 (approximately) 1, 2 and 3 standard deviations for a normally-distributed sample are to first order  
 1302 1, 2 and 3 mb.



1303  
 1304 **Figure 4-1** Estimated surface pressure biases and RMS errors for the U.S. and Europe. Estimated surface pressure  
 1305 biases (top row) and root-mean-square errors (bottom row) for the U.S. (left column) and Europe (right column).  
 1306 Units are in mb. Model data are the NAM regional model and GFS global model for the U.S. and Europe,  
 1307 respectively.



1308  
 1309 **Figure 4-2** RMS differences in surface pressure observations vs fraction of stations with annual RMSE less than  
 1310 defined error.

1311 Cumulative distribution functions for the number of stations whose RMSE surface pressure  
 1312 errors, the RMS difference between NAM/GFS analysis values and surface observations for the  
 1313 U.S. (US), Europe (EU), and global regions. The percent of observation denotes the fraction of  
 1314 stations who yearly average RMSE is less than or equal to the defined error in mb.

1315

1316  
1317**Table 4-1 Regional differences mean bias and RMSE, and inter-modal range RMSE thresholds (in mb) for GFS analysis.**

Region	Mean Bias	Mean RMSE	65%	90%	95%	99%
NH High Latitudes	-0.14	0.74	0.67	1.19	1.67	2.57
NH Mid Latitudes	-0.01	0.88	0.70	2.02	2.47	3.24
Tropics	-0.13	1.02	0.91	1.86	2.52	3.78
SH Mid Latitudes	0.02	0.86	0.80	1.35	1.84	2.83
SH High Latitudes	-0.41	1.25	1.27	1.93	2.12	2.65
All Latitudes	-0.06	0.90	0.75	1.86	2.40	3.31

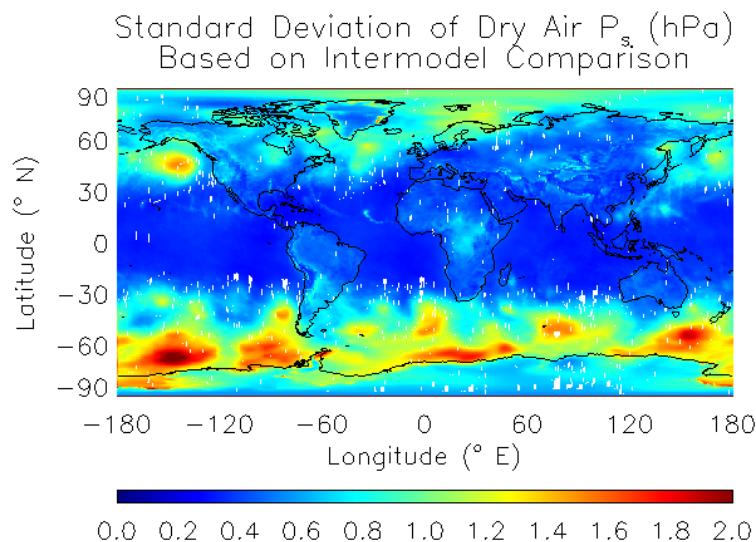
1318

**4.2.1.2 Inter-model Comparison of Surface Pressure Differences**

1320 While comparisons with available observations provide the best assessment of errors in  
1321 meteorological analyses, large areas of the globe remain unobserved including high latitude  
1322 regions of both hemispheres, southern hemisphere oceans, South America, Africa, and Siberia. In  
1323 these regions, comparisons of different meteorological analyses provide the only possible  
1324 estimate of uncertainty. To characterize uncertainty in these regions, we compared surface  
1325 pressure fields from the Modern Era Retrospective-analysis for Research and Applications  
1326 (MERRA) (Rienecker et al., 2011), the European Centre for Medium-Range Weather Forecasts'  
1327 (ECMWF) ERA-Interim reanalysis (Dee et al., 2011), and NOAA's Climate Forecast System  
1328 Reanalysis (CFSR) (Saha et al., 2010). The range of reanalysis surface pressure estimates was  
1329 computed every 6 hours during January, April, July, and October 2009. All reanalysis fields were  
1330 re-gridded to MERRA's nominal half-degree resolution. The lapse rate altitude correction  
1331 discussed above is applied to reduce effects of underlying topography differences. While this  
1332 correction reduces intermodal differences due to topography, it does not entirely remove them.  
1333 Annual mean surface pressure differences are subtracted as a type of bias correction because we  
1334 assume that persistent errors in surface pressure from analyses will be successfully diagnosed and  
1335 adjusted for as part of the ASCENDS retrieval process. Monthly means and standard deviations of  
1336 the instantaneous range were computed. Standard deviations of the surface pressure range are  
1337 shown in Figure 4-3.

1338 In most regions, intermodal differences are less than 1 hPa, consistent with the analysis based on  
1339 surface pressure observations. Largest differences among analyses exist in data poor regions  
1340 where Atmospheric General Circulation Model (AGCM) model physics dominate pressure  
1341 estimates rather than data constraints, which are fairly consistent among models. In particular,  
1342 large errors are evident in the southern ocean translating to 0.5-0.8 ppm in XCO<sub>2</sub>. Not only is this  
1343 area virtually unobserved by conventional observations (radiosonde, aircraft, and automated land  
1344 and ocean stations), but assimilation of satellite observations of other meteorological state

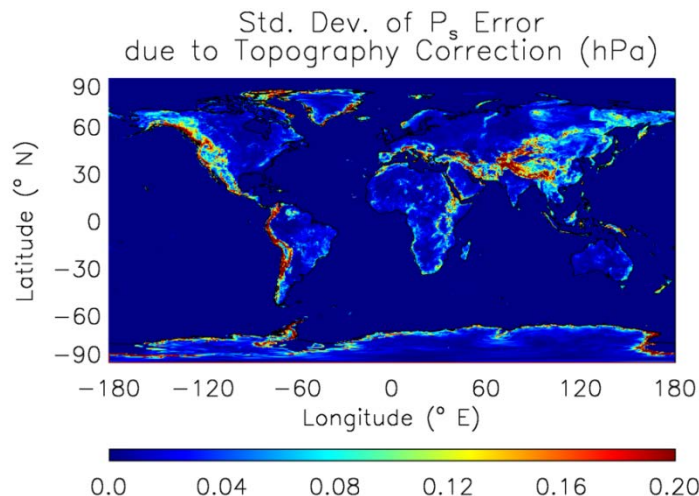
1345 variables, which provide some constraint on surface pressure, is obstructed by persistent  
1346 cloudiness.



1347  
1348 **Figure 4-3** Model comparison between reanalysis surface pressure estimates for dry air. Comparison provides  
1349 insight into model error in data poor regions. Instantaneous ranges were computed between three reanalysis datasets  
1350 for 2009 to determine the standard deviation.

#### 1351 4.2.1.3 Spatial Interpolation Errors in Surface Pressure

1352 In addition to errors in the surface pressure provided by meteorological re-analyses, further error  
1353 can be introduced when surface pressure is adjusted to the measurement location as part of an  
1354 XCO<sub>2</sub> calculation. To estimate the magnitude of such errors, we use a combination of MERRA  
1355 surface pressure estimates and the United States Geological Survey (USGS) GTOPO30 digital  
1356 elevation model map that provides estimates of surface elevation at 1km resolution. We use the  
1357 lapse rate based correction discussed above to adjust from MERRA's ~50 km grid-based surface  
1358 pressure estimates to calculate the 'true' surface pressure at all GTOPO30 elevations. To estimate  
1359 potential errors, we perform the same calculation assuming a 1 K temperature error and then  
1360 calculate the difference in surface pressure from the 'truth'. Figure 4-4 shows the standard  
1361 deviation of surface pressure errors within each 50 km grid cell. Over most of the world, the  
1362 topographic correction assuming a realistic error in temperature introduces a small error less than  
1363 0.1 hPa. Over regions with large topography gradients, errors are still ~0.2 hPa. Even in areas  
1364 with significant topographic variation, adjustment errors are much smaller by an order of  
1365 magnitude than the errors shown in section 4.2.1.1 and 4.2.1.2. This analysis assumes that  
1366 ASCENDS will have perfect information about the elevation associated with a particular  
1367 measurement based on the altimeter. Errors in altimetry, pointing location, or low level  
1368 temperature errors greater than 1 K could all lead to errors larger than those shown in Figure 4-4,  
1369 but are still likely to be smaller inherent uncertainty in surface pressure reanalysis.

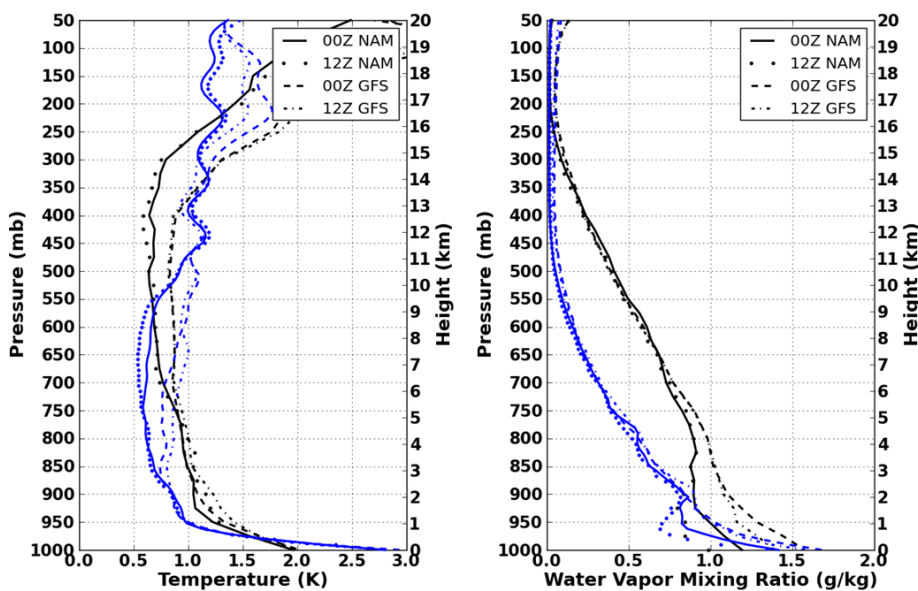


1370

1371 **Figure 4-4** Effects of grid scale on surface pressure errors. Errors induced when relatively coarse resolution  
1372 reanalysis surface pressure fields are adjusted to represent subgrid-scale topographic variations.

1373 **4.2.2 Uncertainties in Temperature and Water Vapor Profiles**

1374 The error characteristics of above ground-level model profiles of temperature and moisture were  
1375 examined by comparing against radiosondes (Figure 4-5). The largest temperature errors appear  
1376 in the lowest 50 mb of the troposphere and again at high altitudes near the tropopause and in the  
1377 stratosphere. Moisture errors are largest near the surface in the boundary layer where water vapor  
1378 content is most abundant.



1379

1380 **Figure 4-5** Ensemble RMS differences for radiosonde soundings in upper air observations for 5000 randomly  
1381 selected soundings and corresponding 0000 and 1200 UTC NAM and GFS NWP analyses for temperature (left) and  
1382 water vapor mixing ratio (right). The black traces are plotted as a function of pressure and blue traces are plotted as a  
1383 function of height above surface.

1384 **4.3 Impact of Uncertainty in Knowledge of Atmospheric State on Retrieved XCO<sub>2</sub>**

1385 The atmospheric state vector analysis described above was combined with a notional vertical CO<sub>2</sub>  
1386 profile with a constant concentration of 385 ppm, and input into the Line-By-Line Radiative

1387 Transfer Model (LBLRTM) (Clough et al., 2005) to construct sets of simulated optical depths  
 1388 (ODs) over a predefined range of wave numbers. LBLRTM optical depths are computed from  
 1389 Voigt line shape functions at atmospheric levels and with a continuum model that includes self-  
 1390 and foreign-broadened water vapor as well as continua for carbon dioxide, oxygen, nitrogen,  
 1391 ozone and extinction due to Rayleigh scattering. The version used in the study included 2012  
 1392 updates to the CO<sub>2</sub> line parameters and coupling coefficients based on the work of Devi et al.  
 1393 (2007a,b), the O<sub>2</sub> line parameters based on HITRAN (Rothman et al., 2009) and additional  
 1394 quadrupole parameters between 7571 - 8171 cm<sup>-1</sup>.

1395 For each of 5000 profile pairs discussed in section 4.2.2 a set of simulated truth, signal and model  
 1396 ODs were computed. The Radiosonde Observation (RAOB) data were used to simulate the “true”  
 1397 optical depths observed by the sensor and the model profiles were used construct the “model”  
 1398 optical depths that would be used in the retrieval approach given an estimate of the atmospheric  
 1399 state. In addition, a set of “signal”  $\tau$ s were constructed based on the “truth” profiles and either an  
 1400 augmented CO<sub>2</sub> profile or a change in surface pressure. In the CO<sub>2</sub> case, the nominal CO<sub>2</sub> profile  
 1401 was augmented by adding a pre-defined concentration to each layer between the surface and  
 1402 simulated observation height. In the O<sub>2</sub> case, the surface pressure was adjusted by modifying the  
 1403 surface height to match the desired surface pressure. In this case, the signal pressure values were  
 1404 assumed to be less than the observed or model values to prevent the use of sub-surface profile  
 1405 values. In the O<sub>2</sub> cases, the observed path length, i.e. the height between the observer and the  
 1406 surface, were held fixed to eliminate changes in optical depths due to path length.

1407 These simulated optical depth values (truth, model, and signal) were then employed to generate  
 1408 spectrally dependent noise and average signal values given a defined set of differential  
 1409 wavelength pairs. This work assumes that retrieved CO<sub>2</sub> column or surface pressure values are  
 1410 derived from the difference in optical depths between the absorption at an “off-line” wavelength  
 1411 whose absorption is dominated by the continuum or constituents other than the feature of interest,  
 1412 and the absorption at an “on-line” wavelength whose absorption is primarily driven by the feature  
 1413 of interest. While this approach does not address all retrieval methods or observational  
 1414 techniques that employ multiple measurements along a given absorption feature, it does provide  
 1415 metric values that can in general be used to constrain the fit between the observed data and  
 1416 Radiative Transfer (RT) modeled values.

1417 The noise at each spectral location in the given simulated waveband was computed as the RMS  
 1418 error associated with the differences between the simulated true  $\tau$ s and the noise  $\tau$ s. In general,  
 1419 these differences in optical depths, for a given off-line wavelength ( $\lambda_{off}$ ), are described as

1420

$$\Delta\tau(\lambda) = (\tau_b(\lambda_{off}) - \tau_b(\lambda)) - (\tau_x(\lambda_{off}) - \tau_x(\lambda)) \quad (4-4)$$

1421

1422 where  $\tau_b(\lambda)$  is the observed or true optical depths derived from RAOB data, and  $\tau_x(\lambda)$  are the  
 1423 optical depths associated with atmospheric state of interest. In the noise case,  $\Delta\tau_{noise}(\lambda)$ , is  
 1424 computed based on  $\tau_x(\lambda)$ s derived from NWP model data, and estimated noise values as a  
 1425 function of wavelength are given as the RMS error

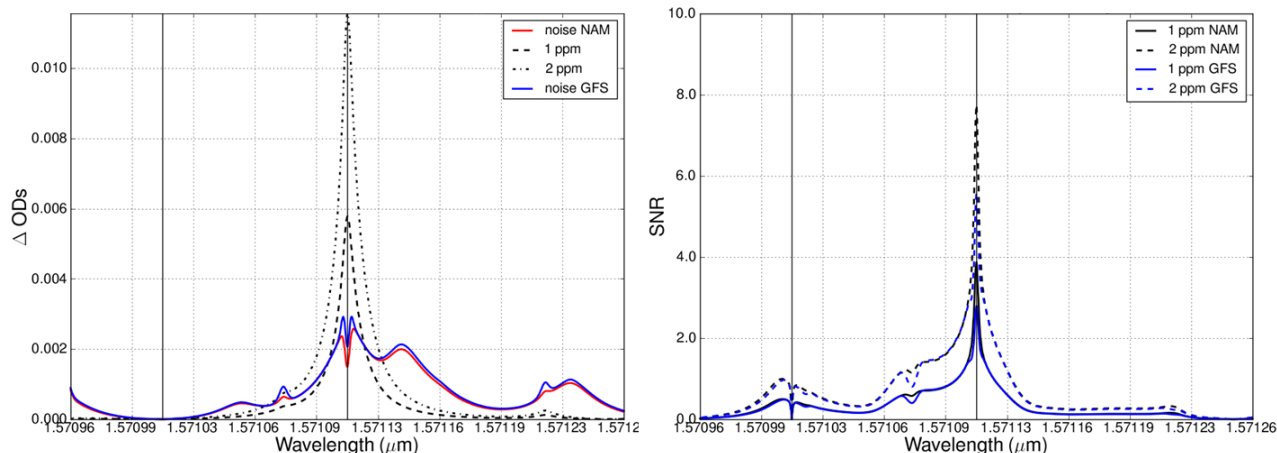
1426

$$noise(\lambda) = \sqrt{\frac{1}{N} \sum_N (\Delta\tau_{noise}(\lambda))^2} \tag{4-5}$$

1427  
1428 where N is the number of profiles in the match pair dataset. In the signal case, the  $\tau_x(\lambda)$ s values  
1429 were those derived from atmospheric state variables derived from the RAOB data plus an  
1430 augmented CO<sub>2</sub> column or surface pressure value. The resulting signal term is then given as the  
1431 absolute average over the ensemble set

$$signal(\lambda) = \frac{1}{N} \left| \sum_N \Delta\tau_{signal}(\lambda) \right| \tag{4-6}$$

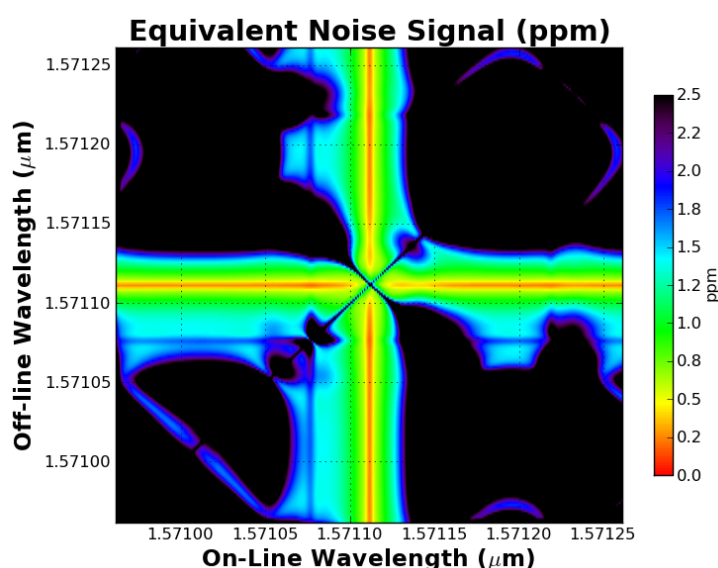
1433  
1434 In this study, the differential signal and noise spectra are computed for four CO<sub>2</sub> and two O<sub>2</sub>  
1435 bands of interest. Each band is 300 pm wide and has center wavelengths at approximately  
1436 1.5711, 1.5723, 1.5805, and 2.0510 μm (6364.92203, 6359.96733, 6327.06095, and 4875.59  
1437 cm<sup>-1</sup>) for the CO<sub>2</sub> bands. The O<sub>2</sub> bands are centered at approximately 0.76468 and 1.2625 μm  
1438 (13077.29386 and 7920.5976 cm<sup>-1</sup>). In addition, a single observational scenario is constructed to  
1439 evaluate the performance of observations from a space-based mission based on a nadir viewing  
1440 geometry. The space-based scenario is based on a 20 km fixed path length. While it is well  
1441 understood that the space-based scenario covers only a fraction of path associated with any  
1442 proposed viewing geometry, the length selected bounds the limits of the observed and NWP data,  
1443 and represents the fraction of the atmosphere that has the most severe impact on these  
1444 measurement techniques.



1445  
1446 **Figure 4-6** Representative signal/noise for 20 km nadir sensor to ground path length. Plots show values (left) and  
1447 ratios (right).

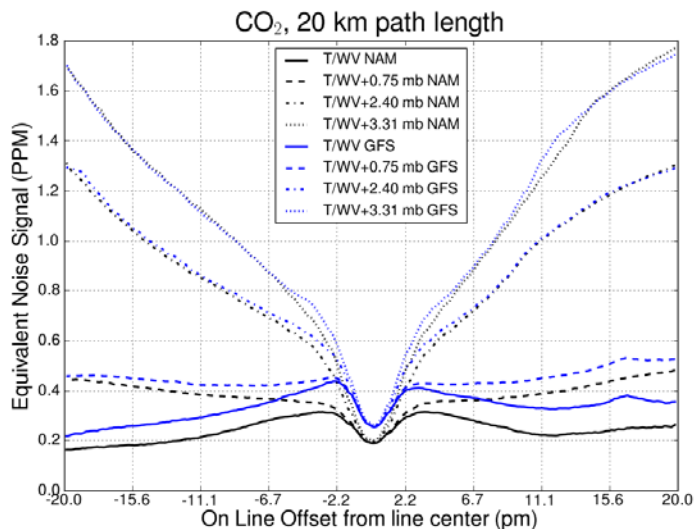
1448 An example set of computed signal and noise values and the associated signal to noise ratios  
1449 (SNRs) as a function of wavelength for select off-line locations are provided in Figure 4-6 for a  
1450 representative CO<sub>2</sub> case. These signal and noise terms form the basis for a number of analyses  
1451 designed to assess and quantify the impact of uncertainties in atmospheric state knowledge on

1452 estimated CO<sub>2</sub> column amounts. The left plot illustrates signal and noise values for a  
 1453 representative CO<sub>2</sub> line for absorption feature centered at 1.5711 μm. The solid lines represent the  
 1454 simulated noise values as a function of wavelength derived from both the Contiguous United  
 1455 States (CONUS) NAM data (red) and the global GFS data (blue). In this CO<sub>2</sub> case, an additional  
 1456 2.40 mb uncertainty in surface pressure was also introduced. The dashed and dotted lines in the  
 1457 left hand plot represent the average signal given by a 1 and 2 ppm change in column amount. The  
 1458 on-line (1.5711 μm) and selected off-line (-100 pm) positions are illustrated in the graphs as solid  
 1459 vertical lines. The right plot shows representative SNRs constructed for a 1 and 2 ppm signal  
 1460 derived from CONUS NAM data (black) and global GFS data (blue). An example two-  
 1461 dimensional representation of associated noise equivalent signal for the CO<sub>2</sub> line at 1.5711 μm  
 1462 and 20 km nadir viewing geometry is shown in Figure 4-7. The noise equivalent signals are  
 1463 constructed by interpolating noise ΔOD to signal values for all on/off-line combinations ±150 pm  
 1464 from line center.



1465  
 1466 **Figure 4-7** Two-dimensional representation of noise equivalent signal for CO<sub>2</sub> line at 1.5711 μm and 20 km  
 1467 nadir viewing geometry.

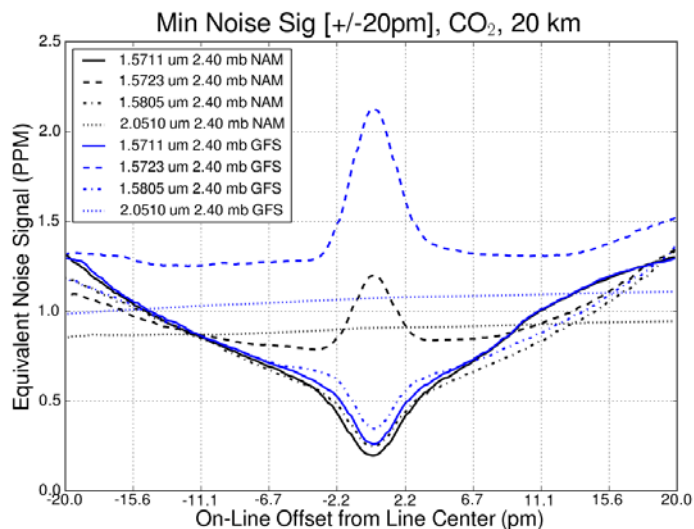
1468 Figure 4-8 illustrates the minimum equivalent noise for on-line positions ±20 pm from line center  
 1469 for the same sample CO<sub>2</sub> line and geometry. Shown is the minimum equivalent noise associated  
 1470 with uncertainties in vertical temperature and water vapor (T/WV) only, and T/WV uncertainties  
 1471 combined with 0.75, 2.40, and 4.31 mb uncertainties in surface pressure derived from both  
 1472 CONUS NAM data (black) and global GFS (blue). Finally, Figure 4-9 shows minimum  
 1473 equivalent noise signals for CO<sub>2</sub> lines centered at 1.5711, 1.5723, 1.5805 and 2.0510 μm given  
 1474 uncertainties in vertical T/WV, a 2.40 mb uncertainty in surface pressure, and a 20 km nadir  
 1475 viewing geometry derived from CONUS NAM NWP data (black) and the global GFS data (blue).  
 1476 The 2.0510 μm center line is chosen in the wing of the 2 μm absorption feature due to the high  
 1477 absorption of CO<sub>2</sub> in this band, which results in low SNR and smooth equivalent noise signal  
 1478 across the ±20 pm region plotted.



1479  
1480

1481 **Figure 4-8** Equivalent noise signal errors for sample CO<sub>2</sub> line at 1.5711 μm. Minimum equivalent noise for on-line  
1482 positions ±20 pm from line center for CO<sub>2</sub> line at 1.5711 μm and 20 km nadir viewing geometry.

1483



1484  
1485

1486 **Figure 4-9** Sample set of minimum equivalent noise errors for CO<sub>2</sub> lines between 1.57 and 2.05 CO<sub>2</sub> lines centered  
1487 at 1.5711, 1.5723, 1.5805 and 2.0510 μm and a 20 km nadir viewing geometry.

**ASCENDS XCO<sub>2</sub> measurements require both state of the art instrument design and precise knowledge of the atmospheric state (temperature, moisture and surface pressure) to ensure desired precision and accuracy.**

1488

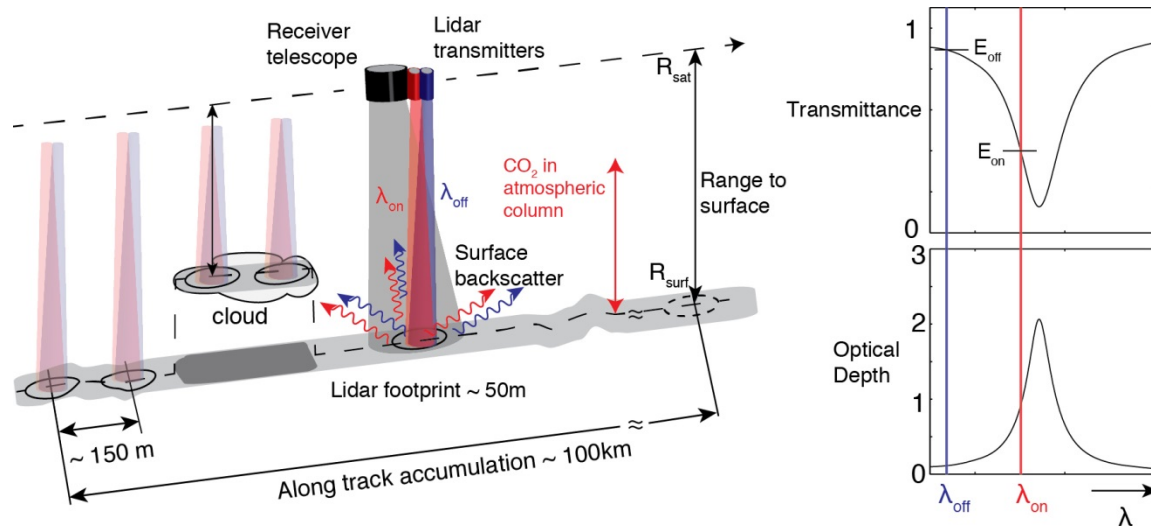
**1489 4.4 Summary**

1490 A baseline assessment of uncertainties in atmospheric state variables (vertical temperature,  
1491 vertical moisture, and surface pressure) and their impact on a generic instrument implementation  
1492 for a selected set of spectral lines/features is provided. This assessment provides a common  
1493 parametric baseline that will evolve over time as the ASCENDS design matures, and will aid in  
1494 instrument and mission definition, design and potential future source selection activities. In  
1495 addition, these analyses will help guide the mission requirements for potential additional space-  
1496 based measurements, e.g. the necessity for an O<sub>2</sub> based surface pressure measurement, and  
1497 provide a single common set of vetted sources of ancillary data that may be incorporated into the  
1498 procurement phase to aid in source selection.

1499 **5. Technical Feasibility**1500 **5.1 Introduction – Lidar Measurements for the ASCENDS Mission**

1501 The ASCENDS lidar uses the Integrated Path Differential Absorption (IPDA) lidar approach to  
 1502 measure the column abundance and mixing ratio of atmospheric CO<sub>2</sub>. Various IPDA lidar  
 1503 approaches may be used to sample the CO<sub>2</sub> line, measure range, and estimate CO<sub>2</sub> mixing ratio.  
 1504 The simplest approach to describe is shown in Figure 5-1 and uses a pulsed approach with the  
 1505 minimum of two wavelengths to sample the absorption line.

1506



1507

1508 **Figure 5-1** Illustration of one approach for an Integrated Path Differential Absorption (IPDA) measurement from  
 1509 space to scattering surfaces on or near the Earth's surface.

1510 While there are several somewhat different candidate measurement approaches for ASCENDS,  
 1511 this drawing is for the two-wavelength pulsed approach considered for the ESA A-SCOPE  
 1512 Mission. Several candidate approaches for ASCENDS use more than two  $\lambda_{on}$  wavelengths to gain  
 1513 some additional information on the vertical distribution of CO<sub>2</sub> and to control biases.

1514 **5.1.1 Overview of Measurement Approach**

1515 The pulsed two-wavelength lidar approach transmits two laser pulses of slightly different  
 1516 wavelengths in quick succession for every IPDA lidar measurement. Figure 5-1 shows two beams  
 1517 (red and blue) directed at nadir corresponding to the laser pulses tuned onto and off the CO<sub>2</sub>  
 1518 absorption line. They pass through the atmospheric column containing an unknown concentration  
 1519 of CO<sub>2</sub> and illuminate nearly the same area on the scattering surface, either the Earth's surface or  
 1520 cloud top. The light reflected by the surface passes back through the atmosphere, and a small  
 1521 fraction of the light is collected by the receiver telescope. The lidar receiver measures the energies  
 1522 of the on- and off-line pulses ( $E_{on}$  and  $E_{off}$ ) and the range to the scattering surface.

1523 Figure 5-1 right insert shows a sketch of the shape of the CO<sub>2</sub> line's transmission (top) and optical  
 1524 depth (bottom) when measured from space. The maximum CO<sub>2</sub> absorption occurs for laser  
 1525 wavelengths tuned to the line's center. The wavelength of the laser's "on-line" pulse is usually  
 1526 selected to be offset from the peak of the CO<sub>2</sub> absorption line and is indicated by the red vertical  
 1527 line. The wavelength of the laser's "off-line" pulse, that undergoes negligible CO<sub>2</sub> absorption, is

1528 indicated by the blue line. The wavelengths  $\lambda_{on}$  and  $\lambda_{off}$  are sufficiently close that the scattering  
1529 and absorption by atmospheric aerosols, clouds, and the illuminated scattering surface are the  
1530 same for both.

1531 The CO<sub>2</sub> column abundance is calculated from the lidar’s measurement of range to the surface and  
1532 ratio of the energies in the on- and off-line return pulse signals. In the IPDA lidar designs  
1533 considered for ASCENDS, averaging of multiple lidar measurements is planned, so the column  
1534 abundance specification is for the average of measurements made (typically for 50-100 km) along  
1535 the orbit’s ground track. The column average mixing ratio XCO<sub>2</sub> is calculated using additional  
1536 information about the density of dry air in the same measurement column. In the baseline  
1537 approach for ASCENDS, a simultaneous O<sub>2</sub> lidar measurement is included as part of the  
1538 instrument. A sufficiently accurate atmospheric model evaluated at the location and time of the  
1539 CO<sub>2</sub> lidar measurement, may be used as an alternative.

1540 The IPDA lidar approach offers a number of unique and important capabilities for column  
1541 measurements of greenhouse gases. A summary is given in Table 5-1.

1542 **Table 5-1 Unique capabilities of the ASCENDS Lidar**

<b>Unique capabilities of the ASCENDS Lidar</b>
The light source (the laser) is in the instrument measuring consistently in a nadir path. This enables day and night measurements at all latitudes in all seasons.
The measurements to the surface are range resolved. This allows accurate, bias-free column CO <sub>2</sub> measurements to the scattering surface through thin clouds and aerosol layers.
The lidar directly measures range, thus the estimates of the scattering surface elevation needed to infer CO <sub>2</sub> column mixing ratio are accurate and not impacted by height errors in DEM’s, variable heights of trees and other above-surface scatterers, and/or reflectance variability within the footprint.
The laser footprint and spatial scale of sampling (~ 100 m) are small. This enables more frequent measurements to the surface in small gaps between optically thick clouds.
Many sources of potential bias are eliminated since the lidar interacts with the atmosphere and surface consistently in a nadir path. Other than causing signal attenuation, atmospheric aerosol scattering does not impact the lidar CO <sub>2</sub> measurement.
The laser’s spectral width is a small fraction of the atmospheric CO <sub>2</sub> absorption linewidth, and it is tunable. Sampling the pressure-broadened CO <sub>2</sub> absorption line at an appropriate offset from its absorption line center enables preferential weighting to the CO <sub>2</sub> molecules in the lower troposphere, where the CO <sub>2</sub> source and sink “signals” are the strongest.
The absorption line can be sampled at a several different offsets from line center wavelength, potentially enabling determination of column concentrations with separate weightings toward both the lower and upper troposphere.
The lidar samples only one selected atmospheric line instead of an entire band. This minimizes errors from interfering gas species. It also greatly reduces the quantity of accurate spectroscopic information needed, and so reduces the potential for spectroscopy-dependent errors.

1543

1544 **5.1.2 General Measurement Principle**

1545 For the two-wavelength approach, the column averaged CO<sub>2</sub> mixing ratio measured from space to  
 1546 the scattering surface can be calculated from (Menzies and Tratt, 2003; Ehret et al., 2008; Browell  
 1547 et al., 2012)

$$X_{CO_2}(R_{surf}) \equiv \frac{N_{CO_2}(R_{surf})}{N_{air}(R_{surf})} = \frac{\int_{R_{surf}}^{R_{sat}} n_{CO_2}(r) [\sigma_{on}(r) - \sigma_{off}(r)] dr}{\int_{R_{surf}}^{R_{sat}} n_{air}(r) dr} \propto \frac{\ln(E_{off}/E_{on})}{2N_{air}(R_{surf})} \quad (5-1)$$

1548 Here  $R_{surf}$  is the elevation of the scattering surface,  $R_{sat}$  is the elevation of the satellite,  $n_{CO_2}(r)$  is  
 1549 the altitude dependent CO<sub>2</sub> number density, and  $n_{air}(r)$  is the altitude dependent dry air number  
 1550 density. At an elevation  $r$ ,  $n_{CO_2}(r) = X_{CO_2}(r)n_{air}(r)$  and the CO<sub>2</sub> line's absorption cross-sections  
 1551 are  $\sigma_{on}(r)$  and  $\sigma_{off}(r)$  at the on- and off-line wavelengths respectively. Equation (5-1) assumes that  
 1552 there is no other absorption from other gas species (such as water vapor) at the CO<sub>2</sub> measurement  
 1553 wavelengths. If other gas species absorb there, then their additional absorption effects must be  
 1554 accounted for.

1555 The lidar receiver measures the return pulse energies,  $E_{on}$  and  $E_{off}$  measured for the on- and off-  
 1556 line pulses reflected from the surface at elevation  $R_{surf}$ . The satellite's elevation (its distance from  
 1557 the Earth's center of mass) can be determined with meter-level or better accuracy by using an  
 1558 orbit model with inputs from the satellite's on-board GPS receiver. Given the lidar's measurement  
 1559 of range  $R$  to the scattering surface, the elevation of the scattering surface is computed from

1560

$$R_{surf} = R_{sat} - R \quad (5-2)$$

1561 The total dry air column density to the scattering surface,  $N_{air}$ , can be estimated either from a  
 1562 simultaneous O<sub>2</sub> lidar measurement made to the same surface, or by evaluating a sufficiently  
 1563 accurate atmospheric model at the lidar's spatial position and measurement time.

1564 Because the width of the CO<sub>2</sub> line is broadened by atmospheric pressure, the line narrows at  
 1565 higher altitudes. This causes the off-set line's absorption cross section to decrease with increasing  
 1566 altitude. The measurement's area normalized weighting function,  $W'(r)$  gives the measurement's  
 1567 relative sensitivity to CO<sub>2</sub> at different geometric altitudes. (See Equation (5-3) below.)

1568

$$W'(r) = \frac{n_{air} [\sigma_{on}(r) - \sigma_{off}(r)]}{\int_{R_{surf}}^{R_{sat}} n_{air} [\sigma_{on}(r) - \sigma_{off}(r)] dr} \quad (5-3)$$

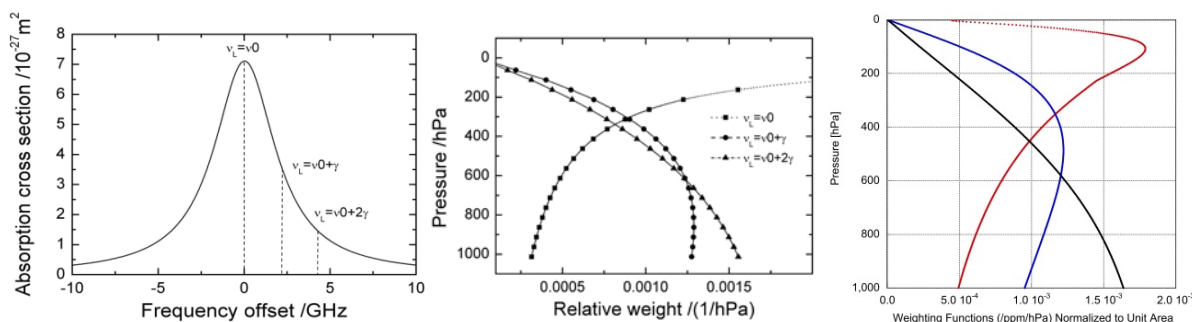
1569 Figure 5-2 shows an example of a CO<sub>2</sub> line's cross sectional shape and weighting function vs  
 1570 pressure altitude. The weighting function's dependence on altitude depends on the absorption  
 1571 line strength, the displacement of the "online" frequency from line center, and dry air density.

1572 Most candidate IPDA lidar approaches exploit the weighting function to enhance the column  
 1573 measurement's sensitivity in the lower atmosphere. By choosing a suitable  $\lambda_{on}$ , the laser signals  
 1574 are preferentially absorbed by the CO<sub>2</sub> molecules in the lower troposphere, where the ambient  
 1575 pressure is higher. This allows  $W'(r)$  to be strongest in the lower troposphere. Thus the lidar  
 1576 measurement can be more sensitive to the lower tropospheric CO<sub>2</sub> than that of a passive reflected  
 1577 solar instrument, by as much as a factor of two.

1578 From equation (5-1), the one-way differential absorption optical depth (DAOD) measured by the  
 1579 lidar can be defined as

$$DAOD \equiv \frac{1}{2} \ln(E_{off} / E_{on}) \quad (5-4)$$

1580 The accurate measurements of XCO<sub>2</sub> needed for ASCENDS require accurate lidar measurements  
 1581 of DAOD and  $R$ , as well as of  $N_{air}$ . The conditions for measuring gas column densities to the  
 1582 Earth's surface from orbit can be complex. There can be variability in  $R_{surf}$ , surface reflectivity, as  
 1583 well as in the spatial coverage, altitude distribution and strength of cloud and aerosol scattering.  
 1584 Generally there are potential error sources from the instrument, spectroscopy of the CO<sub>2</sub> line, and  
 1585 platform altitude and pointing angle (*measurement errors*) as well as potential errors from the  
 1586 knowledge of the parameters of the atmospheric column (*environmental errors*). There are similar  
 1587 potential errors for an O<sub>2</sub> lidar if one is used to estimate  $N_{air}$ . All these factors must be considered  
 1588 when defining the measurement requirements for the ASCENDS lidar. A major strength of the  
 1589 lidar approach is providing accurate and high-resolution measurements under widely varying  
 1590 conditions.



1591  
 1592 **Figure 5-2** Absorption cross section and relative weight by pressure for an example CO<sub>2</sub> line. (Left) Example of  
 1593 the molecular absorption cross section of the 6348 cm<sup>-1</sup> CO<sub>2</sub> line near 1575 nm, as function of frequency offset of the  
 1594 on-line laser frequency from line centre for typical near surface conditions (T= 288 K and P = 1013 hPa). The  
 1595 dashed lines indicate the on-line laser frequency detuned off line center at one and two collisional halfwidths  $\gamma$ . As  
 1596 the atmospheric pressure decreases with increasing altitude,  $\gamma$  decreases and the CO<sub>2</sub> absorption line narrows.  
 1597 (Middle) Relative weight of the CO<sub>2</sub> column content as a function of pressure level for the same example on-line  
 1598 laser frequency positions ( $v_L$ ) with respect to the center of the absorption line ( $v_0$ ) (Ehret et al., 2008)). (Right)  
 1599 Weighting Functions calculated for some CO<sub>2</sub> line candidates for ASCENDS at different on-line wavelength offsets  
 1600 from line center (Red – 1572-nm line with 3-pm offset, Blue – 1572-nm line with 10-pm offset, Black – 2051-nm line  
 1601 with 42-nm offset). These are all normalized to unit area.

1602 The various lidar approaches demonstrated as candidates for ASCENDS have used somewhat  
 1603 different methods for their IPDA measurements. They have sampled different CO<sub>2</sub> and O<sub>2</sub> lines,  
 1604 used different absorption line sampling strategies with different numbers of wavelength samples,  
 1605 and different ways of measuring the elevation of the scattering surface. All CO<sub>2</sub> lidar  
 1606 demonstrations to date have estimated  $N_{air}$  using atmospheric models. The details on their

1607 approaches are described in their respective sections. However, the operation of all the lidar  
1608 candidates generally follow the measurement concept described above.

### 1609 **5.1.3 Measurement Section Overview**

1610 The measurement group of the ASCENDS ad hoc science definition team has developed a  
1611 preliminary set of ten requirements for the lidar measurements on the ASCENDS Mission. They  
1612 are described in Section 5.2. These requirements are the consensus view of the measurement  
1613 group and are intended to be generic and independent of the measurement approach.

1614 During the past decade, NASA has invested in the development of several different lidar  
1615 approaches and technologies which may be candidates for ASCENDS. With the support of the  
1616 Earth Science Technology Office (ESTO), the ASCENDS ad hoc science definition activity,  
1617 NASA centers and some industry investments, the NASA lidar teams have made a number of  
1618 advances in developing candidate lidar approaches, in demonstrating their measurement  
1619 capabilities from aircraft, and in demonstrating data analysis (retrieval) approaches. These are  
1620 summarized in Section 5.3. Work on other approaches has also been pursued and their status is  
1621 summarized in Section 5.4. Several activities are recommended in the near term to improve the  
1622 definition, enhance the performance, and reduce the risk of the ASCENDS mission. Those are  
1623 summarized in Section 5.5.

1624 Although the airborne lidar have been quite valuable in demonstrating capability of candidate  
1625 lidar approaches, a space version requires some additional technology development to allow  
1626 similar measurements for an extended time from orbit. Some teams have also conducted analysis  
1627 on the capabilities needed for a space lidar and made progress in addressing some key  
1628 technologies for it. This work is summarized in Section 5.6. Some general needs for lidar  
1629 development for the ASCENDS space mission are summarized in Section 5.7.

## 1630 **5.2 ASCENDS Lidar Measurement Requirements**

1631 During 2013, the measurement group of the ASCENDS ad hoc science definition team developed  
1632 a preliminary set of measurement requirements for the ASCENDS lidar. These requirements were  
1633 developed based on the team member's prior lidar experience as well as that gained from the  
1634 numerous ASCENDS airborne campaigns that used different candidate lidar measurement  
1635 techniques. These represent the consensus view of the present best understanding of the lidar  
1636 measurement needs for the space mission. The requirements are also consistent with the initial  
1637 mission simulation studies performed by Kawa et al. (2010).

1638 The preliminary requirements are provided in this section with a justification for each. The  
1639 preliminary set of requirements is summarized in Table 5-2, including one requirement that is  
1640 applicable to the ground segment. Each individual lidar requirement ("R-#") is stated  
1641 subsequently, along with its rationale and a discussion of the relevant issues and questions.

1642

1643

**Table 5-2 Summary of Measurement Requirements needed for ASCENDS**

<b>Summary of Measurement Requirements needed for ASCENDS</b>
<p>1. Measure &amp; report the 6 lidar measurements stated below with a spatial resolution equivalent to a sampling rate of at least 50 Hz. (This implies a compatible laser footprint diameter). This spatial resolution is related to (a) the ability to measure scattering surface elevation (SSE) with sufficient accuracy over sloping terrain (R-7), and (b) the ability to obtain data in scattered cloud conditions (R-4, R-8). These six measurements are:</p> <ul style="list-style-type: none"> <li>(1) CO<sub>2</sub> differential absorption optical depth (DAOD),</li> <li>(2) Range to the surface at an “offline” wavelength within the CO<sub>2</sub> absorption band, to allow determination of column length and SSE of CO<sub>2</sub> column density measurement,</li> <li>(3) Range spreading (i.e., variability of SSE) at the “offline” CO<sub>2</sub> wavelength within the spatial resolution element (R-6, R-7) ,</li> <li>(4) O<sub>2</sub> DAOD,</li> <li>(5) Range to the surface at an “offline” wavelength within the O<sub>2</sub> absorption band, to allow determination of column length and SSE of O<sub>2</sub> column density or surface pressure measurement in the O<sub>2</sub> wavelength region, and</li> <li>(6) Range spreading at the “offline” O<sub>2</sub> wavelength.</li> </ul> <p>The uncertainties in these measurements, as stated in the ten individual requirements, must enable computing XCO<sub>2</sub>, the column average CO<sub>2</sub> mixing ratio, consistent with the random error and bias requirements, R-1 and R-2.</p> <p>The altitude sensitivity (or the weighting function) of XCO<sub>2</sub> must have ≥ 50% of its response (or sensitivity) below 5 km.</p>
2. The CO <sub>2</sub> & O <sub>2</sub> lidar measurements must be co-aligned spatially
3. The CO <sub>2</sub> & O <sub>2</sub> measurements must have sufficient resolution and precision to enable computing CO <sub>2</sub> dry air mixing ratio over a virtual bright flat reference surface (with lidar reflectance equivalent to that of Railroad Valley NV) in a clear atmosphere to ≤ 10 ppm at a 50-Hz rate, or ≤ 0.5 ppm using 10-second averaging.
4. The bias in XCO <sub>2</sub> determined from the lidar measurements must be < 2 ppm pre-launch. There must be a credible path to reduce the biases as the mission progresses to < 0.5 ppm, 1 year after launch. See R-2.
5. Measurements made under reduced atmospheric transmission due to thin clouds and to darker surfaces must also be reported, but can have correspondingly reduced precision. See R-3 and R-5 for more information.
6. The lidar must be capable of making CO <sub>2</sub> & O <sub>2</sub> measurements to surfaces whose lidar reflectivity may vary widely (more than 100x) from one measurement sample to the next.
7. The lidar must provide measurements at the lidar-reporting rate when orbiting over rapid changes in height of the reflecting surface of up to 5 km (e.g., to accommodate transitions between cloud tops and the surface).
8. The lidar must provide measurements when orbiting over surfaces that have up to 40 m of range spreading within the sampling interval, such as sloping terrain in mountains and forests with tall trees.
9. The lidar must provide measurements through thin clouds and aerosol layers with performance metrics as stated in R-3 and R-5.
10. The lidar instrument or spacecraft must provide measurements of its orbit position and pointing angle to allow post processing to determine its radial orbit altitude to ≤ 1 m in order to enable conversion of range into scattering surface elevation.
11. The lidar measurements must be processed using adaptable algorithms (“measurement models”) that allow the algorithm parameters and computations to be updated post-launch, for the purpose of improving the processed measurement data accuracy and coverage by incorporating improved knowledge of instrument behavior from on-orbit calibrations, etc.

1644 These requirements are intended to be as general as possible and to be independent of individual  
1645 lidar measurement approaches. These requirements are also preliminary, and the intent is that they  
1646 will be updated as the understanding of the mission's required measurements improve. For  
1647 example, one question still being evaluated is whether the expected improvements in  
1648 meteorological models will be adequate for the dry air mass estimates and thus obviate the need  
1649 for the O<sub>2</sub> lidar measurements.

1650 The requirements take into account the high precision and high degree of stability (or low  
1651 measurement bias) needed for the ASCENDS lidar. They also take into account the complexity of  
1652 making precise measurement of atmospheric gas columns when viewing the Earth from space.  
1653 Some of the complicating factors include the widely varying reflectance and topographic heights  
1654 of the Earth's land and ocean surfaces, the wide variety of cloud types, and the large variations in  
1655 cloud and aerosol attenuation and scattering in the atmosphere. The physics of the IPDA lidar  
1656 approach uniquely enables retrieving CO<sub>2</sub> mixing ratios with high precision and low bias in the  
1657 midst of these complications. Several of the listed requirements relate to essential attributes of  
1658 the lidar system that has these capabilities, as discussed briefly here.

### 1659 **5.2.1 Why Are Ranging Measurements Important?**

1660 Ranging, which allows linking the backscattered online/offline signals with their round-trip time-  
1661 of-flight, provides accurate determination of the column length and enables effective filtering of  
1662 aerosols and optically thin clouds. It is well known that atmospheric scattering, if not accurately  
1663 accounted for or eliminated, is a source of bias in passive optical measurements of CO<sub>2</sub> columns  
1664 (see for example Aben et al. (2007)). For example, a high-altitude cirrus layer having optical  
1665 depth of 0.03 can produce a bias of as much as ~10 ppmv (Menzies et al., 2014). Along-track  
1666 sampling resolution of ~ 100-150 m also provides capability to take advantage of gaps in thick  
1667 clouds to obtain CO<sub>2</sub> data in the lower troposphere to the surface. Requirements R-4 and R-5 are  
1668 relevant to this capability.

1669 Accurate measurements of the column length to the scattering surface are also important. The  
1670 weighting function depends on the pressure of the scattering surface, which is derived from its  
1671 elevation (SSE, scattering surface elevation) together with pressure surface data from atmospheric  
1672 models and the O<sub>2</sub> lidar. A small lidar footprint, or spatial sampling resolution element, has  
1673 significant advantages when measuring over regions with varying topography and/or with tall  
1674 trees, causing the range to vary significantly. This is further justification for along-track sampling  
1675 resolution of 150 m or better (i.e., a sampling rate of at least 50 Hz). There are limitations to the  
1676 use of a Digital Elevation Model (DEM). For example, the DEM is not an accurate indicator of  
1677 the SSE over forests.

1678 Finally it is important to note that the reflectance of surface materials vary for different gas  
1679 absorption bands. For some important cases (snow beneath trees) this can cause the SSE to be  
1680 different for CO<sub>2</sub> and O<sub>2</sub> measurements. Requirements R-4, R-6, and R-7 are relevant to this  
1681 discussion.

### 1682 **5.2.2 Discussion of Requirement Elements**

1683 The ad hoc science definition team has summarized ten specific requirements for the ASCENDS  
1684 lidar. They are discussed in this section. Many of the requirements need some additional work to  
1685 resolve questions, and those needs are summarized under the Discussion headings. The value of

1686 some parameters needed for accurate retrievals will need to improve after launch by using  
1687 calibration/validation (cal/val) activities and campaigns.

### 1688 **R-1: XCO<sub>2</sub> Random Error**

1689 Baseline: ~ 0.5 ppm, for 10-sec averaging, over a surface with a lidar directional reflectance  
1690 equivalent to the Railroad Valley, NV (RRV) surface, with clear atmosphere, and effective  
1691 weighting function with over 50% of its response (or sensitivity) below 5 km.

1692 Rationale: Observational System Simulation Experiments (OSSE's) performed by the  
1693 ASCENDS Modeling team indicate that 0.5-ppm XCO<sub>2</sub> precision for a 10-second average over a  
1694 surface with a lidar directional reflectance equivalent to RRV, will yield adequate precision over a  
1695 wide range of surface types (ocean, forests, snow, ice) (c.f., Kawa et al., 2010).

1696 Comments: This requirement assumes that individual samples are averaging over 10 seconds  
1697 (70 km along track with no gaps), over a surface with a lidar directional reflectance or  
1698 "backscatter" of  $\beta = 0.176 \text{ sr}^{-1}$  (typical RRV playa value), with negligible atmospheric attenuation  
1699 by clouds and aerosols. See R-3 for more surface information.

1700 Discussion: This is weighting function dependent, i.e., the lower in altitude the weighting  
1701 function is peaked; the greater the sensitivity to surfaces sources and sinks. See the modeling  
1702 chapter for examples of this effect.

1703 The requirement is on XCO<sub>2</sub>, and the apportionment of the errors/uncertainties that contribute is  
1704 not specified. Uncertainties in surface pressure, water vapor, and temperature profiles will  
1705 contribute. We estimate roughly half of the mission-required error budget is due to the lidar CO<sub>2</sub>  
1706 column measurement error.

### 1707 **R-2: XCO<sub>2</sub> Biases**

1708 Baseline: Instrument must have sufficient stability so that its "Residual biases" can be  
1709 reduced over the first year of the mission by adding additional instrument characterization & on-  
1710 orbit calibrations and validations. They should be:

1711  $\leq 2$  ppm pre-launch,  $\leq 1$  ppm 6 months after launch;  $\leq 0.5$  ppm, one year after launch

1712 Rationale: Results from Modeling team simulations.

1713 Comments: The main emphasis is on "residual spatially- or temporally-varying biases" (i.e.,  
1714 biases that are likely to vary over spatial and/or time scales which remain after measurement bias  
1715 model corrections). The residuals will decrease as the on-orbit instrument calibration and retrieval  
1716 algorithms improve during the mission (as for GOSAT).

1717 Discussion: Biases could be introduced by variable surface spectral reflectivities; pathlength  
1718 uncertainties; low received signal levels due to aerosol/cloud scattering, calibration errors,  
1719 instrument thermal environment; uncompensated non-linearities in detector response; or errors or  
1720 uncertainties in the spectroscopy of CO<sub>2</sub>, O<sub>2</sub>, or interfering gases. Two simple categories for these  
1721 are "environmental errors" and "instrument errors."

1722 Determining an acceptable level of residual bias for the ASCENDS is complex activity. Although  
1723 important progress has been made, more work is needed. The "forward runs" (i.e., detection

1724 experiments) offer the simplest approach to determine. More study of bias impacts on different  
1725 space and time scales is needed.

1726 **R-3: Return Signal Dynamic Range & Measurement Precision**

1727 Baseline: To provide global coverage, the lidar must make and record measurements to a wide  
1728 variety of surface types and through atmospheres with some thin cloud and/or aerosol attenuation.  
1729 These will present a wide range of signal strengths to the lidar receiver.

1730 **Table 5-3 Return Signal Dynamic Range for 1570-nm CO<sub>2</sub> lidar**

Case:	Surface beta(pi) (ster <sup>-1</sup> )	Effective Lambertian Albedo	Atm Optical Depth	Beta(pi)* atm trans <sup>2</sup>	Received Signal Relative to RRV clear	Received signal as Percent of RRV Clear	Measurement Error Mult*	
Clear RRV	0.176	0.553	0.0	0.18	1.00	100	1.00	
Clear Snow**	0.016	0.050	0.0	1.60E-02	9.09E-02	9.09	3.32	
Clear Calm ocean	0.528		0.0	0.53	3.00E+00	300.00	0.58	
Thin clouds & RRV	0.176	0.553	0.7	4.34E-02	2.47E-01	24.66	2.01	
Polar clouds & Snow**	0.016	0.050	0.2	1.07E-02	6.09E-02	6.09	4.05	
Thin clouds & Rough ocean	0.025		0.7	6.16E-03	3.50E-02	3.50	5.34	
Thin clouds & Calm ocean	0.528		0.7	0.13	7.40E-01	73.98	1.16	
** Snow albedo from Aoki (2000)							Total Signal Dynamic Range (Ratio Strongest to Weakest)	86
Rough Ocean ~ 12 m/sec wind speeds							* based on an ideal signal shot-noise limited lidar receiver	

1731  
1732 Calculations for candidate CO<sub>2</sub> lidar that measure in the 1570-nm and 2051-nm bands shown in  
1733 the following two tables. These are followed by calculations for candidate O<sub>2</sub> lidar that operate in  
1734 the 760-nm O<sub>2</sub> A-band and 1270-nm singlet-delta band. These estimates are based on limiting  
1735 cases with one-way extinction optical depth (OD) ≤ 0.7 at the strong return signal end of the  
1736 range, and one-way OD ≤ 0.2 (1570 nm) or OD ≤ 0.1 (2051 nm) at the weak signal end. The  
1737 upper limit cutoff for the signal is (about 3 times that from Railroad Valley) for measurements to  
1738 smooth water surfaces (i.e., surface wind speed less than ~ 3 m/sec). The instrument CO<sub>2</sub>  
1739 measurement precision must meet or exceed the precision multiplier estimates shown in the last  
1740 column for various signal measurement conditions. This includes allowing for noise from  
1741 detector and optical background.

1742

1743

1744

**Table 5-4 Return Signal Dynamic Range for 2051-nm CO<sub>2</sub> Lidar**

Case:	Surface beta(pi) (ster^-1)	Effective Lambertian Albedo	Atm Optical Depth	Beta(pi)* atm trans^2	Received Signal Relative to RRV clear	Received signal as Percent of RRV Clear	Measurement Error Mult*	
Reference case RRV	1.61E-01	0.506	0.0	0.16	1.00	100	1.00	
Clear atm & Snow**	6.40E-03	0.020	0.0	6.40E-03	3.98E-02	3.98	5.02	
Clear atm & Calm ocean	5.28E-01		0.0	0.53	3.28E+00	327.95	0.55	
Reference case RRV	1.61E-01	0.506	0.7	3.97E-02	2.47E-01	24.66	2.01	
Polar clouds & Snow**	6.40E-03	0.020	0.2	4.29E-03	2.66E-02	2.66	6.13	
Thin clouds & Rough ocean	2.50E-02		0.7	6.16E-03	3.83E-02	3.83	5.11	
Thin clouds & Calm ocean	5.28E-01		0.7	0.13	8.09E-01	80.87	1.11	
** Snow albedo from Aoki (2000)							Total Signal Dynamic Range (Ratio Strongest to Weakest)	123
Rough Ocean ~ 12 m/sec wind speeds							* based on an ideal signal shot-noise limited lidar receiver	

1745

1746

**Table 5-5 Return Signal Dynamic Range for 765-nm O<sub>2</sub> Lidar**

Case:	Surface beta(pi) (ster^-1)	Effective Lambertian Albedo	Atm Optical Depth	Beta(pi)* atm trans^2	Received Signal Relative to RRV clear	Received signal as Percent of RRV Clear	Measurement Error Mult*	
Reference case RRV	0.168	0.53	0.0	0.17	1.00	100	1.00	
Clear Snow**	0.271	0.85	0.0	2.71E-01	1.61E+00	161.05	0.79	
Clear Calm ocean	0.528		0.0	0.53	3.14E+00	314.29	0.56	
Thin clouds RRV	0.168	0.53	0.7	4.14E-02	2.47E-01	24.66	2.01	
Polar clouds Snow**	0.271	0.85	0.2	1.81E-01	1.08E+00	107.95	0.96	
Thin clouds Rough ocean	0.025		0.7	6.16E-03	3.67E-02	3.67	5.22	
Thin clouds Calm ocean	0.528		0.7	0.13	7.75E-01	77.50	1.14	
** Snow albedo from Aoki (2000)							Total Signal Dynamic Range (Ratio Strongest to Weakest)	85.6
Rough Ocean ~ 12 m/sec wind speeds							* based on an ideal signal shot-noise limited lidar receiver	

1747

1748

**Table 5-6 Return Signal Dynamic Range for 1262-nm O<sub>2</sub> Lidar**

Case:	Surface beta(pi) (ster^-1)	Effective Lambertian Albedo	Atm Optical Depth	Beta(pi)* atm trans^2	Received Signal Relative to RRV clear	Received signal as Percent of RRV Clear	Measurement Error Mult*	
Clear RRV	0.168	0.528	0.0	0.17	1.00	100	1.00	
Clear Snow**	0.175	0.550	0.0	1.75E-01	1.04E+00	104.21	0.98	
Clear Calm ocean	0.528		0.0	0.53	3.14E+00	314.29	0.56	
Thin clouds RRV	0.168	0.528	0.7	4.14E-02	2.47E-01	24.66	2.01	
Polar clouds Snow**	0.175	0.550	0.2	1.17E-01	6.99E-01	69.85	1.20	
Thin clouds Rough ocean	0.025		0.7	6.16E-03	3.67E-02	3.67	5.22	
Thin clouds Calm ocean	0.528		0.7	0.13	7.75E-01	77.50	1.14	
** Snow albedo from Aoki (2000)							Total Signal Dynamic Range (Ratio Strongest to Weakest) 85.6	
Rough Ocean ~ 12 m/sec wind speeds							* based on an ideal signal shot-noise limited lidar receiver	

1749

1750 Rationale: ASCENDS must record data over a variety of surface types (including snow &  
1751 water) to get global measurements (including high latitude winter).

1752 **R-4: Along Track Sampling Resolution**

1753 Baseline: ≤ 150 m, (≥ 50 Hz sampling). This sampling rate is driven by the need for  
1754 measurements over cloudy atmospheres and over regions of rapidly changing surface topography  
1755 & reflectance.

1756 The lidar measured parameters that need to be reported at this rate are:

1757 Mean CO<sub>2</sub> DAOD (or column density), Mean Range (or scattering surface elevation) in CO<sub>2</sub>  
1758 wavelength region, Range Spread\*

1759 Mean O<sub>2</sub> DAOD (or column density), Mean Range (or scattering surface elevation) in O<sub>2</sub>  
1760 wavelength region, Range Spread\*

1761 Rationale: The ASCENDS capability in “seeing” through breaks in cloud cover diminishes  
1762 with laser footprint sizes > 150m. ASCENDS also needs to measure to terrain surfaces that  
1763 rapidly vary in elevation and reflectance. A smaller laser footprint reduces error in  
1764 determination/assignment of “effective scattering surface elevation”.

1765 Discussion: This requirement relates to the maximum laser footprint size and along-track spatial  
1766 scale of sampling. One driver for this requirement is to require measurements through scattered  
1767 clouds. Estimates of cloud gap size were obtained from analyzing from laser altimeter  
1768 measurements over Iowa during 2011 ASCENDS airborne campaign (Browell et al., 2012). More

1769 data from the 2011 airborne campaigns are also available. Over mountainous terrain the rapidly  
1770 varying column length causes the measurement to degrade with poorer along-track resolution.

1771 \* See discussion of range spreading in R-7

### 1772 **R-5: Measurements through atmospheric scatter (thin clouds & aerosols)**

1773 Baseline: To ensure adequate coverage of the globe, the lidar DAOD and range  
1774 measurements must be made through scattering & attenuating aerosol layers and partially  
1775 transmissive cloud layers.

1776 The bias requirements (R-2) must be met under these conditions.

1777 The measurement precision is allowed to degrade at the lower received signal levels as given in  
1778 the last columns of the Tables in R-3 (Table 5-3 to Table 5-6).

1779 Rationale: Thin clouds are quite prevalent in the Earth's atmosphere. An important benefit of  
1780 ASCENDS is to allow accurate measurements in regions covered by thin clouds. The random  
1781 errors will increase due to attenuation of energy of surface backscatter signal. Extensive airborne  
1782 measurements of aerosol layer optical properties indicate that atmospheric aerosol OD is  $< 0.1$  at  
1783 2051 nm and  $< 0.2$  at 1570 nm, even for dust layers from Asia and the Sahara that have been  
1784 transported from their source regions (Srivastava et al., 2001; Winker et al., 2010). From these  
1785 results we conclude that aerosol layers alone will not seriously impact ASCENDS global  
1786 coverage.

### 1787 **R-6: Measurements over forests & over sloped or rough bare terrain**

1788 Baseline: Measurements meeting R-1 & R-2 over forests and over surfaces with height  
1789 variations of up to 40 m over a horizontal distance of 150 m are required.

1790 Rationale: Forests are a large fraction of Earth's land surface and are an important part of  
1791 carbon cycle. (Simard et al., 2011) report spatially-resolved tree heights over the globe, based on  
1792 analysis of ICESat/GLAS measurements. Their results showed maximum tree heights of  $\sim 40$  m.  
1793 The ASCENDS lidar also must measure over bare terrain, rough or sloped, whose surface has  
1794 similar range spreading over 175-m distances.

### 1795 **R-7.1: Range (Scattering Surface Elevation) measurement: Precision**

#### 1796 Baseline:

1797 a. Mean Range measurement precision: Baseline:  $\leq 20$  m (at 50-Hz rate) for all cases included  
1798 in the R-3 tables (Table 5-3 to Table 5-6) and range spreading cases in R-6, and  $\leq 2$  m for a  
1799 10-s average over a RRV equivalent surface.

1800 b. The Lidar must report range at both the CO<sub>2</sub> and O<sub>2</sub> measurement wavelength regions, both  
1801 on the same spatial scale (see R-4).

1802 c. Range Spread measurement: Baseline  $\leq 20$  m (at 50-Hz rate) for all cases included in the R-3  
1803 tables and range spreading cases in R-6, for both CO<sub>2</sub> and O<sub>2</sub> wavelength regions.

1804 d. Rate of change in range: The lidar needs to accommodate changes in range of  $\geq 5$  km for  
1805 adjacent footprints, to allow for measurements from cloud tops to the ground through holes in  
1806 clouds.

1807 e. Spacecraft radial orbit height<sup>\*\*</sup>:  $< 1$  m at a rate sufficient to model orbit to  $< 1$ -m radial error

1808 Discussion: A summary of the rationale for measuring range at both CO<sub>2</sub> and O<sub>2</sub> lidar  
1809 wavelengths is below.

1810 a. Some surfaces (e.g., conifers with snow underneath) can have different average scattering  
1811 surface elevations (SSE) at CO<sub>2</sub> & O<sub>2</sub> wavelengths, due to the variability in snow reflectivity  
1812 with wavelength. Snow is quite dark at the CO<sub>2</sub> wavelengths but is much brighter at the O<sub>2</sub>  
1813 wavelengths. In this case, there is a difference in the return signal from the snow surface (CO<sub>2</sub>  
1814 is dim, O<sub>2</sub> is brighter). Consequently the mean range (i.e., the SSE) for these wavelengths  
1815 will be different when there are spatial variations in snow cover across the footprint (e.g.,  
1816 coniferous forests with snow on the ground). Reporting SSE for both wavelengths will allow  
1817 analysis to accurately estimate CO<sub>2</sub> mixing ratios.

1818 b. In order to maximize the number of CO<sub>2</sub> retrievals over, e.g., patchy/broken cloud cover,  
1819 range measurements are required at the 50-Hz reporting interval, with the precision  
1820 requirement stated above. The 20-m uncertainty is equivalent to approximately 1 ppm of  
1821 CO<sub>2</sub>. This uncertainty should decrease with additional along-track samples, although the rate  
1822 of decrease of the uncertainty depends on the cloud structure and the underlying surface  
1823 topography.

1824 c. Some reflecting surfaces (i.e., trees) will have range spreads within the footprint that can be  
1825 20-40 m. Also large surface slopes can occur over mountains. Range spread measurements at  
1826 the 50-Hz sampling rate enable estimates of tree heights and slope magnitudes. Range spread  
1827 with above-stated precision at both CO<sub>2</sub> and O<sub>2</sub> wavelength regions enable mitigation of bias  
1828 over surfaces discussed in (a) above.

1829 <sup>\*\*</sup> Need to know the spacecraft's radial orbit height to compute the scattering surface elevation  
1830 from the lidar measured range.

### 1831 **R-7.2: Range (SSE) measurements: Bias**

#### 1832 Baseline:

1833 a. Baseline for ranging measurements:  $\leq 2$  m per footprint for all cases included in the R-3 tables  
1834 (Table 5-3 to Table 5-6) and satisfying R-4 range spreading. The lidar must also report range at  
1835 both the CO<sub>2</sub> & O<sub>2</sub> offline wavelengths, both on the same spatial scale (see R-4).

1836 b. Baseline for Spacecraft radial orbit height<sup>\*\*</sup>:  $< 1$  m

1837 Discussion: The SSE needs to be measured at 50 Hz for both CO<sub>2</sub> and O<sub>2</sub> lidar wavelengths to  
1838 minimize the bias inherent in rapidly changing terrain. Bias occurs under conditions described in  
1839 R-7.1, due to spectrally varying reflectivity of various surface types. Large changes in, e.g., snow  
1840 cover, can occur over distances of 150 m (the required sampling interval). Measurements are

1841 made though “holes” for conditions of patchy/broken cloud cover, creating rapid changes from  
1842 cloud top to ground.

1843 In addition, over hills/mountains large changes in elevation also occur over km-scale distances.  
1844 Due to the inherent reflectance weighting of the samples, correlations between elevation and  
1845 surface type (and surface reflectivity) could produce bias if using km-scale averaging. Hence  
1846 reporting the range to the SSE at 50-Hz rate, with sufficient precision (< 20-m uncertainty) and  
1847 low bias (< 2 m) is required.

1848 \*\* Need to know the spacecraft’s radial orbit height to compute the scattering surface elevation  
1849 from the lidar measured range.

### 1850 **R-8: Measurements over Cloud Tops and Decks**

1851 Baseline: “Report” measurements over optically-thick cloud tops that meet the other signal  
1852 requirements. (i.e., roughness, signal strength, etc.).

1853 Rationale: These measurements are expected to be useful for future analysis, but currently it  
1854 is judged that they do not have to be of the same measurement quality as those to the surface.  
1855 Further studies are required to better quantify the requirement.

1856 Discussion: Initial Airborne measurements in 2011 over stratus cloud decks show promise  
1857 toward useful values. Some improvement can be expected with additional algorithm development.  
1858 Cloud tops are diffuse scatters, and laser penetration depths may vary from ~ 10 m to > 100 m;  
1859 consequently accurate measurements over cloud decks is more difficult than for solid surfaces.

### 1860 **R-9: Uncertainty in Measurement Footprint’s\* Surface Location (pointing control and 1861 knowledge)**

1862 Nadir angle offset\*: 6 - 20 mrad (TBR)

1863 Baseline Knowledge: ~ 100 m (TBR)

1864 Baseline Control: ~500 m

1865 Rationale: Measurement analysis needs knowledge of measurement locations for use in  
1866 models, cal/val correlative measurements, control of systematic errors/biases due to terrain  
1867 variability, above-ground variability, and effective use of digital elevation models (DEM’s). The  
1868 mission will also need control of measurement locations for effective cal/val (e.g., TCCON  
1869 intercomparisons). See R-10.

1870 Discussion: This requirement applies to both the CO<sub>2</sub> & O<sub>2</sub> beams and assumes that they are  
1871 co-aligned (co-boresighted). Co-alignment requirements are lidar-design specific, consequently  
1872 not quantified here. It is important to recognize that sharp ground-track transitions (e.g., land-to-  
1873 water transitions) must be accommodated in meeting the XCO<sub>2</sub> precision and bias requirements.

1874 The ASCENDS lidar must be pointed slightly offset from local nadir, to allow measurements to  
1875 smooth water and certain flat ice crystals, while avoiding the strongest part of the specular  
1876 reflections from it. ICESat results indicate that we need to stay > 6 mrad from local nadir. The  
1877 maximum angle is uncertain but likely < 20 mrad. The final operational angle will need to be  
1878 found on-orbit.

1879 This requirement is also associated with accurate location of the measurement footprint on the  
1880 surface for improved modeling accuracy. These numbers are consistent with maintaining the path  
1881 length error (SSE estimate error) below a value that compromises the overall error budget. Studies  
1882 using ASCENDS airborne lidar measurement indicate that slopes  $< 15$  degrees over 100-m scales  
1883 occur with  $\sim 50\%$  probability over mountains ranges such as the Sierra Nevada. Any aspect of  
1884 ground spot location uncertainty that affects bias error should be derived from the bias  
1885 requirement stated earlier. Knowledge of spatial location of the column end-point is more  
1886 important for smaller-scale sources. Typical pointing knowledge for the requirements above is  
1887  $200 \mu\text{rad}$ , or  $40 \text{ arcsec}$ .

1888 \* See discussion of range spreading in R-7

### 1889 **R-10: Laser Beam Pointing Off-nadir Limits**

1890 Off nadir operating limits:  $< +/- 15$  degree of nadir

1891 Rationale: Need to allow a finite range of pointing angles away from nadir to permit a useful  
1892 frequency of pointing to TCCON (or other ground-based calibration) sites over land areas.

1893 Discussion: This specifies how far away from the nadir-pointing angle that ASCENDS is  
1894 required to measure. The further off nadir, the more frequently ASCENDS can access (i.e., be  
1895 “within range of”) ground-based cal/val sites. In regular operation, ASCENDS will need to point  
1896 off-nadir (cross-track) to locate footprints near ground-based cal/val sites (e.g., TCCON). Cal/val  
1897 measurements are expected to be important to assess and minimize residual biases. It needs to be  
1898 determined how frequently ASCENDS will need to measure off nadir, to a TCCON site, for  
1899 example. The larger the allowable off-nadir angle, the more frequently a ground based site can be  
1900 sampled.

1901 An additional complication for the  $\text{CO}_2$  measurement is the Doppler shift. When pointed off  
1902 nadir, the Doppler effects from the spacecraft’s velocity, Earth’s rotation, and atmospheric winds  
1903 may shift the absorption line relative to the spacecraft and possibly change its shape. The above  
1904 off-nadir pointing limitations were arrived at from an analysis provided to the ASCENDS ad hoc  
1905 science definition team by Spiers and Menzies. Some aspects (spacecraft velocity & Earth’s  
1906 rotation) are predictable. Estimates of atmospheric wind velocity fields are available from NWP  
1907 models.

### 1908 **5.3 Lidar Development and Measurement Demonstrations**

1909 During the past decade, NASA has invested in the development of several different lidar  
1910 approaches and technologies which are candidates for ASCENDS. With the support of ESTO, the  
1911 ASCENDS ad hoc science definition activity, and NASA Center and corporate investments,  
1912 several NASA lidar teams have made substantial advances in developing suitable lidar systems,  
1913 demonstrating lidar capabilities from aircraft, improving the understanding of the characteristics  
1914 needed in the measurements, and reducing the risk for developing the technology for the space  
1915 lidar.

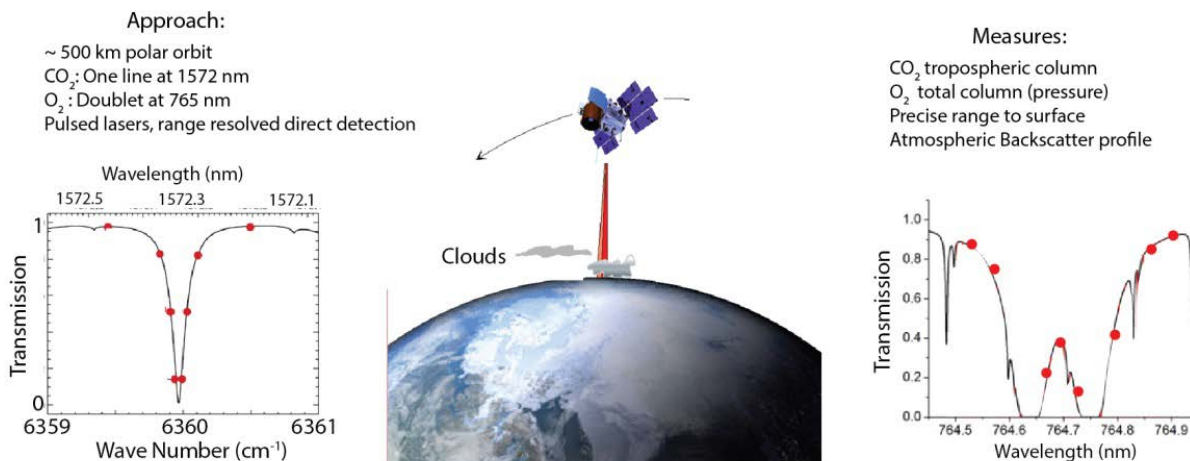
1916 The operating principles for different IPDA lidar approaches have been discussed in detail in  
1917 many publications. Some examples are given by Ehret et al. (2008), Abshire et al. (2010a, 2013),

1918 Spiers et al. (2011a), Browell et al. (2012), Dobler et al. (2013), Menzies et al. (2014) and others.  
1919 A signal to noise analysis is also discussed by Sun and Abshire (2012).

1920 Here we summarize NASA's experimental demonstrations and the results to date. This section  
1921 gives a summary of the work demonstrating capabilities of candidate CO<sub>2</sub> and O<sub>2</sub> lidar  
1922 techniques. Each candidate approach is described along with a description of the instrument and  
1923 its type of measurements. Many have examples of atmospheric measurements from aircraft.

### 1924 5.3.1 CO<sub>2</sub> Sounder Approach and Lidar

1925



1926

1927 **Figure 5-3** The CO<sub>2</sub> Laser Sounder measures column CO<sub>2</sub> & O<sub>2</sub> absorption and range to surface. (Left) Nominal  
1928 CO<sub>2</sub> line (1572.33 nm) targeted for use for 2-way pass to surface from space. The laser sounder measures the shape  
1929 and depth of this CO<sub>2</sub> line and the absorption of a line doublet near 764.7 nm in the O<sub>2</sub> A-band (Right). The  
1930 absorption lines are scanned at a 300 Hz rate from aircraft, and ~1 KHz rate from space.

1931 A team at Goddard has developed the CO<sub>2</sub> Laser Sounder approach to enable space-based lidar  
1932 measurements of CO<sub>2</sub> concentrations like those needed for ASCENDS. Given the high (< 1 ppm)  
1933 accuracies required and the many potential error sources, the design of the measurement approach  
1934 and the lidar instrument are critical (Kawa et al., 2010). The CO<sub>2</sub> Sounder Team has developed  
1935 and demonstrated a pulsed lidar approach (Riris et al., 2007; Allan et al., 2008; Abshire et al.,  
1936 2010a,b, 2011, 2014; Amediek et al., 2013), shown in Figure 5-3 to address the needed CO<sub>2</sub>  
1937 column concentration measurements. It measures the range, line shapes and column abundance of  
1938 CO<sub>2</sub> and O<sub>2</sub> via the integrated path differential absorption (IPDA) technique (Measures, 1992).

1939 The team performed surveys of the spectroscopy (Mao and Kawa, 2004; Mao et al., 2007) and  
1940 selected gas absorption lines with minimum interference from other species and with small  
1941 temperature sensitivity. The CO<sub>2</sub> line at 1572.33 nm and O<sub>2</sub> doublet near 764.7 nm best fit the  
1942 requirements. Another important consideration is the number of wavelength sampling points per  
1943 measurement. The team found that using only a minimum two lines (on- and off-line) makes the  
1944 measurement susceptible to small spectroscopic shifts and instrument errors. For airborne  
1945 measurements, the team has used 20 and 30 samples across the lines, to allow for sampling  
1946 experiments via deletion. For space the CO<sub>2</sub> Sounder approach plans to sample the CO<sub>2</sub> and O<sub>2</sub>  
1947 line shapes with 8 wavelengths. This allows solving for and correcting for both environmental and  
1948 instrument errors. Analysis of airborne lidar measurements shows this approach is quite robust.

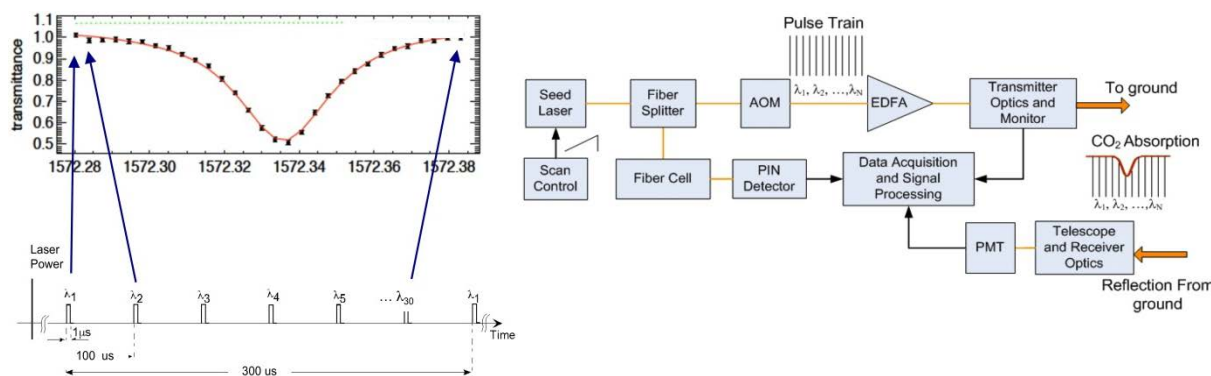
1949 The team’s approach has been to analyze the science and measurement requirements (Kawa et al.,  
1950 2010) and then to pursue the measurement approach and technologies that directly support a path  
1951 toward space (Sun et al., 2013). The team has demonstrated increasingly accurate airborne  
1952 measurements of CO<sub>2</sub> column abundance and range to 13 km in campaigns during 2009, 2010,  
1953 2011 and 2013. The team also demonstrated measurements of O<sub>2</sub> column absorption in the O<sub>2</sub> A-  
1954 band (Stephen et al., 2007; Riris et al., 2011) during the 2011 and 2013 flights. The lidar  
1955 development has been supported by the NASA ESTO Instrument Incubator program and  
1956 summaries of papers and conference presentations are available (NASA Goddard, 2015).

1957 **5.3.1.1 CO<sub>2</sub> Sounder Measurement Approach and Lidar Description**

1958 The team developed its airborne lidar as a precursor/pathfinder for ASCENDS, using lower laser  
1959 energies and a less sensitive CO<sub>2</sub> detector than planned for space. Photographs of the aircraft and  
1960 instrument are shown in Figure 5-4.



1961



1962

CO <sub>2</sub> line center wavelength:	1572.33 nm	Laser beam divergence:	100 urad	Detector quantum efficiency:	10%
Wavelength scan # across line:	30	Telescope diameter:	20 cm	PMT dark count rate:	~500 KHz
CO <sub>2</sub> line scan rate:	300 Hz	Receiver FOV diameter:	200 urad	Receiver time bin width:	8 nsec
Laser pulse energy & rate:	25 uJ, 10 KHz	Receiver optical bandwidth:	800 pm	Rcvr integr time / record:	0.9 sec

1963

1964 **Figure 5-4** Airborne CO<sub>2</sub> Sounder lidar installation, line sampling approach and parameters. (Top) Photos of the  
1965 NASA DC-8 aircraft and CO<sub>2</sub> Sounder lidar installed inside. The transmitter and receiver telescopes are in the black  
1966 box mounted over the aircraft’s aft-most nadir opening and views nadir through a dual optical window assembly.  
1967 (Middle left) Line sampling approach showing the 30 wavelength samples across the line used in the airborne lidar,  
1968 allowing robustness and diagnostic capability. (Middle right) Block diagram of the airborne lidar. (Bottom) Some  
1969 parameters of the airborne CO<sub>2</sub> lidar.

1970 The laser uses a Master Oscillator Power Amplifier (MOPA) approach with single frequency  
1971 DFB diode laser followed by a pulsed acousto-optic modulator (AOM) and a commercial Erbium  
1972 Doped Fiber Amplifier (EDFA). For flights after 2009, the airborne lidar steps the diode laser’s

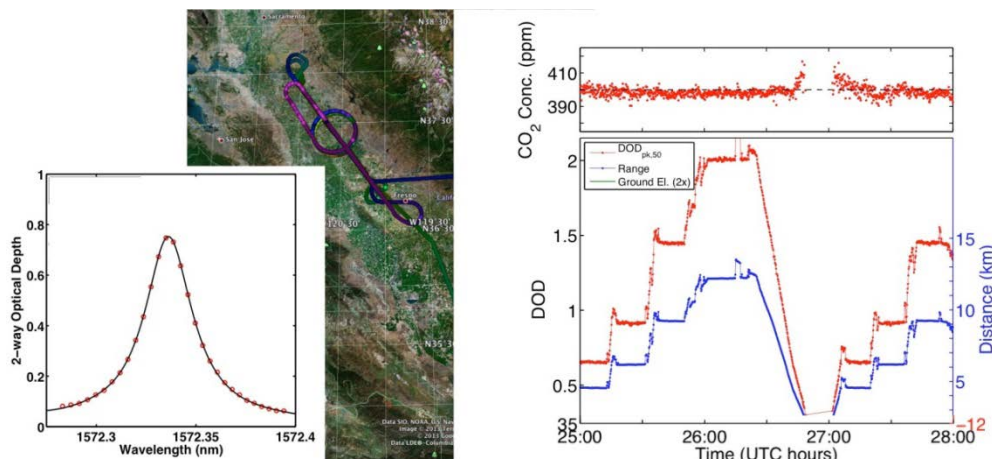
1973 wavelength across the selected CO<sub>2</sub> line at a rate of 300 Hz with 30 steps per scan. The airborne  
1974 lidar uses more wavelength samples than proposed for space, to allow evaluation of tradeoffs  
1975 from the additional information. The time resolved laser backscatter profile is collected by the  
1976 telescope, detected by a photomultiplier, and recorded by a multi-channel scalar.

1977 The column concentration of atmospheric CO<sub>2</sub> must be measured accurately (< 1ppm) to be  
1978 useful for carbon cycle science studies (NRC, 2007; NASA, 2008). The random error level  
1979 (precision) can be determined from analysis by scaling the transmitted laser energy to the level  
1980 needed (i.e. the SNR) to overcome the noise from the detector and detected solar background.

1981 Systematic errors or “drifts” usually limit the accuracies of laser absorption spectrometers (Werle  
1982 et al., 1993, 2004). Sampling the absorption line shape allows solving for a number of parameters  
1983 in the data analysis, including baseline transmission, baseline tilt, line center wavelength,  
1984 linewidth, peak transmission, best-fit line shape, and error in the fitted line. This approach allows  
1985 retrieval and signal processing approaches to measure, model, and minimize systematic  
1986 instrumental errors from etalon fringes and other sources (Abshire et al., 2014) and this analysis  
1987 substantially reduces the magnitude of instrumental errors. It also accommodates environmental  
1988 effects such as the spectral shift of the line with changing atmospheric pressure (Ramanathan et  
1989 al., 2013).

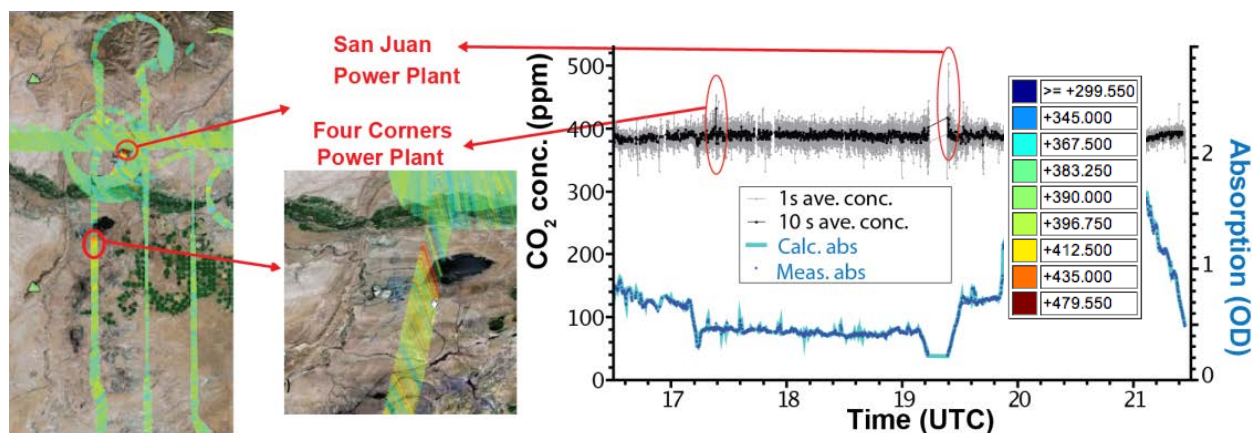
### 1990 5.3.1.2 Airborne Measurements of CO<sub>2</sub> Column Concentration and Range:

1991 The CO<sub>2</sub> Sounder team made initial airborne CO<sub>2</sub> column measurements in 2008 (Abshire et al.,  
1992 2010b). In 2009, additional measurements were taken at altitudes stepped from 3-13 km over a  
1993 variety of locations. These flight data show the precision in CO<sub>2</sub> estimates follow predicted values  
1994 (Abshire et al., 2013), and that the altimetry measurements had an uncertainty of about 3 m  
1995 (Amediak et al., 2013). The team demonstrated improved airborne measurements of CO<sub>2</sub> and O<sub>2</sub>  
1996 column abundance and inferred the mixing ratio in flights on the DC-8 during the 2011 (Abshire  
1997 et al., 2014) and 2013 airborne campaigns. Some examples are shown in Figure 5-5 – Figure 5-  
1998 11. These demonstrate the accuracy and precision that the airborne lidar has achieved to date  
1999 when measuring to a variety of land surfaces, to cloud tops and through thin clouds.

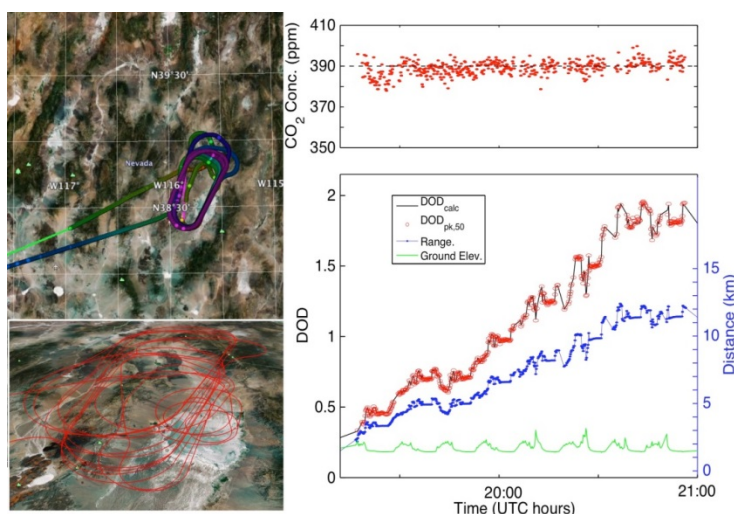


2000  
2001 **Figure 5-5** Results from CO<sub>2</sub> Sounder lidar measurements over a flat Central Valley CA. Data taken with a  
2002 uniform atmosphere on 2/27/13. (Left) The lidar measured absorption lineshapes fit calculations quite well. The  
2003 differential absorption optical depth (DAOD) reported is calculated from the fitted lineshape. (Middle) Ground track  
2004 of flight. (Right) The results (10 sec average, Measured concentration = 394 ppm, Std dev = 1.5 ppm for 12 km  
2005 altitudes) show the retrieved column averaged CO<sub>2</sub> concentration agree very well with in-situ measurements for an  
2006 atmosphere with CO<sub>2</sub> = 396 ppm.

2007 These also demonstrate retrievals and progress toward the space lidar. These flights also  
 2008 demonstrated accurate CO<sub>2</sub> concentration measurements over varying topography, to cloud tops  
 2009 and through thin clouds, conditions that are challenging for passive optical CO<sub>2</sub> sensors.



2010  
 2011  
 2012 **Figure 5-6** Detection of power plant plumes using the CO<sub>2</sub> Sounder lidar. In this flight segment over Four Corners,  
 2013 New Mexico (NM) on 8/9/11, our measurements detect elevated CO<sub>2</sub> in the plumes from power plants. (Left)  
 2014 measurement ground track geolocated on Google Earth, with concentrations color encoded, with color-scale in the  
 2015 inset at right. (Right) the total column measured concentration as a function of time. The two elevated CO<sub>2</sub> spots  
 2016 are seen directly over the two power plants. The CO<sub>2</sub> concentration is nearly constant at 390 ppm elsewhere, as expected.



2017  
 2018 **Figure 5-7** Measurements from the 2011 flight over Railroad Valley NV. This area is a flat playa surrounded by  
 2019 mountains, creating a flight track over rapidly varying ground elevation. The bottom plot shows the measured range  
 2020 to surface in blue, the measured Differential Absorption Optical Depth (DAOD) (pk, 50) in red, and the calculated  
 2021 surface elevation height in green. The DAOD is calculated from the fitted lineshape. The highly variable range and  
 2022 DAOD are due to the varying topography, aircraft banked turns over the mountains and the increasing aircraft  
 2023 altitude in successive passes over the ground track. The measured and calculated DAODs follow each other closely,  
 2024 even as they both vary rapidly during passes over the mountains. The top plot shows the CO<sub>2</sub> concentrations retrieved  
 2025 from the lidar measurements of lineshape. All points are for 10 second averages. The retrieved concentration closely  
 2026 follows the predicted column average value of 390 ppm calculated from the Atmospheric Vertical Observations of  
 2027 Carbon Dioxide in the Earth's Troposphere (AVOCET) measurements.

2029  
2030  
2031  
2032  
2033  
2034  
2035  
2036  
2037

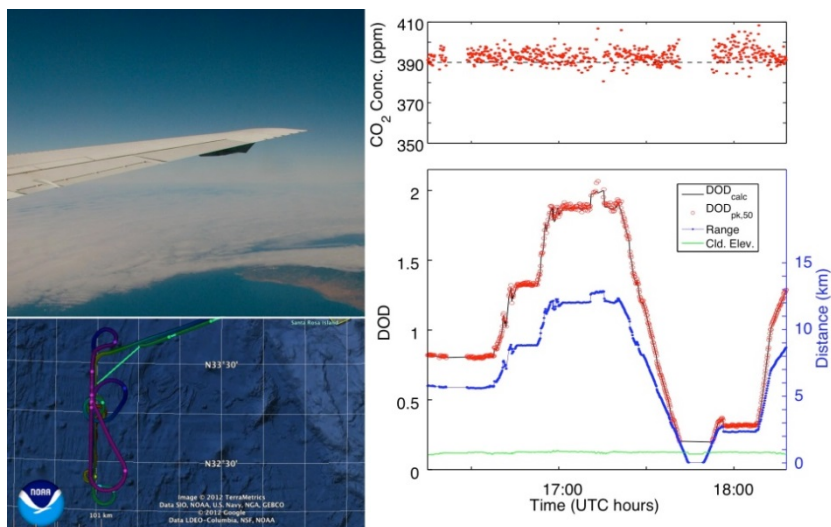


**Figure 5-8** CO<sub>2</sub> Measurements made to the tops of marine stratus clouds. (Left) The ground track of a flight made over to the top of marine stratus cloud layer over the Pacific Ocean on August 2, 2011. The laser return pulses from the top of the stratus clouds allowed accurate CO<sub>2</sub> retrieval measurements. (Right) The retrievals from the lidar’s plane-cloud column averaged CO<sub>2</sub> concentration are in very good agreement with calculated averages based measurements of outside air made by the in-situ Picarro instrument. The cloud tops vary more in range than over land and hence they slightly broaden the errors in the lidar’s measurements.

2038  
2039  
2040  
2041  
2042  
2043  
2044  
2045  
2046  
2047  
2048  
2049

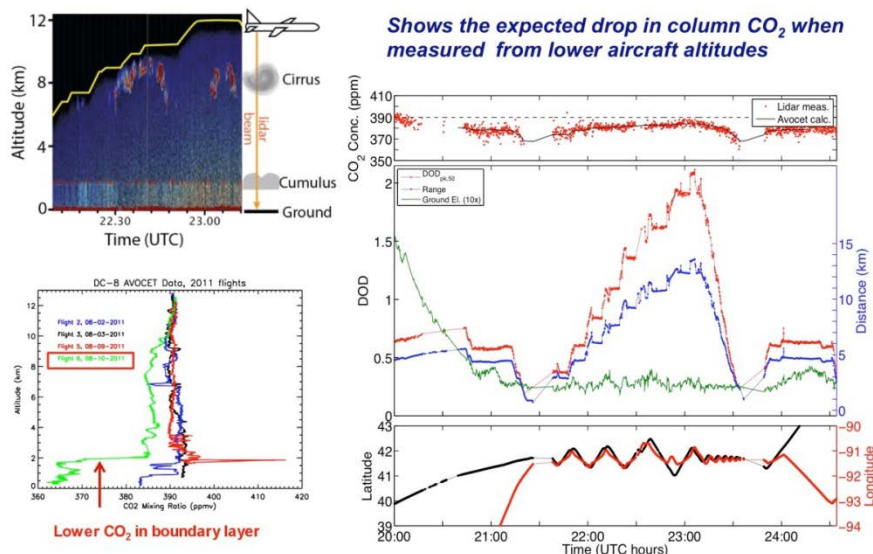
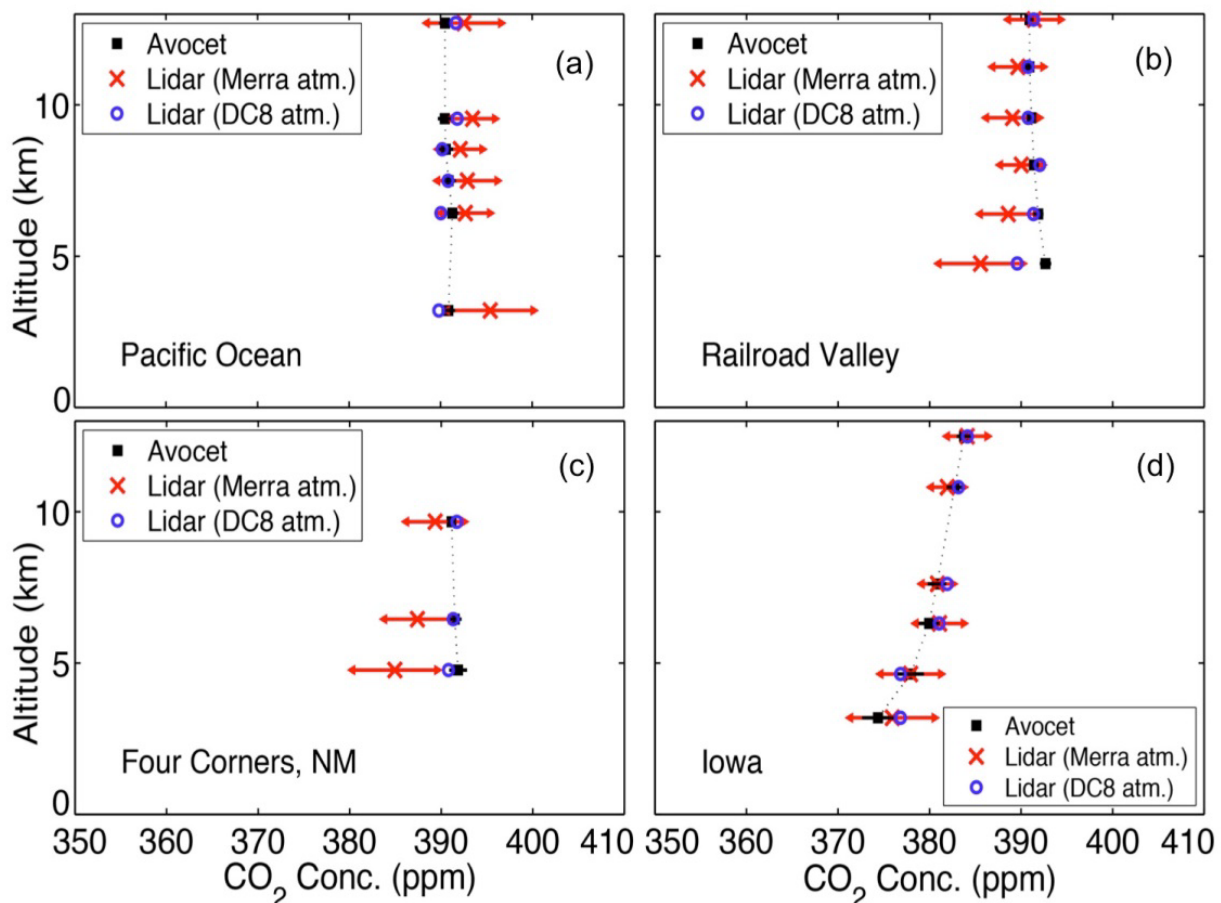


**Figure 5-9** Measurements made to the ground through thin cirrus and gaps in cumulus clouds. Data was taken on flights over Iowa on August 10, 2011. (Top Left) Color coded backscatter profiles (vertical vs time (horizontal) showing scattering from the ground, the boundary layer, cumulus cloud tops and cirrus clouds (Bottom Left) In-situ measurements of CO<sub>2</sub> concentrations for 2011 flights at spiral down locations. The Iowa flight is in green and shows significant drop in concentrations within the boundary layer, from ground to ~2 km. (Right) The retrievals from the lidar for the flight segment from Colorado to Iowa. The range to the surface is in blue, the derived surface elevation is in green, the measured DOD (pk, 50) is in red in the lower plot, and retrieved CO<sub>2</sub> concentration is in red at the top plot. The CO<sub>2</sub> drawdown in the boundary layer from the growing crops reduced the concentration in the plane-ground column compared to plane to cloud, and the draw down in clearly evident in the lidar measurements. This is important since the air in the boundary layer is the most influenced by CO<sub>2</sub> fluxes from the surface.



2050

2051

2052

2053

2054

2055

2056

2057

2058

2059

2060

2061

**Figure 5-10** Comparison of single column average retrievals from airborne lidar versus altitude. Comparison (Abshire et al., 2014) for flights above the (a) Pacific Ocean, (b) Railroad Valley, (c) Four Corners NM and (d) Iowa. The plot shows lidar retrievals using the atmospheric profiles from the MERRA model (*red*), and those using the atmosphere sampled by the DC-8 during the spiral down (*blue*), and the column average CO<sub>2</sub> values from the AVOCET in-situ sensor (*black*). The lidar measurement error bars are +/- 1 standard deviation for a 10 second average, and they apply to retrievals based on MERRA and DC-8 based atmospheres. The impact of the lower CO<sub>2</sub> concentration in the Iowa boundary layer is evident as the trend toward smaller CO<sub>2</sub> column densities for measurements made from lower flight altitudes. The lidar retrievals based on the actual atmospheric conditions measured by the DC-8 in the spiral show a close match to those measured by the in-situ sensor. The lidar retrievals based on the actual atmosphere are in quite good agreement with the in-situ measurements, and within 1.4 ppm for those made at 6 km and higher altitudes.

2062

### 5.3.1.3 Near Term Plans for the CO<sub>2</sub> Sounder

2063

2064

2065

2066

2067

2068

2069

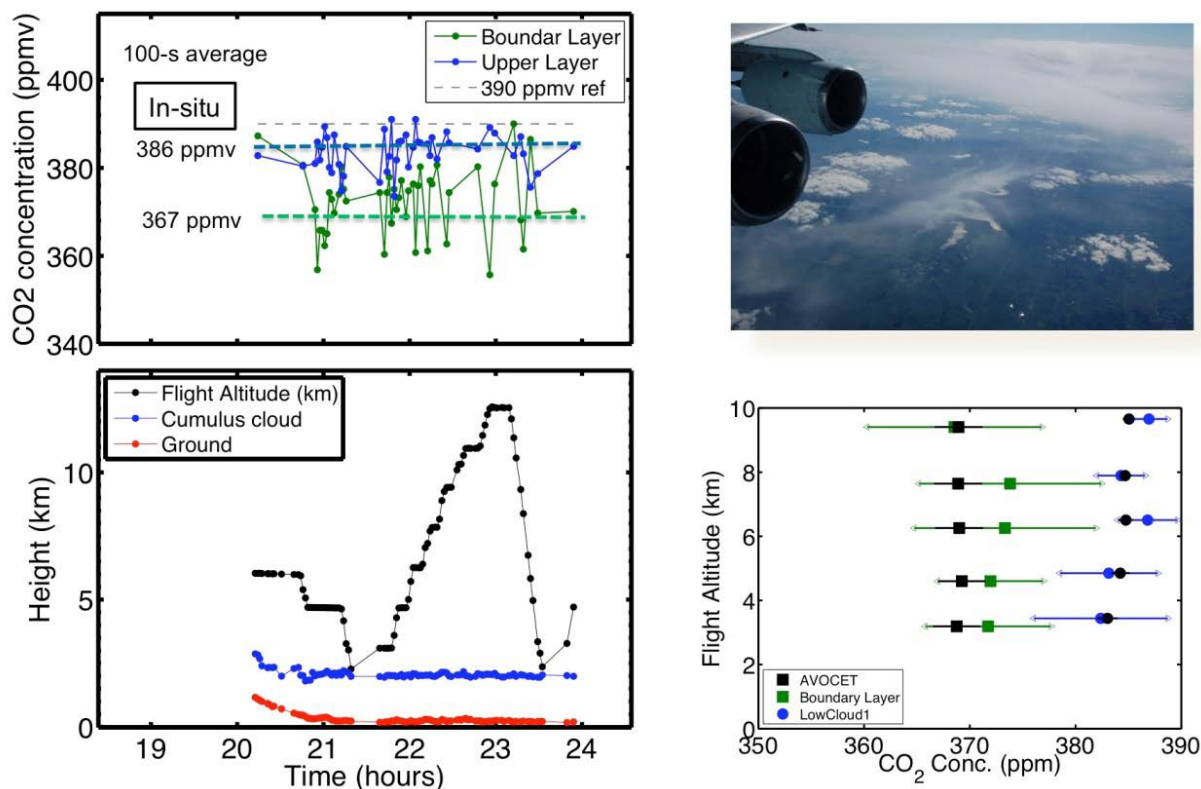
2070

2071

2072

Several components have been developed via support of the ESTO IIP-10 program in work that was conducted in parallel with demonstrating and improving the airborne lidar. These include developing a dynamically step-locked laser diode seed source for CO<sub>2</sub>, developing a power amplifier for the O<sub>2</sub> lidar, developing high sensitivity Mercury Cadmium Telluride (HgCdTe) electron Avalanche Photodiode Detector (eAPD) detector assemblies for the O<sub>2</sub> and CO<sub>2</sub> measurement channels and adding analog signal recording. The present plans are to integrate them into the airborne instrument during the spring of 2014 and demonstrate them in the flight campaigns planned for August 2014. These new components should improve the measurements of both CO<sub>2</sub> and O<sub>2</sub>. Laboratory tests show the sensitivity of HgCdTe APD detector is ~16 times higher at CO<sub>2</sub> wavelengths than the photomultiplier previously used in the airborne CO<sub>2</sub> receiver.

2073 This added sensitivity should reduce the random errors in the airborne measurements by a factor  
2074 of 4, or to  $\sim 0.5$  ppm over most land surfaces.



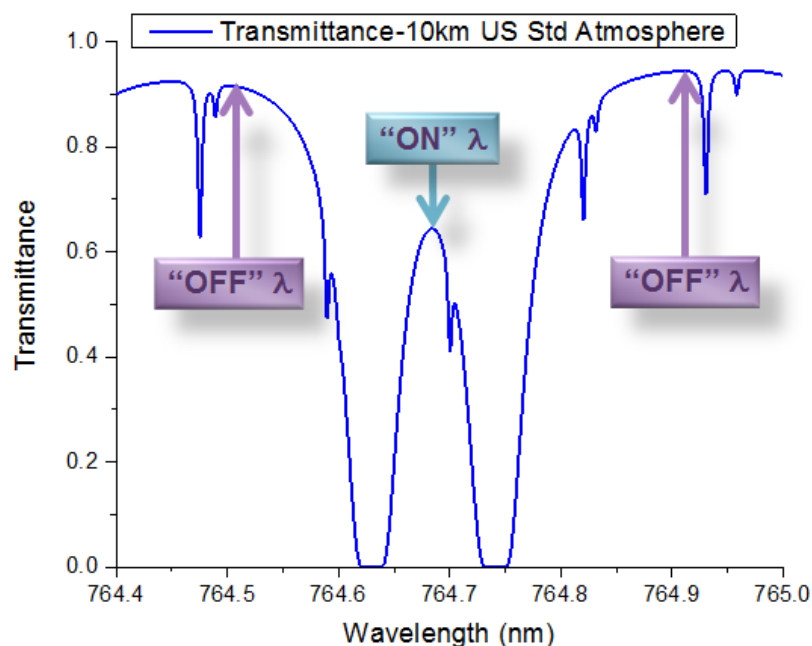
2075  
2076 **Figure 5-11** An initial example of a two-altitude level retrieval from the 2011 flight over Iowa. This demonstrated  
2077 lidar measurements to the ground and to cumulus cloud tops, or “lidar cloud slicing” (Ramanathan et al., 2015). This  
2078 approach separately solves for the best-fit CO<sub>2</sub> line shapes in the column to the ground and in the column to cloud  
2079 tops, subtracts them to infer the CO<sub>2</sub> line shape from the ground to the cloud top, and then retrieves the CO<sub>2</sub> column  
2080 in this lower column, which in this example was in the boundary layer. The demonstration showed the measurement  
2081 worked for these flights and detected the lower concentration of CO<sub>2</sub> in the boundary layer. The best performance  
2082 was from the highest aircraft measurement altitude of 9 km. The error bars in the retrieved boundary layer  
2083 concentration are larger than those for the full column, due to its smaller CO<sub>2</sub> optical depth and that it is being solved  
2084 for by differencing the two different column measurements.

### 2085 5.3.2 Pulsed IPDA Lidar for Measurements of Atmospheric Density Using the Oxygen A- 2086 Band

2087 In North America and most of Eurasia accurate estimates of the dry atmospheric column density  
2088 can be obtained from meteorological sensors and models. However, global accuracy of these  
2089 models is not sufficient to meet the ASCENDS requirements in sparsely populated areas. Since  
2090 Oxygen (O<sub>2</sub>) is a stable and uniformly mixed molecule in the atmosphere at 20.95%, the  
2091 measurement of oxygen absorption can be used to infer the dry air density of CO<sub>2</sub> provided the  
2092 water vapor mixing ratio is known or can be obtained by additional observations. Initial analysis  
2093 for our approach shows that in order to keep the XCO<sub>2</sub> error below 1 ppm, a differential optical  
2094 depth (DOD) error of  $\sim 0.2\%$  will be needed.

2095 Our approach uses the pulsed IPDA approach to measure the transmittance through the  
2096 atmospheric column of a pair of Oxygen A-band lines at 764.7 nm, as shown in Figure 5-12. As  
2097 for CO<sub>2</sub>, our technique uses multiple wavelengths to sample these lines. For the O<sub>2</sub> lines we

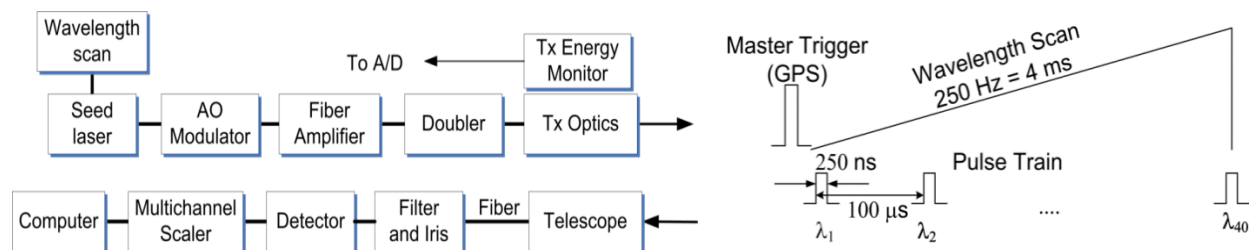
2098 selected, the peak of the absorption is optically thick (i.e. the optical depth is greater than 100 or  
 2099 the transmittance is near zero) so it is not suitable to use as an “on” wavelength. Instead, the  
 2100 trough between the two lines at 764.684 nm, which is not optically thick and it is sensitive to  
 2101 pressure changes, is used as the “on” wavelength. For the “off” wavelength we use the average  
 2102 OD value at the beginning and the end of our scan (764.5 and 764.9 nm respectively).  
 2103



2104  
 2105 **Figure 5-12** Atmospheric transmittance calculated from a 10 km altitude to the surface showing the Oxygen A-  
 2106 band absorption line at 764.7 nm based on a US standard atmosphere.

2107 Our instrument (Figure 5-13) uses a continuous wave (CW) distributed feedback (DFB) diode  
 2108 laser operating at 1529.4 nm whose current and temperature are controlled by a commercial laser  
 2109 driver. The diode laser wavelength is rapidly scanned (at 250 Hertz (Hz)) over the O<sub>2</sub> absorptions  
 2110 by applying a voltage ramp waveform to the drive current. The frequency, amplitude, and shape  
 2111 of the wavelength scan waveform are adjusted using a computer-controlled waveform generator.  
 2112 The output of the diode laser is externally modulated (chopped) with a fiber-coupled acousto-  
 2113 optic modulator (AOM) to yield relatively short (~250 ns Full Width at Half Maximum (FWHM))  
 2114 laser pulses. A master trigger, from a Global Positioning System (GPS) receiver 1 pulse per  
 2115 second (pps) signal, initiates a wavelength scan with a series of laser pulses separated by 100 μs  
 2116 (~0.011 nm) that are used to sample the oxygen absorption lines. The 100 μs time separation  
 2117 between pulses (equivalent to a range of 15 km) ensures that all wavelengths are sufficiently  
 2118 separated in time to avoid smearing due to atmospheric scattering so that only one wavelength is  
 2119 detected by the receiver at a time. Physically, the O<sub>2</sub> lidar subsystem is packaged as part of the  
 2120 CO<sub>2</sub> Sounder, shown in Figure 5.4.

2121  
 2122



2123 **Figure 5-13** Block diagram (left) and the timing sequence (right) of the O<sub>2</sub> IPDA Lidar. The optical pulses from  
 2124 the AOM are amplified by an Erbium Doped Fiber Amplifier (EDFA) and then fiber-coupled into a periodically  
 2125 poled Potassium Titanyl Phosphate (KTP) crystal assembly which frequency doubles the 1529.4 nm laser radiation to  
 2126 764.7 nm. The free-space output from the doubling crystal is directed to the transmit optics assembly and through the  
 2127 aircraft nadir port to the ground. The reflected ground returns are collected by a commercial 20 cm diameter receiver  
 2128 telescope and are fiber-coupled onto a single photon counting module. A multi-channel scaler produces a histogram  
 2129 of the return pulses as a function of time (or range) over the entire atmospheric column with a 1 second averaging  
 2130 time. The parameters of the airborne lidar are summarized in Table 5-7.

2131 **5.3.2.1 Airborne Campaigns and Data Analysis**

2132 We have demonstrated O<sub>2</sub> measurements using the multi-wavelength IPDA technique from the  
 2133 ground and from NASA’s DC-8 airborne laboratory based in Palmdale, CA. In 2010, 2011 and  
 2134 2013 we participated in a multi-instrument airborne campaign sponsored by the NASA  
 2135 ASCENDS program to measure CO<sub>2</sub> and O<sub>2</sub> fluxes in the United States.

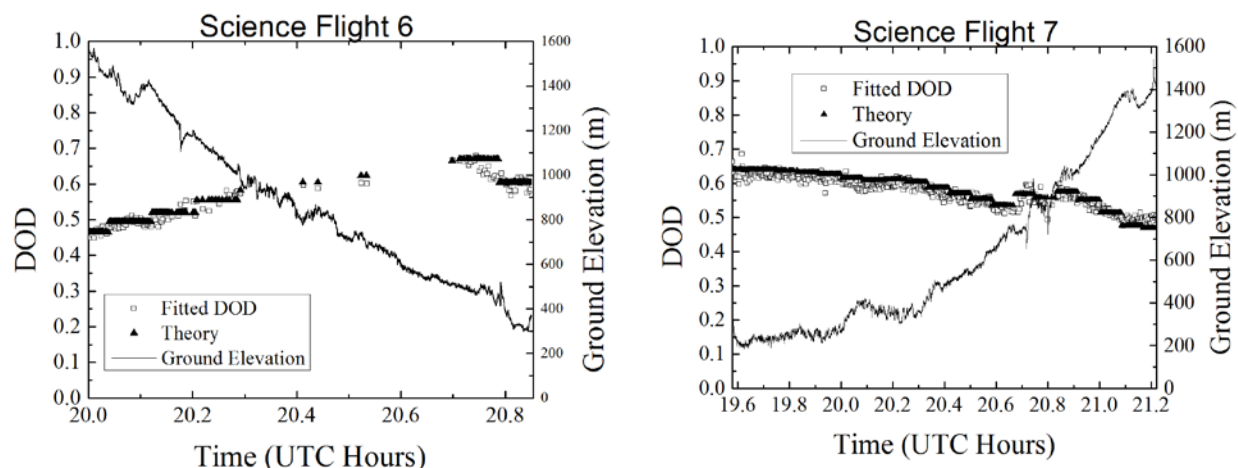
2136 **Table 5-7 O<sub>2</sub> Sounder Lidar Parameters**

Parameter	Value	Parameter	Value
Center (“on”) Wavelength	764.685 nm	Histogram Bin width	32 ns
“off” wavelengths	764.5 & 764.9 nm	Divergence	110 μrad
Pulse Rate	10 kHz	Rcvr Diameter	20 cm
Pulse Width	250 ns	Rcvr Field of view	200 μrad
Energy/pulse	~2.0 μJ	Receiver band pass	0.5 nm (FWHM)
Scan rate	250 Hz	Averaging period	1 s
Wavelength Spacing	~0.011 nm		

2137  
 2138 The flights typically included multiple segments at increasing altitudes from 3 to 13.5 km over  
 2139 varying topography, type and atmospheric conditions. In addition, for most flights, a spiral  
 2140 descent from ~13.5 km to near the surface (30-70 m) was included in the flight plan in order to  
 2141 sample vertical profiles of meteorological parameters (pressure, temperature, humidity, etc.) using  
 2142 the aircraft’s data acquisition system.

2143 Our retrieval algorithm estimates the column average O<sub>2</sub> transmittance of the atmosphere by  
 2144 integrating the pulse returns from the surface return signals at each wavelength, after normalizing  
 2145 by the transmitted pulse energy, the filter transmission, and other instrument calibrations. The

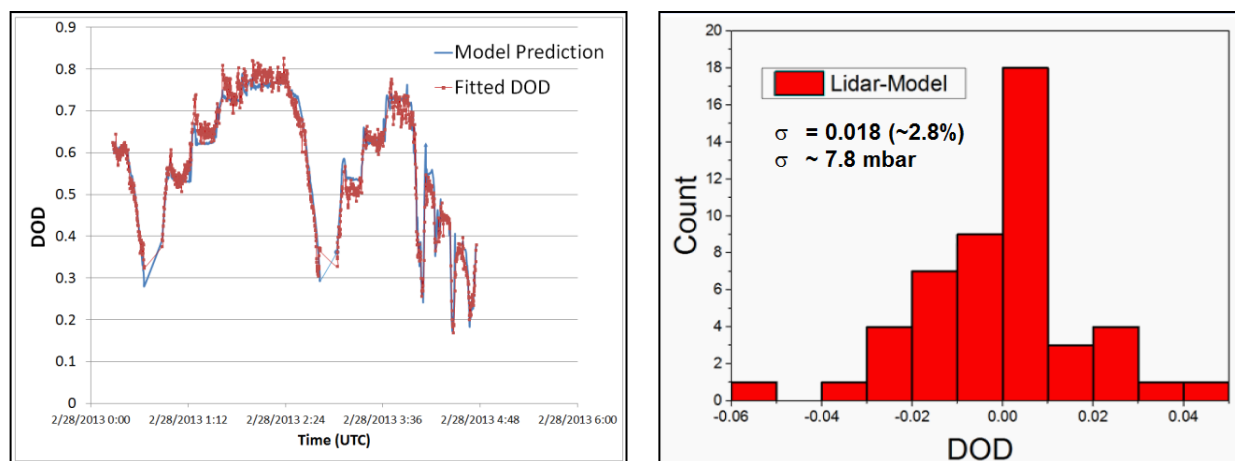
2146 algorithm then compares the experimental with the theoretically calculated transmittance values  
 2147 and adjusts the fit parameters to minimize the error. For the analysis to date, the theoretical  
 2148 calculations use a vertical profile of atmospheric information (measured during a flight segment  
 2149 or from a model) the lineshape parameters from the High Resolution Transmission (HITRAN)  
 2150 2008 database (Dufour and Bréon, 2003) and line-by-line radiative transfer calculations (ESA,  
 2151 2008). Although a Voigt profile was used for these calculations, recent spectroscopic studies  
 2152 suggest that more complex profiles and line mixing should be considered for more accurate  
 2153 retrievals (Mao et al., 2007; Kawa et al., 2010; Long et al., 2011).



2154 **Figure 5-14** Plots of the results from the O<sub>2</sub> IPDA lidar flights for 2011. Flight 6 (left) and Flight 7 (right). The plots  
 2155 show the measured DOAD (“fitted”) and those predicted DOD (“theory”) along with ground elevation, as a function  
 2156 of time of day and hence location. The flight segments traverse approximately the region between Davenport, Iowa to  
 2157 Denver, Colorado where the ground elevation changes gradually. The ground elevation was calculated from the  
 2158 aircraft radar altimeter and the GPS readings. The predicted DOD was calculated using GMAO data with 5 minute  
 2159 intervals.

2160 The range from the aircraft to the surface is determined from the laser pulse time of flight  
 2161 following the approach by (Amediek et al., 2013), correlating the first return pulse with the  
 2162 outgoing energy monitor pulse and measuring the time delay of the correlation peak. The  
 2163 meteorological data for the vertical profile of the atmosphere beneath the aircraft was obtained in  
 2164 two different ways. For flight segments near the spiral down point, it was obtained from in-situ  
 2165 measurements made from the aircraft. For flight segments distant from the spiral down points, our  
 2166 analysis used data from the Goddard Modeling and Assimilation Office (GMAO) Modern Era  
 2167 Retrospective –Analysis for Research and Applications (MERRA) along the flight paths with a  
 2168 sampling/interpolating interval of 5-minutes and using the 42 lowest atmospheric levels.

2169 For the 2011 ASCENDS campaign, Flights 6 and 7 (from Palmdale, CA to Iowa, and from  
 2170 Wisconsin and back) provided the best opportunity to test the O<sub>2</sub> lidar measurements. The  
 2171 surface elevation from central Colorado to the plains of eastern Iowa changes gradually from  
 2172 ~1600 m to ~200 m. In the absence of significant weather that can change the local  
 2173 meteorological conditions, the changes in surface elevation produce a corresponding change in  
 2174 surface pressure. Figure 5-14 shows the DOD comparison and the ground elevation change, for  
 2175 the flight segment from Davenport, Iowa to Denver, Colorado for Flights 6 and 7. The agreement  
 2176 between the O<sub>2</sub> IPDA lidar measurements of optical depth and the theoretical predictions was  
 2177 good, and the averaged lidar measurements tracked the pressure change due to the changes in  
 2178 surface elevation.



2179 **Figure 5-15** Results for the O<sub>2</sub> laser from the 2013 flight 2 over California's Central Valley. (Left) Plot of  
 2180 measured and predicted DOD versus flight time, showing they track one another over the flight altitude changes.  
 2181 (Right) The corresponding standard deviation of DOD (and pressure in the inset) for the 8 km segment of the same flight.  
 2182 The measurement precision is consistent with that expected from the low (~20 mW) average power laser  
 2183 transmitter.

2184 During the 2013 ASCENDS campaign, Flight 2 was made over California's Central Valley.  
 2185 Since the meteorological conditions did not change significantly in the Valley, the atmospheric  
 2186 data measuring during the spiral down segment of this flight provided a good representation of the  
 2187 atmosphere for the entire flight. Figure 5-15 (left panel) shows the experimental and predicted  
 2188 DOD time series. The fitted data agreed well with predictions for all flight altitudes. Using data  
 2189 from the 8 km altitude segment of the flight we estimated that the standard deviation of the fitted  
 2190 DOD minus the model (predicted) DOD values was 2.8% that is equivalent to 7.8 mbar. This  
 2191 measurement precision is consistent with that expected with low (~20 mW) average power of the  
 2192 present O<sub>2</sub> lidar transmitter.

### 2193 5.3.2.2 Summary

2194 We have demonstrated airborne IPDA lidar measurements of O<sub>2</sub> column absorption using the  
 2195 Oxygen A-band at 765 nm. Measurements were made over varying surface elevations and up to  
 2196 altitudes of 13 km. Although this version of the lidar has significant limits in laser power, the  
 2197 results from several flights show good agreement between the measured differential optical depth  
 2198 with the theoretical predictions for aircraft altitudes from 3 to 13 km. Our primary random error  
 2199 sources are the low laser signal levels and the high solar background. We expect that, with a new  
 2200 higher power laser amplifier, we will increase the average laser power by ~10 times and reduce  
 2201 the random noise component by a factor of 3. We are also in the process of increasing the  
 2202 dynamic range of our receiver by increasing the number of Single Photon Counting Module  
 2203 (SPCM) detectors.

### 2204 5.3.2.3 Near-Term Plans for O<sub>2</sub> Lidar

2205 In work being conducted in parallel with the airborne lidar, several new components for the O<sub>2</sub>  
 2206 lidar are being developed as part of the ESTO Instrument Incubator Program (IIP)-10 program.  
 2207 These include new a power amplifier for the O<sub>2</sub> lidar, improving the O<sub>2</sub> detector's dynamic range,  
 2208 and adding analog signal recording to increase the receiver's dynamic range. The present plans  
 2209 are to integrate these improvements into the airborne instrument and to demonstrate them in the

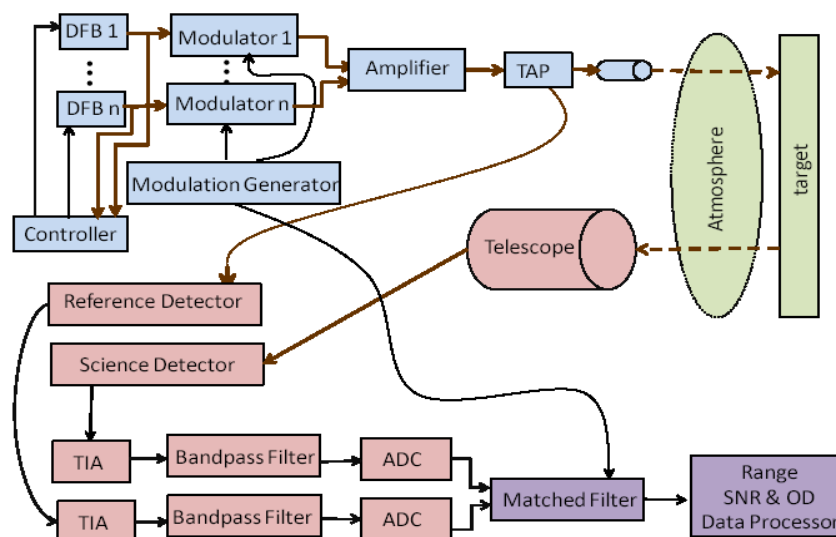
2210 summer 2014 ASCENDS flight campaigns. These new components are expected to increase the  
2211 O<sub>2</sub> measurement precision by a factor of 3 or more.

### 2212 5.3.3 Overview of the IM-CW Measurement Approach

2213 The NASA Langley Research Center (LaRC) in collaboration with ITT Exelis, Inc. (Exelis) has  
2214 been developing and testing advanced lidar technologies for application to the ASCENDS space  
2215 mission. The critical aspect of these activities is the development of a prototype Intensity-  
2216 Modulated Continuous-Wave (IM-CW) Laser Absorption Spectrometer (LAS) for high-precision,  
2217 CO<sub>2</sub> column mixing ratio (XCO<sub>2</sub>) measurements using the Integrated Path Differential Absorption  
2218 (IPDA) approach. Airborne flight campaigns demonstrate that the CO<sub>2</sub> measurements of the  
2219 current IM-CW LAS systems meet the accuracy and precision requirements of the ASCENDS  
2220 mission. Also, model simulations have shown that this IM-CW LAS technology and approach  
2221 can be used for the space ASCENDS mission to reach its science goals.

2222 The first IM-CW LAS system, called the Multifunctional Fiber Laser Lidar (MFLL) and  
2223 developed by Exelis (Dobbs et al., 2007, 2008; Dobler et al., 2013), demonstrated the capability  
2224 of CO<sub>2</sub> column measurements from several aircraft under a variety of atmospheric and surface  
2225 conditions (Browell et al., 2008, 2009a, 2009b, 2010, 2012; Dobler et al., 2013). More recently,  
2226 MFLL has been modified to measure O<sub>2</sub> column amounts. O<sub>2</sub> column amounts are used to  
2227 retrieve the surface dry-air pressure which is needed in the calculation of XCO<sub>2</sub> from CO<sub>2</sub> column  
2228 amounts. Extensive demonstrations of this capability were conducted in laboratory and horizontal  
2229 ground test range environments and in flight campaigns. The MFLL CO<sub>2</sub> column measurements  
2230 over desert and vegetated surfaces are found to agree with those calculated from in-situ  
2231 measurements of atmospheric meteorological and CO<sub>2</sub> profiles to within an average of 0.17% or  
2232 ~0.65 ppmv. A measurement precision of ~0.3 ppmv for a 10-s average over these surfaces has  
2233 also been achieved (Browell et al., 2009a, 2009b; Dobler et al., 2013).

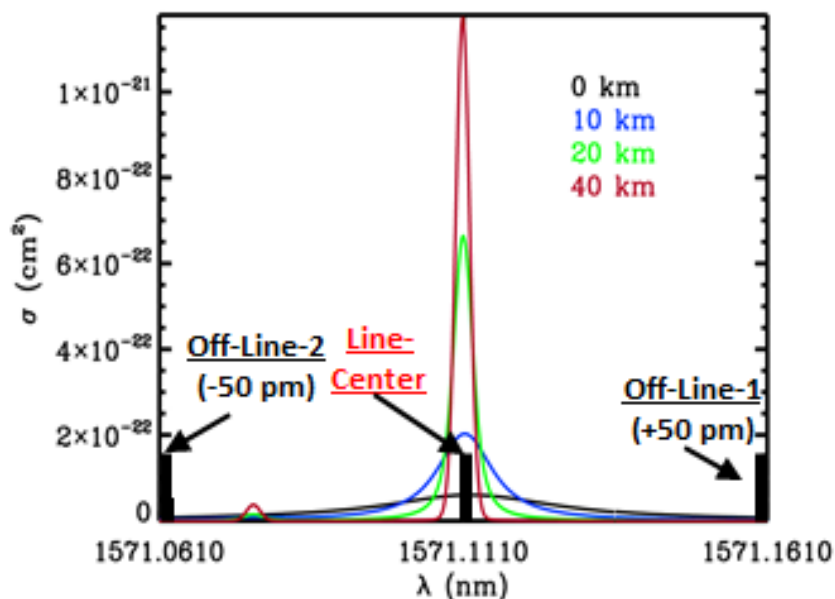
#### 2234 5.3.3.1 Basic Characteristics of IM-CW LAS System



2235  
2236 **Figure 5-16** Architecture of the airborne prototype MFLL lidar.

2237 The lidar discussed here is based on the airborne prototype LAS system, MFLL (Dobbs et al.,  
2238 2007, 2008; Dobler et al., 2013; Lin et al., 2013). Figure 5-16 shows the lidar design.

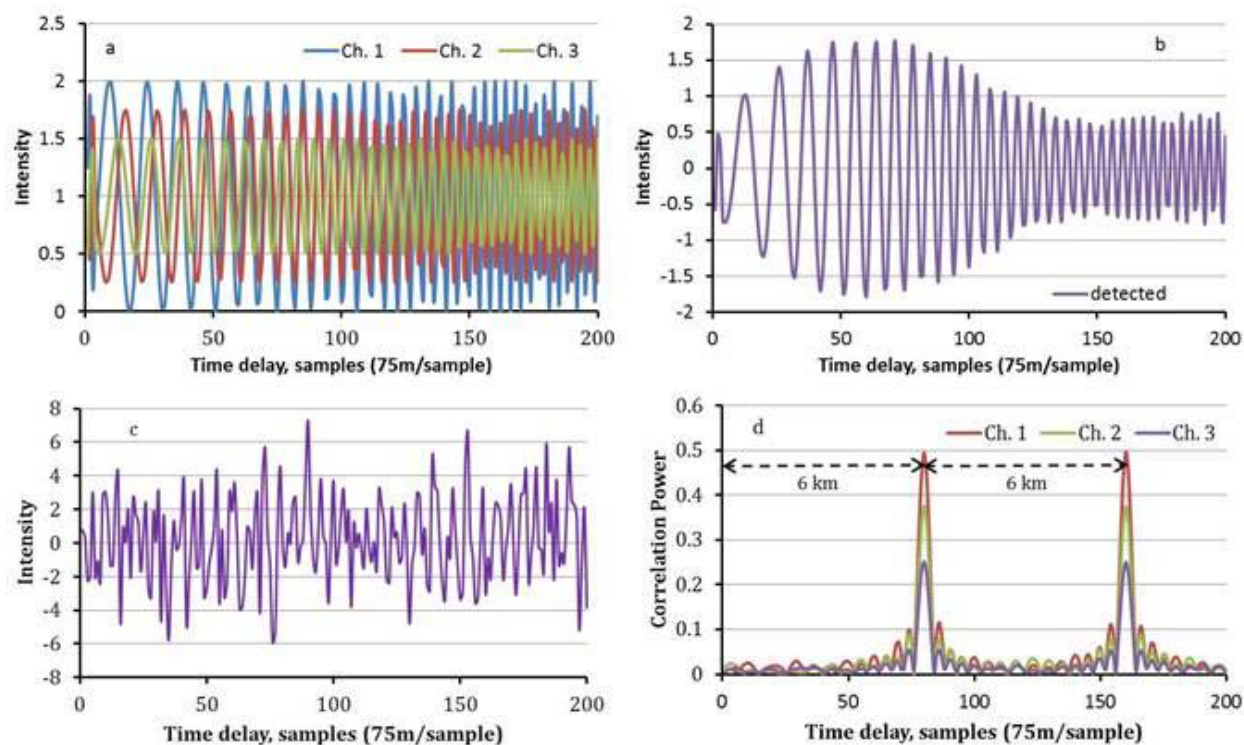
2239 The LAS system incorporates CO<sub>2</sub> and O<sub>2</sub> laser transmitters, a receiving telescope, a data  
 2240 acquisition system, and a signal-processing unit. The CO<sub>2</sub> and O<sub>2</sub> subsystems are all similar in  
 2241 form and function except they use a 5-W Erbium-Doped Fiber Amplifier (EDFA) and a 1.6-W  
 2242 fiber Raman amplifier (Dobler et al., 2011), respectively. The CO<sub>2</sub> subsystem has one laser  
 2243 wavelength positioned at the center of the CO<sub>2</sub> absorption line at 1571.112 nm (“online”) and two  
 2244 other laser wavelengths in the distant wings of the absorption line at offsets of ±50 pm  
 2245 (“offlines”) for the CO<sub>2</sub> IPDA measurements, as shown in Figure 5-17. Additional lasers  
 2246 operating at an online of 1262.531 nm and an offline of 1262.578 nm are used for O<sub>2</sub> IPDA  
 2247 measurements. All the CO<sub>2</sub> and O<sub>2</sub> wavelengths were selected to minimize water vapor and other  
 2248 trace gas interference effects on the IPDA measurements and to simultaneously maximize the  
 2249 signal-to-noise ratio (SNR) of the differential absorption optical depth (DAOD) measurements  
 2250 (Ismail and Browell, 1989; Remsberg and Gordley, 1978). Other major considerations in the  
 2251 laser line selection include the altitude-dependent gas absorption weighting function; the DAOD  
 2252 sensitivity to knowledge of the laser wavelength and line-width; and the wavelength stability of  
 2253 the laser spectra (Menzies and Tratt, 2003; Ehret et al., 2008; Kameyama et al., 2010; Lin et al.,  
 2254 2013).



2255  
 2256 **Figure 5-17** The wavelength sampling approach for the airborne MFL lidar and the altitude dependence of the  
 2257 CO<sub>2</sub> absorption cross section ( $\sigma$ ).

2258 An essential capability to achieve high accuracy XCO<sub>2</sub> measurements is to apply a range-encoded  
 2259 intensity-modulation technique to the IM-CW lidar system for CO<sub>2</sub> and O<sub>2</sub> column measurements  
 2260 and range determination. The use of range encoding with a phase sensitive detection subsystem  
 2261 clearly discriminates the magnitude and timing/range of laser signals reflected from surface  
 2262 against those from other intermediate backscatters. A commonly used technique in the detection  
 2263 subsystem for the signal discrimination is a matched filter that correlates the range-encoded  
 2264 modulation waveforms with the recorded signals. Figure 5-18 illustrates the modeled capability  
 2265 of a range-encoded IM system using a swept frequency technique with three measurement  
 2266 channels. The illustration is for an idealized case of a target at 12-km range with an intermediate  
 2267 backscatterer at 6 km to represent the presence of a cloud/aerosol layer. Fractional intensity units

2268 are used as the return power is normalized by the output power. The DC components for all  
 2269 signals were removed after the detector. The sampling rate, swept frequency bandwidth of the IM  
 2270 waveform, and unambiguous range (UR) are set to be 2 MHz, 500 KHz and 15 km, respectively,  
 2271 which are consistent with current airborne systems. The sampling rate and UR lead to a 75-m  
 2272 range per sample and 200 samples per IM cycle, respectively. Although the range sampling rate is  
 2273 75 m, considerably smaller range errors of about 3 m can be achieved by applying curve-fitting  
 2274 techniques to the shape of correlation power of the matched filter outputs. The IM bandwidth  
 2275 dictates the sharpness of the main-lobe peaks of the correlation power of the matched filter.



2276  
 2277 **Figure 5-18** Sample laser signals detected by the airborne MFLL lidar.

2278 In Figure 5-18, Panel A shows the individual laser signals that are combined to yield the  
 2279 modulated signal shown in panel b. The beat frequencies among the three channels are clearly  
 2280 shown in the variations of the signal power with the time delay due to the IM scheme used. The  
 2281 detector receives the combined signal, including noise, and this is then passed through an  
 2282 electronic bandpass filter to reduce background noise and to avoid spectral aliasing. The  
 2283 bandpass filter also removes the DC component of the signal. To show the importance of  
 2284 intermediate scatterers, the received signal power from the intermediate scatterer is assumed to be  
 2285 equal to that of the target, and the noise level is as high as the return signal power from both  
 2286 scatterers. Compared to candidate IM waveforms (panels a & b), the signature of the received  
 2287 signal (panel c) appears to be very weak due to 3 channel signal mixing, a combination of signals  
 2288 from target and intermediate backscatter with different time delays, and noises. Even in this case,  
 2289 the matched filter technique with 0.1-s integration period clearly demonstrates the capabilities of  
 2290 detecting weak target signals and minimizing the effects of intermediate scatterers and noise. The  
 2291 outputs of the matched filter show two distinct correlation peaks corresponding to the target and  
 2292 intermediate scatterer (panel d). The wider the IM bandwidth, the narrower the peaks and the  
 2293 easier it is to differentiate between two closely spaced scattering objects. Besides the detection of

2294 target signals, panel d also illustrates that the target range can be estimated by measuring the time  
2295 delay of the peak power of the target or intermediate reflection. The range capability and CO<sub>2</sub>  
2296 column measurements to both surface and cloud tops under cloudy conditions are clearly  
2297 illustrated by this figure.

2298 The panels show: a) Range-encoded lidar signals from the target without noises for individual  
2299 channels coming onto detector; b) The intensity modulated lidar signals of the three channels  
2300 produce a single time series at the detector; c) Recorded lidar return, which is a combination of  
2301 lidar signals from the target and intermediate backscatterer as well as of all noises; d) Lidar signal  
2302 power as a function of range obtained by the correlation of the matched filter of lidar system.

2303 A photograph of the MFLL lidar onboard the NASA DC-8 aircraft is shown in Figure 5-19. The  
2304 onboard data processing and onboard display unit, detection system, and CO<sub>2</sub> transmitter  
2305 subsystems are in the front while the O<sub>2</sub> subsystems are in the two racks in the back. The  
2306 telescope and transmit optics are housed under the black laser curtain in the middle. Table 5-8  
2307 lists the key parameters of the lidar system. The CO<sub>2</sub> and O<sub>2</sub> subsystems of the LAS have been  
2308 implemented using similar IM-CW techniques that include both sine wave and rolling tone  
2309 frequencies, and more recently a swept frequency IM approach. The swept frequency IM provides  
2310 ranging and capabilities to discriminate clouds and aerosols. After the receiver and data  
2311 acquisition subsystems record lidar return signals, a matched filter that correlates the transmitted  
2312 IM waveforms with the received IM waveforms reflected from the surface and clouds. The  
2313 location and magnitude of correlation peak power values are estimated from the matched filter  
2314 output. The peak magnitudes of individual channels are proportional to the powers received for  
2315 their corresponding channels and used in the retrievals of CO<sub>2</sub> and O<sub>2</sub> column amounts. Thus,  
2316 they lead to the calculation of the two DAOD values, while the location of the peaks and shape of  
2317 the entire correlation functions are used to determine the range. From flight campaign and range  
2318 testing, the accuracy and precision of the calculated range was found to be better than 3 m (Dobler  
2319 et al., 2013; Lin et al., 2013) that is equivalent to a XCO<sub>2</sub> error of about 0.12 ppmv. Details on  
2320 the instrument and data processing can be found in Dobler et al. (2013) and Lin et al. (2013).

2321



2322

2323 **Figure 5-19** Photograph of the MFLL lidar mounted inside the NASA DC-8 aircraft.

2324

**Table 5-8 Airborne MFL LIDAR Parameters**

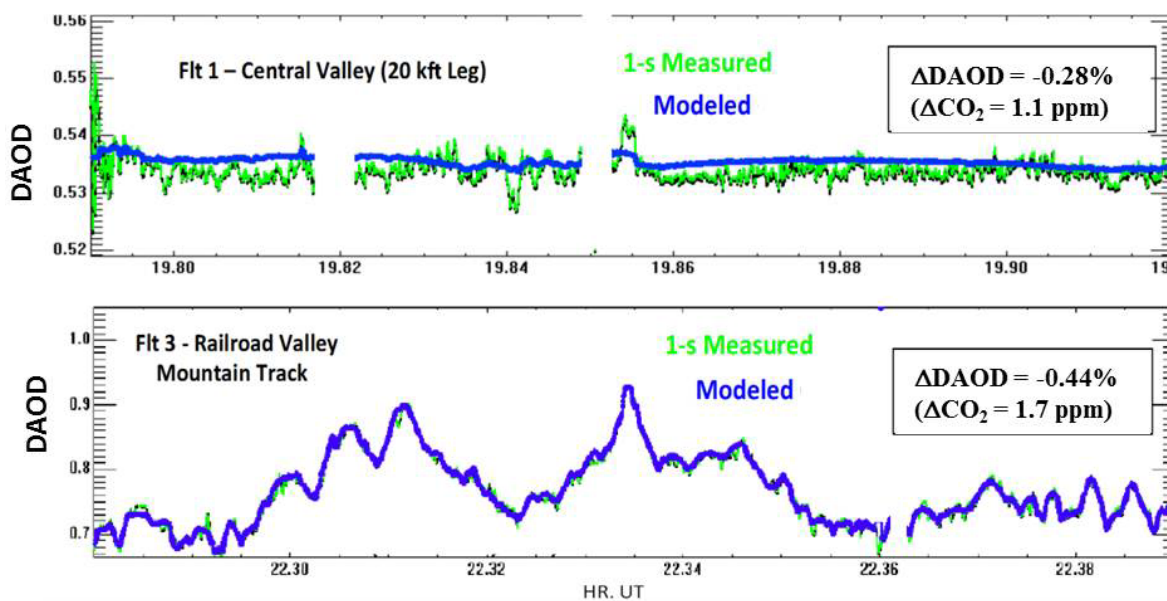
Airborne MFL LIDAR Parameters	
Seed laser type:	DFB diode laser
Line width	< 6 MHz each wavelength
Side mode suppression	Ratio > 45 dB
CO <sub>2</sub> lines: (vacuum)	1.571112 μm (On), 1.571061 μm (Off 1), 1.571161 μm (Off 2)
O <sub>2</sub> lines: (vacuum)	1.262531 μm (On), 1.262578 μm (Off)
Modulator:	Semiconductor Optical Amplifier
Modulation type:	Intensity-modulated continuous-wave (IM-CW)
Optical amplifier:	CO <sub>2</sub> : EDFA, O <sub>2</sub> : Raman Amplifier
Output power:	5 Watts for CO <sub>2</sub> ; 1.6 Watts for O <sub>2</sub>
Optical bandpass filter:	2.4 nm
Telescope	Cassegrain, 8 in. diameter.
Receiver optical throughput	8.5%
Detectors	DRS; HgCdTe APD gain: ~940; Excess noise factor ~1.3, 77 K as operated
Transimpedance amplifier	Gain: 10 <sup>6</sup>
Sample rate of digitizer	2 MHz
Encoding scheme:	Swept-frequency; ~350 ± 250 KHz; Rolling tone; ~50 ± 3 KHz
Max unambiguous range:	15-km (or 200 samples); 30-km (or 400 samples)
Laser divergence angle:	190 urad (half angle)
Receiver FOV:	240 urad (half angle)
Receiver duty cycle:	100%
Reporting interval:	100 msec (10 Hz)

2325

2326 **5.3.3.2 Approach for Determining CO<sub>2</sub> Column Differential Absorption Optical Depth**

2327 To evaluate the accuracy and precision of the MFL remotely-sensed CO<sub>2</sub> column measurements,  
2328 actual CO<sub>2</sub> DAOD values are needed. These DAOD values are derived based on the knowledge

2329 of the in-situ observed vertical profiles of XCO<sub>2</sub> and meteorological conditions; the altitude- and  
 2330 meteorologically-dependent spectroscopy of CO<sub>2</sub> and interfering gases, such as water vapor; the  
 2331 path length from the aircraft to the surface; and the off-nadir pointing of the laser beam (Browell  
 2332 et al., 2008, 2009, 2010, 2012; Dobler et al., 2013; Lin et al., 2013). High-quality in-situ  
 2333 measurements of XCO<sub>2</sub> (Choi et al., 2008; Vay et al., 2003), temperature (T), pressure (P), and  
 2334 relative humidity (q) profiles and other meteorological conditions were obtained from onboard  
 2335 instruments during aircraft spirals and collocated with contemporaneous radiosonde launches. A  
 2336 laser altimeter was also included as a part of the MFL suite of subsystems to make an  
 2337 independent measurement of the range to the surface or cloud tops. A GPS receiver and the  
 2338 aircraft navigation system provided additional aircraft location including altitude and attitude  
 2339 information. Comparisons of MFL and in-situ-derived DAOD values were typically limited to a  
 2340 horizontal distance of less than 10 km of the aircraft spiral and radiosonde comparison locations.  
 2341 When multiple in-situ spirals were conducted during a flight, the spiral data corresponding to the  
 2342 closest MFL overpass time was used.



2343  
 2344 **Figure 5-20** Comparison of airborne measured and modeled CO<sub>2</sub> DAODs. The figure shows flights over  
 2345 California's Central Valley (top) and the Rocky Mountains (bottom) in route to Railroad Valley, NV.

### 2346 5.3.3.3 Airborne CO<sub>2</sub> Column Measurements

2347 The LaRC ASCENDS team conducted a total of 13 flight campaigns with various aircraft such as  
 2348 NASA UC-12 and DC-8 since May 2005 to evaluate the capability in making remote CO<sub>2</sub> and  
 2349 XCO<sub>2</sub> column measurements for the ASCENDS mission. Accurate CO<sub>2</sub> column measurements  
 2350 have been demonstrated by these comprehensive aircraft flight tests. For example, 1-s averaged  
 2351 CO<sub>2</sub> column measurements over desert regions resulted in high precision measurements with  
 2352 SNR of DAOD (SNR<sub>DAOD</sub>) higher than 600 (Browell et al., 2012; Dobler et al., 2013). Figure 5-  
 2353 20 shows two comparison examples of 1-s MFL CO<sub>2</sub> DAOD measurements and in-situ-derived  
 2354 (modeled) values in drastically different geographic regions.

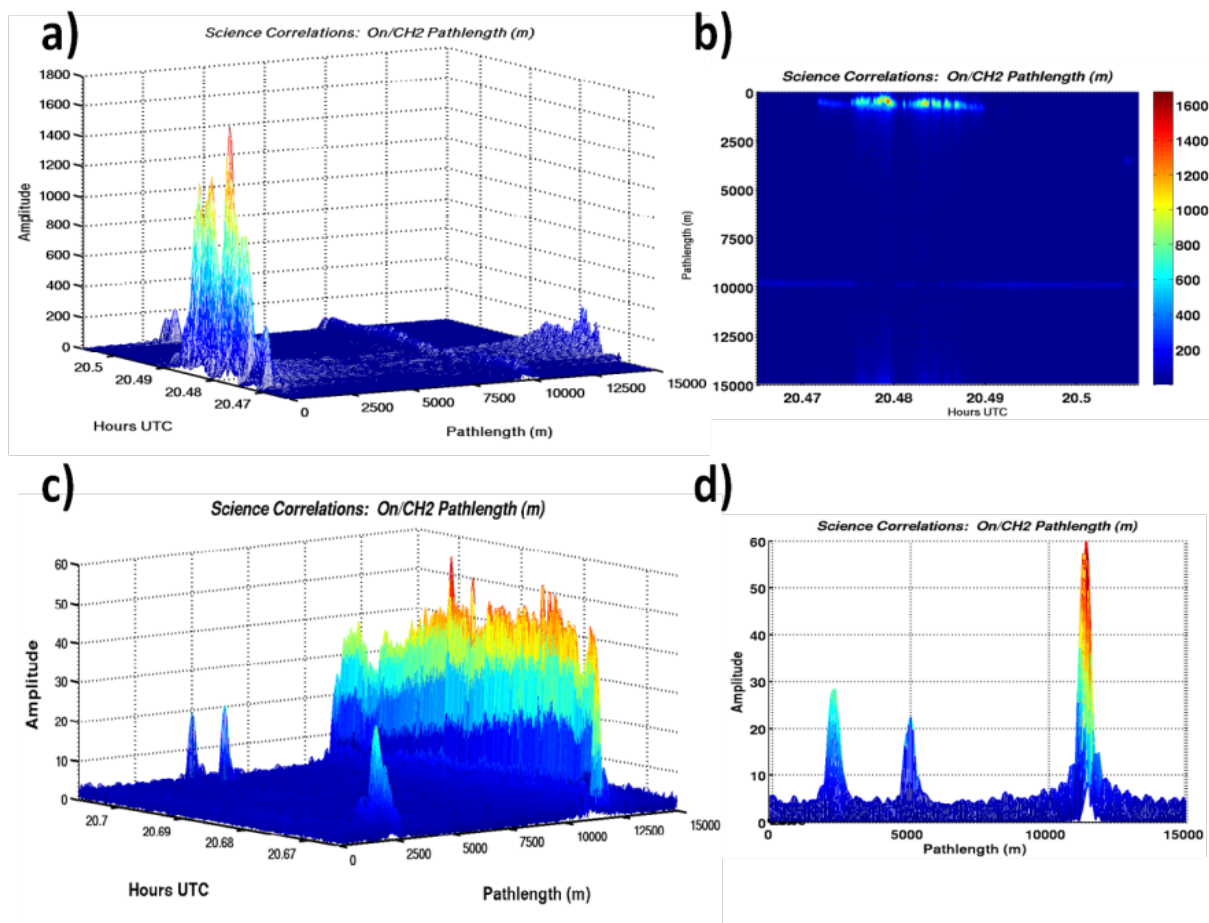
2355 The top panel of Figure 5-20 shows the CO<sub>2</sub> measurements on a constant altitude flight leg over  
 2356 the Central Valley, CA in comparison to modeled DAOD values derived from in-situ CO<sub>2</sub> data of  
 2357 a DC-8 spiral at the center of the leg and radiosonde data obtained within about 1 hour of the

2358 over-flight. The small variations in the in-situ-derived (i.e., modeled) DAOD across the flight leg  
2359 were due to small changes in the range from the aircraft to the surface. The resulting difference  
2360 of 1-s averages between the measured and modeled DAOD values on the Central Valley flight leg  
2361 was found to be -0.28% or the equivalent of  $\sim 1.1$  ppmv. The bottom panel shows the DAOD  
2362 comparison while transiting across the Rocky Mountains. The in-situ data (spiral and radiosonde)  
2363 came from Railroad Valley, NV, and the variation in DAOD values across the mountains was  
2364 almost entirely due to surface elevation changes as the aircraft was at a constant altitude. The  
2365 comparison of 1-s measured and modeled DAOD values demonstrated a high level of agreement  
2366 ( $\Delta$ DAOD = -0.44% or  $\sim 1.7$  ppmv) even when one expects some change in CO<sub>2</sub> across the  
2367 mountains that could not be captured in the modeled DAOD due to the lack of in-situ data. Flight  
2368 tests of the current LAS instrument have demonstrated very high-precision CO<sub>2</sub> DAOD  
2369 measurements ( $\text{SNR}_{\text{DAOD}} > 1300$ ) with a 10-s averaging interval (Browell et al., 2012; Dobler et  
2370 al., 2013).

#### 2371 **5.3.3.4 Surface Reflectance, Thin Cloud Discrimination, and Range Measurements**

2372 Since variations in surface types and reflectance can significantly affect lidar return powers and  
2373 thus CO<sub>2</sub> column retrievals, different surface conditions were analyzed from MFL data.  
2374 For farm fields and deserts, moderate to high reflectance values were observed, and strong signals  
2375 for CO<sub>2</sub> column retrievals were received. For some surfaces especially snow, ice, and rough  
2376 water surfaces, very low reflectance was expected and was observed. From MFL data, the  
2377 measured surface reflectance of snow and ice was as low as about 0.02/sr. Fresh snow (less than  
2378 1-2 days old) was found to have even significantly lower reflectance (about  $\sim 0.01$ /sr). Even in  
2379 these low reflectance cases, MFL received enough backscattered signal for CO<sub>2</sub> column  
2380 retrievals from high altitude flight legs. The variability in the surface reflectance for complete  
2381 snow covered terrain was found to be relatively homogeneous, however the magnitude of the  
2382 surface reflectivity for both snow covered mountainous and farmland terrain was observed to vary  
2383 by more than an order of magnitude over distances of less than 10-20 meters from the nominal  
2384 snow and ice surface reflectance values.

2385 In addition to surface types, the presence of thin clouds and aerosol layers are an important factor  
2386 that can affect the accuracy of CO<sub>2</sub> and O<sub>2</sub> column measurements. The capability for  
2387 discrimination of cloud returns from ground returns is achieved using the swept frequency IM-  
2388 CW approach as shown in Figure 5-21. The data were obtained from the DC-8 flight on 04  
2389 August 2011 over Railroad Valley, NV. Distinct altitudes and reflectances of the surface and  
2390 clouds were clearly derived from the swept-frequency measurements. The presence of  
2391 intermediate thin clouds and aerosols will definitely reduce the lidar return signals and likewise  
2392 reduce the precision of CO<sub>2</sub> column estimates, but the CO<sub>2</sub> measurements will still satisfy the  
2393 mission requirements when cloud attenuation scaling is considered (c.f., Section 1.2, R-3; Lin et  
2394 al. 2013). Ranging accuracies of about 3 m for these surfaces and clouds have also been achieved  
2395 (Dobler et al. 2013; Lin et al. 2013).



2396  
2397  
2398

**Figure 5-21** Range discrimination of cloud returns from ground returns using the swept frequency IM-CW approach.

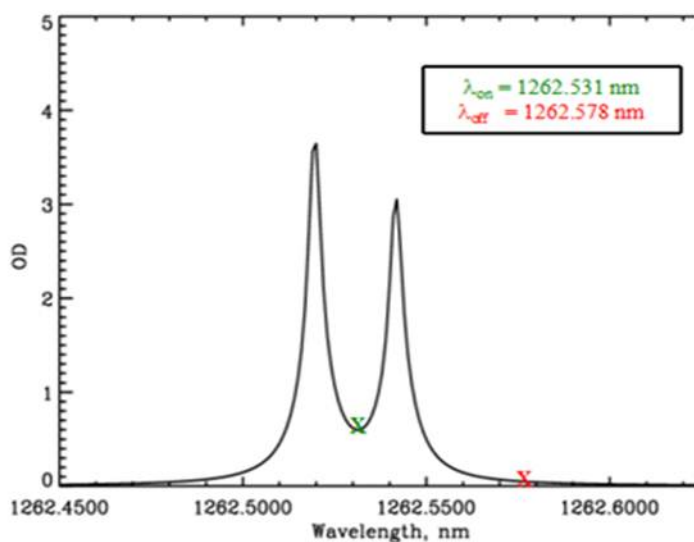
2399 Panels a) and b) show 3-D and 2-D, respectively, representation of a large cloud return above a  
2400 small ground return; panel c) shows the distribution of signals from weak clouds and strong  
2401 ground return signals, and panel d) is a superposition of data from c) on a signal vs. path length.

### 2402 5.3.3.5 Airborne O<sub>2</sub> Column Measurements

2403 The capability to measure O<sub>2</sub> column amounts was added to MFL for the 2011 flight campaign.  
2404 O<sub>2</sub> column amounts are needed to determine surface dry air pressure and then to calculate XCO<sub>2</sub>  
2405 from CO<sub>2</sub> column amounts. The spectral lines in the 1.26- $\mu$ m O<sub>2</sub> absorption band are selected for  
2406 IPDA measurements of O<sub>2</sub> column. The O<sub>2</sub> IPDA lidar operates with the same IM-CW LAS  
2407 approach as the CO<sub>2</sub> instrument on the MFL. The major difference is that the O<sub>2</sub> lidar uses a  
2408 low-power 1.6-W fiber Raman amplifier rather than an EDFA to amplify the combined O<sub>2</sub> on-line  
2409 and off-line laser signals at 1.26  $\mu$ m before transmission. Figure 5-22 shows the placement of on-  
2410 line and off-line laser beams transmitted with respect to the O<sub>2</sub> absorption lines used in the MFL  
2411 IPDA O<sub>2</sub> measurements. The key line parameters of the 1.26  $\mu$ m O<sub>2</sub> absorption lines are  
2412 summarized in Table 5-9.

2413 The 2011 flight campaign provided the proof of concept demonstration of the O<sub>2</sub> lidar subsystem  
2414 and utilized a standard PIN diode as the detector. The low gain of the PIN detector and low  
2415 transmitted power at the O<sub>2</sub> wavelengths resulted in lower O<sub>2</sub> SNR<sub>DAOD</sub> than that for CO<sub>2</sub>

2416 SNR<sub>DAOD</sub> during the same measurement period. The PIN detector was replaced by the DRS  
 2417 HgCdTe APD detector cited in Table 5-8 during the March 2013 DC-8 flight campaign. A rolling  
 2418 tone modulation scheme was used for O<sub>2</sub> transmitted laser beams during the 2011 campaigns.  
 2419 This modulation scheme had four discrete frequencies in the 50-kHz region and allowed  
 2420 independent detection and discrimination of the O<sub>2</sub> on-line and off-line backscatter signals.  
 2421 During the 2013 campaign, the swept frequency IM scheme was used. Besides the CO<sub>2</sub> and O<sub>2</sub>  
 2422 lidars, a Pseudorandom Noise (PN) code laser altimeter was used during the flight campaigns to  
 2423 determine the reference range to compare to the swept-frequency-derived range.



2424  
 2425 **Figure 5-22** Calculated spectral profile of the O<sub>2</sub> absorption line doublet at 1262.52195 and 1262.5416 nm (c.f.,  
 2426 Table 5-9) and the spectral locations of the on- and off-line laser beams.

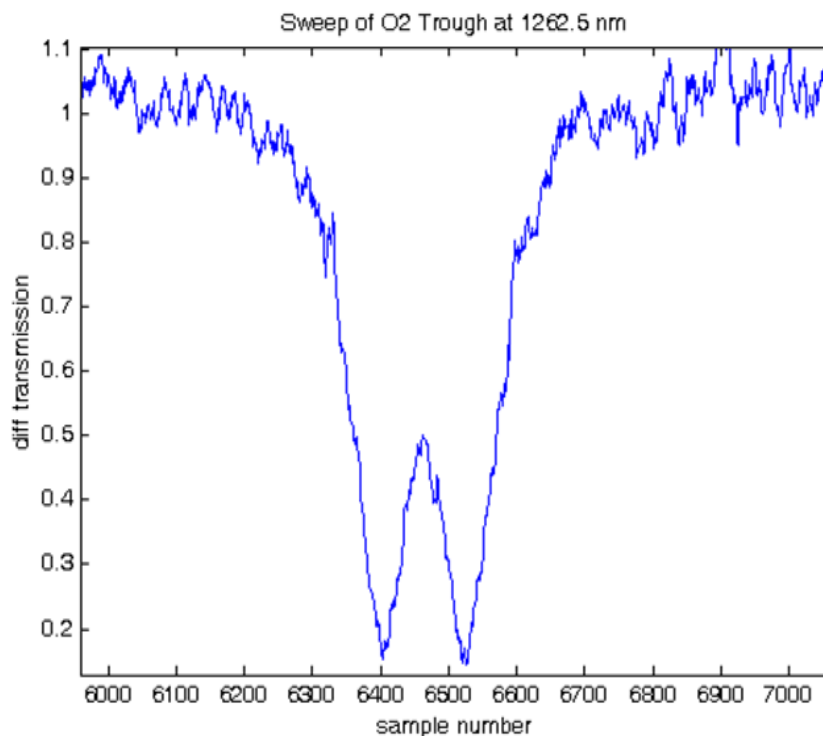
2427 The plotted values represent the vertically integrated optical depth (OD) of the O<sub>2</sub> absorption  
 2428 lines.

2429 **Table 5-9 Line parameters of the O<sub>2</sub> absorption lines**

	Line center (μm)	ID	Line strength (cm/mol.)	Linewidth (cm <sup>-1</sup> )	Energy of lower state (E'') (cm <sup>-1</sup> )
O <sub>2</sub> (1)	1.2625195	RQ5	4.99E-26	0.047	260.50
O <sub>2</sub> (2)	1.2625416	SR5	4.63E-26	0.052	42.224

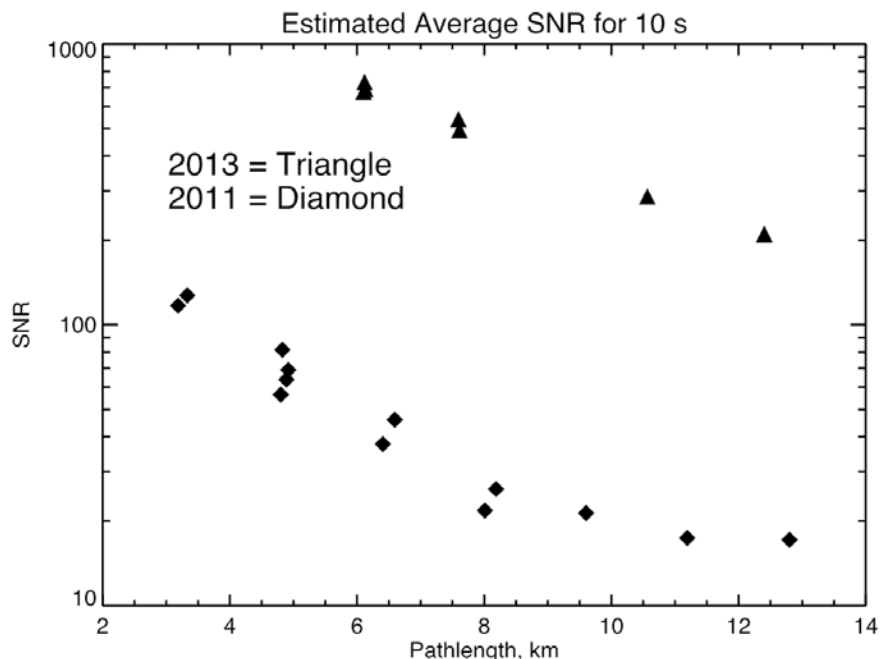
2430  
 2431 Figure 5-23 shows a rapid spectral scan of the O<sub>2</sub> doublet measured from 6-km altitude on 7  
 2432 August 2011 with approximately the same spectral coverage as the O<sub>2</sub> doublet spectra shown in  
 2433 Figure 5-22. It illustrates the ability to tune across the absorption feature resulting from the O<sub>2</sub>  
 2434 absorption lines with high spectral resolution (Browell et al., 2012). Column O<sub>2</sub> optical depths  
 2435 were calculated using the IPDA approach, and Figure 5-24 shows the variation of O<sub>2</sub> SNR<sub>DAOD</sub> as  
 2436 a function of range to the surface. The data with diamond points in Figure 5-24 were collected on  
 2437 two flights (27 July, 20011 and 3 August, 2011) that each operated from several altitudes. No  
 2438 background subtraction was included in the calculations, but the data were screened to remove

2439 cloudy regions. The 10-s  $O_2$   $SNR_{DAOD}$  values were estimated using the 10-Hz  $O_2$   $SNR_{DAOD}$   
 2440 statistics.



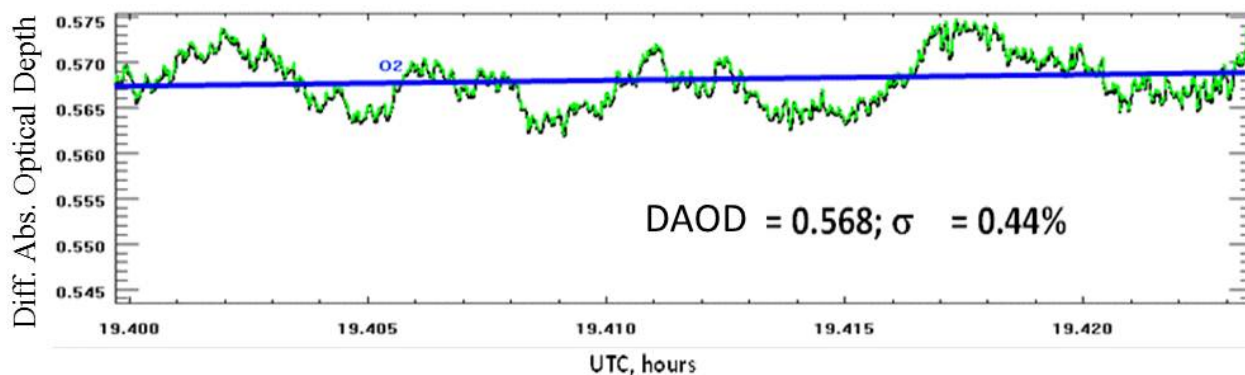
2441  
 2442 **Figure 5-23** A lidar spectral sweep across the  $O_2$  doublet from 6 km altitude on 7 August 2011.

2443 Figure 5-24 shows that the  $O_2$   $SNR_{DAOD}$  varied as the inverse of the range squared, as expected  
 2444 from shot noise limited performance, in the presence of daytime background. Initial analysis of  
 2445 the measurements from the March 2013 flight campaign shows significant improvement in  $O_2$   
 2446  $SNR_{DAOD}$  as shown by the triangle data points in Figure 5-24. These data were collected from  
 2447 several altitude levels in a single flight on 26 March 2013 over similar terrain as that of the 2011  
 2448 data. More than an order of magnitude improvement in SNR over long ranges (6-12 km) has  
 2449 been found. This improvement is the result of the incorporation of the DRS HgCdTe detector in  
 2450 place of the PIN diode detector used in the 2011 campaign. This demonstrates the capability of  
 2451 airborne retrieval of  $O_2$  column amounts in the presence of high solar background conditions.  
 2452 Figure 5-25 shows a comparison between the measured and in-situ derived column  $O_2$  DAOD to  
 2453 the surface from a range of about 3.5 km (Browell et al., 2012). These data were taken from a  
 2454 flight to Castle, CA on 27 July 2011. In situ measurements were used within 10 km of the MFL  
 2455 DAOD measurement region. A 10-s signal averaging was done prior to DAOD calculation, and  
 2456 in-situ derived DAODs were calculated using a procedure similar to that for the  $CO_2$  DAODs.  
 2457 The 1-standard deviation difference between the in situ and measured DAODs was 1.26% and the  
 2458 average difference of the DAODs was  $< 0.5\%$  (Browell et al., 2012). These measurements show  
 2459 an encouraging result that an  $O_2$   $SNR_{DAOD}$  of 700 or higher can be achieved by the technology  
 2460 development.



2461  
2462  
2463  
2464

**Figure 5-24** Variation of SNR in the measurements of O<sub>2</sub> SNR<sub>DAOD</sub> with range from the DC-8 on 27 July and 3 August 2011(diamonds) compared with measurements from the 26 March 2013 flight with an improved detector (triangles).



2465  
2466  
2467  
2468

**Figure 5-25** Comparison of measured and in-situ derived O<sub>2</sub> DAOD from the DC-8 on 27 July 2011. Measured values (green line) and in-situ derived values (blue line) are plotted. It illustrates high precision measurements of O<sub>2</sub> DAODs.

2469 **5.3.3.6 Laboratory and Ground-Based Measurements**

2470 Many efforts have been made for the demonstration of the IM-CW IPDA approach and towards  
 2471 the development of technologies for a future space-based LAS system. In a typical example, the  
 2472 LaRC team conducted a comprehensive MFL ground test on an 860-m horizontal test range at  
 2473 NASA LaRC during July-August 2012 (Lin et al. 2013). Several surface targets covering a wide  
 2474 range of reflection were tested and calibrated using standard diffuse reflectance products. Very  
 2475 good agreement between model predictions and LAS signal measurements for the tested albedos  
 2476 was obtained, which significantly enhances the scaling and evaluation capabilities for space  
 2477 missions (Lin et al. 2013).

**2478 5.3.3.7 Near-term Plans**

2479 The key areas for the LaRC team near-term measurement development and demonstration plan  
2480 include maturing low-mass, high-power high-efficiency lasers, optical receiver subsystems, and  
2481 electronics required for the ASCENDS space mission via the ASCENDS CarbonHawk  
2482 Experiment Simulator (ACES; Obland et al., 2012, 2013) program and further demonstrating the  
2483 capabilities of CO<sub>2</sub> column measurements in various environmental conditions. The LaRC team  
2484 conducted ACES ground tests at LaRC's lidar test range in April 2014 with flight tests in July  
2485 2014. Initial results are very encouraging because of significantly increased transmitted power.  
2486 Additional flight tests are planned for August 2015 to further demonstrate the CO<sub>2</sub> column  
2487 measurement capability of the ACES instrument. The LaRC team is close to achieving the laser  
2488 power required for the space mission through the ACES program and has developed an  
2489 achievable path to meet the ASCENDS mission requirements on the relevant time scale. A DC-8  
2490 flight campaign for making measurements of CO<sub>2</sub> drawdown over cornfields was conducted  
2491 during summer 2014 and flights to examine CO<sub>2</sub> during the cold season are planned during winter  
2492 2016. CO<sub>2</sub> column measurements over snow and ice surfaces will be analyzed extensively from  
2493 existing and future flight data. The CO<sub>2</sub> measurement accuracy and precision over low  
2494 reflectance rough ocean surfaces and the length of integration period to increase SNR<sub>DAOD</sub> to  
2495 required level will be tested through open ocean flight campaigns. The accuracy and systematic  
2496 errors in the retrievals of CO<sub>2</sub> column amounts from low and high thin clouds will be further  
2497 assessed using summer 2011, winter 2013 and future flight campaign data sets.

2498 The cloud slicing technique, which is enabled by the ranging-encoded lidar approach, such as the  
2499 swept-frequency IM-CW, will be investigated from various airborne data sets. This should  
2500 provide the capability to determine CO<sub>2</sub> columns across both the free troposphere and the  
2501 planetary boundary layer. Further improvements on the atmospheric slicing capability will be  
2502 achieved by using sideline wavelengths that are considered for space applications (Lin et al.,  
2503 2013) because of the differences in atmospheric weighting functions. Furthermore, advanced lidar  
2504 intensity modulation algorithms that eliminate cloud impacts on lidar surface returns when clouds  
2505 are very close to the surface are developed (Campbell et al., 2013) and will be tested. Along with  
2506 these efforts, modeling of LAS atmospheric CO<sub>2</sub> column measurements is also a key part of the  
2507 measurement development and demonstration plan (Lin et al., 2013).

**2508 5.3.4 CO<sub>2</sub> Laser Absorption Spectrometer (LAS)**

2509 A team at JPL developed an airborne CO<sub>2</sub> Laser Absorption Spectrometer (JPL CO<sub>2</sub>LAS) in the  
2510 2002-2006 time frame to demonstrate the airborne IPDA lidar technique as a stepping stone to an  
2511 Earth-orbiting capability for global-scale measurements of CO<sub>2</sub> concentrations. The first airborne  
2512 measurements were conducted in summer, 2006 on a Twin Otter aircraft. The JPL CO<sub>2</sub>LAS has  
2513 flown on the NASA DC-8 since summer, 2010. This instrument utilizes the 2.05 $\mu$ m CO<sub>2</sub> band,  
2514 which has a band-strength nearly an order of magnitude larger than the 1.57  $\mu$ m band. This  
2515 enables probing CO<sub>2</sub> at frequencies suitably displaced from line center such that the IPDA  
2516 measurement preferentially weights the lower tropospheric CO<sub>2</sub> molecules, while maintaining a  
2517 differential absorption optical depth (DAOD) at its optimum value for maximizing the DAOD  
2518 signal (Bruneau et al., 2006) and simultaneously minimizing the impacts of sources of bias. The  
2519 instrument uses a heterodyne detection receiver, which provides optimum photon detection  
2520 efficiency.

**2521 5.3.4.1 JPL CO<sub>2</sub> LAS Instrument Description and Data Processing**

2522 The CO<sub>2</sub> LAS instrument developed jointly by JPL and Coherent Technologies, Inc. (later  
2523 Lockheed Martin Coherent Technologies) (Spiers et al., 2002; Spiers et al., 2011a) consists of  
2524 five key subsystems: (1) the optical assembly, (2) the control electronics unit, (3) the control  
2525 software unit, (4) the thermal management assembly, and (5) the signal processing / data  
2526 acquisition electronics. In operation, the optical assembly is completely autonomous, no  
2527 adjustments are required. The optics alignment has not been adjusted since the instrument  
2528 integration and tested in 2004.

2529 The CO<sub>2</sub> LAS transceiver approach utilizes heterodyne detection, implementing a narrow  
2530 bandwidth receiver, with frequency-stabilized narrow-linewidth laser transmitters and local  
2531 oscillators. The lasers are diode-pumped Tm/Ho-doped YLF crystal lasers (McGuckin and  
2532 Menzies, 1992), that emit in the 2.05 μm spectral region. The transceiver consists of two separate  
2533 transmit/receive channels for the on-line and off-line measurements. The off-axis beam  
2534 expanding telescopes for each channel are identical in size and configuration. The transmitter  
2535 frequencies are stabilized with respect to a selected CO<sub>2</sub> absorption line. Each channel has a  
2536 dedicated heterodyne detector, and a continuous-wave (cw) single frequency laser which acts both  
2537 as the transmit laser and the local oscillator for heterodyne detection of the return signal. The  
2538 transceiver also includes a separate low-power cw laser that provides a reference for frequency  
2539 offset-locking of the on-line and off-line lasers.

2540 A comprehensive study of candidate CO<sub>2</sub> absorption lines was conducted considering (1)  
2541 minimizing interference from water vapor lines, (2) minimizing susceptibility to atmospheric  
2542 temperature profile uncertainty, (3) optimizing line strength (Menzies and Tratt, 2003). The  
2543 R(30) line of the (2001)III ← (0000) band, with line center at 4875.749 cm<sup>-1</sup>, was selected based  
2544 on this evaluation. The choice of R(30) as the optimum line in the 2.05-μm band has been  
2545 validated in recent more comprehensive wavelength optimization studies (Caron and Durand,  
2546 2009). The instrument contains an onboard low pressure CO<sub>2</sub> gas absorption cell for locking the  
2547 reference laser to the CO<sub>2</sub> R(30) line. The on-line laser is tunable over a range of several GHz  
2548 with respect to the fixed reference laser frequency. A few mW from the on-line laser is tapped off  
2549 to act as the local oscillator (LO) for heterodyne detection of the return on-line signal.) The  
2550 offline laser channel configuration is similar.

2551 Offset locking is accomplished using wide-band photomixers that monitor the beat frequencies  
2552 between the outputs of the on-line and off-line lasers with respect to the reference laser. Dating  
2553 from the time of first integrated performance tests, the on-line and off-line lasers have been tuned  
2554 to the same offset frequencies with respect to the CO<sub>2</sub> R(30) line center, namely +4.00 GHz and -  
2555 15.72 GHz respectively.

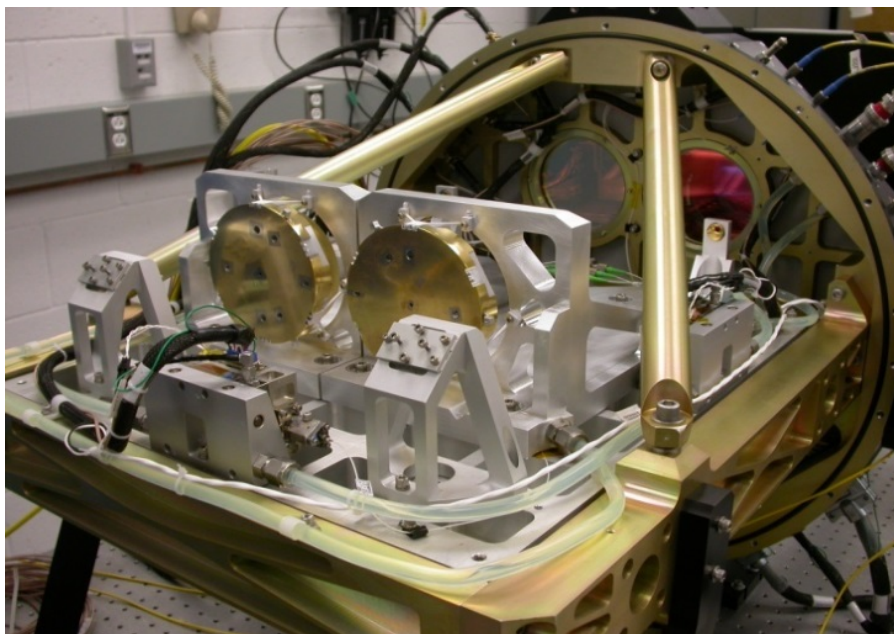
2556 A frequency offset is required between the return signals and their corresponding local oscillators  
2557 for heterodyne detection. By pointing the transmit beams at a known offset from nadir, the return  
2558 signals are Doppler shifted by the aircraft velocity, eliminating the need for a frequency shifting  
2559 device in the instrument. The aircraft pitch angle adds to the fixed off-nadir pointing angle and is  
2560 taken into account both in mounting hardware and retrieval software.

2561 The transceiver assembly is mounted to a 2-sided optical bench, with custom-designed mounts for  
2562 the optical components. This optical bench is edge-mounted to a base plate, as pictured in Figure  
2563 5-26. In operational configuration, the optical bench is in a near-vertical plane, and a cover is  
2564 fastened to the base plate. Thus the assembly is contained within an enclosure with electrical

2565 feed-throughs and optical windows. (See Figure 5-27.) The baseplate/enclosure assembly includes  
 2566 vibration isolation. With the cover in place, the transceiver subsystem is ready to be mounted to  
 2567 an aircraft interface frame. In the DC-8, it is mounted in the rear cargo bay.

2568 The key airborne LAS instrument parameters are summarized in Table 5-10 below.

2569



2570

2571 **Figure 5-26** LAS with optical bench horizontal, telescope side up, base plate in background.

#### 2572 **5.3.4.2 Signal Processing and Data Analysis**

2573 The approach to data analysis and CO<sub>2</sub> retrieval is as follows. The LAS on-line and off-line  
 2574 signals are sampled, stored, and processed as described below, to calculate for various  
 2575 atmospheric layers the values of

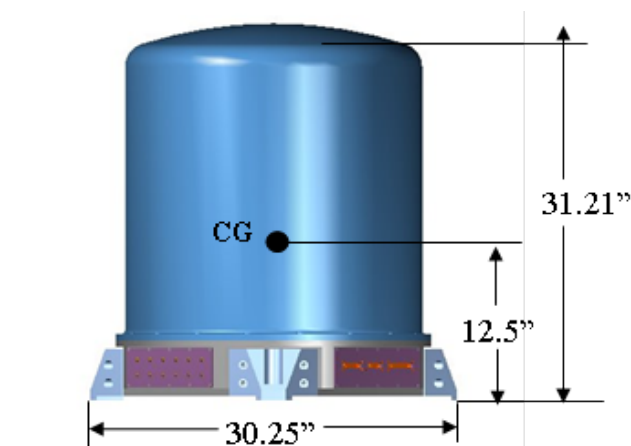
2576

$$2577 \ln (P_{off}/P_{on}) = (2 DAOD) \quad (5-5)$$

2577

2578 The  $P_{off}$  and  $P_{on}$  are the estimates of return power at the off-line and on-line frequencies, properly  
 2579 normalized by the transmitted laser powers at these two frequencies. Then these results, derived  
 2580 from the measurements, are compared with forward model predictions of  $DAOD$ . We use the  
 2581 LBLRTM (Line-By-Line Radiative Transfer Model) provided by the Atmospheric and  
 2582 Environmental Research Inc. (AER), modified to include a merged line parameter database in the  
 2583 5 cm<sup>-1</sup> region centered at 4875.5 cm<sup>-1</sup>. The forward model is based on this modified LBLRTM  
 2584 code, plus the atmospheric meteorological data needed to provide the altitude-dependent  
 2585 weighting function. The on-board GPS system provides the aircraft position knowledge  
 2586 (including altitude with respect to the geoid). Lacking an on-board co-aligned laser altimeter, the  
 2587 surface elevation is obtained using the Shuttle Radar Topography Mission (SRTM) digital  
 2588 elevation database along with the laser pointing angle, updated at 10 Hz rate.

2589



2590  
2591 **Figure 5-27** LAS transceiver in hermetically sealed enclosure.

2592 **Table 5-10 JPL airborne LAS instrument parameters**

Parameter	Value
CO <sub>2</sub> line center frequency	4875.749 cm <sup>-1</sup>
JPL LAS ON frequency	4875.882 cm <sup>-1</sup>
JPL LAS OFF frequency	4875.225 cm <sup>-1</sup>
Laser output power	100 mW
Transmit/Receive Telescope apertures	10 cm diameter
Receiver FOV (diffraction limited)	60 μrad
Photomixer type	InGaAs
Receiver heterodyne frequency window	9-21 MHz
Signal Digitization	14 bits / 50 MHz

2593  
2594 The normalized return signal power values are determined as follows. The Intermediate  
2595 Frequency (IF) photomixer signals from the on-line and off-line channels are amplified and are  
2596 bandwidth limited to a nominal 9-21 MHz window. The signals from each channel are digitized  
2597 with a 50 Msamples/sec, 14-bit digitizer. The samples are transformed into the spectral domain  
2598 using a Fast Fourier Transform (FFT) operation followed by conversion to periodograms. The  
2599 return power is proportional to the size of the signal in the frequency space of the periodogram.  
2600 On-line and off-line signal power calculations are performed, followed by normalization steps to  
2601 account for variations in slant path length between instrument and footprint on the surface, small  
2602 variations in laser power, or other small drifts in ch1, ch2 overall system gain. System stability is  
2603 quantified through the use of “validation” data collection periods, when an on-board

2604 backscattering Validator subsystem is inserted into the instrument field-of-view, intercepting the  
2605 transmitter beams.

#### 2606 **5.3.4.3 Cloud Detection and Filtering**

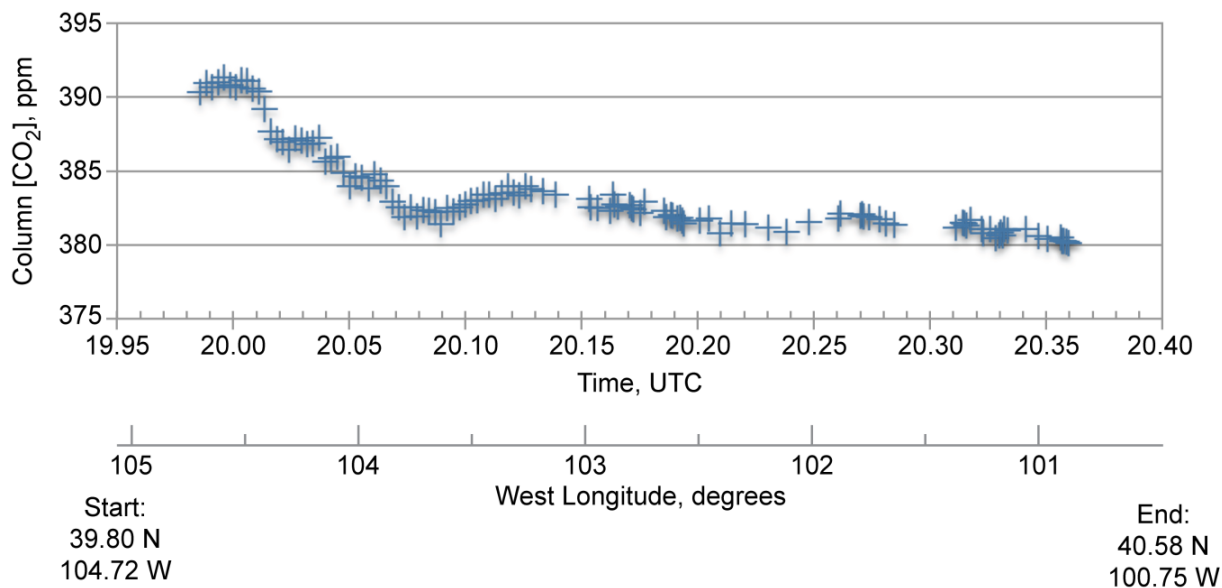
2607 To obtain adequate coverage, (weighted) column CO<sub>2</sub> mole fractions must be collected in the  
2608 presence of broken clouds. Clouds in the FOV reduce the path length, and if not recognized, bias  
2609 the CO<sub>2</sub> retrieval. In cases of scattered cloud cover, breaks or holes permit soundings down to the  
2610 surface some fraction of the time. The small transmitter footprint of the lidar provides an inherent  
2611 capability to acquire retrievals in such circumstances. If the lidar provides time-of-flight to the  
2612 backscatter source (e.g. a range-gated pulsed system, or a Frequency-Modulated/Continuous  
2613 Wave (FM/CW) system), any sources of backscatter other than that which occurs at the expected  
2614 delay time corresponding to range to the surface can be set aside or filtered out. With the current  
2615 implementation of our airborne system, we do not have this capability. We do not chirp  
2616 (frequency modulate) our transmitters. However we do employ alternative methods to detect and  
2617 filter out the backscatter signals that are due to clouds in the FOV (field of view). The following  
2618 methods are very effective in identifying a large variety of clouds.

- 2619 • Heterodyne detection provides capability to see both intensity and spectral properties of  
2620 backscatter signal;
- 2621 • Cloud motion provides a discriminating tool, both broadening and shifting the backscatter  
2622 signal in the spectral/frequency domain;
- 2623 • Clouds in FOV also cause shortening of atmospheric sounding path length – reduced  
2624 values of retrieved CO<sub>2</sub> column;

2625 The heterodyne signals backscattered from the surface are sufficiently narrow to permit  
2626 identification of cloud backscatter if the cloud movement relative to the surface, along the line-of-  
2627 sight, exceeds 0.5 m/s. Since the typical point-ahead angle in the DC-8 is ~ 0.1 rad, this  
2628 corresponds to a threshold horizontal motion of 5 m/s. However, in practice, the backscatter  
2629 signals from cumulus and stratocumulus are also spectrally broadened, compared with the ~ 200  
2630 kHz FWHM (full width at half maximum) signals backscattered from the surface in clear air  
2631 conditions. This provides another filtering method. This spectral broadening is typical of  
2632 backscatter from cumulus and also stratocumulus (Spiers et al., 2012).

#### 2633 **5.3.4.4 Observation of CO<sub>2</sub> Drawdown**

2634 The August 10, 2011 flight's primary objective was the upper Midwest, arriving over the target  
2635 area (Iowa) near mid-day, with the expectation that CO<sub>2</sub> drawdown in the boundary layer would  
2636 be observed due to the photosynthetic assimilation by crops over this large-scale agricultural  
2637 region. The JPL LAS data clearly indicated a steady decrease in CO<sub>2</sub> weighted column mole  
2638 fraction (or mixing ratio) en route to Iowa beginning with the overflight of the Eastern Colorado  
2639 high plains (Spiers et al., 2011b; Spiers et al., 2012; Menzies et al., 2014). After arriving in the  
2640 vicinity of the West Branch Iowa (WBI) tall tower (Miles et al., 2012), a spiral was implemented  
2641 in order to profile the CO<sub>2</sub> mole fraction using an on-board cavity ring-down spectroscopy sensor  
2642 [Picarro, Inc.], and several fixed-altitude "tower transits" were conducted at different altitudes.  
2643 (The NASA DC-8 also has on-board sensors providing atmospheric temperature, pressure, and  
2644 relative humidity data to the investigator teams.)



2645

2646 **Figure 5-28** LAS weighted column CO<sub>2</sub> mole fraction retrievals during flight over Central US. The segment from  
 2647 Denver, Colorado vicinity to middle of Nebraska, was flown on August 10, 2011. (Locations: 39.80 N / 104.72 W at  
 2648 19.98 UTC; 40.58 N / 100.75 W at 20.37 UTC. Distance travelled: 310 km.) The 1-sigma precision level for this  
 2649 retrieval is equivalent to 1.1 ppm. The steady decrease in column CO<sub>2</sub> is due to mid-day drawdown in the  
 2650 atmospheric boundary layer.

2651 The flight to the Midwest included a long transit at fixed pressure altitude starting near Denver,  
 2652 CO and continuing to the vicinity of the WBI Tower in Iowa. We encountered clear atmosphere  
 2653 over the Denver area, with scattered fair weather cumulus appearing over the eastern Colorado  
 2654 plains. Cloud fraction steadily increased as the flight ground track moved into Nebraska. The  
 2655 observed weighted-column CO<sub>2</sub> mixing ratio decreased during this time period as shown in  
 2656 Figure 5-28. The aircraft flew at a constant 15 kft pressure altitude during this transit. The  
 2657 SRTM DEM data were used to obtain the along-track elevation. The atmospheric meteorological  
 2658 data that were incorporated into our retrieval algorithm came from the MERRA (Modern Era  
 2659 Retrospective Analysis for Research and Applications) products available from the NASA  
 2660 Goddard Space Flight Center GMAO (Global Modeling and Assimilation Office) (MERRA,  
 2661 2012). For example, the surface pressure from MERRA, interpolated along this ground track and  
 2662 “corrected” using the higher resolution topographical data along the ground track, was used in the  
 2663 CO<sub>2</sub> retrieval algorithm.

2664 The Figure 5-28 record starts a few km south of the Denver International Airport, and the distance  
 2665 covered from left to right is 340 km. The along-track averaging corresponds to about 4 km along-  
 2666 track resolution for the plotted data. The flight altitude CO<sub>2</sub> readings from the in situ Picarro  
 2667 instrument measurements trended lower over a narrow range from approximately 389.5 to 387.5  
 2668 ppmv during the period of time plotted. The column is likely sampling urban-influenced regional  
 2669 boundary layer air at the beginning. Nadir camera imagery shows a transition to agricultural  
 2670 activity (occasional crop circles) beginning at 20.02 UTC, with increasing land use for  
 2671 agricultural activity occurring as the ground track continues eastward. Crossing into Nebraska  
 2672 occurred near 20 hr 13 min UTC. Gaps in the data are due to presence of fair weather cumulus.  
 2673 The ground track is in the middle of Nebraska at the end of the plotted data. By this time the  
 2674 cumulus coverage had increased, with corresponding decrease in the durations of the clear air  
 2675 gaps between clouds, precluding the continuation of the high precision retrievals.

2676 The conclusion that the observed steady decrease in column CO<sub>2</sub> abundance is due to drawdown  
2677 is supported by later measurements in Iowa during a traverse over the West Branch Iowa (WBI)  
2678 tower at 10 km altitude, where in situ vertical profile data obtained near the WBI tower from the  
2679 on-board Picarro instrument indicated boundary layer CO<sub>2</sub> mole fraction values ~ 365 ppm, and  
2680 free troposphere values averaging 382 ppm. The magnitude of this mid-day decrease in the  
2681 boundary layer mixing ratio is consistent with other reported measurements and simulations  
2682 (Miles et al., 2012; Denning et al., 1996). Regional-scale simulations of the CO<sub>2</sub> exchange  
2683 between the atmosphere and the terrestrial ecosystems (Denning et al., 1996) and measurements  
2684 at the U.S. upper Midwest tall towers (Miles et al., 2012) show peak daytime NEE (Net  
2685 Ecosystem Exchange) flux values of -50 to -60  $\mu\text{mol m}^{-2} \text{s}^{-1}$  in the summertime, corresponding to  
2686 mid-day boundary layer CO<sub>2</sub> mole fractions in the 360-365 ppm range at corn dominated sites  
2687 such as the WBI tower site and the Mead tower site in western Nebraska. Mid-day CO<sub>2</sub> levels in  
2688 this region during early August are among the lowest in North America due to strong uptake by  
2689 corn and other crops.



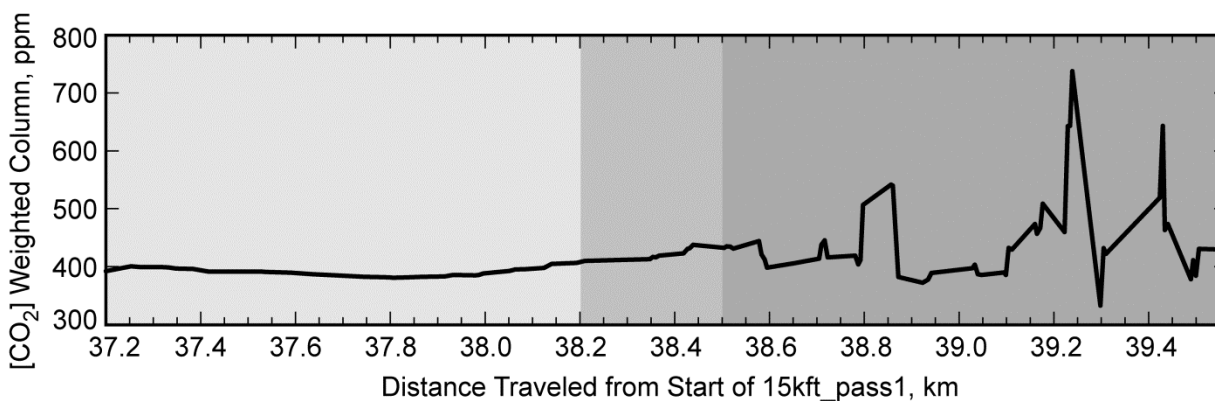
2690  
2691 **Figure 5-29** Four-Corners Power Plant, New Mexico, U.S showing 3 main clusters of stacks. From left to right,  
2692 starting with the tall stack (cluster #1): Clusters #1 - #2 separation ~ 400 m; Clusters #2 - #3 separation ~ 150-200 m.

#### 2693 **5.3.4.5 Observation of Power Plant CO<sub>2</sub> Plume and CO<sub>2</sub> Emission Rate Calculation**

2694 On August 9, 2011, the DC-8 flew a northward flight segment at 15,000 foot pressure altitude  
2695 whose ground track was downwind of the 4-Corners Power Plant, located in San Juan County,  
2696 New Mexico (36.690 N, 108.483 W). The JPL LAS data indicated multiple spatially distinct  
2697 plumes emanating from the power plant complex (Spiers et al., 2012; Menzies et al., 2014). The  
2698 ground track was within a few hundred meters of the plant site. The plant has five coal-fired  
2699 units, with spacing such that the emissions appear to originate from three sources. The source  
2700 encountered first during this flight leg (leftmost in Figure 5-29) is the tall stack. Approximately  
2701 400 m from this source are a pair of stacks, and approximately 200 m from this pair is a third  
2702 stack cluster, dark in appearance from the camera imagery. Figure 5-30 is a plot of the weighted  
2703 column CO<sub>2</sub> mole fraction during the pass, with variable along-track resolution. The along-track  
2704 resolution is 15 m during the 1-km segment immediately downwind of the plant, which is clearly  
2705 sufficient to resolve plumes from the various stacks or stack clusters.

2706 A simple box model estimate of the power plant CO<sub>2</sub> emission rate during the mid-day time of  
2707 this flight leg can be made by calculating the CO<sub>2</sub> mass crossing a plane of height equal to the  
2708 aircraft height above ground (3135 m) and ground track segment length of 1.0 km for which the  
2709 mole fraction is above the background or baseline value. The speed of the wind carrying the CO<sub>2</sub>  
2710 plume across the plane at this time, 2.15 m s<sup>-1</sup>, is obtained from the MERRA reanalysis (MERRA,

2711 2013). The atmospheric temperature in the lowest MERRA layer at this time was 299 K. Taking  
2712 the weighting function into account, and assuming the plume is within the first 200 m above the  
2713 surface, where the weighting function is nearly constant, a source of  $470 \text{ kg s}^{-1}$  emission rate is  
2714 derived, based on the observed integrated weighted column increment (Menzies et al., 2014).



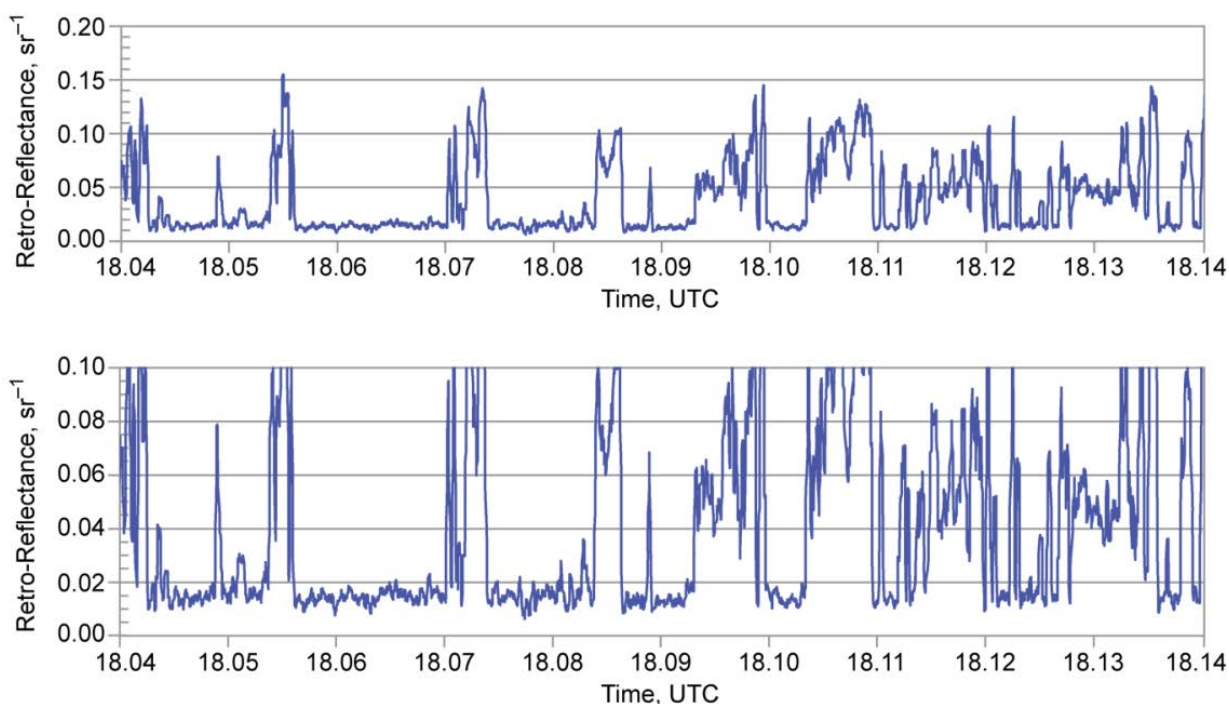
2715  
2716 **Figure 5-30** Weighted column  $\text{CO}_2$  retrievals during flyby of the Four-Corners Power Plant at 15 kft pressure  
2717 altitude along a south-to-north track and a few hundred meters downwind. The shading corresponds to three spatial  
2718 resolution segments: (1) 37.2 – 38.2: 150 m along track resolution; (2) 38.2 – 38.5: 50 m resolution; (3) 38.5 – 39.5:  
2719 15 m resolution.

2720 The Four Corners Power Plant complex emits in the neighborhood of  $14 \times 10^6$  metric tons of  $\text{CO}_2$   
2721 annually, according to a 2011 study prepared by RMT, Inc. for the California Public Utilities  
2722 Commission (RMT, 2011). (A pdf of this document is available.) This corresponds to an average  
2723  $\text{CO}_2$  emission of  $440 \text{ kg s}^{-1}$ . Surely there is some temporal variability in the emission rate – on  
2724 daily, weekly, or monthly time scales, but we do not have that information. However we do have  
2725 a measurement that corresponds closely with the average emission rate. This demonstrates the  
2726 potential capability of the IPDA measurement method.

#### 2727 **5.3.4.6 $\text{CO}_2$ Retrievals over Snow-Covered Surfaces: Evidence of Plumes from** 2728 **Developments**

2729 Assessment of the capability to retrieve  $\text{CO}_2$  weighted column mole fraction over snow-covered  
2730 surfaces is an important objective in ASCENDS planning. Snow reflectance at the 1.57 and 2.05  
2731  $\mu\text{m}$  wavelengths is relatively low (Aoki et al., 2000), but quantitative values of lidar directional  
2732 reflectance at these wavelengths did not exist prior to the ASCENDS campaigns of 2011 and  
2733 2013. These campaigns offered the opportunity to measure reflectances of a variety of snow-  
2734 covered surfaces. The basis of our 2.05  $\mu\text{m}$  snow reflectance derivation is the linkage that we  
2735 have to ocean surface reflectance as measured over the clear Pacific Ocean off the coast of  
2736 California. The CALIPSO mission provides by far the largest study of lidar backscatter from the  
2737 ocean surface, and we rely on data from Hu et al. (2008) for determination of the surface  
2738 directional reflectance (backscatter) over this region of the Pacific Ocean, given the estimated  
2739 surface wind. (Correction was made for the wavelength-dependence of water refractive index  
2740 between 1.06 and 2.05  $\mu\text{m}$ .) We are able to take advantage of the fact that at the JPL LAS  
2741 nominal 5-degree off-nadir angle, the surface backscatter is only weakly dependent on surface  
2742 wind speed in the range from  $\sim 2.5$ -12 m/s (Menzies et al., 1998). Comparison were made of  
2743 range-corrected off-line return signal values from the Pacific Ocean flight and the 8/07/2011  
2744 flight values over the snow-capped British Columbia coastal mountains. The LAS instrument  
2745 radiometric stability is good to within 10% from flight-to-flight, and flight-to-flight and in-flight

2746 variations are monitored with the internal Validator. This allows the determination of surface  
2747 reflectance during the flight segment over the BC coastal mountains, as in Figure 5-31. In this  
2748 case the snow backscatter averaged over the ground track is  $\sim 0.012 \text{ sr}^{-1}$  (Menzie et al., 2014).



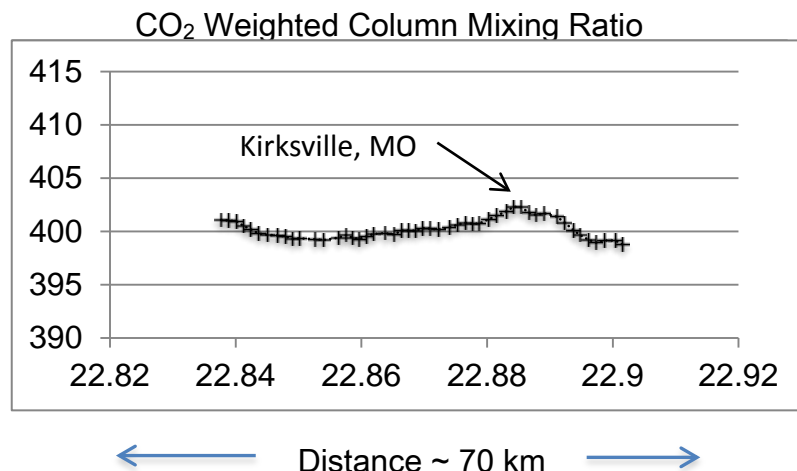
2749  
2750 **Figure 5-31** LAS measured surface reflectance during a portion of the “snowline out” flight segment over the  
2751 British Columbia Coastal Mountains, August 7, 2011 at  $2.05 \mu\text{m}$  wavelength (in units of  $\text{sr}^{-1}$ ). Snow covered areas  
2752 (low backscatter) were mixed with patches of bare rock, dirt, alpine flora. Time duration from left to right: 0.1 hr (6  
2753 min). The two panels differ only in scale.

2754 Snow-covered terrain was also encountered on the March 7, 2013 flight to the upper Midwest.  
2755 The low reflectance over snow-covered land was often interrupted by road crossings, structures,  
2756 and patches of bare land that show larger reflectances. We found during this flight and the March  
2757 5 flight that targeted the Colorado Rocky Mountains a range of values for snow reflectance (i.e.,  
2758 lidar directional reflectance), with values at the  $2.05 \mu\text{m}$  lidar wavelength from  $0.07$  to  $0.2 \text{ sr}^{-1}$ .

2759 The  $\text{CO}_2$  retrievals over the upper Midwest flight tracks show bulges or plumes that appear to be  
2760 associated with developed areas, e.g. cities in the vicinity of the ground tracks. Through the use  
2761 of the combination of nadir camera imagery, MERRA wind direction, and Google Earth, we  
2762 observe cases when ground tracks are over urban areas, developments near cities, or downwind of  
2763 nearby urban areas. Figure 5-32 shows an example. In this case, the wind direction was  
2764 primarily westward, with a small northward component. Space heating in cold winter weather  
2765 may be the primary source of these  $\text{CO}_2$  plumes from populated areas.

2766 The flights of the JPL  $\text{CO}_2$  Laser Absorption Spectrometer have enabled us to assess and  
2767 demonstrate the performance of a  $2.05 \mu\text{m}$  IPDA lidar using a heterodyne detection receiver to  
2768 obtain  $\text{CO}_2$  retrievals for a variety of atmospheric and surface conditions. Measurements made  
2769 during a mid-day flight over the U.S. Upper Midwest clearly indicate that we can observe the  $\text{CO}_2$   
2770 drawdown due to photosynthesis at the surface. Measurements made in the vicinity of the Four  
2771 Corners power plant demonstrate the capability to resolve the plumes with high spatial resolution  
2772 and estimate the source emission rate. We demonstrated the capability to measure  $\text{CO}_2$  over

2773 snow-covered surfaces in the Upper Mid-West during winter, 2013, and we observed CO<sub>2</sub>  
 2774 bulges/plumes that appear to be associated with developed areas that were encountered along the  
 2775 flight tracks. The 2- $\mu$ m weighting function, which gives added weight to the atmospheric  
 2776 boundary layer (ABL), enables enhanced sensitivity to sources and sinks that alter the CO<sub>2</sub> mole  
 2777 fraction in the ABL.



2778  
 2779  
 2780  
 2781 **Figure 5-32** CO<sub>2</sub> retrieval in vicinity of Kirksville, Missouri on March 7, 2013 (Left) JPL nadir camera image of  
 2782 partially snow-covered landscape in Kirksville vicinity, taken from the DC-8 rear cargo bay at 22.886 (22:53:08)  
 2783 UTC. (Right) Weighted column CO<sub>2</sub> along a 70 km length flight segment heading south, near 92.5° west longitude.  
 2784 The time is UTC, covering 6 min from left to right. The track went over the west edge of Kirksville, downwind side,  
 2785 showing a plume that is associated with the city.

#### 2786 5.3.4.7 Near-term Plans for the LAS

2787 Improvements to the airborne system were implemented in 2014, and more are planned in 2015.  
 2788 The most significant 2014 modification included (1) installation of a faster data acquisition  
 2789 system in the airborne LAS instrument, in order to increase the speckle-limited sensitivity on  
 2790 short time scales; (2) replacement of 10-yr old RF electronics with current commercially available  
 2791 electronics. The 2015 planned improvements include installation of a fiber amplifier in the online  
 2792 channel to boost the online transmit power output, and the addition of a laser altimetric capability.  
 2793 Improvements in ground-based data processing and analysis algorithms are continuing. Goals are  
 2794 (1) to decrease the data latency between in-flight acquisition and availability of CO<sub>2</sub> products; (2)  
 2795 to utilize digital noise filtering and contrast enhancement techniques in order to reduce the  
 2796 impacts of speckle noise on the CO<sub>2</sub> retrievals.

### 2797 5.4 Development of Additional Lidar Measurement Approaches

2798 NASA has also supported the development of two additional lidar approaches to measure the CO<sub>2</sub>  
 2799 column. These use CO<sub>2</sub> column lidar measurement using different approaches than those  
 2800 described earlier. They are earlier in their evolution and so have not been fully demonstrated in  
 2801 airborne campaigns.

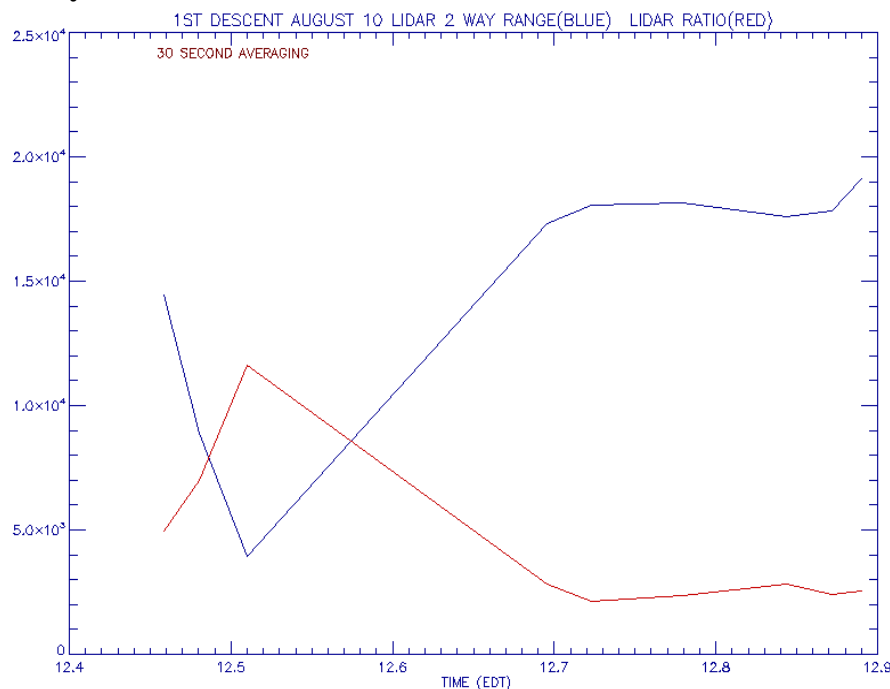
#### 2802 5.4.1 Broad Band Lidar Approach

2803 There are two principal elements involved in the IPDA measurement: the source and the detector.  
 2804 Most laser-based instruments use tunable laser sources to provide different wavelengths needed to  
 2805 sample the selected CO<sub>2</sub> line. The Broad Band Lidar (BBL) uses an alternative approach. It

2806 transmits a spectrally wide ( $\sim 1$  nm) laser pulse and uses a spectrally (wavelength) resolved  
 2807 detector to differentiate the wavelengths on a finer scale. Thus the broadband lidar uses a  
 2808 combination of active illumination with a receiver similar to those in passive sensors. In fact, the  
 2809 BBL detector was originally developed as a passive sensor for measuring CO<sub>2</sub> using reflected  
 2810 sunlight. The BBL approach is made possible by the use of new broadband laser sources that can  
 2811 emit over several nanometers of continuous bandwidth rather than single, narrowly defined  
 2812 wavelengths. This permits a differential absorption measurement employing a single source with  
 2813 all wavelength differentiation done in the detector.

2814 Several versions of the BBL have been developed. A ground based version employing a  
 2815 superluminescent diode (SLED) source was demonstrated in 2010 as well as at 2.05  $\mu\text{m}$   
 2816 employing a fiber laser source. A 1.57  $\mu\text{m}$  version using an Optical Parametric Amplifier (OPA)  
 2817 source was flown in the 2011 ASCENDS intercomparison and a second lidar operating at 1.57  
 2818  $\mu\text{m}$  employing an array detector was flown in the 2013 campaign. Performance has been quite  
 2819 limited in the aircraft tests because of the unfortunate location of the instrument in the DC-8 cargo  
 2820 pit where it is subjected to temperature extremes that tend to drive it off wavelength and out of  
 2821 alignment. Figure 5-33 shows the instrument responding to changing CO<sub>2</sub> column density with  
 2822 altitude early in a test flight before the change in temperature detuned the laser and the receiver.

#### 2823 5.4.1.1 BBL Fabry-Perot Interferometer and Detector



2824  
 2825 **Figure 5-33** BBL measurements made shortly after takeoff on August 10 test flight. The anti-correlation of total  
 2826 absorption (aircraft to ground) in red versus altitude in blue shows that the Broad Band Lidar is responding to CO<sub>2</sub>  
 2827 along the changing path length.

2828 The BBL receiver uses a Fabry-Perot (FP) interferometer as the wavelength selective element for  
 2829 its detector. Aligning multiple adjacent passbands of the FP with several CO<sub>2</sub> absorption lines  
 2830 increases the lidar signal and permits selection of absorption lines that respond to temperature  
 2831 changes in opposite directions, reducing the overall instrument sensitivity to atmospheric  
 2832 temperature change. The width of the Fabry-Perot passbands can be adjusted with very high

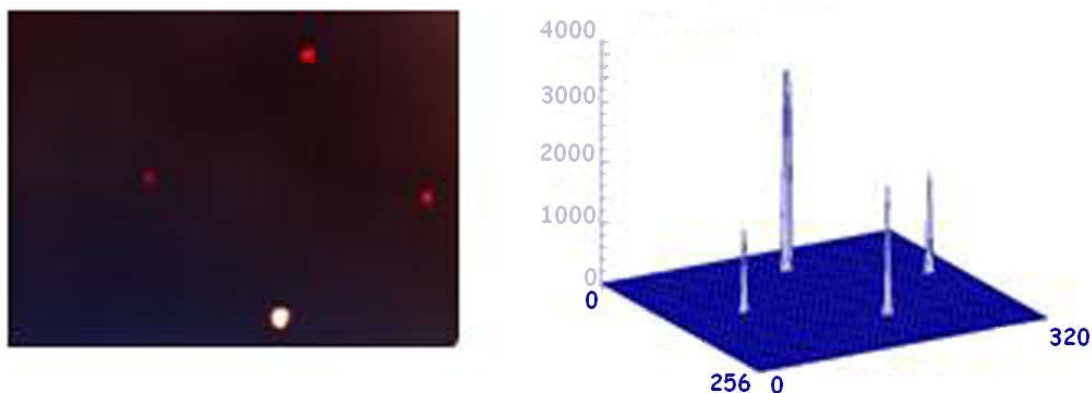
2833 fidelity by changing the reflectivity of the coatings used in its manufacture. Passbands can be  
 2834 selected to surround the full widths of the various CO<sub>2</sub> absorption features reducing the sensitivity  
 2835 of the instrument to slight changes in line position and width caused by changing atmospheric  
 2836 pressure. The fine alignment between etalon fringes and CO<sub>2</sub> absorption lines is achieved by  
 2837 temperature tuning of the Fabry–Perot. The passive Fabry-Perot detector was developed at GSFC  
 2838 from 2003-2006 as a sensor to measure atmospheric CO<sub>2</sub> column using scattered solar flux in the  
 2839 1.57- $\mu\text{m}$  region. It was tested during two successful flight campaigns. It demonstrated very high  
 2840 sensitivity to changes in the CO<sub>2</sub> column abundance, but was subject to errors arising from  
 2841 atmospheric scattering of the sunlight, a problem that lidar instruments eliminate (Georgieva et  
 2842 al., 2006, 2008; Wilson et al., 2007; Heaps et al., 2008).

#### 2843 5.4.1.2 BBL Receiver Design.

2844 The detector in an IPDA lidar performs two functions simultaneously. It determines the length of  
 2845 the atmospheric column by measuring the amount of time that elapses between the emission of  
 2846 the laser light pulse into the atmosphere and its subsequent return. It also measures the intensity  
 2847 of the returning light pulse. This intensity measurement is then used to determine the magnitude  
 2848 of the atmospheric absorption in the path.

2849 Our previous version of the Broad Band lidar used an avalanche photodiode detector (APD) both  
 2850 for ranging and for signal level measurement, but its performance was not suitable for space.  
 2851 More recently we have built a lidar receiver that uses two different detectors to perform the  
 2852 receiver functions. In this design an APD was used to make precise measurements of range. An  
 2853 InGaAs camera was used to measure signal intensities. The camera is not range resolved.  
 2854 However it is very sensitive to photons (it can count single photons) and it generates very little  
 2855 noise during the measurement process. Our simulations of this receiver design indicate that a  
 2856 system based on this configuration could meet the requirements for the ASCENDS lidar.

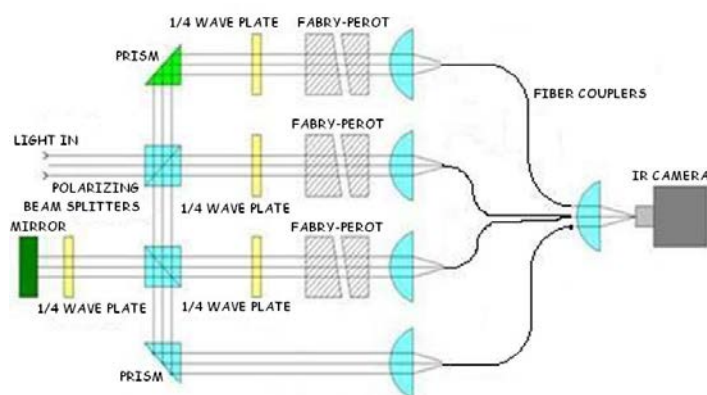
THE FOUR SIGNALS IMAGED ON THE CAMERA FOCAL PLANE



2857  
 2858 **Figure 5-34** Image and plot of the four signals represented in the InGaAs camera focal plane.

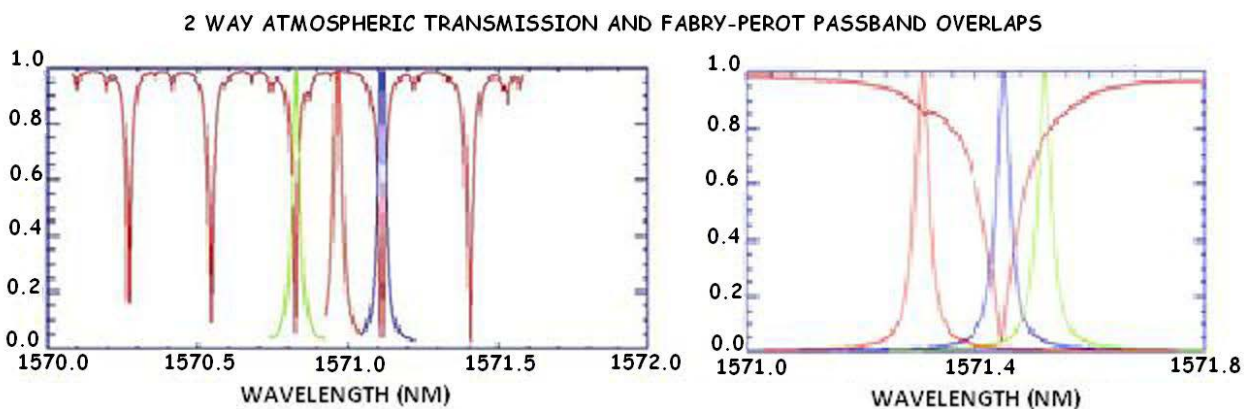
2859 Figure 5-34 shows the focal plane of the InGaAs camera and a plot of the signals measured during  
 2860 a recent airborne flight test campaign. The four dots represent the “on-line” and “off-line”  
 2861 intensity for the transmitted beam and for the reflected signal. A receiver for the ASCENDS  
 2862 space mission would use three Fabry-Perots and so would have three “on line” spots and one “off-  
 2863 line” spot each for the transmitted and return measurement—eight spots in all.

2864 Figure 5-35 shows the arrangement of the detector for the lidar. Beams from the receiver  
 2865 telescope and the outgoing laser sampling system are fiber coupled into the receiver. Polarizing  
 2866 beam splitters and quarter wave plates are used to introduce light into 3 individual Fabry-Perots  
 2867 (FP) that are tuned to sample different portions of the broad-band signal. And a 4<sup>th</sup> channel  
 2868 uses no FP representing the “off-line” of “reference” channel. Two outputs each (one from the  
 2869 receiver telescope and one from the laser sampler) from the 4 channels are imaged onto the focal  
 2870 plane of the single camera resulting in 8 measurement spots from which the CO<sub>2</sub> absorption can  
 2871 be determined.



2872  
 2873 **Figure 5-35** Drawing showing light path in instrument to reach 3 FPs and reference channel. Light reflecting from  
 2874 the FPs has its polarization rotated by the combination of ¼ wave plates so if it reflected from a beamsplitter at first  
 2875 incidence it passes through at the 2<sup>nd</sup> incidence. All signals are collected by fibers then recorded on the focal plane of  
 2876 a single camera.

2877 Figure 5-36 shows how a multiple FP receiver system operating in the 1.57- $\mu\text{m}$  region can  
 2878 remotely sense CO<sub>2</sub> columns.

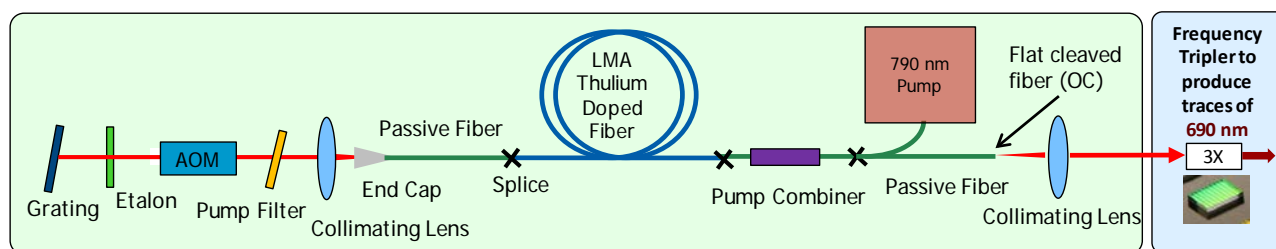


2879  
 2880 **Figure 5-36** Two possible ways that the Multiple FP detector can investigate CO<sub>2</sub> absorptions. The approach on  
 2881 the left samples two separate CO<sub>2</sub> lines providing information that can be used to correct for atmospheric temperature  
 2882 effects.

### 2883 5.4.1.3 Laser for BBL:

2884 In 2011 Northrop Grumman Aerospace (NGA) delivered a prototype Tm-fiber laser to Goddard.  
 2885 Output power was 3 W and pulses were spectrally and temporally stable over several hours of

2886 continuous operation during the laboratory demonstration. The system was used to test and  
 2887 develop the 2.05  $\mu\text{m}$  broadband CO<sub>2</sub> lidar concept. Fiber lasers are a proven method for  
 2888 producing photons at high efficiency in compact, robust packages.



2889  
 2890 **Figure 5-37** A Q-switched fiber laser architecture is used to generate multi-line broadband wavelengths near 2.05  
 2891  $\mu\text{m}$ .

2892 The BBL version of the ASCENDS mission will use a Tm-fiber laser operating at 2.05  $\mu\text{m}$ . The  
 2893 choice of a fiber laser inherently mitigates several risks associated with other types of lasers. The  
 2894 fiber nature of the system allows simply achieved mechanically robust operation in a compact  
 2895 footprint. Thulium's 2.05  $\mu\text{m}$  wavelength enables the use of larger diameter fiber cores without  
 2896 loss in beam quality compared to other fiber lasers. This reduces the risk of catastrophic optical  
 2897 fiber damage and the onset of deleterious nonlinear effects enabling higher pulse energies and  
 2898 peak powers since damage and nonlinear effects scale down with increase in core area. The  
 2899 Efficiency of thulium fiber lasers can also be very high due to a cross relaxation process in  
 2900 thulium's energy levels whereby one pump photon can create two laser photons, leading to  
 2901 potential laser slope efficiencies approaching 70% (Jackson, 2004; Ehrenreich et al., 2010;  
 2902 Goodno et al., 2009; Creeden et al., 2008). For a space-based lidar the laser power would be  
 2903 scaled to the 30-40 Watt level. Our work shows it will be capable of wall plug efficiencies >15%.

## 2904 5.4.2 Pulsed 2- $\mu\text{m}$ Differential Absorption Lidar (DIAL)/IPDA Lidar

2905 Pulsed 2- $\mu\text{m}$  lasers have narrow linewidths and can have high energies that make them suitable  
 2906 for a CO<sub>2</sub> IPDA lidar. The strong 2.0- $\mu\text{m}$  CO<sub>2</sub> lines also have weighting functions that are  
 2907 strongly peaked near the surface. NASA Langley Research Center (LaRC) has been involved for  
 2908 over 15 years in developing pulsed 2- $\mu\text{m}$  lasers and lidar technologies. Recently we have applied  
 2909 them to the measurement objectives of ASCENDS (Koch et al., 2008; Refaat et al., 2010, 2011;  
 2910 Yu et al., 2003, 2012). This section describes the development of ground-based DIAL and  
 2911 airborne IPDA systems for CO<sub>2</sub> measurements.

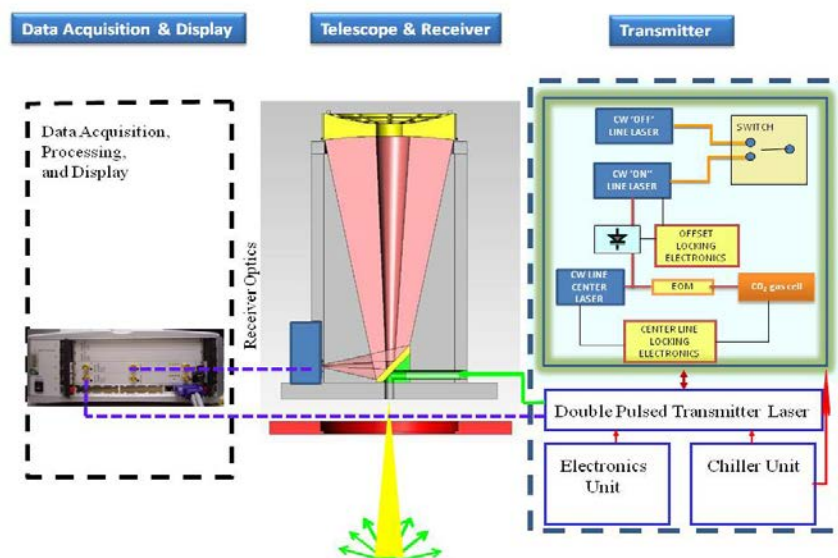
### 2912 5.4.2.1 Single-Pulsed 2- $\mu\text{m}$ CO<sub>2</sub> DIAL Demonstration

2913 Range Resolved CO<sub>2</sub> DIAL measurement using single-pulse 2- $\mu\text{m}$  laser have been demonstrated  
 2914 by NASA LaRC (Koch et al., 2008; Refaat et al., 2010, 2011). For these initial demonstrations,  
 2915 the wavelength of the output laser pulses alternated between on-line and off-line positions at a 5-  
 2916 10 Hz rate. Using heterodyne detection, CO<sub>2</sub> DIAL measurements were attempted with a 90 mJ,  
 2917 140 ns, 5 Hz pulsed Ho:Tm:LuLiF laser transmitter (Koch et al., 2008). The laser used a  
 2918 wavelength control to precisely tune and lock the operating wavelength at any desired offset, up  
 2919 to 2.9 GHz, from the center of a CO<sub>2</sub> absorption line. Once detuned from the line center the laser  
 2920 wavelength is actively locked to keep the wavelength within 1.9 MHz. The laser transmitter has  
 2921 been coupled with a coherent heterodyne receiver for measurements of CO<sub>2</sub> concentration using  
 2922 aerosol backscatter.

2923 Detector technology usually limits the CO<sub>2</sub> DIAL profiling capability at 2 μm. Therefore, 2-μm  
 2924 phototransistors have been developed and integrated for the first time in lidar applications and  
 2925 using direct detection, another 2-μm CO<sub>2</sub> DIAL system was developed at NASA LaRC using the  
 2926 same transmitter (Refaat et al., 2010, 2011). Field experiments were conducted at West Branch,  
 2927 Iowa, for evaluating the system for CO<sub>2</sub> measurement by comparing with NOAA in-situ sensors  
 2928 located on the WBI tower at 31, 99 and 379 m altitudes. Results demonstrated the capabilities of  
 2929 the DIAL system in profiling atmospheric CO<sub>2</sub> using the 2-μm wavelength with both range  
 2930 resolved and integrated column content (Refaat et al., 2010).

2931 The results from single-pulse 2-μm CO<sub>2</sub> DIAL experiments highlight several desirable  
 2932 improvements to enhance their measurement capability. First, the selected and demonstrated  
 2933 target CO<sub>2</sub> R22 line includes high water vapor interference that coexists at the same operating  
 2934 wavelength. Operating on the CO<sub>2</sub> R30 line potentially increases the lidar sensitivity while  
 2935 reducing the impact of water vapor interference. These improvements require upgrading the 2-  
 2936 μm laser transmitter. The laser pulse repetition rate also must be increased. With single-pulse, 5-  
 2937 Hz transmitter, the on-line and off-line pulses are separated by a long period resulting in  
 2938 inconsistent volume sampling between the two wavelengths. This led to the adoption of the higher  
 2939 pulse rate double-pulsed 2-μm laser transmitter. In the double-pulse operation, two pulses are  
 2940 generated, which are separated by 150 to 200 μs, and thus requires only one laser to generate the  
 2941 on-line and off-line pulses for DIAL/IPDA profile or column measurement of CO<sub>2</sub>.

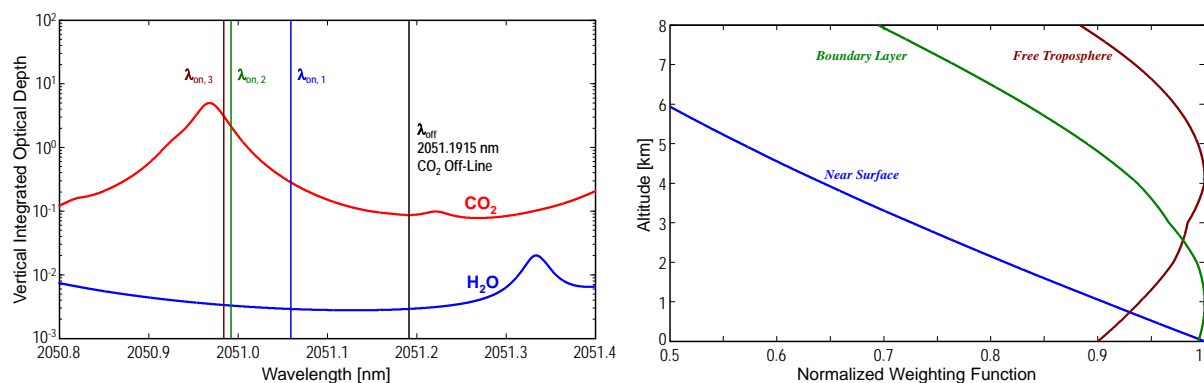
#### 2942 5.4.2.2 Double-Pulsed CO<sub>2</sub> IPDA Lidar for Aircraft



2943  
 2944 **Figure 5-38** Schematic of the 2-μm, double-pulsed, CO<sub>2</sub> IPDA lidar. Given an estimate of the O<sub>2</sub> column, a  
 2945 weighted-average dry-air volume mixing ratio of the target gas can be retrieved from this measurement by using the  
 2946 CO<sub>2</sub> weighting function, defined by the differential absorption cross section and the dry air mass. Figure 5-39 shows  
 2947 the total integrated vertical optical depth variation with wavelength for atmospheric CO<sub>2</sub> and H<sub>2</sub>O, the dominant  
 2948 interfering molecule. Optical depth calculations were conducted using the US Standard model for metrological  
 2949 profiles and gases mixing ratios and HITRAN for line parameters. IPDA operation is achieved by proper selection of  
 2950 the wavelengths of the laser pulses that are transmitted sequentially within the short time interval. The principle of  
 2951 wavelength selection in this technique is shown in Figure 5-39. The figure shows the normalized CO<sub>2</sub> pressure-based  
 2952 weighting functions at selected spectral positions for nadir IPDA measurement from an airborne platform versus  
 2953 altitude. The weighting function defines the altitude sensitivity of the measurement.

2954 Because it uses the strong reflection from hard targets, the IPDA lidar approach provides higher  
 2955 signal-to-noise ratio measurement compared to the range-resolved DIAL that depends on  
 2956 atmospheric backscatter. If the online wavelength setting is changed, then it will change the  
 2957 column weighting function. Therefore, the transmitter could be tuned to weight the column  
 2958 measurement near the surface for optimum CO<sub>2</sub> interaction studies or closer to line center for  
 2959 measurements of the free troposphere. Currently, NASA LaRC is developing a double-pulsed 2-  
 2960 μm direct detection IPDA lidar for CO<sub>2</sub> column measurement from an airborne platform (Singh et  
 2961 al., 2013) shown in Figure 5-38.

2962 By tuning the on-line position different weighting can be achieved. For example, tuning the on-  
 2963 line to  $\lambda_{on,1}$  weights the measurement toward the surface where CO<sub>2</sub> sources and sinks interactions  
 2964 take place. Tuning the on-line to  $\lambda_{on,2}$  weights the measurements toward the free troposphere.  
 2965 System simulations resulted of 0.2% total CO<sub>2</sub> optical depth error for  $\lambda_{on,1}$  operation, for 8 km  
 2966 flight altitude and 10 sec average. The corresponding signal-to-noise ratios for the on-line and off-  
 2967 line ocean return signals are  $1.1 \times 10^4$  and  $4.1 \times 10^3$ , respectively.



2968  
 2969 **Figure 5-39** Comparison of the CO<sub>2</sub> and H<sub>2</sub>O integrated optical depths. (Left) Comparison derived using the  
 2970 HITRAN 2008 database for line parameters and US Standard model for meteorological profiles. The vertical lines  
 2971 indicate wavelengths for the three laser pulses, for simultaneous CO<sub>2</sub> measurements with two different weighting  
 2972 functions (Right).

### 2973 5.4.2.3 Laser and Receiver Development

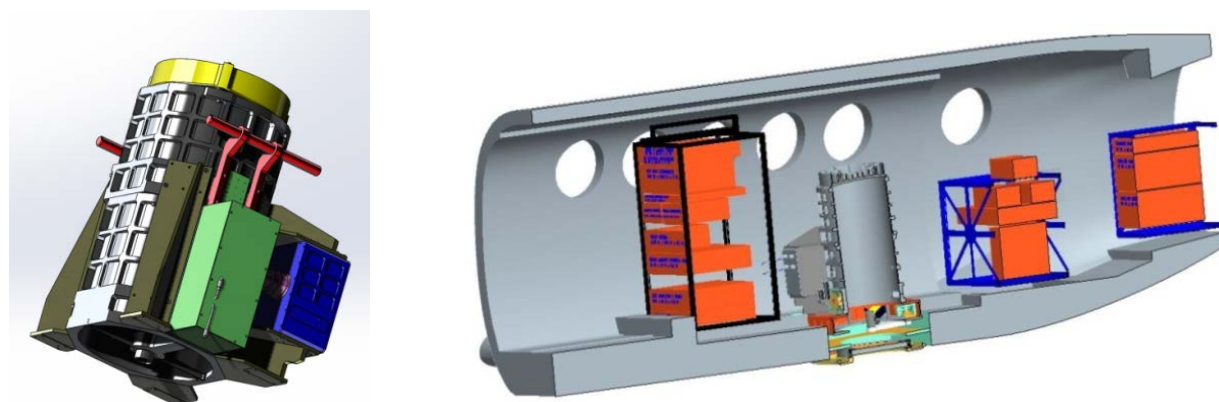
2974 Double-pulsed 2-μm lasers have been demonstrated with energy as high as 600 mJ and up to 10-  
 2975 Hz repetition rate (Yu et al., 2003). The two laser pulses are separated by 150 μs and can be tuned  
 2976 and locked separately. The CO<sub>2</sub> IPDA laser transmitter is based on the Ho:Tm:YLF high-energy  
 2977 2-μm pulsed laser technology. This laser transmitter is side pumped by AlGaAs diode arrays at  
 2978 792 nm. It is capable of generating two pulses with 100-mJ and 30-mJ energies at 10 Hz. For  
 2979 airborne use, the double-pulse operation allows maximizing the overlap between the on-line and  
 2980 off-line footprint on the ground resulting in sampling the same atmospheric volume. This feature  
 2981 enhances the IPDA measurement by reducing the sampling error. The emission wavelengths of  
 2982 the pulsed laser are determined by the wavelength control unit. The first pulse and the second  
 2983 pulse are injection seeded alternately by the on-line frequency and the off-line frequency,  
 2984 respectively. The laser transmitter is 29 x 67.3 x 16.5 cm in size, and weighs less than 70 lbs.

2985 The receiver telescope is a custom designed Newtonian with 40-cm diameter aluminum primary  
 2986 mirror. The shape of the primary mirror is hyperbolic allowing the returning signal can be focused  
 2987 to a spot with a diameter < 300 micron. A 300-μm diameter InGaAs pin photodiode detector has

2988 selected. Detector characterization showed a Noise-Equivalent Power (NEP) of  $6.8 \times 10^{-14} \text{ W/Hz}^{0.5}$   
 2989 at 30°C. After amplification the lidar signals are digitized and stored by a data acquisition unit.  
 2990 The data acquisition unit is based on two 200-MHz, 12-bit digitizers, where one monitors the  
 2991 laser energy and the other for the lidar return.

#### 2992 **5.4.2.4 Plans for Ground and Aircraft Testing**

2993 The IPDA lidar is designed for integration into a small research aircraft such as the NASA B-200.  
 2994 The mechanical design of the CO<sub>2</sub> IPDA lidar is compact and light weighted to meet the payload  
 2995 requirements for the aircraft, simultaneously with any CO<sub>2</sub> validation instruments. Figure 5-40  
 2996 shows a preliminary design concept of the Transmitter-Telescope-Receiver Integrating Structure  
 2997 of the CO<sub>2</sub> IPDA Lidar system as installed in a B-200 aircraft. The optical portal has already been  
 2998 modified and installed to readily accept the lidar system.



2999  
 3000 **Figure 5-40** Illustration of 2- $\mu\text{m}$ , double-pulsed IPDA lidar for airborne CO<sub>2</sub> measurements. (Left) Integrated, 2-  
 3001  $\mu\text{m}$ , double-pulsed IPDA lidar for airborne CO<sub>2</sub> measurement (Ramanathan et al., 2013). (Right) 2- $\mu\text{m}$  CO<sub>2</sub> double-  
 3002 pulsed IPDA system integration inside an aircraft, such as the NASA B-200 (Ramanathan et al., 2013).

3003 Initially the assembled CO<sub>2</sub> IPDA instrument will be ground tested in a mobile trailer with a  
 3004 calibrated horizontal hard target setup and then will be airborne demonstrated on the NASA  
 3005 Langley UC-12/B-200 aircraft. In ground testing the number density of CO<sub>2</sub> along with pressure,  
 3006 temperature, and relative humidity information obtained from ancillary measurements from in situ  
 3007 sensors are used to retrieve dry CO<sub>2</sub> mixing ratios. The data obtained during instrument testing  
 3008 will be evaluated, including comparisons to the in situ instruments and validation of the data with  
 3009 respect to the weather and geographical environment. IPDA instrument ground testing will  
 3010 include CO<sub>2</sub> retrieval algorithms development and comparison with in-situ sensors. The main  
 3011 validation goal is to evaluate the IPDA performance relative to the scientific objectives.

3012 CO<sub>2</sub> airborne validation will be achieved by comparison with in situ sensors (Picarro, Inc., and  
 3013 Li-Cor, Inc.) that will be included in the aircraft. Once validated, the plan is that this lidar will be  
 3014 useful for providing correlative measurements of column CO<sub>2</sub> to support the passive remote  
 3015 sensing satellites such as OCO-2, and GOSAT.

### 3016 **5.5 Plans for Demonstration of New Capabilities and Measurements**

3017 The airborne lidar campaigns provide an important opportunity to demonstrate the performance of  
 3018 candidate lidar techniques for ASCENDS. This is valuable given the wide variety of  
 3019 combinations of atmospheric scattering and extinction and surface backscatter and morphology  
 3020 that CO<sub>2</sub> measurements must be made under. As stated in the introduction, ASCENDS has several

3021 fundamentally unique capabilities. The airborne campaigns enable demonstrations of those  
3022 capabilities and performance assessments for a variety of environmental conditions. With each  
3023 successive campaign, the instruments, data analysis approaches and CO<sub>2</sub> retrieval algorithms  
3024 improve. These demonstrations and measurements result in improved modeling of candidate lidar  
3025 techniques for the ASCENDS mission. This section highlights the present plans for new  
3026 demonstrations and measurements during the next few years.

### 3027 **5.5.1 Additional Measurements Over Snow**

3028 Due to the optical absorption bands of water ice near 1560 and 2000 nm, snow has a low  
3029 reflectivity (typically a few percent) at both candidate CO<sub>2</sub> measurement wavelengths. The  
3030 reflectivity varies with the grain size of the ice crystals, and hence with the age and temperature of  
3031 the snow. In addition to these effects on the lidar backscatter, the degree to which other materials  
3032 are deposited on the snow can have a dramatic influence on the strength of the backscatter. Due to  
3033 the importance of the ASCENDS measurements at high latitudes, particularly in the winter  
3034 season, it is important to assess how the candidate lidars operate over a variety of snow-covered  
3035 surfaces and conditions.

3036 As described in Section 5.3, an ASCENDS airborne campaign was conducted during March 2013  
3037 primarily to target measurements over different types of snow-covered areas. One flight was  
3038 made over fresh snow-fields in high altitude mountain basins in the Rocky Mountains in  
3039 Colorado. A longer flight was also made east over the Rocky Mountains over Missouri, Iowa and  
3040 Wisconsin. When east of Nebraska, the second flight had extensive snow cover, intermixed with  
3041 houses and roads. The lidar directional reflectance (backscatter) as measured by the lidars when  
3042 flying over snow was largely consistent with Aoki et al. (2000) measurements. Flights over  
3043 snow-covered areas will be included in future flight campaigns, since demonstrating performance  
3044 over these conditions is directly relevant to the all-latitudes, all-seasons ASCENDS capability.  
3045 One characteristic of the snow-covered land areas that have been encountered to date is that they  
3046 are not completely snow-covered, which causes a wide dynamic range of lidar backscatter to  
3047 occur over relatively small spatial scales. Bare surfaces with much different reflectances include  
3048 trees, roads, rocks, dirt, and buildings. This raises the backscattered signal level when averaged  
3049 over a few km along the flight track. To what extent is there a reduction in dynamic range in  
3050 remote areas that are nearly or completely snow-covered? Currently we do not have an accurate  
3051 model for aged snow, or “dirty” snow due to deposition processes. Additional flight  
3052 measurements will address these questions and needs.

### 3053 **5.5.2 Measurements Over Forests**

3054 Lidar measurements over areas with tall trees are also of interest. These are more complex due to  
3055 the rapidly varying amount of time spreading (or time smear) in the reflected laser signals that  
3056 simultaneously illuminate the tree top, mid canopy, and ground beneath the tree. ASCENDS will  
3057 have a unique capability to measure the scattering surface elevation (SSE) over these areas and  
3058 use the SSE data to reduce uncertainties in CO<sub>2</sub> column retrievals. Since some areas of high  
3059 interest for the ASCENDS mission (such as Amazon region) are forested, understanding  
3060 measurement characteristics over areas with tall trees is important. Rapid changes in topographic  
3061 height when measuring over mountains also may cause a similar effect. During the 2013  
3062 campaign a flight was conducted over the coastal range of redwood trees from San Francisco CA  
3063 north to the Oregon border. This permitted a variety of lidar measurements over hills and low  
3064 mountains covered by redwood trees of various densities. All the primary lidar systems operated

3065 well over this region, and their measurement datasets are being analyzed now. The 2014  
3066 ASCENDS airborne campaign also included additional lidar measurements over forested areas,  
3067 and these data are also being investigated. Future flights are needed to address lidar  
3068 measurements over the snow-covered forest environment.

### 3069 **5.5.3 Demonstrating CO<sub>2</sub> Flux Measurements with Airborne Lidar**

3070 It is important to further demonstrate the capabilities of airborne CO<sub>2</sub> IPDA lidars to provide  
3071 measurements related to the determination of CO<sub>2</sub> fluxes from both natural and anthropogenic  
3072 sources. Logical candidates are CO<sub>2</sub> fluxes from large areas of rapidly growing crops (such as  
3073 corn) in the summertime, and CO<sub>2</sub> emissions from cities. Airborne campaigns that target these  
3074 types of measurements are important as initial demonstrations of ASCENDS-type measurements  
3075 to address local and regional scale questions about carbon exchange between the surface and  
3076 atmosphere.

### 3077 **5.5.4 Comparisons with Satellite Measurements Made with Passive Spectrometers**

3078 It will be valuable to compare airborne lidar measurements of CO<sub>2</sub> with those from passive  
3079 satellite instruments. Some initial attempts at these comparisons have been made with GOSAT.  
3080 OCO-2 has a denser sampling pattern on the Earth's surface. The planned start of measurements  
3081 with OCO-2 in August 2014 might allow for the first comparisons with that instrument.  
3082 Comparing lidar and OCO-2 measurements made nearly simultaneously under a variety of  
3083 conditions should be quite valuable and informative to the remote sensing community.  
3084 Underflights would most likely take place within the continental U.S. Lidar cal/val would also  
3085 include comparisons with on-board in situ CO<sub>2</sub> data made during spirals down to and within the  
3086 boundary layer. Methods for modeling the CO<sub>2</sub> column above the aircraft (~ 10-12 km) will be a  
3087 topic of discussion.

### 3088 **5.5.5 Improvements in Numerical Simulations of the ASCENDS Mission**

3089 The initial space mission simulations (Kawa et al., 2010) have been quite useful to start the  
3090 requirements analysis for the mission, to initiate simulations of flux retrievals, and to start to  
3091 assess the impacts of random and bias errors in the lidar measurements. However the initial  
3092 representations of the lidar measurements in these simulations were simplified. The existing  
3093 simulations are not yet adequate to fully exploit key features of the ASCENDS mission, such as  
3094 day/night measurements or measurements in polar regions during winter and during freeze/thaw  
3095 periods. It is highly desirable to improve the fidelity of the lidar measurement models in these  
3096 simulations. It is also desirable to expand the simulations to include range and CO<sub>2</sub> column  
3097 measurement to the tops of certain types of optically opaque clouds, such as marine stratus and  
3098 fair weather cumulus. Airborne measurements are beginning to show that such measurements can  
3099 provide useful additional information.

## 3100 **5.6 Needed Technology Developments for the ASCENDS Space Lidar**

3101 Many important capabilities for ASCENDS have been demonstrated by several of the airborne  
3102 lidar teams. These include CO<sub>2</sub> column absorption and range measurements with high precisions  
3103 and low biases over a wide variety of surface types, and measurements over a wide range of  
3104 altitudes. Some measurements have been demonstrated to cloud tops and through thin clouds.  
3105 Several teams have demonstrated accurate retrievals of CO<sub>2</sub> mixing ratios based on the airborne  
3106 lidar data in comparison with in situ data. Airborne measurements of O<sub>2</sub> column absorption and

3107 range have also been demonstrated which showed the expected variability with surface pressure.  
3108 Almost all measurement results have been presented at conferences and most have been published  
3109 in peer-reviewed journals. This work has greatly improved the ad hoc science definition team's  
3110 understanding of the capabilities needed from space for ASCENDS and represents significant  
3111 progress toward meeting the demands of the space mission. However, this work has also  
3112 identified key challenges that must be addressed to meet the requirements of the ASCENDS  
3113 mission. Some specific improvements needed in technology are summarized below.

#### 3114 **5.6.1 Generic Needs for Up-scaling Existing Airborne Lidar as "Bridge" to Space**

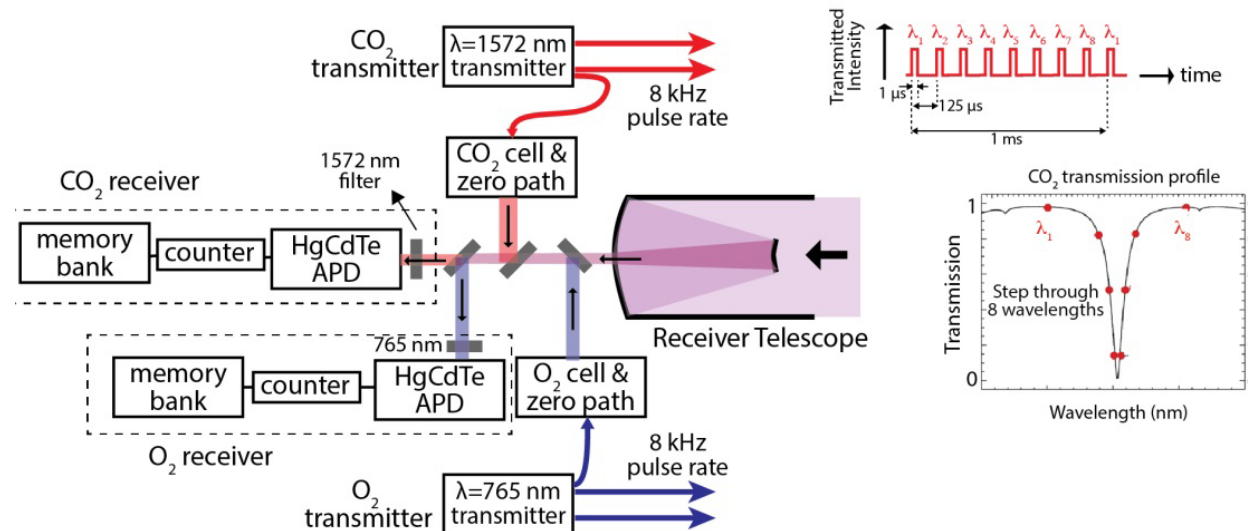
3115 For space use, a lidar has additional technical and engineering challenges beyond those for an  
3116 airborne lidar. These include: (1) a much longer range to the scattering surface (typically 400 km  
3117 for space vs  $\leq 12$  km for airborne). This significantly increases the loss from photon scattering to  
3118 the receiver (typically a factor of  $\geq 1100$ ), which must be overcome by much more laser power  
3119 and a larger receiver telescope. (2) A much faster along track velocity (7 km/sec vs 0.25 km/sec)  
3120 which increases the rate of reflectance variability. (3) A larger spot diameter (typically 100 m vs 2  
3121 m) on the surface, which can increase range spreading. (4) The need to withstand the launch  
3122 vibration and the vacuum and radiation environment of space. (5) For space, the lidar design and  
3123 instrument technology (including components like detectors) also must provide a high confidence  
3124 for at least 3-5 years of unattended operation.

3125 All the airborne lidar candidates need further investments to attain a high technical readiness for  
3126 space. The largest common factor is the need for improvement of the product of laser power and  
3127 telescope area to overcome the signal loss due to increased range from orbit. Direct detection lidar  
3128 can benefit by using a larger diameter telescope, but the laser power still must be increased  
3129 significantly, typically by a factor of 10-100, over current airborne instruments. The highest  
3130 common need is for a laser, that meets all other requirements and that also has the needed power  
3131 for space. The approach needs to have a viable technical path to achieve these ends in a robust  
3132 and mechanically rugged design that can be shown to have long unattended lifetime and also can  
3133 withstand the radiation and vacuum environment of space. The individual teams have addressed  
3134 the scaling of their approaches to space, and their progress towards this are summarized below.

##### 3135 **5.6.1.1 Scaling the CO<sub>2</sub> Sounder to Space**

3136 For space the CO<sub>2</sub> Sounder plan is to sample both gas absorption lines with 8 wavelengths, as  
3137 shown in Figure 5-41 and Figure 5-43. The time resolved laser backscatter is detected and range  
3138 resolution is used to isolate the return pulses from the surface and measure range.

3139 A block diagram of the space lidar concept is shown in Figure 5-41. The seed lasers are rapidly  
3140 switched from fixed locked wavelengths points, producing a repeating wavelength-stepped pulse  
3141 train. The lasers cycle through their wavelength steps every 1 msec. At an 8-KHz pulse rate, the  
3142 pulses are separated by 125  $\mu$ sec, which permits them to clear the bottom 19 km of the  
3143 atmosphere before the next pulse, to minimize crosstalk from cloud scattering. A 5-KHz pulse  
3144 rate can also be used to allow a 30 km unambiguous range, if needed, to accommodate higher  
3145 clouds. At the 7-km/sec spacecraft velocity the  $\sim 50$ -m diameter laser spot in the surface moves  
3146 0.9 m for each wavelength step. It is easy to show that in 10-second averaging time, this  
3147 sampling with highly overlapped footprints minimizes any random errors caused by variability in  
3148 surface reflectivity.

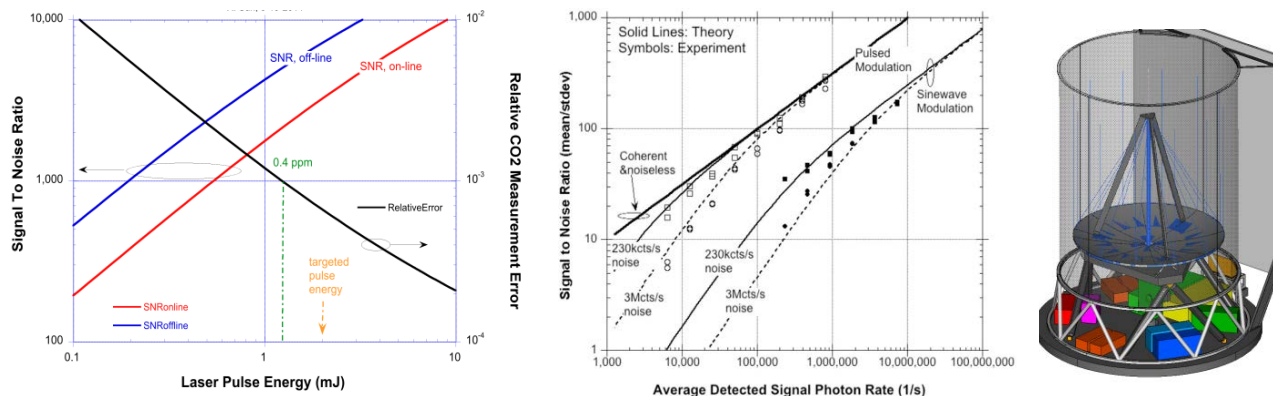


3149  
3150 **Figure 5-41** Block diagram of the space lidar instrument and wavelength-stepped pulse-train. (Left) Simultaneous  
3151 measurements are made of CO<sub>2</sub>, and O<sub>2</sub>, absorption line shapes, time of flight, and backscatter profiles at 1572.33 and  
3152 764.7 nm, respectively. The return light is collected by a common 1.2-m telescope and detected. (Right) Diagram of  
3153 the wavelength-stepped laser pulse-train used to measure the CO<sub>2</sub> & O<sub>2</sub> line absorptions.

3154 The CO<sub>2</sub> Sounder team has regularly assessed the measurement performance needed for the space  
3155 measurement. This work builds on space lidar SNR models, which their team has evolved from  
3156 work on the CO<sub>2</sub> Sounder airborne instrument and from ICESat/GLAS (Ice, Cloud and land  
3157 Elevation Satellite/Geoscience Laser Altimeter System) (Abshire et al., 2005). The calculations  
3158 analyze the signal, noise, and uncertainty in gas concentrations by calculating the average number  
3159 of signal photons, solar background photons, and detector noise observed over each 1-μsec pulse  
3160 interval. Preliminary analyses of errors in the airborne lidar are given in (Abshire et al., 2013,  
3161 2014). Recent examples and the presently targeted specifications for a space lidar are shown in  
3162 Figure 5-42.

3163 The calculations for space show that the random errors are limited by the detected signal photons  
3164 for the measurement wavelengths near the peak of the absorption line. That is the retrievals are  
3165 limited by the shot noise of the detected signal photons on the absorption line. The analysis of the  
3166 2011 airborne measurements is consistent with this model (Abshire et al., 2014), although the  
3167 space measurements benefit substantially from the higher sensitivity of the HgCdTe APD  
3168 detector.

3169 At the accuracies required for ASCENDS, there are many potential sources of bias error, both  
3170 from the environment (the atmosphere and the surface) and from the instrument. Some are  
3171 atmospheric scatter, varying topographic height, line spectroscopy, pressure shifts of the  
3172 absorption line, and instrument wavelength or baseline offsets. The CO<sub>2</sub> Sounder approach using  
3173 pulsed measurements with multiple wavelength samples on both sides of the CO<sub>2</sub> line allows  
3174 additional parameters to be “solved for” in the retrievals. This makes the measurements quite  
3175 robust against many potential causes of measurement bias. Analysis of the 2011 airborne  
3176 measurements shows that presently the bias errors are small (< 1.4 ppm) for aircraft altitudes > 5  
3177 km (Abshire et al., 2014). This residual error level will be reduced further as the airborne lidar  
3178 and the retrievals algorithms are improved.



3179  
3180

Common Parameters	Value	Specific values for :	CO2
Orbit Altitude	400 km	Online wavelength	1572.33 nm
Equator crossing time	dawn/dusk	Beam divergence	125 urad
Integration Time	10 sec (70 km)	Wavelength sequence rate	1.25 KHz
Telescope diameter	1.5 m	# of wavelengths in scan	8
Time between laser pulses	125 usec	On line (side of line) absorptio	40%
Laser Pulse widths	1 usec	Detector type & QE	HgCdTe APD, 75%

3181

3182 **Figure 5-42** Modeled and measured SNR for efficient pulse modulation technique. (Left top) Calculations of SNR  
 3183 and relative error in CO<sub>2</sub> column densities for the space lidar vs laser energy. 1.2-mJ laser pulse energies are needed  
 3184 for a 0.4-ppm precise measurement over a 40% diffuse reflectivity surface, similar to RRV Nevada. A conservative  
 3185 goal (with margin) is assuming 2-mJ energy is needed. The calculations above also have 3-dB margin. (Middle top)  
 3186 Results of a comparison (Sun and Abshire, 2012) of the receiver SNR vs signal for IPDA lidar using coherent  
 3187 detection with continuous wave (CW) lasers and direct detection with sinewave and pulse modulations. Our pulse  
 3188 modulation technique is much more efficient and requires only ~10% of the laser power to achieve the same SNR as  
 3189 sine wave modulation. (Right top) Drawing from a previous space instrument design lab study for the space lidar.  
 3190 (Bottom) Parameters for the SNR calculations.

3191 *Lidar Requirements Analysis for Space* – The CO<sub>2</sub> Sounder team periodically assesses the lidar  
 3192 performance needed for the space CO<sub>2</sub> measurement. This builds on our space lidar SNR models,  
 3193 which we have evolved from ICESat/GLAS (Ice, Cloud and land Elevation Satellite/Geoscience  
 3194 Laser Altimeter System) (Ehret et al., 2008) and applied to the IPDA measurement of CO<sub>2</sub>. The  
 3195 calculations analyze the signal, noise, and uncertainty in gas concentrations by calculating the  
 3196 average number of signal photons, solar background photons, and detector noise observed over  
 3197 each 1-μsec interval of the laser pulses. Recent results are shown in Figure 5-42.

3198 The calculations show that the CO<sub>2</sub> transmitter must emit ~1.2 mJ/pulse (12-W average power) to  
 3199 produce a 0.4-ppmv mixing ratio measurements from space to desert surfaces with a 1.5-m  
 3200 diameter telescope. To allow margin, our targeted energy is 2 mJ. The analysis of the CO<sub>2</sub>  
 3201 Sounder team (Sun et al., 2010) shows this is a very power-efficient approach to meet the CO<sub>2</sub>  
 3202 measurement requirements.

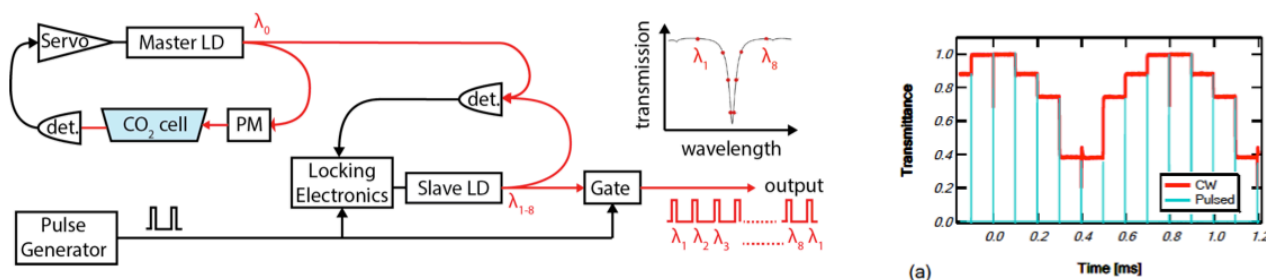
3203 **5.6.1.1.1 Space Lidar Technology for the CO<sub>2</sub> Sounder**

3204 *Laser Transmitter* – The CO<sub>2</sub> Sounder approach uses a master-oscillator power-amplifier  
 3205 (MOPA) approach for both the lasers. It uses tunable diode seed lasers, fiber laser preamplifiers,  
 3206 and power amplifier stages. This modular approach is flexible, and it leverages the lower power

3207 stages that have already been demonstrated in airborne campaigns. The power increase needed for  
3208 space is achieved adding power amplifiers to the prior stages, and so that the space laser is an  
3209 incremental step and is not a new development.

3210 The diode seed lasers for the CO<sub>2</sub> and O<sub>2</sub> wavelengths are highly developed, and have been space  
3211 qualified. To meet the precision, the online lasers need to be frequency stabilized to ~1 MHz  
3212 (Numata et al., 2012). The CO<sub>2</sub> Sounder Team has demonstrated locking the master laser diode  
3213 (DFB-LD) to the CO<sub>2</sub> line center and achieved frequency drifts < 0.3 MHz over 72 hours. They  
3214 have also demonstrated a new dynamically step-locked single laser diode seed source shown in  
3215 Figure 5-43. This source accurately and dynamically locks its output to 8 or more wavelengths  
3216 around the CO<sub>2</sub> absorption line. This allows a significant simplification to the seed laser stage.

3217 *Laser amplifiers* - The airborne lidar uses a commercial Erbium Doped Fiber Amplifier (EDFA)  
3218 as a preamplifier, and the total output energy is 25 μJ/pulse with 0.25-W average power. Lucent  
3219 LGS (Lucent Government Solutions) had previously developed a set of highly reliable EDFA  
3220 technologies for aircraft and space use. They previously space-qualified a 10-W brassboard  
3221 EDFA (Wysocki et al., 2006).



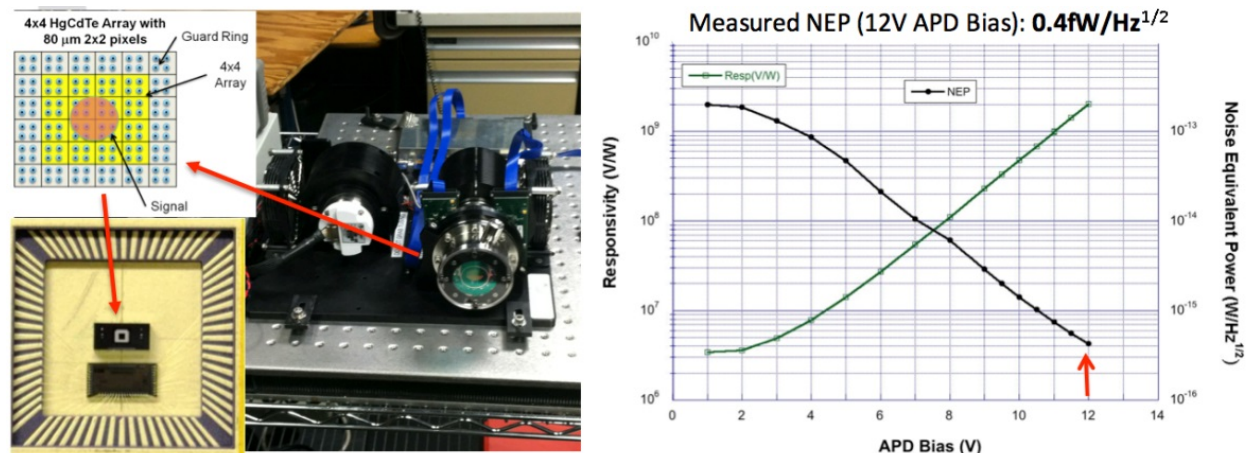
3222  
3223 **Figure 5-43** Schematic of a stepped wavelength locked source as shown in (Numata et al., 2012). (Left) The  
3224 master wavelength is locked to a CO<sub>2</sub> absorption cell. By offset-locking a slave laser at different frequency offsets to  
3225 the master, this approach generates a pulse train step-locked 8 discrete points on the 1572.335 nm CO<sub>2</sub> line. (Right)  
3226 Output from the laboratory demonstration when seed laser was wavelength stepping across a CO<sub>2</sub> line, as in the  
3227 middle sketch.

3228 For space this needs to be increased by ~80 times by a laser power amplifier. The team has  
3229 investigated two different approaches for the power amplifier stage: using a single channel Planar  
3230 WaveGuide amplifier (PWG - Raytheon) and using multiple large mode area fiber amplifier  
3231 channels in parallel (Fibertek). These amplifier approaches can be used both for the CO<sub>2</sub> and O<sub>2</sub>  
3232 lasers. Both approaches are attractive, although they have different engineering aspects and  
3233 tradeoffs. A breadboard of the Raytheon planar waveguide power amplifier is under final  
3234 development now, and a demonstration is planned during fall 2014.

3235 *Receiver Telescope* – For a space lidar, a large receiver telescope collects more backscatter, and  
3236 so be used reduce the laser power. The calculation above assumed a 1.5-m diameter receiver  
3237 telescope, which is available.

3238 *Lidar Detectors* –Both the CO<sub>2</sub> and O<sub>2</sub> lidar receivers need sensitive detectors. The CO<sub>2</sub> Sounder  
3239 plan is to utilize the new DRS HgCdTe e-APD (Beck et al., 2013) developed under the IIP-10  
3240 shown in Figure 5-44 as the detector for both channels. This detector has gain > 500, Quantum  
3241 Efficiency (QE) > 70% from 0.5 to 4 μm, photon-noise limited response) and a NEP < 0.4 fW/

3242 Hz<sup>1/2</sup>. Initial radiation tests show the detector is tolerant to the expected space radiation dose.  
3243 More radiation tests are scheduled.



3244  
3245 **Figure 5-44** The highly sensitive 4x4 element HgCdTe APD array inside a mini-dewar/cryocooler assembly  
3246 (*Photo*). This was developed by DRS for the CO<sub>2</sub> Sounder's IIP-10 task and was delivered in April 2013. The pixels  
3247 are square 80 μm on a side, which was chosen to match the needs for a CO<sub>2</sub> space lidar receiver. (*Plot*) Results from  
3248 Goddard's evaluation of the detector sensitivity shows at 12-V bias, the pixels have QE = 80% and noise equivalent  
3249 power of ~0.4 fW/root (HZ). This > 30 times more sensitive than previous solid-state detectors at 1.57 μm.

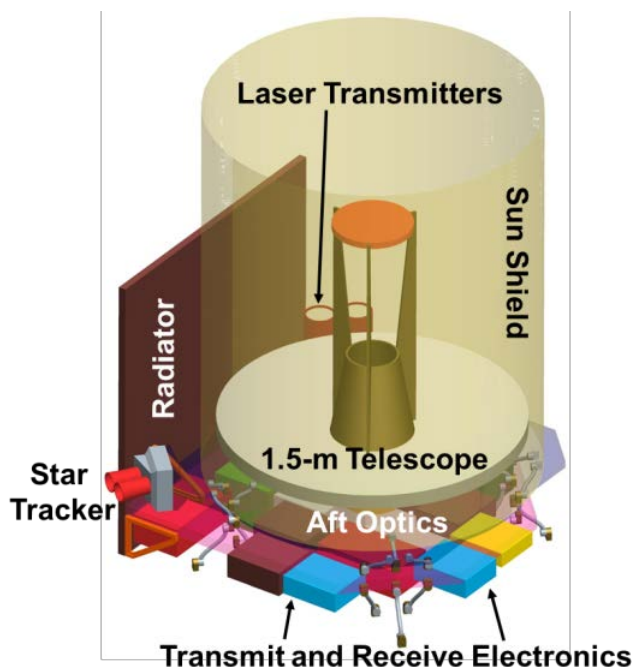
3250 The DRS detector operates at 80 K, which requires a cryo-cooler. A recent paper (Raab et al.,  
3251 2010) summarizes space cryocoolers since 1995. One option is a pulse-tube microcooler from  
3252 Northrup Grumman. This is attractive because it is small and can pump 1.3 W from a source load  
3253 at 77 K, more than is needed.

### 3254 5.6.1.2 Advancing Airborne IM-CW instruments to Space

3255 The LaRC ASCENDS team has developed a model for LAS system and CO<sub>2</sub> measurement  
3256 simulations (Lin et al., 2013). Such models are essential for the improvement of LAS systems and  
3257 the prediction of the performance of space CO<sub>2</sub> measurements for future space missions.  
3258 Validation tests show excellent agreements of simulated results with ground-based and airborne  
3259 LAS measurements (Lin et al., 2013). The simulations show a potential for the ASCENDS  
3260 mission using technologies that currently exist or are expected to be available within next few  
3261 years. The studied spaceborne IM-CW LAS instrument will achieve root-mean-square errors of  
3262 CO<sub>2</sub> column measurements for surfaces similar to the playa of Railroad Valley, NV within 0.1%  
3263 for 10-s averages (Lin et al., 2013). Figure 5-45 illustrates the basic structure of the space LAS  
3264 instrument which is expected to have a system architecture similar to that of the airborne LAS  
3265 instrument.

3266 Compared to the airborne lidar, the main changes for space are using two sideline wavelengths  
3267 with one at +3 pm (called Side-1) and the other at +10 pm (called Side-2) offset from the CO<sub>2</sub>  
3268 absorption line center; increasing the transmitted laser output power to 42 W; increasing the  
3269 telescope diameter to 1.5 m; reducing the receiver optical bandpass filter bandwidth to 0.5 nm  
3270 FWHM; and reducing the laser half-angle divergence to 50 μrad (Lin et al., 2013). The receiver's  
3271 FOV will be set to be 33% larger than that of laser divergence, and the optical throughput is  
3272 expected to be 0.65. The sideline wavelengths are selected to avoid excessive absorption by CO<sub>2</sub>  
3273 in the upper troposphere and lower stratosphere when tuned to the absorption line center, and to  
3274 have more sensitivity to CO<sub>2</sub> absorption across the mid to lower troposphere (lower-altitude

3275 weighting function), where most of the CO<sub>2</sub> flux exchanges with ecosystems and transports  
3276 within the atmosphere take place.



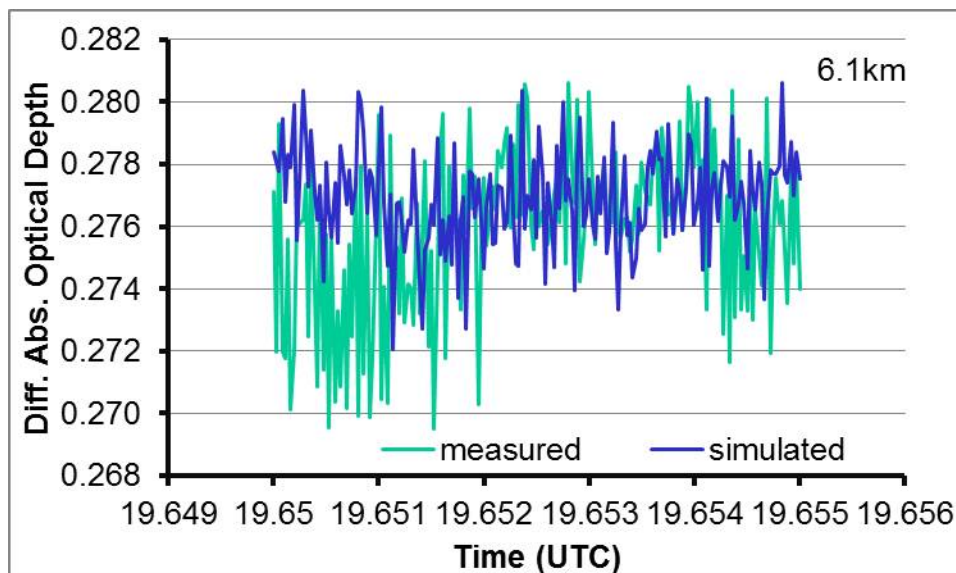
3277  
3278 **Figure 5-45** Concept for a space-based LAS lidar.

#### 3279 5.6.1.2.1 Model and Simulations for MFL Space Lidar

3280 The performance of the space lidar for CO<sub>2</sub> measurements was simulated using a model  
3281 developed by the LaRC Team (Lin et al., 2013). This model for the lidar and its measurement  
3282 environment are important to guide improvement of LAS systems and allows for predictions of  
3283 CO<sub>2</sub> measurements for future space missions. The model accounts for fundamental physics and  
3284 characteristics of the instruments and their related measurement environments. The model results  
3285 are presented statistically from simulation ensembles that include noise sources and uncertainties  
3286 related to the LAS instruments and the CO<sub>2</sub> measurement environment. The characteristics of  
3287 simulated LAS systems are based on existing technologies and their implementation in existing  
3288 systems.

3289 The modeled lidar is assumed to be IM-CW LAS systems such as the Multifunctional Fiber Laser  
3290 Lidar (MFL) operating in the 1.57 μm CO<sub>2</sub> absorption band. Environmental effects due to  
3291 variations in atmospheric CO<sub>2</sub>, solar radiation, turbulence, surface reflectance, and aerosols and  
3292 thin clouds are also included in the model. The simulated results show excellent agreement with  
3293 measurements (Lin et al., 2013). Figure 5-46 shows an example of the comparison of model-  
3294 simulated results with instrument measurements for the Railroad Valley playa flight on 3 August  
3295 2011 at 6.1-km altitude. The differences in CO<sub>2</sub> DAOD between model results and observations  
3296 are very small, clearly demonstrating the capability of the model in modeling the performance of  
3297 LAS systems and their CO<sub>2</sub> column measurements.

3298

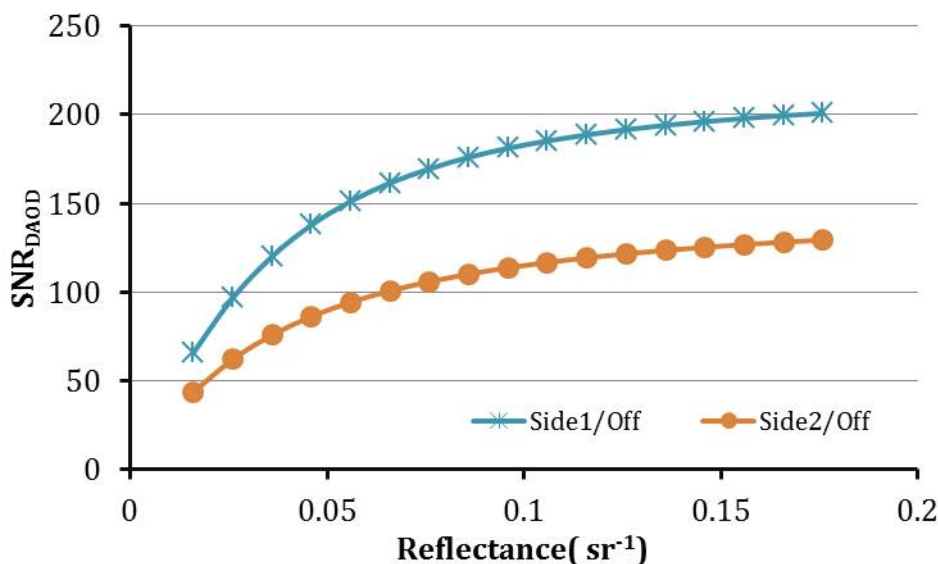


3299

3300 **Figure 5-46** Comparison of simulated results of DAODs with observations for RRV. The Railroad Valley playa  
3301 flight was on 3 August 2011. Data analyzed are for the flights at 6.1-km altitude.

3302 For the ASCENDS space mission, the assumptions are a sun-synchronous, dawn/dusk orbit (Ehret  
3303 et al., 2008) with an altitude of 390 km. Under clear conditions, simulation shows that the  
3304 precision of the DAOD measurements for surfaces similar to the playa of Railroad Valley, NV  
3305 (reflectance  $0.176 \text{ sr}^{-1}$ ) will be better than 0.07% for 10-s averages (Figure 5-47).

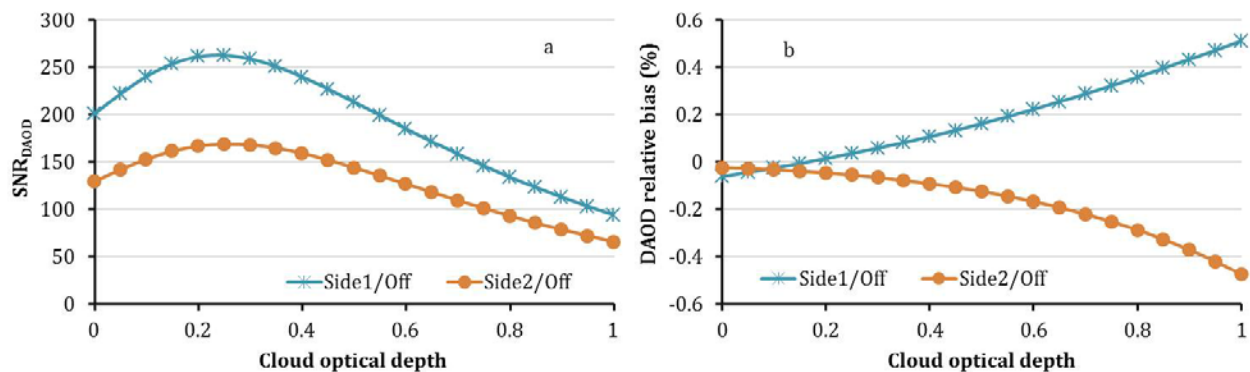
3306



3307

3308 **Figure 5-47** Simulated 0.1-s SNR<sub>DAOD</sub> for the space IM-CW LAS instrument for a range of surface reflectance  
3309 conditions.

3310 For other types of surfaces such as low-reflectivity snow and ice surfaces, the precision will be  
3311 within 0.23%. Including measurements through thin clouds with optical depths up to 1, the CO<sub>2</sub>  
3312 SNR<sub>DAOD</sub> measurements with 0.1-s integration period for surfaces similar to that of Railroad  
3313 Valley, NV will be greater than 94 and 65 for Side-1 and Side-2, respectively (Figure 5-48).



3314

3315 **Figure 5-48** Simulated 0.1-s results for a spaceborne lidar under thin cirrus cloud conditions. The CO<sub>2</sub> SNR<sub>DAOD</sub>  
 3316 (a) and relative bias error (b) values are calculated for the surface assuming the reflectance of Railroad Valley, NV.

3317 The CO<sub>2</sub> column bias errors introduced by the thin clouds are  $\leq 0.1\%$  for cloud optical depth  $\leq$   
 3318 0.4, but they could reach  $\sim 0.5\%$  for more optically thick clouds with optical depths up to 1  
 3319 (Figure 5-48 b).

3320 When the cloud and surface ranges and scattering amplitudes are obtained from the analysis of  
 3321 matched filter outputs, the cloud bias errors can be further reduced as seen from the compensating  
 3322 feature of the bias errors between the retrievals of the two sidelines (Figure 5-48 b). Other  
 3323 simulation studies indicate that the present IM-CW LAS concept for space can provide  
 3324 ASCENDS required CO<sub>2</sub> measurements from not only the dawn/dusk orbit but also other Low  
 3325 Earth Orbits (LEOs) such as sun-synchronous, day/night orbits, maximizing the flexibility of the  
 3326 space instrumentation to various CO<sub>2</sub> measurement needs.

### 3327 5.6.1.3 Scaling the BBL Lidar to Space

3328 It can be shown using simple arguments that to achieve a precision of 1 ppm the lidar receiver  
 3329 must detect on the order of 1-2 million photons per integration time. With a large telescope and  
 3330 sensitive detectors the million photons threshold can be reached with 20-40 Watts of emitted laser  
 3331 power. It is highly desirable that the detector used for ASCENDS have a high Quantum  
 3332 Efficiency (QE) and be able to respond to individual photons. As noted the latest version of the  
 3333 BBL splits the two detector functions—ranging and signal level measurement between two  
 3334 separate detectors. The BBL lidar plan is to use single photon counting modules (SPCM) used on  
 3335 ICESAT are employed to measure the LIDAR range and InGaAs or Mercury Cadmium Telluride  
 3336 (MCT) cameras as employed on SCanning Imaging Absorption Spectrometer for Atmospheric  
 3337 Cartography (SCIAMACHY) are used to measure signal level. The BBL calculations show this  
 3338 combination of detectors allows the BBL to achieve  $\sim 2$  million detected photons with a laser  
 3339 source that emits  $\sim 40$  Watts. The BBL performance simulations show that the Broad Band Lidar  
 3340 meeting the specifications summarized in Table 5-11 can meet the ASCENDS measurement  
 3341 requirements operating in clear air over surfaces including snow and open ocean.

3342

3343

**Table 5-11 Space-based Broad Band Lidar Parameters**

<b>Space-based Broad Band Lidar Parameters</b>	
Laser Average Output power:	
2.05 $\mu\text{m}$	30-40 W
0.68 $\mu\text{m}$	1 W
Laser-Pulse-Rate	8000 Hz
Telescope-Diameter	1 m
Detector type:	
2.05 $\mu\text{m}$	Rockwell HgCdTe Array
0.68 $\mu\text{m}$	Perkin-Elmer SPCM

3344

#### 3345 **5.6.1.4 Scaling the Pulsed 2- $\mu\text{m}$ CO<sub>2</sub> IPDA Lidar to Space**

3346 The 2- $\mu\text{m}$  IPDA lidar approach has also examined its pathway for CO<sub>2</sub> measurements from space.  
 3347 Table 5-12 summarizes technology parameters of the present airborne IPDA lidar, future IPDA  
 3348 system, and recently released pulsed 2- $\mu\text{m}$  IPDA technology development requirements from  
 3349 European Space Agency (ESA) (Ingmann et al., 2008) for their future space borne active sensing  
 3350 mission for measuring the dry-air mixing ratio of carbon dioxide throughout the atmosphere with  
 3351 a accuracy on the ppm level (Ingmann et al., 2008; NASA, 2008; Lawrence, 2011).

3352 The plans for laser development are consistent with the transmitter requirements as summarized  
 3353 in the table. This early development of a space qualifiable laser and airborne operation will reduce  
 3354 the risk towards space operation. Extending the CO<sub>2</sub> IPDA instrument capability to space also  
 3355 requires a detector with better performance than the present InGaAs pin detector. The electron  
 3356 avalanche photodiodes (eAPD) developed by DRS Technologies provide a possible solution  
 3357 (Beck et al., 2011). Table 5-12 lists a comparison between the selected pin detector and the eAPD  
 3358 with space requirements. The detector approach is an important aspect in this comparison.

3359

3360 **Table 5-12 Comparison of CO<sub>2</sub> state-of-the-art 2-μm current and proposed technology with**  
3361 **space requirement**

	Current Technology	Proposed Technology	Projected Space Requirement [2]
	<b>Laser Transmitter</b>		
	<b>Single Laser</b>	<b>Single Laser</b>	<b>Two Lasers</b>
Technology	Liquid-Cooled, Airborne laser	Conductively-Cooled Space Qualifiable laser	Column CO <sub>2</sub> Space Mission
Technique	Double-Pulse	Triple-Pulse	Single-Pulse
Laser Wavelength (μm)	2.051	2.051	2.051
Pulse Energy (mJ) 1 <sup>st</sup> /2 <sup>nd</sup> /3 <sup>rd</sup> Pulse	100/30 Double Pulse	50/15/5 Triple Pulse	40/5 Single Pulse
Pulse Repetition Rate (Hz)	10	50	50
Power (W)	1.3	3.5	2.25
Pulse Width FWHM (ns)	200	30-100	50
Optical to Optical Efficiency (%)	4.0	5.0	5.0
Wall Plug Efficiency (%)	1.44	2.1	>2.0
Delay between pulses (200 μsec)	200	200	250+/-25
Transverse/Longitudinal Modes	TEM <sub>00</sub> /Single Mode	TEM <sub>00</sub> /Single Mode	TEM <sub>00</sub> /Single Mode
Pulse Spectral Width FWHM (MHz)	2.2	4-14	> 60
Beam Quality (M2)	2	2	< 2
Frequency Control Accuracy (MHz)	0.3	0.3	0.2
Seeding Success Rate /Spectral Purity (%)	>99/99.9	>99/99.9	>99/99.9
	<b>Detector</b>		
Material	InGaAs	HgCdTe	N/A
Structure	Pin photodiode	eAPD	APD
Quantum Efficiency (%)	68	80	75
Excess-Noise-Factor	---	1.1	1.5
Noise-Equivalent-Power (fW/Hz <sup>1/2</sup> )	200	8	100

3362

3363 **5.7 Ongoing Technology Development Activities and Planned for Results**

3364 So far during the formulation of the ASCENDS mission, NASA has supported several different  
3365 candidate lidar approaches and teams. This has yielded many benefits, has engaged many lidar  
3366 researchers, and has helped develop a broader understanding of the mission needs and candidate  
3367 lidar approaches. This work, including the airborne campaigns, has been very valuable and it

3368 should continue. However as the ASCENDS mission matures, the mission needs will shift more  
3369 toward lidar technology and engineering.

3370 Several of the airborne instrument teams are addressing different aspects of the space instrument  
3371 needs. These include studies to determine the required laser power, simulations of space  
3372 measurements, and preliminary engineering studies of candidate space instruments. Some initial  
3373 airborne lidar demonstrations of the O<sub>2</sub> column measurements have also been made. Under ESTO  
3374 IIP support there has been the successful development of candidate detectors for the space  
3375 mission, and there is ongoing work to demonstrate some approaches toward laser power scaling.

### 3376 **5.7.1 Technology Developments Needed for ASCENDS**

3377 There are several types of technology development activities needed to increase the readiness and  
3378 reduce the risk of the ASCENDS space lidar(s). The lowest risk approach is to incrementally  
3379 build on capabilities already demonstrated in airborne campaigns. These include work to:

- 3380 a. Improve the fidelity of the space instrument requirements via more realistic  
3381 mission simulations and with improved models to infer CO<sub>2</sub> fluxes.
- 3382 b. Update tradeoff assessments addressing mission benefits vs costs/risks for the O<sub>2</sub>  
3383 lidar.
- 3384 c. Improve the airborne O<sub>2</sub> lidar's column measurement capabilities with the goal to  
3385 reach a similar state of readiness already shown for CO<sub>2</sub>. A particular need is for  
3386 increased O<sub>2</sub> laser power in the airborne lidar.
- 3387 d. In the context of an overall lidar instrument design, including spacecraft resource  
3388 requirements (mass, power, envelope, data rate), demonstrate the space-needed  
3389 power for the CO<sub>2</sub> laser(s), while maintaining the other required laser properties.
- 3390 e. Depending on the outcome of (b), demonstrate the space-needed output power and  
3391 efficiency for the O<sub>2</sub> laser, while maintaining the other required laser properties.
- 3392 f. Demonstrate measurements with the space evolving subsystems, perhaps via an  
3393 ASCENDS airborne simulator, to verify they achieve the needed performance and  
3394 science measurements.
- 3395 g. Conduct preliminary designs for the space lasers that address the required output  
3396 power; power conversion efficiency; mechanical design; thermal, vacuum and  
3397 radiation tolerance; and lifetimes.
- 3398 h. Assess lifetime and radiation tolerance of candidate detectors.
- 3399 i. Conduct preliminary lidar instrument and mission studies to allow an early view  
3400 on tradeoffs and an initial assessment of critical areas.
- 3401

3402 To be cost effective it is recommended that NASA: (1) develop a process for evaluating and  
3403 selecting the highest priority space lidar approaches to concentrate on for this part of the mission  
3404 development, and (2) develop acquisition and implementation strategies for the ASCENDS  
3405 payload.

3406 **6. Mission Design**3407 **6.1 Introduction**

3408 In 2012, NASA's Earth Science Division (ESD) requested the Earth Systematic Mission Program  
 3409 Office (ESMPO) to perform a mission study to determine the feasibility of accommodating a  
 3410 conceptual ASCENDS instrument on commercially available spacecraft buses as well as the  
 3411 feasibility of flying a conceptual observatory on an Evolved Expendable Launch Vehicle (EELV)  
 3412 and in a Dual Spacecraft System (DSS) configuration. The team was made up of representatives  
 3413 from the ESMPO, the Goddard Space Flight Center (GSFC), the Jet Propulsion Laboratory (JPL)  
 3414 and the Langley Research Center (LaRC). The mission study covered eight areas and includes  
 3415 assessments in the areas of mass, power, mechanical/thermal interface, volumetric, attitude  
 3416 determination and control (AD&CS), telecom, mission operations, and de-orbit considerations.  
 3417 Assessments captured design requirements, assumptions, finding and results, design rationale,  
 3418 design risks, and additional comments. The generic instrument parameters used in the study are  
 3419 captured in the Table 6-1 shown below. The final report (Hyon et al., 2012) has documented the  
 3420 results and findings of the assessments, summarized those results and findings, and provided  
 3421 recommendations for future studies.

3422 Throughout the report, Ball's BCP 2000 bus has been used as an example of a bus appropriate for  
 3423 supporting the ASCENDS mission. Buses from other manufacturers, including Boeing, Lockheed  
 3424 Martin, Northrop Grumman, Orbital Dulles and Orbital Gilbert are also quite capable of  
 3425 supporting the ASCENDS mission. The Figure 6-1 depicts one of the spacecraft configurations  
 3426 with hosted payload and the ASCENDS instrument.

3427 **Table 6-1 ASCENDS Generic Instrument Parameters**

Parameter	Generic Payload 1	Generic Payload 2
<b>Mission Parameters:</b>		
Measurement	CO <sub>2</sub> , O <sub>2</sub> , and altimetry	CO <sub>2</sub> and altimetry
<b>Launch Requirements:</b>		
Nominal Orbit	Sun-sync, ~noon crossing	Sun-sync, ~noon crossing
Altitude (Km)	~450 km ± TBD km	~450 km ± TBD km
Inclination	Polar	Polar
Design Operational Life	3 yrs with propellant for 6 yrs	3 yrs with propellant for 6 yrs
Current Best Estimate (CBE) Instrument Size (m)	<2.5 tall x 2 x 2	<2.5 tall x 1.5 x 1.5

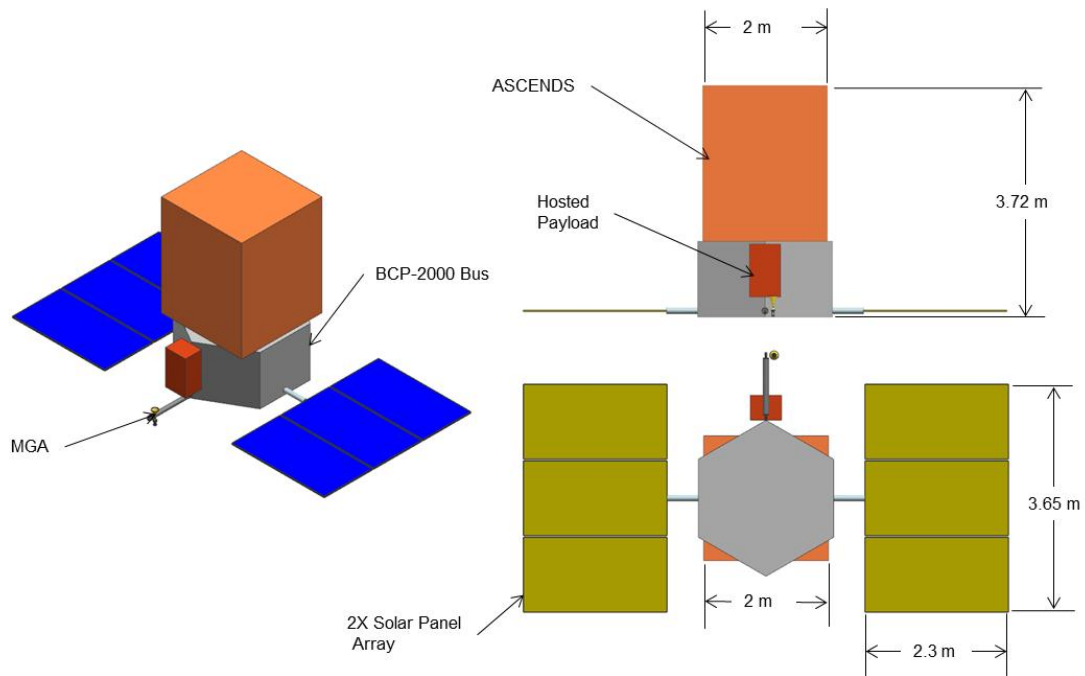
Parameter	Generic Payload 1	Generic Payload 2
<b>Science and C&amp;D Handling:</b>		
Average Science Data Rate (Mbps)	20	20
Maximum Science Data Rate (Mbps)	-	-
Instrument Housekeeping Telemetry		
Instrument Housekeeping Telemetry Data Rate (Mbps)	0.1	0.1
Onboard Data Storage (Gbits/day)	~1750/day	~1750/day
<b>Instrument Mass:</b>		
Total Instrument Mass Allocation (CBE+Margin, kg)	<470	<400
<b>Instrument Power:</b>		
Total Instrument Power Allocation (CBE+Margin, W)	<1100	<750
<b>Mechanical Interface:</b>		
Mechanical Interface, e.g., kinematic, planar, etc.	Instrument to I/F panel - Kinematic	Instrument to I/F panel - Kinematic
Interface Panel or hard mount to bus	I/F panel	I/F panel
Field of View (FOV)	<1.5° about nadir	<1.5° about nadir
<b>Attitude Control:</b>		
Pointing Knowledge	5 arc sec	5 arc sec
Pointing Control	20 arc sec	20 arc sec
Jitter	0.4 arc sec over 4 ms and 5 arc sec over 20 ms	0.4 arc sec over 4 ms and 5 arc sec over 20 ms
<b>Attitude Control Subsystem (ACS):</b>		

Parameter	Generic Payload 1	Generic Payload 2
Global Positioning System (GPS) Receiver	YES	YES
Post Processing GPS onboard knowledge	-	-
Star Trackers	YES	YES
Major Maneuvers	Yaw flip as required; calibration as required; on orbit stability after maneuvers	Yaw flip as required; calibration as required; on orbit stability after maneuvers
<b>Instrument Thermal Requirement:</b>		
Thermally isolated	YES	YES
Thermal FOV	Based on instrument thermal requirements	Based on instrument thermal requirements
Cryo Cooler	Will be provided as part of the ASCENDS instrument	Will be provided as part of the ASCENDS instrument
<b>Propulsion</b>		
	Required for orbit maintenance.	Required for orbit maintenance.
Design	Standard biprop or monoprop blowdown	Standard biprop or monoprop blowdown
<b>Observatory Environmental &amp; Facility (driven by Instrument):</b>		
NASA Risk Classification	Sensor: C Platform: B	Sensor: C Platform: B
Electromagnetic Interference / Electromagnetic Compatibility (EMI/EMC)	Per MIL-STD-461C, tailored as required	Per MIL-STD-461C, tailored as required
Vibe	General Environmental Verification Specification (GEVS) for Atlas & F9 LV	GEVS for Atlas & F9 LV
Thermal Vacuum (TVAC)	YES	YES
Radiation	Meet orbit levels	Meet orbit levels
Cleanroom Class	As required	As required

Parameter	Generic Payload 1	Generic Payload 2
Special Facility Needs	Per instrument type	Per instrument type
<b>Mission Operations:</b>		
S/C ballistic coefficient	2.2	2.2
Cross-sectional area	19.1 m <sup>2</sup>	19.1 m <sup>2</sup>

3428

3429



3430

3431 **Figure 6-1** Hosted payload mounted to the side of the spacecraft bus.

3432

**The team has concluded that there are many commercial buses available with Falcon 9 or Atlas V launch vehicle in order to accommodate existing lidar concepts. With a CO<sub>2</sub> lidar only option, a follow-on study will develop more cost effective spacecraft bus and launch options.**

3433

## 3434 **6.2 Summary of Assessment**

### 3435 **6.2.1 Summary**

3436 A preliminary study of conducting a lidar-based, CO<sub>2</sub> mapping mission of ASCENDS has been  
3437 published in the report (Hyon et al., 2012). Although a variety of potential spacecraft buses have  
3438 been included in the sections on volumetric assessment of accommodating the ASCENDS  
3439 instrument, the Ball BCP2000 bus has been assumed as the baseline for the sections on power,  
3440 mechanical/thermal, AD&CS, and telecom assessment. The design assessments are developed  
3441 based on a preliminary design from Ball, as enhanced via a JPL Team X study conducted in June  
3442 2012

3443 Therefore, the results of this study are that multiple commercially available spacecraft buses  
3444 should be able to support accommodating an ASCENDS instrument with the parameters used in  
3445 this study with minor mission specific modifications. Examples include but are not limited to a  
3446 larger propulsion system and propellant for orbit maintenance maneuvers as well as a larger  
3447 power system to accommodate the instrument power requirements. Additionally, the Falcon 9 or  
3448 Atlas V (EELV) launch vehicle can accommodate an ASCENDS observatory with the parameters  
3449 used in this study in a single manifest configuration. A dual manifest configuration is also  
3450 possible if the ASCENDS instrument is limited in volume to approximately 2.5m tall by 1.8m by  
3451 1.8m.

### 3452 **6.2.2 Recommendations for Future Studies**

3453 Future studies of spacecraft buses capable of supporting the ASCENDS mission and a TBD  
3454 hosted payload (e.g., EV-I) should consider a more thorough and detail approach to describing the  
3455 subsystems as documented in the report (Hyon et al., 2012). Of course, the point-of-departure  
3456 should be the existing buses as documented by Ball, Boeing, Lockheed Martin, Northrop  
3457 Grumman, and Orbital. Any other approach that assumes the design of a customized bus would  
3458 result in an ASCENDS mission priced beyond the estimated, future NASA budget for the  
3459 ASCENDS mission.

3460 In addition to future spacecraft studies mentioned above, the trade studies listed below are  
3461 planned to be assessed by each center in the near future.

- 3462 1. Determination of risk classification for the spacecraft bus and instrument
- 3463 2. Orbital debris assessment to determine if a controlled re-entry will be required
- 3464 3. Evaluating orbit altitudes from 350 – 450 km and impact on the mission
- 3465 4. Examination of the trade space for the next generation of laser instruments
- 3466 5. Investigations to determine if the instrument resolution needs to change to accommodate  
3467 orbit and/or spacecraft attitude control capability

### 3468 **6.2.3 Recommendation for an Implementation Schedule**

3469 As a notional launch date of no earlier than 2021, we recommend a mission implementation  
3470 duration for 5.5 years between start of Phase A to launch. From the past mission implementations  
3471 of this class of missions, it is reasonable to have this phase duration with sufficient reserves to  
3472 control risks. As a result, the project Preliminary Design Review (PDR) can occur as late as 5  
3473 years before the launch and Mission Concept Review (MCR) will occur 2 years before PDR.

3474 Table 6-2 provides a notional schedule of mission implementation, where FY N denotes the first  
 3475 year of Phase A. Establishment of a science working group will occur 3 years before Phase A.  
 3476 The level 1 mission requirements will be finalized 1 year before Phase A, and the level 2 mission  
 3477 requirements will be finalized by MCR.

3478 **Table 6-2 Notional schedule of mission implementation**

ASCENDS Phase A-E schedule		FY N				FY N+1				FY N+2				FY N+3				FY N+4				FY N+5				FY N+6			
		Q4	Q1	Q2	Q3	Q4	Q1	Q2	Q3	Q4	Q1	Q2	Q3	Q4	Q1	Q2	Q3	Q4	Q1	Q2	Q3	Q4	Q1	Q2	Q3	Q4	Q1	Q2	Q3
Sept30 revision		Phase A				Phase B				KDP C				KDP D				KDP E											
Mission milestones		Δ SRR/MDR				Δ PDR				Δ CDR				Δ SIR				FRR Δ launch											
Instrument schedules						Δ Inst PDR				Δ Inst CDR				Δ Del Rev															
o Instrument milestones						Res																							
o Instrument formulation						Res																							
o Instrument Prototype to TRL 6		Upgrade to TRL 6*				Res																							
o Instrument FM implementation														Res															
Spacecraft schedule						Δ SC PDR				Δ SC CDR																			
o SC milestones						Δ Selected				Res																			
o Procurement activities (GSFC schedule)						Res																							
o SC formulation						Res																							
o SC subsystem implementation														Res															
Integration and test schedule																		Res											
o I&T Milestones														Δ SIR				ETRR Δ				PSR Δ							
MOS/GDS schedule										Δ PDR				Δ CDR								ORR Δ							
o MOS/GDS milestones										Res																			
o MOS/GDS formulation										Res																			
o Testbeds														Res															
o MOS/GDS implementation																		Res											

3479

## 3480 **7. Summary**

### 3481 **7.1 Summary**

3482 Globally-distributed atmospheric CO<sub>2</sub> measurements are essential for understanding the Earth's  
3483 carbon cycle and its interactions with the climate. A critical remote sensing challenge is to  
3484 provide atmospheric CO<sub>2</sub> measurements with sufficient coverage, accuracy and sampling  
3485 frequency to allow the locations and magnitudes of CO<sub>2</sub> sources and sinks to be inferred from the  
3486 small changes they cause in atmospheric CO<sub>2</sub> concentrations.

3487 Two satellite missions have been developed specifically to measure atmospheric CO<sub>2</sub> using  
3488 passive spectrometers: the Japanese GOSAT satellite and NASA's OCO-2 mission. The  
3489 contributions of these passive missions to understanding the global carbon cycle are significant.  
3490 When conditions are favorable, these approaches allow accurate measurements of atmospheric  
3491 CO<sub>2</sub> from space.

3492 However, passive approaches also have inherent limitations in coverage, since favorable  
3493 conditions require sunlit scenes, free of clouds, with low scattering, and with accurate estimates of  
3494 surface elevation within their footprint. There are many important regions for carbon cycle and  
3495 climate studies where favorable conditions seldom occur. For passive sensors, atmospheric  
3496 conditions such as clouds and variations in scattering, coupled with surface elevation errors  
3497 (which change the length of the measurement path) can cause bias. These biases grow with  
3498 cloudy scenes and with solar zenith angle and so are particularly troublesome in the tropics and at  
3499 high latitudes. The sparse coverage at high latitudes is a serious limitation, particularly for the  
3500 Northern Hemisphere, since this region exhibits substantial emissions even in low-light  
3501 conditions.

3502 In contrast, the ASCENDS mission carries its own laser source whose characteristics are carefully  
3503 optimized for these measurements. This approach allows simultaneous measurements of CO<sub>2</sub>  
3504 column absorption and range to be taken day and night, over ocean and land surfaces, at all  
3505 latitudes, and at all times of year. The lidar approach also allows altitude-weighted measurements  
3506 with enhanced sensitivity to CO<sub>2</sub> in the lower troposphere, where the CO<sub>2</sub> concentrations respond  
3507 more strongly to surface fluxes. Because the lidar has a small FOV and is nadir pointed, it can see  
3508 through gaps in clouds. The ASCENDS capability will enable more frequent observations of the  
3509 southern ocean, especially in the wintertime, where the oceans are otherwise inaccessible to  
3510 passive measurements. Since ASCENDS can make measurements regardless of sun angle and  
3511 local time, various non-sun synchronous orbits also can be considered to provide additional  
3512 information about the diurnal cycle of flux.

3513 NASA has organized the ASCENDS Ad Hoc Science Definition Team to lead the mission  
3514 definition activities. Their work has focused on developing the mission's science and  
3515 measurement objectives, conducting science mission modeling studies, and carrying out initial  
3516 engineering studies of spacecraft concepts. A large fraction of the ASCENDS work has involved  
3517 developing and demonstrating candidate lidar approaches in airborne campaigns. Candidate  
3518 techniques that have been demonstrated include two direct-detection lidar approaches that  
3519 measure both range and CO<sub>2</sub> using an absorption line near 1570 nm. Two approaches have  
3520 demonstrated measurements of CO<sub>2</sub> using a line near 2051 nm: a CW heterodyne approach and a  
3521 pulsed direct detection approach that measures both range and CO<sub>2</sub> absorption using the same

3522 line. NASA's Earth Science Technology Office has supported the development of the key lidar  
3523 technologies.

3524 In parallel with the technique development and system-level demonstrations, Observing System  
3525 Simulation Experiments (OSSEs) are being conducted to assess the characteristics of the CO<sub>2</sub>  
3526 fluxes that can be inferred from space-based lidar measurements with various candidate levels of  
3527 measurement precision and accuracy. The mission simulations have used a lidar measurement  
3528 model with surface reflectivity maps from MODIS and information on cloud and aerosol heights  
3529 and extinctions from the Calipso Mission. OSSE analysis has identified some mission science  
3530 tradeoffs and the formulation of an initial set of ASCENDS measurement requirements.

3531 Preliminary instrument and space mission engineering studies also have been conducted on  
3532 generic lidar candidate instruments that are suitable for the mission. The payload parameters are  
3533 consistent with a medium-sized spacecraft bus to be flown in a polar ~400 km altitude orbit. No  
3534 significant engineering issues have been identified at this stage of mission definition.

## 3535 7.2 Ongoing Work and Plans

3536 A number of activities are either ongoing or planned for the near future. These are summarized  
3537 below by focus area.

3538

3539 7.2.1. Activities Planned for the Modeling Group Include:

3540 • *Further quantification of bias reduction impacts on CO<sub>2</sub> flux inference. These include*  
3541 *assembling and better estimating OCO-2 biases, refining the ASCENDS bias scenarios,*  
3542 *and computing updated flux and uncertainty reduction estimates.*

3543 • *Updating random error comparison with actual OCO-2 error magnitudes and*  
3544 *distributions.*

3545 • *Testing the impact of surface pressure errors from meteorological analyses on flux errors*  
3546 *and comparing those to the expected flux errors from a laser-based O<sub>2</sub> pressure*  
3547 *measurement*

3548 • *Testing the possible benefit of ASCENDS diurnal information by examining dawn/dusk*  
3549 *and precessing orbits.*

3550 • *Exploring the potential advantages of vertical profile information from ASCENDS*  
3551 *measurements above cloud tops*

3552 • *More closely examining the impact of solving for flux processes*

3553 • *Developing recommendations to NRC's Decadal Survey for CO<sub>2</sub> measurement*  
3554 *requirements from space in the post-OCO-2 timeframe*

3555 7.2.2 Activities Planned for Atmospheric Analysis Include:

3556 • *Completing the baseline analyses of surface and upper-air model uncertainties, and*  
3557 *developing common statistical metrics to provide uniform analysis results, and enable*  
3558 *comparisons between metric results*

3559 • *Summarizing the analyses of surface and upper-air model uncertainties results in a peer*  
3560 *review publication.*

3561 • *Completing the baseline impact analysis of uncertainty in knowledge of atmospheric state*

3562 *on retrieved XCO<sub>2</sub> by expanding study to 2051 nm and 765 nm wavebands, and providing*  
3563 *the characterization of expected end-to-end errors on notional retrieval process.*

3564 • *Providing a common representative data set of surface/upper-air observed and modeled*  
3565 *atmospheric state values for use in assessment of proposed instrument performance.*

3566 7.2.3 Activities Planned and Needed for the Measurement Group Include Further  
3567 Demonstrating Capabilities and Measurements from Aircraft. Some Ongoing Needs  
3568 are:

3569 • *Additional measurements over snow - Snow has a low reflectivity at CO<sub>2</sub> measurement*  
3570 *wavelengths. The reflectivity varies with the age and temperature of the snow.*

3571 • *Additional measurements over forests - Some areas of high interest for the ASCENDS*  
3572 *mission (such as Amazon region) are forested, understanding measurements over areas*  
3573 *with tall trees is important.*

3574 • *Demonstrating CO<sub>2</sub> flux retrievals based on airborne lidar data - Logical candidates are*  
3575 *CO<sub>2</sub> fluxes from large areas of rapidly growing crops (such as corn) in the summertime,*  
3576 *and CO<sub>2</sub> emissions from cities.*

3577 • *Comparing airborne lidar to satellite measurements – Further comparing lidar and OCO-*  
3578 *2 measurements made nearly simultaneously, under a variety of conditions, will be quite*  
3579 *valuable and informative*

3580 • *Improving the fidelity of numerical simulations of instrument performance for the*  
3581 *ASCENDS mission.*

3582 • *Expanding the mission simulations to include measurements to the tops of some clouds,*  
3583 *where initial analysis of airborne measurements show they provide valuable information.*

3584 7.2.4 Activities are Needed to Further Develop Lidar Technology.

3585 All the lidar candidate approaches need technology improvements to attain a high  
3586 technical readiness for space. The lowest risk approach is to incrementally build on capabilities  
3587 already demonstrated in the airborne campaigns. These include work to:

3588 • *Improve the fidelity of the derived space instrument requirements via more realistic*  
3589 *mission simulations and with improved models to infer CO<sub>2</sub> fluxes.*

3590 • *Demonstrate the laser power needed to meet the required performance for the ASCENDS*  
3591 *mission, while maintaining the other required laser properties.*

3592 • *Update tradeoff assessments addressing mission benefits vs. costs/risks for the O<sub>2</sub> lidar.*

3593 • *If the O<sub>2</sub> measurement is retained as a mission requirement, then improve the airborne O<sub>2</sub>*  
3594 *lidar column measurement capabilities to reach a similar state of readiness as CO<sub>2</sub>.*

3595 • *Assess space lifetime of candidate detectors.*

3596 • *Conduct further lidar instrument and mission studies to allow updated views on tradeoffs*  
3597 *and assessments of critical areas.*

3598 7.2.5 Activities Needed for the ASCENDS Mission Planning and Development Include:

3599 • *Assessing instrument accommodations for CO<sub>2</sub> and range measurement-only options,*

3600 • *Studying launch vehicle accommodations, and*

- 3601       • *Updating the preliminary study of lidar and mission costs.*
- 3602       Accurate and globally-distributed atmospheric CO<sub>2</sub> measurements are essential to improve our  
3603       understanding the Earth's carbon cycle and its interactions with the climate. The ASCENDS  
3604       approach, using an orbital IPDA lidar, will allow these measurements over a much wider variety  
3605       of conditions than is possible with passive sensors. These more accurate measurements, with  
3606       wider spatial coverage, are key to address important questions about the locations, strengths and  
3607       evolution of the regional CO<sub>2</sub> fluxes needed for climate models.
- 3608

3609 **Appendices**3610 **A. References**

- 3611
- 3612 [ACOS B2.10 REF] ACOS Level 2 Standard Product: Data User's Guide, v3.4. (2013). *CO<sub>2</sub>*  
3613 *Virtual Science Data Environment*. Retrieved from:  
3614 [https://co2.jpl.nasa.gov/static/docs/v3.4\\_DataUsersGuide-RevB\\_131028.pdf](https://co2.jpl.nasa.gov/static/docs/v3.4_DataUsersGuide-RevB_131028.pdf)
- 3615 [Anon, n.d.] Anon. (n.d.). Standard atmospheric lapse rate. *National Oceanic and Atmospheric*  
3616 *Administration (NOAA), NASA, United States Air Force*. Retrieved from:  
3617 <http://ntrs.nasa.gov/archive/nasa/casi.ntrs.nasa.gov/19770009539.pdf>
- 3618 [Aben et al., 2007] Aben, I., O. Hasekamp and W. Hartmann. (2007, April 3). Uncertainties in  
3619 the space-based measurements of CO<sub>2</sub> columns due to scattering in the Earth's  
3620 atmosphere. *J. Quant. Spectrosc. Radiat. Transfer, Vol. 104* (Issue 3), pp. 450-459
- 3621 [Abshire et al., 2005] Abshire J. B., X. Sun, H. Riris, J. M. Sirota, J. F. McGarry, S. Palm, D. Yi  
3622 and P. Liiva. (2005, November). Geoscience Laser Altimeter System (GLAS) on the  
3623 ICESat Mission: On-orbit measurement performance. *Geophys. Res. Lett., Vol. 32* (Issue  
3624 21). L21S02. DOI: 10.1029/2005GL024028
- 3625 [Abshire et al., 2008] Abshire, J. B., H. Riris, G. Allan, S. Kawa, J. Mao, E. Wilson, M. Stephen,  
3626 M. Krainak, X. Sun and C. Weaver. (2008). Laser sounder approach for global  
3627 measurements of tropospheric CO<sub>2</sub> mixing ratio from space. 24<sup>th</sup> International Laser Radar  
3628 Conference, Boulder, Colorado.
- 3629 [Abshire et al., 2010a] Abshire, J. B., H. Riris, G. R. Allan, C. J. Weaver, J. Mao, X. Sun, W. E.  
3630 Hasselbrack, ... and E. V. Browell. (2010, November 2). A lidar approach to measure CO<sub>2</sub>  
3631 concentrations from space for the ASCENDS Mission. *Proc. SPIE Vol. 7832, Lidar*  
3632 *Technologies, Techniques, and Measurements for Atmospheric Remote Sensing VI*, paper  
3633 78320D. Retrieved from: <http://dx.doi.org/10.1117/12.868567>. DOI: 10.1117/12.868567
- 3634 [Abshire et al., 2010b] Abshire, J. B., H. Riris, G. R. Allan, C. J. Weaver, J. Mao, X. Sun, W. E.  
3635 Hasselbrack, S. R. Kawa, and S. Biraud. (2010, November). Pulsed airborne lidar  
3636 measurements of atmospheric CO<sub>2</sub> column absorption. *Tellus B, Vol. 62* (Issue 5), pp.  
3637 770-783. DOI: 10.1111/j.1600-0889.2010.00502.x
- 3638 [Abshire et al., 2011] Abshire, J. B., H. Riris, G. R. Allan, C. J. Weaver, J. Mao, X. Sun, W. E.  
3639 Hasselbrack, M. Rodriguez, and E. V. Browell. (2011). Pulsed airborne lidar  
3640 measurements of CO<sub>2</sub> column absorption. 2011 Earth Science Technology Forum  
3641 (ESTF2011), Pasadena, CA, June 21-23, 2011, NASA ESTO ESTF-2011 Conference.  
3642 Avail from: [http://esto.nasa.gov/conferences/estf2011/papers/Abshire\\_ESTF2011.pdf](http://esto.nasa.gov/conferences/estf2011/papers/Abshire_ESTF2011.pdf)
- 3643 [Abshire et al., 2013] Abshire, J. B., H. Riris, C. J. Weaver, J. Mao, G. R. Allan, W. E.  
3644 Hasselbrack and E.V. Browell. (2013). Airborne measurements of CO<sub>2</sub> column absorption  
3645 and range using a pulsed direct-detection integrated path differential absorption lidar.  
3646 *Appl. Opt., Vol. 52* (Issue 19), pp. 4446-4461
- 3647 [Abshire et al., 2014] Abshire, J.B., A. Ramanathan, H. Riris, J. Mao, G.R. Allan, W.E.  
3648 Hasselbrack, C.J. Weaver, and E.V. Browell. (2014). Airborne Measurements of CO<sub>2</sub>

- 3649 Column Concentration and Range Using a Pulsed Direct-Detection IPDA Lidar. *Remote*  
3650 *Sensing, Vol. 6* (Issue 1), pp. 443-469. DOI:10.3390/rs6010443
- 3651 [Allan et al., 2008] Allan, G.R., H. Riris, J.B. Abshire, X. Sun; E. Wilson, J. F. Burris, and M. A.  
3652 Krainak. (2008, March). Laser Sounder for Active Remote Sensing Measurements of CO<sub>2</sub>  
3653 Concentrations. *Proceedings of Aerospace Conference, 2008 IEEE*, pp. 1-7. DOI:  
3654 10.1109/AERO.2008.4526387
- 3655 [Amediak et al., 2008] Amediak, A., A. Fix, M. Wirth and G. Ehret. (2008). Development of an  
3656 OPO system at 1.57  $\mu\text{m}$  for integrated path DIAL measurement of atmospheric carbon  
3657 dioxide. *Applied Physics B*, 92, pp. 295
- 3658 [Amediak et al., 2012] Amediak A., X. Sun, J. B. Abshire. (2012, May). Analysis of Range  
3659 Measurements From a Pulsed Airborne CO<sub>2</sub> Integrated Path Differential Absorption Lidar.  
3660 *IEEE Transactions on Geoscience and Remote Sensing, Vol. 51* (Issue 5), pp. 1-7. DOI:  
3661 10.1109/TGRS.2012.2216884
- 3662 [Amediak et al., 2013] Amediak A., X. Sun, and J. B. Abshire. (2013, May). Analysis of Range  
3663 Measurements From a Pulsed Airborne CO<sub>2</sub> Integrated Path Differential Absorption Lidar.  
3664 *IEEE Transactions on Geoscience and Remote Sensing, Vol. 51* (Issue 5), pp. 2498-2504.  
3665 DOI: 10.1109/TGRS.2012.2216884
- 3666 [Andres et al., 2011] Andres, R. J., J. S. Gregg, L. Losey, G. Marland, and T. A. Boden. (2011,  
3667 July). Monthly, global emissions of carbon dioxide from fossil fuel consumption. *Tellus B*,  
3668 *Vol. 63* (Issue 3), pp. 309-327.. DOI: 10.1111/j.1600-0889.2011.00530.x
- 3669 [Andres et al., 2012] Andres, R. J., T. A Boden, F.-M. Bréon, P. Ciais, S. Davis, D. Erickson, J.  
3670 S. Gregg, ... and K. Treanton. (2012). A synthesis of carbon dioxide emissions from  
3671 fossil-fuel combustion. *Biogeosciences Discuss, Vol. 9*, pp. 1299-1376. DOI:  
3672 10.5194/bgd-9-1299-2012
- 3673 [Aoki et al., 2000] Aoki, T., T. Aoki, M. Fukabori, A. Hachikubo, Y. Tachibana, and F. Nishio.  
3674 (2000). Effects of snow physical parameters on spectral albedo and bidirectional  
3675 reflectance of snow surface. *J. Geophys. Res.: Atmospheres, Vol. 105* (Issue D8), pp.  
3676 10219-10236. DOI: 10.1029/1999JD901122
- 3677 [Archer et al., 2009] Archer, D., M. Eby, V. Brovkin, A. Ridgwell, L. Cao, U. Mikolajewicz, K.  
3678 Caldeira, ... and K. Tokos. (2009, May). Atmospheric Lifetime of Fossil Fuel Carbon  
3679 Dioxide. *Annual Review of Earth and Planetary Sciences, Vol. 37*, pp. 117 -134.
- 3680 [Badger et al., 2013] Badger, M. P. S., D. N. Schmidt, A. Mackensen, and R. D. Pancost. (2013,  
3681 October 28). High-resolution alkenone palaeobarometry indicates relatively stable pCO<sub>2</sub>  
3682 during the Pliocene (3.3–2.8 Ma). *Phil. Trans. R. Soc. A, Vol. 371*.
- 3683 [Baker et al., 2006] Baker, D. F., S. C. Doney, and D. S. Schimel. (2006, November). Variational  
3684 data assimilation for atmospheric CO<sub>2</sub>. *Tellus Series B Chemical and Physical*  
3685 *Meteorology, Vol. 58* (Issue 5), pp. 359-365.
- 3686 [Baker et al., 2008] Baker, I.T., L. Prihodko, A.S. Denning, M. Goulden, S. Miller, and H.R. da  
3687 Rocha. (2008, March). Seasonal drought stress in the Amazon: Reconciling models and  
3688 observations. *Journal of Geophysical Research: Biogeosciences (2005–2012), Vol. 113*,  
3689 (Issue G1). G00B01, DOI: 10.1029/2007JG000644

- 3690 [Ballantyne et al., 2012] Ballantyne, A. P., C.B. Alden, J.B. Miller, P.P. Tans, and J.W.C. White.  
3691 (2012, August 2). Increase in observed net carbon dioxide uptake by land and oceans  
3692 during the past 50 years. *Nature* 488, pp.70-72. DOI: 10.1038/nature11299
- 3693 [Basu et al., 2013] Basu, S., S. Guerlet, A. Butz, S. Houweling, O. Hasekamp, I. Aben, P.  
3694 Krummel, ... and D. Worthy. (2013). Global CO<sub>2</sub> fluxes estimated from GOSAT  
3695 retrievals of total column CO<sub>2</sub>. *Atmospheric Chemistry and Physics*, 13, pp. 8695–8717.  
3696 DOI: 10.5194/acp-13-8695-2013
- 3697 [Beck et al., 2011] Beck, J.D., R. Scritchfield, P. Mitra, W. Sullivan III, A.D. Gleckler, R.  
3698 Strittmatter and R.J. Martin. (2011, May 12). Linear-mode photon counting with the  
3699 noiseless gain HgCdTe e-APD. *Proc. SPIE 8033, Advanced Photon Counting Techniques*  
3700 V, 80330N. DOI: 10.1117/12.886161
- 3701 [Beck et al., 2013] Beck, J., J. McCurdy, M. Skokan, C. Kamilar, R. Scritchfield, T. Welch, P.  
3702 Mitra, X. Sun, J. Abshire, and K. Reiff. (2013, May 21). A highly sensitive multi-element  
3703 HgCdTe e-APD detector for IPDA lidar applications. *Proc. SPIE 8739, Sensors and*  
3704 *Systems for Space Applications VI*, 87390V. Retrieved from:  
3705 <http://dx.doi.org/10.1117/12.2018083>. DOI: 10.1117/12.2018083
- 3706 [Belikov et al., 2014] Belikov, D.A., A. Bril, S. Maksyutov, S. Oshchepkov, T. Saeki, H. Takagi,  
3707 Y. Yoshida, ... and T. Yokota. (2014). Column-averaged CO<sub>2</sub> concentrations in the  
3708 subarctic from GOSAT retrievals and NIES transport model simulations *Polar*  
3709 *Science*. Retrieved from: <http://dx.doi.org/10.1016/j.polar.2014.02.002>
- 3710 [Boden et al., 2013] Boden, T.A., G. Marland, and R.J. Andres. (2013). Global, Regional, and  
3711 National Fossil-Fuel CO<sub>2</sub> Emissions. *Carbon Dioxide Information Analysis Center*.  
3712 Retrieved from [http://cdiac.ornl.gov/trends/emis/meth\\_reg.html](http://cdiac.ornl.gov/trends/emis/meth_reg.html) DOI:  
3713 10.3334/CDIAC/00001\_V20
- 3714 [Bösch et al., 2011] Bösch, H., D. Baker, B. Connor, D. Crisp and C. Miller. (2011). Global  
3715 Characterization of CO<sub>2</sub> Column Retrievals from Shortwave-Infrared Satellite  
3716 Observations of the Orbiting Carbon Observatory-2 Mission. *Remote Sens., Vol. 3* (Issue  
3717 2), pp. 270-304. DOI: 10.3390/rs3020270, 2011
- 3718 [Bovensmann et al., 2010] Bovensmann, H., M. Buchwitz, J. P. Burrows, M. Reuter, T. Krings,  
3719 K. Gerilowski, O. Schneising, J. Heymann, A. Tretner, and J. Erzinger. (2010). A remote  
3720 sensing technique for global monitoring of power plant CO<sub>2</sub> emissions from space and  
3721 related applications. *Atmos. Meas. Tech.*, 3, pp. 781–811. DOI: 10.5194/amt-3-781-2010
- 3722 [Browell et al., 2008] Browell, E. V., M. E. Dobbs, J. Dobler, S. Kooi, Y. Choi, F. W. Harrison,  
3723 B. Moore III, and T. S. Zaccheo. (2008). Airborne demonstration of 1.57-micron laser  
3724 absorption spectrometer for atmospheric CO<sub>2</sub> measurements. Proc. of 24th International  
3725 Laser Radar Conference, S06P-13, Boulder, CO, June 23-27, 2008.
- 3726 [Browell et al., 2009a] Browell, E. V., M. E. Dobbs, J. Dobler, S. Kooi, Y. Choi, F. W. Harrison,  
3727 B. Moore III, and T. S. Zaccheo. (2009). First airborne laser remote measurements of  
3728 atmospheric CO<sub>2</sub> for future active sensing of CO<sub>2</sub> from Space. Presented at the  
3729 Proceedings of the 8th International Carbon Dioxide Conference, Jena, Germany, 13–18  
3730 September 2009a.

- 3731 [Browell et al., 2009b] Browell, E. V., M. E. Dobbs, J. Dobler, S. Kooi, Y. Choi, F. W. Harrison,  
3732 B. Moore III, and T. S. Zaccheo. (2009). First Airborne Laser Remote Measurements Of  
3733 Atmospheric Carbon Dioxide. Presented at Fourth Symposium on Lidar Atmospheric  
3734 Applications, Proc. 89<sup>th</sup> AMS Annual Meeting, Phoenix, Arizona, January 11-15, 2009.
- 3735 [Browell et al., 2010] Browell, E.V., J. Dobler, S. Kooi, Y. Choi, F.W. Harrison, B. Moore III,  
3736 and T. Scott Zaccheo. (2010). Airborne Validation of Laser Remote Measurements of  
3737 Atmospheric Carbon Dioxide. Proc., 25th International Laser Radar Conference 2010,  
3738 S6O-03, St. Petersburg, Russia, July 5-9, 2010 (ILRC 25).
- 3739 [Browell et al., 2011] Browell, E.V., J.T. Dobler, S.A. Kooi, M.A. Fenn, Y. Choi, S.A. Vay,  
3740 F.W. Harrison, and B. Moore. (2011). Airborne laser CO<sub>2</sub> column measurements:  
3741 Evaluation of precision and accuracy under wide range of conditions. Presented at the Fall  
3742 AGU Meeting, San Francisco, California, 5–9 December 2011.
- 3743 [Browell et al., 2012] Browell, E.V., J.T. Dobler, S.A. Kooi, M.A. Fenn, Y. Choi, S.A. Vay, F.  
3744 W. Harrison, and B. Moore III. (2012). Airborne Validation of Laser CO<sub>2</sub> and O<sub>2</sub> Column  
3745 Measurements. Proc. 92<sup>nd</sup> AMS Annual Meeting, New Orleans, LA, January 22-26, 2012.
- 3746 [Bruneau et al., 2006] Bruneau, D., F. Gibert, P.H. Flamant and J. Pelon. (2006). Complementary  
3747 study of differential absorption lidar optimization in direct and heterodyne detections.  
3748 *Appl. Opt.*, Vol. 45 (Issue 20), pp. 4898-4908.
- 3749 [Campbell et al., 2014] Campbell, J.F., B. Lin, and A. Nehrir. (2014). Advanced sine wave  
3750 modulation of continuous wave laser system for atmospheric CO<sub>2</sub> differential absorption  
3751 measurements. *Applied Optics, Volume 53* (ssue 5), pp. 816-829.  
3752 Retrieved from: <http://www.opticsinfobase.org/ao/abstract.cfm?URI=ao-53-5-816>
- 3753 [Caron and Durand, 2009] Caron, J., and Y. Durand. (2009). Operating wavelengths optimization  
3754 for a spaceborne lidar measuring atmospheric CO<sub>2</sub>. *Appl. Opt.*, Vol. 48 (Issue 28), pp.  
3755 5413-5422.
- 3756 [Chen et al., 2006] Chen, Y., S. Sun-Mack, R. F. Arduini, and P. Minnis. (2006). Clear-sky and  
3757 surface narrowband albedo variations derived from VIRS and MODIS data. Proc. AMS  
3758 12th Conf. Atmos. Radiation, Madison, WI, July 10-14, CD-ROM, 5.6.
- 3759 [Chevallier et al., 2007] Chevallier, F., F.-M. Bréon, and P. J. Rayner. (2007). Contribution of the  
3760 Orbiting Carbon Observatory to the estimation of CO<sub>2</sub> sources and sinks: Theoretical  
3761 study in a variational data assimilation framework. *J. Geophys. Res.*, 112, D09307, DOI:  
3762 10.1029/2006JD007375
- 3763 [Chevallier et al., 2009] Chevallier, F., S. Maksyutov, P. Bousquet, F. M. Bréon, R. Saito, Y.  
3764 Yoshida, and T. Yokota. (2009). On the accuracy of the CO<sub>2</sub> surface fluxes to be  
3765 estimated from the GOSAT observations. *Geophys. Res. Lett.*, Vol. 36, L19807. DOI:  
3766 10.1029/2009GL040108
- 3767 [Chevallier et al., 2014] Chevallier, F., P. I. Palmer, L. Feng, H. Boesch, C. W. O'Dell, and P.  
3768 Bousquet. (2014). Toward robust and consistent regional CO<sub>2</sub> flux estimates from in situ  
3769 and spaceborne measurements of atmospheric CO<sub>2</sub>. *Geophys. Res. Lett.*, Vol. 41 (Issue 3),  
3770 pp. 1065–1070. DOI: 10.1002/2013GL058772

- 3771 [Choi et al., 2008] Choi, Y., S. A. Vay, K. P. Vadrevu, A. J. Soja, J-H Woo, S. R. Nolf, G. W.  
3772 Sachse, ... and H. E. Fuelberg. (2008). Characteristics of the atmospheric CO<sub>2</sub> signal as  
3773 observed over the conterminous United States during INTEX NA (Intercontinental  
3774 Chemical Transport Experiment-North America). *J. Geophys. Res.*, Vol. 113 (Issue D7).  
3775 D07301, DOI: 10.1029/2007JD008899
- 3776 [Ciais et al., 2010] Ciais, P., J. G. Canadell, S. Luysaert, F. Chevallier, A. Shvidenko, Z. Poussi,  
3777 M. Jonas, P. Peylin, A. W. King, E.-D. Schulze, S. Piao, C. Rödenbeck, W. Peters, and F.-  
3778 M. Bréon. (2010, October). Can we reconcile atmospheric estimates of the Northern  
3779 terrestrial carbon sink with land-based accounting? *Current Opinion in Environmental*  
3780 *Sustainability*, Vol. 2 (Issue 4), pp. 225-230.
- 3781 [Clough and Iacono, 1995] Clough, S. A., and M. J. Iacono. (1995). Line-by-line calculation of  
3782 atmospheric fluxes and cooling rates: 2. Application to carbon dioxide, ozone, methane,  
3783 nitrous oxide and the halocarbons. *J. of Geophys. Res.*, Vol. 100 (Issue D8), pp. 16519-  
3784 16535. DOI: 10.1029/95JD01386
- 3785 [Clough et al., 2005] Clough, S.A., M. W. Shephard, E.J. Mlawer, J.S. Delamere, M.J. Iacono, K.  
3786 Cady-Pereira, S. Boukabara, and P.D. Brown. (2005, March). Atmospheric radiative  
3787 transfer modeling: a summary of the AER codes. Short Communication. *J. Quant.*  
3788 *Spectrosc. Radiat. Transfer*, Vol. 91 (Issue 2), pp.233-244.
- 3789 [Conway et al., 1994] Conway, T. J., P. P. Tans, L. S. Waterman, K. W. Thoning, D. R. Kitzis, K.  
3790 A. Masarie, and N. Zhang. (1994). Evidence for interannual variability of the carbon cycle  
3791 from the National Oceanic and Atmospheric Administration/Climate Monitoring and  
3792 Diagnostics Laboratory Global Air Sampling Network. *J. Geophys. Res.*, Vol. 99, (Issue  
3793 D11), pp. 22831–22855. DOI: 10.1029/94JD01951
- 3794 [Conway et al., 2009] Conway, T.J., P.M. Lang, and K.A. Masarie. (2009, July 15). Atmospheric  
3795 Carbon Dioxide Dry Air Mole Fractions from the NOAA ESRL Carbon Cycle  
3796 Cooperative Global Air Sampling Network, 1968-2008., Version: 2009-07-15. Retrieved  
3797 from: [ftp://cdiac.ornl.gov/pub/ndp005/README\\_flask\\_co2.html](ftp://cdiac.ornl.gov/pub/ndp005/README_flask_co2.html)
- 3798 [Creeden et al., 2008] Creeden D., M. Jiang, P. A. Budni, P. A. Ketteridge, S. D. Setzler, Y. E.  
3799 Young, J. C. McCarthy, P. G. Schunemann, T. M. Pollak, P. Tayebati, and E. P. Chicklis.  
3800 (2008, April 14). Thulium fiber laser-pumped mid-IR OPO. *SPIE Proc.*, Vol. 6952. DOI:  
3801 10.1117/12.775196
- 3802 [Crisp et al., 2012] Crisp, D., B. M. Fisher, C. O'Dell, C. Frankenberg, R. Basilio, H. Bösch, L.  
3803 R. Brown, ... and Y. L. Yung. (2012). The ACOS CO<sub>2</sub> retrieval algorithm -- Part II:  
3804 Global X<sub>CO2</sub> data characterization. (2012). *Atmos. Meas. Tech.*, Vol. 5, pp. 687–707. DOI:  
3805 10.5194/amt-5-687-2012
- 3806 [Davis and Grainger, 2003] Davis, and C. A. Grainger. (2003). A near-field tool for simulating  
3807 the upstream influence of atmospheric observations: The Stochastic Time-Inverted  
3808 Lagrangian Transport (STILT) model, *Geophys. Res.*, Vol. 108 (D16), pp. 4493. DOI:  
3809 10.1029/2002JD003161
- 3810 [Dee et al., 2011] Dee, D.P., S. M. Uppala, A. J. Simmons, P. Berrisford, P. Poli, S. Kobayashi,  
3811 U. Andrae, ... and F. Vitart. (2011, April 28). The ERA-Interim reanalysis: configuration  
3812 and performance of the data assimilation system. *Quarterly Journal of the Royal*

- 3813 *Meteorological Society, Vol. 137* (Issue 656), pp.553-597. DOI: 10.1002/qj.828. Retrieved  
3814 from <http://onlinelibrary.wiley.com/doi/10.1002/qj.828/abstract>
- 3815 [DeFries et al., 2002] DeFries, R.S., R. A. Houghton, M. C. Hansen, C. B. Field, D. Skole, and  
3816 J. Townshend. (2002). Carbon emissions from tropical deforestation and regrowth based  
3817 on satellite observations for the 1980s and 1990s. *Proc. Natl. Acad. Sci., Vol. 99* (No. 22),  
3818 pp.14256-14261. DOI: 10.1073/pnas.182560099
- 3819 [Denning et al., 1996] Denning, A.S., G.J. Collatz, C. Zhang, D.A. Randall, J.A. Berry, P.J.  
3820 Sellers, G.D. Colello, and D.A. Dazlich. (1996, September). Simulations of terrestrial  
3821 carbon metabolism and atmospheric CO<sub>2</sub> in a general circulation model, Part 1: Surface  
3822 carbon fluxes. *Tellus B, Vol. 48* (Issue 4), pp. 521-542. DOI: 10.1034/j.1600-  
3823 0889.1996.t01-2-00009.x
- 3824 [Deng, et al., 2014] Deng, F., D. B. A. Jones, D. K. Henze, N. Bousserrez, K. W. Bowman, J. B.  
3825 Fisher, R. Nassar, ... T. Warneke. (2014, April 11). Inferring regional sources and sinks of  
3826 atmospheric CO<sub>2</sub> from GOSAT XCO<sub>2</sub> data. *Atmos. Chem. Phys., Vol. 14*, pp. 3703–3727.  
3827 DOI: 10.5194/acp-14-3703-2014
- 3828 [Devi et al., 2007a] Malathy Devi, V., D. C. Benner, L. R. Brown, C. E. Miller, and R. A. Toth.  
3829 (2007). Line mixing and speed dependence in CO<sub>2</sub> at 6348cm<sup>-1</sup>: Positions, intensities, and  
3830 air- and self-broadening derived with constrained multispectrum analysis. *Journal of*  
3831 *Molecular Spectroscopy, Vol. 242* (Issue 2), pp. 90-117. Retrieved from  
3832 <http://adsabs.harvard.edu/abs/2007JMoSp.242.90M>
- 3833 [Devi et al., 2007b] Malathy Devi, V., D. C. Benner, L. R. Brown, C. E. Miller, and R. A. Toth.  
3834 (2007, September). Line mixing and speed dependence in CO<sub>2</sub> at 6227.9cm<sup>-1</sup>: Constrained  
3835 multispectrum analysis of intensities and line shapes in the 30013←00001 band. *Journal*  
3836 *of Molecular Spectroscopy, Vol. 245* (Issue 1), pp.52-80. Retrieved from  
3837 <http://www.sciencedirect.com/science/article/pii/S0022285207001300>
- 3838 [Disney et al., 2009] Disney, M. I., P. E. Lewis, M. Bouvet, A Prieto-Blanco, and S. Hancock.  
3839 (2009). Quantifying surface reflectivity for spaceborne lidar via two independent methods,  
3840 *IEEE Trans. on Geoscience and Remote Sensing, Vol. 47*, pp. 3262-3271.  
3841 DOI:10.1109/TGRS.2009.2019268
- 3842 [Dlugokencky et al., 2013] Dlugokencky, E.J., P.M. Lang, K.A. Masarie, A.M. Crotwell, and  
3843 M.J. Crotwell. (2013). Atmospheric Carbon Dioxide Dry Air Mole Fractions from the  
3844 NOAA ESRL Carbon Cycle Cooperative Global Air Sampling Network, 1968-2012,  
3845 Version: 2013-08-28. Retrieved from:  
3846 [ftp://aftp.cmdl.noaa.gov/data/trace\\_gases/co2/flask/surface/](ftp://aftp.cmdl.noaa.gov/data/trace_gases/co2/flask/surface/)
- 3847 [Dobbs et al., 2007] Dobbs, M., W. Sharp, and J. Jenny. (2007). A Sinusoidal Modulated-CW  
3848 Integrated Path Differential Absorption LIDAR for Mapping Sources and Sinks of Carbon  
3849 Dioxide from Space. Proc. 14<sup>th</sup> Coherent Laser Radar Conference 2007, Snowmass, CO,  
3850 July 8-13, 2007.
- 3851 [Dobbs et al., 2008] Dobbs, M., J. Dobler, M. Braun, D. McGregor, J. Overbeck, B. Moore III, E.  
3852 Browell, and T. S. Zaccheo. (2008). A Modulated CW Fiber Laser-Lidar Suite for the  
3853 ASCENDS Mission. Proc. 24<sup>th</sup> International Laser Radar Conference, S010-04, Boulder,  
3854 CO, June 23-27, 2008.

- 3855 [Dobler et al., 2011] Dobler, J. T., J. Nagel, V. Temyanko, B. Karpowicz, S. Zaccheo, and M.  
3856 Braun. (2011). Fiber Raman Amplifier Development for Laser Absorption Spectroscopy  
3857 Measurements of Atmospheric Oxygen near 1.26 Micron. *The 2011 Earth Science*  
3858 *Technology Forum (ESTF2011)*, Pasadena, CA, June 21-23, 2011. Retrieved from:  
3859 [http://esto.nasa.gov/conferences/estf2011/papers/Dobler\\_ESTF2011.pdf](http://esto.nasa.gov/conferences/estf2011/papers/Dobler_ESTF2011.pdf)
- 3860 [Dobler et al., 2013] Dobler, J. T., F. W. Harrison, E. V. Browell, B. Lin, D. McGregor, S. Kooi,  
3861 Y. Choi, and S. Ismail. (2013). Atmospheric CO<sub>2</sub> column measurements with an airborne  
3862 intensity-modulated continuous-wave 1.57 μm fiber laser lidar. *Applied Optics, Vol. 52*  
3863 (Issue 12), pp. 2874-2892. Retrieved from: <http://dx.doi.org/10.1364/AO.52.002874>
- 3864 [Doney et al., 2006] Doney, S.C., K. Lindsay, I. Fung and J. John. (2006, July). Natural  
3865 Variability in a Stable, 1000-Yr Global Coupled Climate-Carbon Cycle Simulation. *J.*  
3866 *Climate, Vol. 19 (Issue 13)* pp. 3033-3054.
- 3867 [Doney et al., 2009] Doney, S. C., I. Lima, R. A. Feely, D.M. Glover, K. Lindsay, N.Mahowald,  
3868 J. K. Moore, and R. Wanninkhof. (2009, April). Mechanisms governing interannual  
3869 variability in upper-ocean inorganic carbon system and air-sea CO<sub>2</sub> fluxes: Physical  
3870 climate and atmospheric dust. *Deep Sea Res., Part II, Vol. 56 (Issues 8–10)*, pp. 640–655.  
3871 DOI: 10.1016/j.dsr2.2008.12.006
- 3872 [DTC, n.d.] Developmental Testbed Center (DTC). (n. d.). *Model evaluation tools* [Data file].  
3873 Retrieved from: [http://www.dtcenter.org/met/users/downloads/observation\\_data.php](http://www.dtcenter.org/met/users/downloads/observation_data.php)
- 3874 [Dufour and Bréon, 2003] Dufour, E. and F.-M. Bréon. (2003). Spaceborne Estimate of  
3875 Atmospheric CO<sub>2</sub> Column by Use of the Differential Absorption Method: Error Analysis.  
3876 *Applied Optics, Vol. 42 (Issue 18)*, pp. 3595-3609. Retrieved from:  
3877 <http://dx.doi.org/10.1364/AO.42.003595>
- 3878 [Dumont et al., 2010] Dumont, M., O. Brissaud, G. Picard, B. Schmitt, J.-C. Gallet, and Y.  
3879 Arnaud. (2010). High-accuracy measurements of snow bidirectional reflectance  
3880 distribution function at visible and NIR wavelengths -- comparison with modeling results.  
3881 *Atmos. Chem, Phys., Vol. 10*, pp. 2507-2520. [www.atmos-chem-phys.net/10/2507/2010/](http://www.atmos-chem-phys.net/10/2507/2010/)
- 3882 [Duren and Miller, 2012] Duren, R. M. and C. E. Miller. (2012, August). Measuring the carbon  
3883 emissions of megacities. *Nature Climate Change, Vol. 2*, pp. 560–562. DOI: 10.1038/  
3884 nclimate1629
- 3885 [Ehrenreich et al., 2010] Ehrenreich T., R. Leveille, I. Majid, K. Tankala, G. Rines, and P.  
3886 Moulton. (2010, January 28). 1-kW, All-Glass Tm: fiber Laser. *SPIE Photonics West,*  
3887 *2010: LASE, Fiber Lasers VII: Technology, Systems, and Applications, Conference 7580,*  
3888 *Session 16: Late Breaking News.* Retrieved from:  
3889 [http://www.qpeak.com/Meetings/PW%202010%201kW%20Tm\\_fiber%20laser.pdf](http://www.qpeak.com/Meetings/PW%202010%201kW%20Tm_fiber%20laser.pdf)
- 3890 [Ehret et al., 2008] Ehret, G., C. Kiemle, M. Wirth, A. Amediek, A. Fix, and S. Houweling.  
3891 (2008). Space-borne remote sensing of CO<sub>2</sub>, CH<sub>4</sub>, and N<sub>2</sub>O by integrated path differential  
3892 absorption lidar: a sensitivity analysis. *Appl. Phys. B 90*, pp. 593–608. DOI:  
3893 10.1007/s00340-007-2892-3
- 3894 [Engelen et al., 2002] Engelen, R. J., A. S. Denning, K. R. Gurney, and TransCom3 modelers.  
3895 (2002). On error estimation in atmospheric CO<sub>2</sub> inversions. *J. Geophys. Res., Vol. 107*  
3896 (Issue D22), pp. 4635. DOI: 10.1029/2002JD002195

- 3897 [Enting, 2002] Enting, I.G. (2002). *Inverse Problems in Atmospheric Constituent Transport*.  
3898 Cambridge University Press, Cambridge.
- 3899 [EPA, 2010] Environmental Protection Agency. (2010, April 15). *Inventory of U.S. Greenhouse*  
3900 *Gas Emissions and Sinks: 1990 – 2008*, pp. 407. Retrieved from:  
3901 [http://www.epa.gov/climatechange/Downloads/ghgemissions/508\\_Complete\\_GHG\\_1990](http://www.epa.gov/climatechange/Downloads/ghgemissions/508_Complete_GHG_1990)  
3902 [\\_2008.pdf](http://www.epa.gov/climatechange/Downloads/ghgemissions/508_Complete_GHG_1990)
- 3903 [ESA, 2008] European Space Agency (ESA). (2008, November). *A-SCOPE (Advanced Space*  
3904 *Carbon and Climate Observation of Planet Earth) Mission Assessment report*, Chapter 4.  
3905 Retrieved from: [http://esamultimedia.esa.int/docs/SP1313-1\\_ASCOPE.pdf](http://esamultimedia.esa.int/docs/SP1313-1_ASCOPE.pdf)
- 3906 [Etheridge et al., 1998] Etheridge, D. M., L. P. Steele, R. J. Francey, and R. L. Langenfelds.  
3907 (1998). Atmospheric methane between 1000 AD and present: Evidence of anthropogenic  
3908 emissions and climatic variability. *Journal of Geophysical Research-Atmospheres*, Vol.  
3909 *103*, pp. 15979-15993.
- 3910 [Evensen, 2004] Evensen, G. (2004). Sampling strategies and square root analysis schemes for the  
3911 EnKF. *Ocean Dynamics*, Vol. *54*, pp. 539-560. DOI: 10.1007/s10236-004-0099-2
- 3912 [Fan et al., 1998] Fan, S., M. Gloor, J. Mahlman, S. Pacala, J. Sarmiento, T. Takahashi, and P.  
3913 Tans. (1998, October 16). A Large Terrestrial Carbon Sink in North America Implied by  
3914 Atmospheric and Oceanic Carbon Dioxide Data and Models. *Science*, Vol. *282* (No.  
3915 *5388*), pp. 442-446. DOI: 10.1126/science.282.5388.442
- 3916 [Geibel et al., 2012] Geibel, M. C., J. Messerschmidt, C. Gerbig, T. Blumenstock, H. Chen, F.  
3917 Hase, O. Kolle, ... and D. G. Feist. (2012). Calibration of column-averaged CH<sub>4</sub> over  
3918 European TCCON FTS sites with airborne in-situ measurements. *Atmos. Chem. Phys.*,  
3919 Vol. *12*, pp. 8763–8775. DOI: 10.5194/acp-12-8763-2012
- 3920 [Georgieva et al., 2006] Georgieva E.M., E. L. Wilson, M. Miodek, and W.S. Heaps. (2006,  
3921 November). Total column oxygen detection using a Fabry-Perot interferometer. *Optical*  
3922 *Engineering*, Vol. *45* (Issue 11), pp. 115001. DOI: 10.1117/1.2387878
- 3923 [Georgieva et al., 2008] Georgieva E.M., W. S. Heaps, and E. L. Wilson. (2008, October),  
3924 Differential Radiometers Using Fabry-Perot Interferometric Technique for Remote  
3925 Sensing of Greenhouse Gases. *IEEE Transactions on Geoscience and Remote Sensing*  
3926 (*TGARS*), Vol. *46* (Issue 10), pp. 3115-3122. DOI: 10.1109/TGRS.2008.921570
- 3927 [Gibert et al., 2006] Gibert F., P. Flamant, D. Bruneau and C. Loth. (2006). Two-micrometer  
3928 heterodyne differential absorption lidar measurements of the atmospheric CO<sub>2</sub> mixing  
3929 ratio in the boundary layer. *Applied Optics*, Vol. *45*, pp. 4448.
- 3930 [Goodno et al., 2009] Goodno G.D., L. D. Book, and J. E. Rothenberg. (2009). Low-phase-noise,  
3931 single-frequency, single-mode 608 W thulium fiber amplifier. *Opt. Lett.* Vol. *34* (Issue 8),  
3932 pp. 1204-1206.
- 3933 [Gourdji et al., 2012] Gourdji, S. M., K. L. Mueller, V. Yadav, D. N. Huntzinger, A. E. Andrews,  
3934 M. Trudeau, G. Petron, ... and A. M. Michalak. (2012). North American CO<sub>2</sub> exchange:  
3935 intercomparison of modeled estimates with results from a fine-scale atmospheric  
3936 inversion, *Biogeosciences*, Vol. *9*, pp. 457–475. DOI: 10.5194/bgd-8-6775-2011
- 3937 [Guan et al., 2012] Guan, D., Z. Liu, Y. Geng, S. Lindner, and K. Hubacek. (2012). The

- 3938 gigatonne gap in China's carbon dioxide inventories. *Nature Climate Change*, Vol. 2  
3939 (Issue 9), pp. 672-675. DOI: 10.1038/nclimate1560
- 3940 [Guerlet et al., 2013] Guerlet, S., S. Basu, A. Butz, M. Krol, P. Hahne, S. Houweling, O. P.  
3941 Hasekamp, and I. Aben. (2013). Reduced carbon uptake during the 2010 Northern  
3942 Hemisphere summer from GOSAT. *Geophysical Research Letters*, Vol. 40 (Issue 10), pp.  
3943 2378–2383. DOI: 10.1002/grl.50402
- 3944 [Gurney et al., 2002] Gurney, K. G., et al. (2002). Towards robust regional estimates of CO<sub>2</sub>  
3945 sources and sinks using atmospheric transport models, *Nature*, 415, pp. 626–630. DOI:  
3946 10.1038/415626a
- 3947 [Gurney et al., 2009] Gurney, K. R., D. L. Mendoza, Y. Zhou, M. L. Fischer, C.C. Miller, S.  
3948 Geethakumar, and S. de la Rue du Can. (2009). High Resolution Fossil Fuel Combustion  
3949 CO<sub>2</sub> Emission Fluxes for the United States. *Environmental Science & Technology*, Vol. 43  
3950 (Issue 14), pp. 5535-5541. DOI: 10.1021/es900806c
- 3951 [Hammerling et al., 2012a] Hammerling, D.M., A.M. Michalak, and S.R. Kawa. (2012). Mapping  
3952 of CO<sub>2</sub> at high spatiotemporal resolution using satellite observations: Global distributions  
3953 from OCO-2. *J. Geophys. Res.*, Vol. 117 (Issue D6). DOI: 10.1029/2011JD017015
- 3954 [Hammerling et al., 2012b] Hammerling, D. M., A. M. Michalak, C. O'Dell, and S. R. Kawa  
3955 (2012). Global CO<sub>2</sub> distributions over land from the Greenhouse Gases Observing  
3956 Satellite (GOSAT). *Geophys. Res. Lett.*, Vol. 39 (Issue 8). DOI: 10.1029/2012GL051203
- 3957 [Hammerling et al., 2015] Hammerling, D. M., S. R. Kawa, K. Schaefer, S. Doney, A. M.  
3958 Michalak. (2015). Detectability of CO<sub>2</sub> flux signals by a space-based lidar mission, *J.*  
3959 *Geophys. Res. Atmos.*, Vol. 120 (Issue 5), pp. 1794–1807. DOI: 10.1002/2014JD022483
- 3960 [Heaps et al., 2008] Heaps, W.S., E.L. Wilson, and E.M. Georgieva. (2008, September). Precision  
3961 Measurement of Atmospheric Trace Constituents Using a Compact Fabry-Perot  
3962 Radiometer. *International Journal of High Speed Electronics and Systems (IJHSES)*, Vol.  
3963 18 (Issue 3), pp. 601. DOI: 10.1142/S0129156408005606
- 3964 [Hintze, et al., 1998] Hintze, J. L. and R. D. Nelson. (1998). Violin plots: a box plot-density trace  
3965 synergism. *The American Statistician*, Vol. 52 (Issue 2), pp. 181-4. Retrieved from:  
3966 <http://www.jstor.org/discover/10.2307/2685478?uid=16777912&uid=3739560&uid=2&uid=3&uid=16752808&uid=67&uid=62&uid=3739256&sid=21106108757843>  
3967  
3968
- 3969 [Houghton, 1999] Houghton, R. A. (1999, April). The annual net flux of carbon to the  
3970 atmosphere from changes in land use 1850–1990, *Tellus B*, Vol. 51 (Issue 2), pp. 298–313.  
3971 DOI: 10.1034/j.1600-0889.1999.00013.x
- 3972 [Houghton, 2003] Houghton, R. A. (2003, April). Revised estimates of the annual net flux of  
3973 carbon to the atmosphere from changes in land use and land management 1850-2000.  
3974 *Tellus B*, Vol. 55 (Issue 2), pp. 378-390. DOI: 10.1034/j.1600-0889.2003.01450.x
- 3975 [Houweling et al., 2004] Houweling, S., F. M. Breon, I. Aben, C. Rödenbeck, M. Gloor, M.  
3976 Heimann and P. Ciais. (2004). Inverse modeling of CO<sub>2</sub> sources and sinks using satellite  
3977 data: A synthetic inter-comparison of measurement techniques and their performance as a  
3978 function of space and time. *Atmos. Chem. Phys.*, Vol. 4, pp. 523-548.

- 3979 [Hu et al., 2008] Hu, Y., K. Stamnes, M. Vaughan, J. Pelon, C. Weimer, D. Wu, M. Cisewski, W.  
3980 Sun, P. Yang, B. Lin, A. Omar, D. Flittner, C. Hostetler, C. Trepte, D. Winker, G. Gibson,  
3981 and M. Santa-Maria. (2008). Sea surface wind speed estimation from space-based lidar  
3982 measurements. *Atmos. Chem. Phys.*, Vol. 8, pp. 2771-2793 and 3593-3601. DOI:  
3983 10.5194/acp-8-3593-2008
- 3984 [Hudson et al., 2006] Hudson, S. R., S. G. Warren, R. E. Brandt, T. C. Grenfell, and D. Six.  
3985 (2006). Spectral bidirectional reflectance of Antarctic snow: Measurements and  
3986 parameterization. *J. Geophys. Res.*, Vol. 111, D18106, doi:10.1029/2006JD007290
- 3987 [Hungershoefer et al., 2010] Hungershoefer, K., F.-M. Breon, P. Peylin, F. Chevallier, P. Rayner,  
3988 A. Klonecki, S. Houweling, and J. Marshall. (2010). Evaluation of various observing  
3989 systems for the global monitoring of CO<sub>2</sub> surface fluxes. *Atmospheric Chemistry and*  
3990 *Physics*, Vol. 10 (Issue 21), pp.10503–10520. DOI: 10.5194/acp-10-10503-2010
- 3991 [Hyon et al., 2012] Hyon, J., K. Anderson, B. Bienstock, G. Andrew, M. DiJoseph, J. Demsey, C.  
3992 Jones (2012, August). ASCENDS Mission Study Summary. *NASA SER-SE-001*, Vol. 1.0.
- 3993 [Ingmann et al., 2008] Ingmann P., P. Bensi, Y. Durand, A. Griva, and P. Clissold. (2008,  
3994 November). A-Scope – advanced space carbon and climate observation of planet earth.  
3995 *ESA Report for Assessment*. SP-1313/1. ISBN 978-92-9221-406-7, ISSN 0379-6566
- 3996 [Inoue et al., 2013] Inoue, M., I. Morino, O. Uchino, Y. Miyamoto, Y. Yoshida, T. Yokota, T.  
3997 Machida, ... and P. K. Patra. (2013). Validation of XCO<sub>2</sub> derived from SWIR spectra of  
3998 GOSAT TANSO-FTS with aircraft measurement data. *Atmos. Chem. Phys.*, Vol. 13, pp.  
3999 9771-9788. DOI: 10.5194/acp-13-9771-2013
- 4000 [IPCC, 2007] IPCC. (2007, September 19-21). Towards new scenarios for analysis of emissions,  
4001 climate change, impacts, and response strategies. Intergovernmental Panel on Climate  
4002 Change Report, IPCC Expert Meeting Report. Noordwijkerhout, The Netherlands.  
4003 Retrieved from: [http://www.ipcc.ch/pdf/supporting-material/expert-meeting-report-](http://www.ipcc.ch/pdf/supporting-material/expert-meeting-report-scenarios.pdf)  
4004 [scenarios.pdf](http://www.ipcc.ch/pdf/supporting-material/expert-meeting-report-scenarios.pdf)
- 4005 [IPCC, 2007] Core Writing Team, Pachauri, R.K and Reisinger, A. (eds.) (2007). Synthesis  
4006 report. Contribution of working groups I, II and III to the fourth assessment report of the  
4007 intergovernmental panel on climate change. *Climate Change 2007, IPCC*, Geneva,  
4008 Switzerland, pp. 104.
- 4009 [IPCC, 2013] Stocker, T.F., D. Qin, G.-K. Plattner, M. Tignor, S.K. Allen, J. Boschung, A.  
4010 Nauels, Y. Xia, V. Bex and P.M. Midgley (eds.). (2013). The Physical Science Basis.  
4011 Contribution of Working Group I to the Fifth Assessment Report of the Intergovernmental  
4012 Panel on Climate Change. *Climate Change 2013*, Cambridge University Press,  
4013 Cambridge, United Kingdom and New York, NY, USA, 1535 pp. DOI:  
4014 10.1017/CBO9781107415324
- 4015 [Irvine and Pollack, 1968] Irvine, W.M. and J.B. Pollack. (1968). Infrared optical properties of  
4016 water and ice spheres. *Icarus*, Vol. 8, pp. 324-360.
- 4017 [Ismail and Browell, 1989] Ismail, S., and E. V. Browell. (1989, September 1). Airborne and  
4018 spaceborne lidar measurements of water vapor profiles: a sensitivity analysis. *Applied*  
4019 *Optics*, Vol. 28 (No. 17), pp. 3603-3615.

- 4020 [Ishii et al., 2008] Ishii, S., K. Mizutani, H. Fukuoka, T. Ishikawa, H. Iwai, P. Baron, J. Mendrok,  
4021 ... and T. Itabe. (2008). "Development of 2 micron coherent differential absorption lidar,"  
4022 *24th International Laser Radar Conference*, Boulder, Colorado.
- 4023 [Jackson, 2004] Jackson, S.D. (2004, January 2004). Cross relaxation and energy transfer  
4024 upconversion processes relevant to the functioning of 2  $\mu\text{m}$   $\text{Tm}^{3+}$ -doped silica fibre lasers.  
4025 *Optics Communications Vol. 230* (Issues 1-3), pp.197-203. DOI:  
4026 10.1016/j.optcom.2003.11.045
- 4027 [Kameyama et al., 2011] Kameyama, S., M. Imaki, Y. Hirano, S. Ueno, S. Kawakami, D.  
4028 Sakaizawa, T. Kimura and M. Nakajima. (2011). Feasibility study on 1.6  $\mu\text{m}$  continuous-  
4029 wave modulation laser absorption spectrometer system for measurement of global  $\text{CO}_2$   
4030 concentration from a satellite. *Appl. Opt.*, Vol. 50 (Issue 14), pp. 2055-2068.
- 4031 [Kaminski et al., 2001] Kaminski, T., P. J. Rayner, M. Heimann, and I. G. Enting. (2001, March  
4032 16). On aggregation errors in atmospheric transport inversions. *Journal of Geophys. Res.*,  
4033 Vol. 106 (Issue D5), pp. 4703–4715. DOI: 10.1029/2000JD900581
- 4034 [Kawa et al., 2004] Kawa, S. R., D. J. Erickson III, S. Pawson, and Z. Zhu. (2004). Global  $\text{CO}_2$   
4035 transport simulations using meteorological data from the NASA data assimilation system.  
4036 *J. Geophys. Res.*, Vol. 109 (Issue D18). DOI: 10.1029/2004JD004554
- 4037 [Kawa et al., 2010] Kawa, S. R., J. Mao, J. B. Abshire, G. J. Collatz, X. Sun and C. J. Weaver.  
4038 (2010, November). Simulation studies for a space-based  $\text{CO}_2$  lidar mission. *Tellus B*, Vol.  
4039 62 (Issue 5), pp.759-769. DOI: 10.1111/j.1600-0889.2010.00486.x
- 4040 [Keeling, 1960] Keeling, C. D. (1960). The concentration and isotopic abundances of carbon  
4041 dioxide in the atmosphere. *Tellus*, Vol. 12 (Issue 2), pp. 200-203. DOI: 10.1111/j.2153-  
4042 3490.1960.tb01300.x
- 4043 [Keppel-Aleks et al., 2012] Keppel-Aleks, G., P. O. Wennberg, R. A. Washenfelder, D. Wunch,  
4044 T. Schneider, G. C. Toon, R. J. Andres, ... and S. C. Wofsy (2012). The imprint of surface  
4045 fluxes and transport on variations in total column carbon dioxide. *Biogeosciences*, Vol. 9,  
4046 pp. 875-891. DOI: 10.5194/bg-9-875-2012
- 4047 [Kiemle et al., 2014] Kiemle, C, S. R. Kawa, M. Quatrevalet, E. V. Browell. (2014). Performance  
4048 simulations for a spaceborne methane lidar mission. *J Geophys Res Atmos*, Vol. 119 (Issue  
4049 7), pp. 4365–79. Retrieved from: <http://dx.doi.org/10.1002/2013JD021253>
- 4050 [Koch et al., 2008] Koch G. J., J. Y. Beyon, F. Gibert, B. W. Barnes, S. Ismail, M. Petros, P. J.  
4051 Petzar, ... and U. N. Singh (2008). Side-line tunable laser transmitter for differential  
4052 absorption lidar measurements of  $\text{CO}_2$ : design and application to atmospheric  
4053 measurements. *Applied Optics*, Vol. 47 (Issue 7), pp. 944-956.
- 4054 [Kulawik et al., 2015] Kulawik, S., D. Wunch, C. O'Dell, C. Frankenberg, A. R. Jacobson,  
4055 M. Reuter, T. Oda, and C. Miller. (2015). Consistent evaluation of GOSAT,  
4056 SCIAMACHY, CarbonTracker, and MACC through comparisons to TCCON. *Atmos.*  
4057 *Chem. Phys. Disc.*
- 4058 [Kuze et al., in press] Kuze, A., D. M. O'Brien, T. E. Taylor, J. O. Day, C. W. O'Dell, F. Kataoka,  
4059 M. Yoshida, ... and H. Suto. (in press). *IEEE Trans. on Geoscience and Remote Sensing*.  
4060 DOI: 10.1109/TGRS.2010.2089527

- 4061 [Lancaster et al., 2005] Lancaster, R. S., J. D. Spinhirne, and S. P. Palm. (2005). *Geophys. Res.*  
4062 *Letts.*, Vol. 32, L22S10. DOI: 10.1029/2005GL023732
- 4063 [Larsson et al., 2006] Larsson, H., O. Steinvall, T. Chevalier, and F. Gustafsson. (2006).  
4064 Characterizing laser radar snow reflection for the wavelengths 0.9 and 1.5  $\mu\text{m}$ . *Optical*  
4065 *Eng.*, Vol. 45, pp. 116201-1-11. doi:10.1117/1.2386026
- 4066 [Lawrence, 2011] Lawrence, James. (2011). Differential absorption lidar for the total column  
4067 measurement of atmospheric CO<sub>2</sub> from space. *Department of Physics and Astronomy*  
4068 *Dissertation*, University of Leicester. Retrieved from: <http://hdl.handle.net/2381/10379>
- 4069 [Lemke et al., 2007] Lemke, P., J. Ren, R. B. Alley, I. Allison, J. Carrasco, G. Flato, Y. Fujii,  
4070 ... and T. Zhang. (2007). Observations: changes in snow, ice and frozen ground. *Climate*  
4071 *Change 2007: the physical science basis; summary for policymakers, technical summary*  
4072 *and frequently asked questions. Part of the Working Group I contribution to the Fourth*  
4073 *Assessment Report of the Intergovernmental Panel on Climate Change*. Cambridge Univ.  
4074 Press, Cambridge, UK. ISBN: 92-9169-121-6.
- 4075 [Le Quéré et al., 2009] Le Quéré, C., M. R. Raupach, J. G. Canadell, G. Marland, L. Bopp, P.  
4076 Ciais, T. J. Conway, ... and F. I. Woodward. (2009). Trends in the sources and sinks of  
4077 carbon dioxide. *Nature Geosci.*, Vol. 2, pp. 831-836. DOI: 10.1038/ngeo689
- 4078 [Le Quéré et al., 2013] Le Quéré, C., G. P. Peters, R. J. Andres, R. M. Andrew, T. Boden, P.  
4079 Ciais, P. Friedlingstein, ... and C. Yue. (2013). Global carbon budget 2013. *Earth System*  
4080 *Science Data Discussions*, Vol. 6, pp. 689-760. Retrieved from: [http://www.earth-syst-sci-](http://www.earth-syst-sci-data-discuss.net/6/689/2013)  
4081 [data-discuss.net/6/689/2013](http://www.earth-syst-sci-data-discuss.net/6/689/2013), DOI: 10.5194/essdd-6-689-2013
- 4082 [Lin et al., 2003] Lin, J. C., C. Gerbig, S. C. Wofsy, A. E. Andrews, B. C. Daube, K. J. Davis, and  
4083 C. A. Grainger. (2003, August 19). A near-field tool for simulating the upstream influence  
4084 of atmospheric observations: the stochastic time-inverted lagrangian transport (stilt)  
4085 model. *Journal of Geophysical Research: Atmospheres*, Vol. 108 (Issue D16), pp. 10001-  
4086 10021. DOI: 10.1029/2002JD003161
- 4087 [Lin et al., 2013] Lin, B., S. Ismail, F. W. Harrison, E. V. Browell, A. R. Nehrir, J. Dobler, B.  
4088 Moore, T. Refaat and S. A. Kooi. (2013). Modeling of intensity-modulated continuous-  
4089 wave laser absorption spectrometer systems for atmospheric CO<sub>2</sub> column measurements.  
4090 *Applied Optics*, Vol. 52 (Issue 29), pp. 7062-7077.
- 4091 [Long et al., 2010] Long D. A., D.K. Havey, M. Okumura, C.E. Miller, and J.T. Hodges. (2010).  
4092 O<sub>2</sub> A-band line parameters to support atmospheric remote sensing. *J. of Quant. Spectr.*  
4093 *And Rad. Transfer*, Vol. 111 (Issue 14), pp. 2021-2036.
- 4094 [Long et al., 2011] Long, D. A., K. Bielska, D. Lisak, D. K. Havey, M. Okumura, C. E. Miller,  
4095 and J. T. Hodges. (2011). The air-broadened, near-infrared CO<sub>2</sub> line shape in the  
4096 spectrally isolated regime: Evidence of simultaneous Dicke narrowing and speed  
4097 dependence, *Journal of Chemical Physics*, Vol. 135, 064308. Retrieved from:  
4098 <http://dx.doi.org/10.1063/1.3624527>
- 4099 [Lüthi et al., 2008] Lüthi, D., M. Le Floch, B. Bereiter, T. Blunier, J.-M. Barnola, U.  
4100 Siegenthaler, D. Raynaud, ... and T. F. Stocker (2008). High-resolution carbon dioxide  
4101 concentration record 650,000-800,000 years before present. *Nature* 453, pp. 379-382.  
4102 DOI: 10.1038/nature06949

- 4103 [Mao and Kawa, 2004] Mao, J. and S. R. Kawa. (2004). Sensitivity studies for space-based  
4104 measurement of atmospheric total column carbon dioxide by reflected sunlight. *Applied*  
4105 *Optics, Vol. 43* (Issue 4), pp. 914-927.
- 4106 [Mao et al., 2007] Mao, J., S. R. Kawa, J. B. Abshire and H. Riris. (2007). Sensitivity studies for  
4107 a space-based CO<sub>2</sub> laser sounder. *Eos Trans., Vol 88 (Issue 52), AGU 2007 Fall Meeting,*  
4108 *Suppl. Abstract A13D-1500. 2007AGUFM.A13D1500M*
- 4109 [Mao et al., 2013] Mao, J., A. Ramanathan, M. Rodriguez, G. R. Allan, W. Hasselbrack, J. B.  
4110 Abshire, H. Riris, ... and E. V. Browell. (2013). Retrieval of vertical structure of  
4111 atmospheric CO<sub>2</sub> concentration from airborne lidar measurements during the 2011 and  
4112 2013 ascends science campaigns. *2013 Fall AGU Meeting, San Francisco, December 9-*  
4113 *13, 2013, Paper A23H-03.*
- 4114 [Marland et al., 2009] Marland, G., K. Hamal and M. Jonas. (2009). How uncertain are estimates  
4115 of CO<sub>2</sub> emissions? *J. Ind. Ecol., Vol. 13*, pp. 4-7. DOI: 10.1111/j.1530-9290.2009.00108.x
- 4116 [McGuckin and Menzies, 1992] McGuckin B.T. and R.T. Menzies. (1992). Efficient CW diode-  
4117 pumped tm<sub>0</sub> laser with tunability near 2.06 μm. *IEEE J. Quantum Electronics, Vol.*  
4118 *28*, pp. 1025-1028.
- 4119 [Measures, 1992] Measures, R. (1992, January 1). Laser remote sensing: fundamentals and  
4120 applications, *Krieger Publishing Company, New York.*
- 4121 [Menzies et al., 1998] Menzies, R.T., D. M. Tratt, and W. H. Hunt. (1998). Lidar in-space  
4122 technology experiment measurements of sea surface directional reflectance and the link to  
4123 surface wind speed. *Appl. Opt, Vol. 37* (Issue 24), pp. 5550-5558.
- 4124 [Menzies and Tratt, 2003] Menzies, R. T., and D. M. Tratt. (2003). Differential laser absorption  
4125 spectrometry for global profiling of tropospheric carbon dioxide: selection of optimum  
4126 sounding frequencies for high-precision measurements. *Appl. Opt., Vol. 42 (Issue 33)*, pp.  
4127 6569-6577. Retrieved from: <http://dx.doi.org/10.1364/AO.42.006569>
- 4128 [Menzies and Spiers, 2008] R. Menzies and G. Spiers. (2008). Airborne laser absorption  
4129 spectrometer for IPDA measurement of atmospheric effects on attainable precision and a  
4130 technique for cloud and aerosol filtering. 24th International Laser Radar Conference,  
4131 Boulder, Colorado.
- 4132 [Menzies et al., 2014] Menzies, R.T., G.D. Spiers, and J. Jacob. (2014, February). Airborne laser  
4133 absorption spectrometer measurements of atmospheric CO<sub>2</sub> column mole fractions: source  
4134 and sink detection and environmental impacts on retrievals. *J. Atmos. And Oceanic*  
4135 *Technology, Vol. 31*, pp. 404–421. DOI: <http://dx.doi.org/10.1175/JTECH-D-13-00128.1>
- 4136 [Meredith et al., 2012] Meredith, M. P., A. C. N. Garabato, A. M. Hogg, and R. Farneti. (2012,  
4137 January). Sensitivity of the overturning circulation in the southern ocean to decadal  
4138 changes in wind forcing. *J.Climate, Vol. 25* (Issue 1), pp. 99-110.
- 4139 [MERRA, 1979-Present] MERRA. (1979-Present). *Modern Era-Retrospective Analysis for*  
4140 *Research and Applications* [Data file]. Retrieved from:  
4141 <http://gmao.gsfc.nasa.gov/research/merra/intro.php> and [http://disc.sci.gsfc.nasa.gov/daac-](http://disc.sci.gsfc.nasa.gov/daac-bin/FTPSubset.pl)  
4142 [bin/FTPSubset.pl](http://disc.sci.gsfc.nasa.gov/daac-bin/FTPSubset.pl)
- 4143 [Messerschmidt et al., 2013] Messerschmidt, J., N. Parazoo, D. Wunch, N.M. Deutscher, C.  
4144 Roehl, T. Warneke, and P. O. Wennberg. (2013). Evaluation of seasonal atmosphere–

- 4145 biosphere exchange estimations with TCCON measurements. *Atmos. Chem. Phys.*, Vol.  
4146 13, pp. 5103-5115. DOI: 10.5194/acp-13-5103-2013
- 4147 [Michalak et al., 2004] Michalak, A.M., L. Bruhwiler, and P.P. Tans. (2004, July 27). A  
4148 geostatistical approach to surface flux estimation of atmospheric trace gases. *Journal of*  
4149 *Geophysical Research*, Vol. 109 (Issue D14), D14109. DOI: 10.1029/2003JD004422
- 4150 [Miles et al., 2012] Miles, N.L., S.J. Richardson, K.J. Davis, T. Lauvaux, A.E. Andrews, T.O.  
4151 West, V. Bandaru, and E.R. Crosson. (2012). Large amplitude spatial and temporal  
4152 gradients in atmospheric boundary layer CO<sub>2</sub> mole fractions detected with a tower-based  
4153 network in the U.S. upper Midwest. *J. Geophys. Res.*, Vol. 117, G01019. DOI:  
4154 10.1029/2011JG001781
- 4155 [Miller et al., 2007] Miller, C.E., D. Crisp, P. L. DeCola, S. C. Olsen, J. T. Randerson, A. M.  
4156 Michalak, A. Alkhaled, ... and R. M. Law. (2007, May 27). Precision requirements for  
4157 space-based XCO<sub>2</sub> data. *J. Geophys. Res.-Atmos.*, Vol. 112 (Issue D10), D10314. DOI:  
4158 10.1029/2006JD007659
- 4159 [Najjar et al., 2007] Najjar, R.G., X. Jin, F. Louanchi, O. Aumont, K. Caldeira, S. C. Doney, J.-C.  
4160 Dutay, ... and A. Yool. (2007, September). Impact of circulation on export production,  
4161 dissolved organic matter, and dissolved oxygen in the ocean: Results from phase ii of the  
4162 ocean carbon-cycle model intercomparison project (OCMIP-2). *Global Biogeochem. Cy.*,  
4163 Vol. 21 (Issue 3), GB3007. DOI: 10.1029/2006GB002857
- 4164 [NAC, 2007] The 2007 NRC Decadal Survey for Earth Science. (2007). *National Academies*  
4165 *Press*. Retrieved from: [http://www.nap.edu/catalog/11820/earth-science-and-applications-](http://www.nap.edu/catalog/11820/earth-science-and-applications-from-space-national-imperatives-for-the)  
4166 [from-space-national-imperatives-for-the](http://www.nap.edu/catalog/11820/earth-science-and-applications-from-space-national-imperatives-for-the)
- 4167 [NASA, n.d.] The NASA ASCENDS Mission. Retrieved from:  
4168 <http://decadal.gsfc.nasa.gov/ascends.html>
- 4169 [NASA, n.d.] NASA Goddard Space Flight Center. CO<sub>2</sub> sounder. *Papers, Posters, and Related*  
4170 *Studies*. Retrieved from: <http://ssed.gsfc.nasa.gov/co2sounder/>
- 4171 [NASA, 2008] NASA. (2008). Active sensing of CO<sub>2</sub> emission over nights, days, and seasons  
4172 (ASCENDS) mission. *NASA Science Definition and Planning Workshop Report*,  
4173 University of Michigan in Ann Arbor, Michigan, July 23-25, 2008. Retrieved from:  
4174 [http://cce.nasa.gov/ascends/12-30-08%20ASCENDS\\_Workshop\\_Report%20clean.pdf](http://cce.nasa.gov/ascends/12-30-08%20ASCENDS_Workshop_Report%20clean.pdf)
- 4175 [NASA, 2008] NASA Science Definition and Planning Workshop Report for ASCENDS  
4176 Mission. (2008). University of Michigan in Ann Arbor, Michigan. Retrieved from:  
4177 [http://decadal.gsfc.nasa.gov/documents/12-30-08-ASCENDS\\_Workshop.pdf](http://decadal.gsfc.nasa.gov/documents/12-30-08-ASCENDS_Workshop.pdf)
- 4178 [NCDC, n.d.] NCDC. (n.d.). *NCDC's Integrated Surface Database (ISD)* [Data file]. Retrieved  
4179 from: <http://www.ncdc.noaa.gov/oa/climate/isd/index.php>
- 4180 [NCDC, n.d. b] NCDC. (n.d.). *NCDC's NOMADS* [Data file]. Retrieved from:  
4181 <ftp://nomads.ncdc.noaa.gov>
- 4182 [NCEP, n.d. c] NCEP. (n.d.). *PREPBUFR Usage* [Data file]. Retrieved from:  
4183 [http://www.emc.ncep.noaa.gov/mmb/data\\_processing/prepbuf.doc](http://www.emc.ncep.noaa.gov/mmb/data_processing/prepbuf.doc)
- 4184 [Nehrkorn et al., 2010] Nehrkorn, T., J. Eluszkiewicz, S. C. Wofsy, J. C. Lin, C. Gerbig, M.  
4185 Longo, and S. Freitas. (2010). Coupled weather research and forecasting -- stochastic

- 4186 time-inverted Lagrangian transport (WRF-STILT) model. *Meteor. Atmos. Phys., Vol. 107*  
4187 (Issues 1-2), pp. 51–64.
- 4188 [NOAA, 2003] NOAA, Washington, D.C. (2003, November). The GFS Atmospheric Model,  
4189 *NCEP Office Note 422*, Environmental Modeling Center. Retrieved from:  
4190 [http://search.usa.gov/search?affiliate=nws.noaa.gov&v%3Aproject=firstgov&query=The+](http://search.usa.gov/search?affiliate=nws.noaa.gov&v%3Aproject=firstgov&query=The+GFS+Atmospheric+Model%2C+NCEP+Office+Note+422)  
4191 [GFS+Atmospheric+Model%2C+NCEP+Office+Note+422](http://search.usa.gov/search?affiliate=nws.noaa.gov&v%3Aproject=firstgov&query=The+GFS+Atmospheric+Model%2C+NCEP+Office+Note+422)
- 4192 [NOAA, n.d.] NOAA. (n.d.). *NOAA's ESRL's archive*. [Data file]. Retrieved from:  
4193 <http://www.esrl.noaa.gov/raobs/intl/> and <http://www.esrl.noaa.gov/raobs/> or  
4194 [http://www.esrl.noaa.gov/raobs/General\\_Information.html](http://www.esrl.noaa.gov/raobs/General_Information.html)
- 4195 [NRC, 2007] NRC. (2007). Earth science and applications from space: national imperatives for  
4196 the next decade and beyond. *The National Academies Press*, Washington, DC. Retrieved  
4197 from: <http://www.nap.edu/>
- 4198 [NRC, 2013] NRC. (2013). Abrupt Impacts of Climate Change: Anticipating Surprises.  
4199 Committee on Understanding and Monitoring Abrupt Climate Change and its Impacts. *US*  
4200 *National Research Council, National Academies Press*, Washington, DC.
- 4201 [Numata et al., 2012] Numata, K., J. R. Chen and S. T. Wu. (2012). Precision and fast wavelength  
4202 tuning of a dynamically phase-locked widely-tunable laser. *Optics Express, Vol. 20 (Issue*  
4203 *13)*, pp. 14234-14243. <http://dx.doi.org/10.1364/OE.20.014234>
- 4204 [Obland et al., 2012] Obland, M. D., N. S. Prasad, F. W. Harrison, E. V. Browell, S. Ismail, J. T.  
4205 Dobler, B. Moore, ... and W. Welch. (2012). ACES: the ASCENDS carbonhawk  
4206 experiment simulator. *2012 American Geophysical Union Fall Meeting*, San Francisco,  
4207 CA, December 3-7, 2012. Paper A53H-0230.
- 4208 [Obland et al., 2013] Obland, M. D., C. Antill, E. V. Browell, J. F. Campbell, S. Chen, C.  
4209 Cleckner, M. S. Dijoseph, ... and W. Welch. (2013). Technology advancement for the  
4210 ASCENDS mission using the ASCENDS carbonhawk experiment simulator (ACES),  
4211 *2013 American Geophysical Union Fall Meeting*, San Francisco, CA, December 9-13,  
4212 2013, Paper A13C-0212.
- 4213 [O'Brien and Rayner, 2002] O'Brien, D. M. and Rayner, P. J. (2002). Global observations of the  
4214 carbon budget 2. CO<sub>2</sub> column from differential absorption of reflected sunlight in the 1.61  
4215  $\mu\text{m}$  band of CO<sub>2</sub>. *J. Geophys. Res., Vol. 107*, ACH6-1. DOI: 10.1029/2001JD000617
- 4216 [Oda and Maksyutov, 2011] Oda, T., and S. Maksyutov. (2011). A very high-resolution (1 km $\times$ 1  
4217 km) global fossil fuel CO<sub>2</sub> emission inventory derived using a point source database and  
4218 satellite observations of nighttime lights. *Atmos. Chem. Phys.* Vol. 11, pp. 543-556.
- 4219 [O'Dell et al., 2012] O'Dell, C. W., B. Connor, H. Bösch, D. O'Brien, C. Frankenberg, R.  
4220 Castano, M. Christi, D., ... and D. Wunch. (2012). The ACOS CO<sub>2</sub> retrieval algorithm –  
4221 Part 1: Description and validation against synthetic observations. *Atmos. Meas. Tech., Vol.*  
4222 *5*, pp. 99–121. DOI: 10.5194/amt-5-99-2012
- 4223 [Olivier et al., 2012] Olivier, J. G., J. A. Peters and G. Janssens-Maenhout. (2012). Trends in  
4224 global CO<sub>2</sub> emissions 2012 report. *PBL Netherlands Environmental Assessment Agency;*  
4225 *Ispra: Joint Research Centre, The Hague, The Netherlands.*

- 4226 [Oren et al., 2001] Oren, R., D.S. Ellsworth, K. H. Johnsen, N. Phillips, B. E. Ewers, C. Maler,  
4227 K.V. R. Schafer, ... and G. G. Katul. (2001), Soil fertility limits carbon sequestration by  
4228 forest ecosystems in a CO<sub>2</sub>-enriched atmosphere. *Nature* Vol. 411, pp. 469-472. DOI:  
4229 10.1038/35078064
- 4230 [Pan et al., 2011] Pan Y., Birdsey R.A., Fang J., et al. (2011). A large and persistent carbon sink  
4231 in the world's forests. *Science*, Vol. 333 (No. 6045). pp. 988-993. DOI:  
4232 10.1126/science.1201609
- 4233 [Peters et al., 2010] Peters, W., M. C. Krol, G. R. Van Der Werf, S. Houweling, C. D. Jones, J.  
4234 Hughes, K. Schaefer, ... and P. P. Tans. (2010). Seven years of recent European net  
4235 terrestrial carbon dioxide exchange constrained by atmospheric observations. *Global*  
4236 *Change Biology*, Vol. 16 (Issue 4), pp. 1317-1337. DOI: 10.1111/j.1365-  
4237 2486.2009.02078.x
- 4238 [Peters et al., 2011] Peters, G. P., G. Marland, C. L. Quéré, T. Boden, J. G. Canadell, and M. R.  
4239 Raupach. (2011). Rapid growth in CO<sub>2</sub> emissions after the 2008-2009 global financial  
4240 crisis. *Nature Climate Change*, Vol. 2, pp. 2-4. DOI: 10.1038/nclimate1332
- 4241 [Peters et al., 2012] Peters, G. P., G. Marland, C. Le Quere, T. Boden, J. G. Canadell, and M. R.  
4242 Raupach. (2012). Rapid growth in CO<sub>2</sub> emissions after the 2008-2009 global financial  
4243 crisis. *Nature Climate Change*, Vol. 2 (Issue 1), pp. 2-4. DOI: 10.1038/nclimate1332
- 4244 [Picarro, Inc.] Picarro, Inc., 480 Oakmead Parkway, Sunnyvale, CA 94085, USA.
- 4245 [Pillai et al., 2010] Pillai, D., C. Gerbig, J. Marshall, R. Ahmadov, R. Kretschmer, T. Koch, and  
4246 U. Karstens. (2010). High resolution modeling of CO<sub>2</sub> over Europe: implications for  
4247 representation errors of satellite retrievals. *Atmos. Chem. Phys.*, Vol. 10, pp. 83-94. DOI:  
4248 10.5194/acp-10-83-2010
- 4249 [Raab and Tward, 2010] Raab, J., and E. Tward. (2010, September). Northrop Grumman  
4250 Aerospace Systems cryocooler overview. *Cryogenics*, Volume 50 (Issue 9), pp. 572-581.  
4251 ISSN 0011-2275. DOI: 10.1016/j.cryogenics.2010.02.009
- 4252 [Ramanathan et al., 2013] Ramanathan, A., J. Mao, G. R. Allan, H. Riris, C. J. Weaver, W. E.  
4253 Hasselbrack, E. V. Browell, and J. B. Abshire. (2013). Spectroscopic measurements of a  
4254 CO<sub>2</sub> absorption line in an open vertical path using an airborne lidar. *Applied Physics*  
4255 *Letters*, Vol. 103 (Issue 21), 214102. DOI: <http://dx.doi.org/10.1063/1.4832616>
- 4256 [Ramanathan et al., 2015] Ramanathan, A. K., J. Mao, J. B. Abshire, and G. R. Allan. (2015).  
4257 Remote sensing measurements of the CO<sub>2</sub> mixing ratio in the planetary boundary layer  
4258 using cloud slicing with airborne lidar. *Geophys. Res. Lett.*, Vol. 42. DOI:  
4259 10.1002/2014GL062749
- 4260 [Randerson et al., 1997] Randerson, J.T., M.V. Thompson, T. J. Conway, I. Y. Fung and C. B.  
4261 Field. (1997, December). The contribution of terrestrial sources and sinks to trends in the  
4262 seasonal cycle of atmospheric carbon dioxide. *Global Biogeochem. Cy.*, Vol. 11 (Issue 4),  
4263 pp. 535-560. DOI: 10.1029/97GB02268
- 4264 [Rayner and O'Brien, 2001] Rayner, P. J., and D. M. O'Brien. (2001). The utility of remotely  
4265 sensed CO<sub>2</sub> concentration data in surface source inversions. *Geophysical Research Letters*,  
4266 Vol. 28 (Issue 1), pp. 175-178. DOI: 10.1029/2000GLO 11912

- 4267 [Rayner et al., 2002] Rayner, P. J., R. M. Law, D. M. O'Brien, T. M. Butler, and A. C. Dilley.  
4268 (2002). Global observations of the carbon budget - 3. Initial assessment of the impact of  
4269 satellite orbit, scan geometry, and cloud on measuring CO<sub>2</sub> from space. *Journal of*  
4270 *Geophysical Research-Atmospheres*, Vol. 107 (Issue D21). DOI: 10.1029/2001JD000618
- 4271 [Rayner et al., 2010] Rayner, P. J., M. R. Raupach, M. Paget, P. Peylin, and E. Koffi. (2010). A  
4272 new global gridded data set of CO<sub>2</sub> emissions from fossil fuel combustion: Methodology  
4273 and evaluation. *J. Geophys. Res.*, Vol. 115, D19306, DOI: 10.1029/2009JD013439
- 4274 [Refaat et al., 2010] Refaat, T. F., S. Ismail, G. J. Koch, L. Diaz, K. Davis, and M. Rubio. (2010).  
4275 Field Testing of a Two-Micron DIAL System for Profiling Atmospheric Carbon Dioxide.  
4276 *25th International Laser Radar Conference*, 5-9 Jul. 2010, St. Petersburg, Russia.
- 4277 [Refaat et al., 2011] Refaat, T. F., S. Ismail, G. J. Koch, M. Rubio, T. L. Mack, A. Notari, J. E.  
4278 Collins, ... and U. N. Singh. (2011, January). Backscatter 2- $\mu$ m Lidar Validation for  
4279 Atmospheric CO<sub>2</sub> Differential Absorption Lidar Applications. *IEEE Transaction on*  
4280 *Geoscience and Remote Sensing*, Vol. 49 (Issue 1) pp. 572-580. DOI:  
4281 10.1109/TGRS.2010.2055874
- 4282 [Remsberg and Gordley, 1978] Remsberg, E. E., and L. L. Gordley. (1978). Analysis of  
4283 differential absorption lidar from the space shuttle. *Appl. Opt. Vol. 17 (Issue 4)*, pp. 624-  
4284 630. Retrieved from: <http://dx.doi.org/10.1364/AO.17.000624>
- 4285 [Rienecker et al., 2011] Rienecker, M. M., M. J. Suarez, R. Gelaro. R. Todling, J. Bacmeister, E.  
4286 Liu, M. G. Bosilovich, ... and J. Woollen. (2011, July). MERRA: NASA's Modern-Era  
4287 Retrospective Analysis for Research and Applications. *Journal of Climate*, Vol. 24 (Issue  
4288 14), pp.3624-3648. Retrieved from: <http://journals.ametsoc.org/doi/abs/10.1175/jcli-d-11-00015.1>
- 4290 [Riris et al., 2011] Riris, H., M. D. Rodriguez, G. R. Allan, W. E. Hasselbrack, M. A. Stephen,  
4291 and J. B. Abshire. (2011, September 13). Airborne lidar measurements of atmospheric  
4292 pressure made using the oxygen A-band. *Proc. SPIE 8159, Lidar Remote Sensing for*  
4293 *Environmental Monitoring XII*, 815909. DOI: 10.1117/12.892021
- 4294 [Riris et al., 2007] Riris, H., J. Abshire, G. Allan, J. Burris, J. Chen, S. Kawa, J.-P. Mao, ... and  
4295 E. Wilson. (2007, October 3). A laser sounder for measuring atmospheric trace gases from  
4296 space. *Proc. of SPIE Vol. 6750, Lidar Technologies, Techniques, and Measurements for*  
4297 *Atmospheric Remote Sensing III*, 67500U. DOI: 10.1117/12.737607
- 4298 [RMT, Inc., 2011] RMT, Inc. (2011). *Four Corners Generating Station Project*. Retrieved from:  
4299 [http://www.cpuc.ca.gov/environment/info/mha/fourcorners/images/FourCorners\\_Sept2011web.pdf](http://www.cpuc.ca.gov/environment/info/mha/fourcorners/images/FourCorners_Sept2011web.pdf)
- 4301 [Rothman et al., 2009] Rothman, L. S., I. E. Gordon, A. Barbe, D. C. Benner, P.F. Bernath, M.  
4302 Birk, V. Boudon, ... and J. Vander Auwera. (2009). The HITRAN 2008 molecular  
4303 spectroscopic database. *Journal of Quantitative Spectroscopy and Radiative Transfer*, Vol.  
4304 110 (Issues 9-10), pp.533-72. Retrieved from:  
4305 <http://adsabs.harvard.edu/abs/2009JQSRT.110.533R>. DOI: 10.1016/j.jqsrt.2009.02.013
- 4306 [Saha et al., 2010] Saha, S., S. Moorthi, H.-L. Pan, X. Wu, J. Wang, S. Nadiga, P. Tripp, R. ...  
4307 and M. Goldberg. (2010). The NCEP Climate Forecast System Reanalysis. *Bulletin of the*

- 4308 *American Meteorological Society, Volume 91* (Issue 8), pp.1015-57. Retrieved from:  
4309 <http://www.sciencedirect.com/science/article/pii/S0022407309000727>
- 4310 [Sakaizawa et al., 2008] D. Sakaizawa, C. Nagasawa, M. Abo, Y. Shibata, and T. Nagai. (2008).  
4311 Development of a 1.6  $\mu\text{m}$  CO<sub>2</sub> DIAL transmitter using OPM-OPO. *24th International*  
4312 *Laser Radar Conference*.
- 4313 [Salstein et al., 2008] Salstein, D.A., R.M. Ponte, and K. Cady-Pereira. (2008). Uncertainties in  
4314 atmospheric surface pressure fields from global analyses. *Journal of Geophysical*  
4315 *Research: Atmospheres, Vol. 113* (Issue D14), Retrieved from:  
4316 <http://onlinelibrary.wiley.com/doi/10.1029/2007JD009531/abstract>.  
4317 DOI: 10.1029/2007JD009531
- 4318 [Sarmiento et al., 2002] Sarmiento, J. L. and N. Gruber. (2002). Sinks for Anthropogenic Carbon.  
4319 *Physics Today*, Vol. 55 (Issue 8), pp.30-36.
- 4320 [Schaefer et al., 2011] Schaefer, K., T. Zhang, L. Bruhwiler, and A. P. Barrett. (2011). Amount  
4321 and timing of permafrost carbon release in response to climate warming. *Tellus B, Vol. 63*  
4322 *(Issue 2)*, pp. 165-180. DOI: 10.1111/j.1600-0889.2011.00527.x
- 4323 [Shiga et al, 2014] Shiga, Y. P., A. M. Michalak, S. M. Gourdjji, K. L. Mueller, and V. Yadav.  
4324 (2014). Detecting fossil fuel emissions patterns from sub-continental regions using North  
4325 American in-situ CO<sub>2</sub> measurements. *Geophys. Res. Lett.*, 2014GL059684. DOI:  
4326 10.1002/2014GL059684
- 4327 [Simard, et al., 2011] Simard, M., N. Pinto, J. B. Fisher, and A. Baccini. (2011). Mapping forest  
4328 canopy height globally with spaceborne lidar. *J. Geophys. Res.*, Vol. 116, G04021. DOI:  
4329 10.1029/2011JG001708
- 4330 [Singh et al., 2013] Singh, U. N., J. Yu, M. Petros, T. Refaat, and K. Reithmaier. (2013,  
4331 September 17). Development of a pulsed 2-micron integrated path differential absorption  
4332 lidar for CO<sub>2</sub> measurement. *Proceeding of SPIE. Vol. 8872, Lidar Remote Sensing for*  
4333 *Environmental Monitoring XIV, 887209*. San Diego, CA, DOI: 10.1117/12.2028245
- 4334 [Sitch et al., 2003] Sitch, S., B. Smith, I.C. Prentice, A. Arneth, A. Bondeau, W. Cramer, J.O.  
4335 Kaplan, ... and S. Venevsky. (2003). Evaluation of ecosystem dynamics, plant geography  
4336 and terrestrial carbon cycling in the LPJ dynamic global vegetation model. *Global Change*  
4337 *Biology, Vol 9* (Issue 2), pp. 161-185.
- 4338 [Skamarock et al., 2008] Skamarock, W. C. and J. B. Klemp. (2008, March). A time-split  
4339 nonhydrostatic atmospheric model for weather research and forecasting applications. *J.*  
4340 *Comput. Phys.*, Vol. 227 (Issue 7), pp. 3465–3485.
- 4341 [SOCCR, 2008] SOCCR. (2008). The First State of the Carbon Cycle Report (SOCCR):  
4342 The North American Carbon Budget and Implications for the Global Carbon Cycle. A  
4343 Report by the U.S. Climate Change Science Program and the Subcommittee on Global  
4344 Change Research. Ashville, TN: National Oceanic and Atmospheric Administration,  
4345 National Climatic Data Center. Retrieved from:  
4346 <http://www.carboncyclescience.gov/sites/default/files/documents/2013/sap2-2-final-all.pdf>
- 4347 [Solomon et al., 2007] Solomon, S., Qin, D., Manning, M., Chen, Z., Marquis, M., Averyt, K.,  
4348 M.Tignor and Miller, H., ed. (2007). IPCC, 2007: Climate Change 2007: The Physical  
4349 Science Basis. *Contribution of Working Group I to the Fourth Assessment Report of the*

- 4350 *Intergovernmental Panel on Climate Change*. Cambridge, United Kingdom and New  
4351 York, NY, USA.
- 4352 [Spiers et al., 2002] Spiers, G.D., R.T. Menzies, D.M. Tratt, and M. Phillips. (2002). The Laser  
4353 Absorption Spectrometer for Carbon Dioxide Sink and Source Detection. Proceedings of  
4354 the Second Annual Earth Science Technology Conference, Greenbelt, MD.
- 4355 [Spiers et al., 2011a] Spiers, G.D., R.T. Menzies, J. Jacob, L.E. Christensen, M.W. Phillips, Y.  
4356 Choi, and E.V. Browell. (2011a). Atmospheric CO<sub>2</sub> measurements with a 2 μm airborne  
4357 laser absorption spectrometer employing coherent detection. *Appl. Opt. Vol. 50* (Issue 14),  
4358 pp. 2098-2111.
- 4359 [Spiers et al., 2011b] Spiers, G.D., R.T. Menzies, and J.C. Jacob. (2011b). CO<sub>2</sub> Mixing Ratio  
4360 Retrievals from JPL Airborne Laser Absorption Spectrometer Flight Campaigns in 2010-  
4361 11. 2011 AGU Fall Meeting, Paper A21D-0105.
- 4362 [Spiers et al., 2012] Spiers, G.D., R.T. Menzies, J.C. Jacob, and S. Geier. (2012). The Remote  
4363 Measurement of Carbon Dioxide by the CO<sub>2</sub>LAS Instrument during the 2011 ASCENDS  
4364 Field Campaign. 2012 AGU Fall Meeting, Paper, A51H-04.
- 4365 [Spiers et al., 2013] Spiers, G. D., R.T. Menzies, J. Jacob, J.B. Abshire, H. Riris, M.M. Yang, Y.  
4366 Choi, and B.L. Meadows. (2013). Recent measurement results from the Carbon Dioxide  
4367 Laser Absorption Spectrometer for the ASCENDS Mission. 2013 AGU Fall Meeting,  
4368 Paper A23H-02.
- 4369 [Stephen et al., 2007] Stephen, M., M. Krainak, H. Riris and G. R. Allan. (2007, August).  
4370 Narrowband, tunable, frequency-doubled, erbium-doped fiber-amplified transmitter.  
4371 *Optics Letters, Vol. 32* (No. 15), pp. 2073-2075.
- 4372 [Stohl, 1998] Stohl, A. (1998). Computation, accuracy and applications of trajectories – A review  
4373 and bibliography. *Atmos. Environ., Vol. 32* (Issue 6), pp. 947–966.
- 4374 [Sun et al., 2010] Sun, B., A. Reale, D. J. Seidel, and D. C. Hunt. (2010). Comparing radiosonde  
4375 and COSMIC atmospheric profile data to quantify differences among radiosonde types  
4376 and the effects of imperfect collocation on comparison statistics. *J. Geophys. Res.:  
4377 Atmospheres, Vol. 115* (Issue D23), D23104. DOI: 10.1029/2010JD014457
- 4378 [Sun and Abshire, 2012] X. Sun and J. B. Abshire. (2012). Comparison of IPDA lidar receiver  
4379 sensitivity for coherent detection and for direct detection using sine-wave and pulsed  
4380 modulation. *Opt. Express, Vol. 20* (Issue 19), pp. 21291-21304. Retrieved from:  
4381 <http://dx.doi.org/10.1364/OE.20.021291>
- 4382 [Sun et al., 2013] Sun, X., J.B. Abshire, J.F. McGarry, G.A. Neumann, J.C. Smith, J.F.  
4383 Cavanaugh, D. J. Harding, ... and M.T. Zuber. (2013, June). Space lidar developed at the  
4384 nasa goddard space flight center - the first 20 years. *IEEE Journal of Selected Topics in  
4385 Applied Earth Observations and Remote Sensing, Vol.6* (No. 3), pp. 1660-1675. DOI:  
4386 10.1109/JSTARS.2013.2259578
- 4387 [Takahashi et al., 1999] Takahashi, T., R. H. Wanninkhof, R. A. Feely, R. F. Weiss, D. W.  
4388 Chipman, N. Bates, J. Olafsson, C. Sabine, and S.C. Sutherland. (1999). Net sea-air CO<sub>2</sub>  
4389 flux over the global oceans: an improved estimate based on the sea-air pCO<sub>2</sub> difference.  
4390 Proceedings of the 2nd International Symposium: CO<sub>2</sub> in the Oceans, the 12th Global  
4391 Environmental Tsukuba, 18-22 January 1999, Tsukuba Center of Institutes.

- 4392 [Takahashi et al., 2002] Takahashi, T., S. C. Sutherland, C. Sweeney, A. Poisson, N. Metzl, B.  
4393 Tilbrook, N. Bates, ... and Y. Nojiri. (2002). Global sea-air CO<sub>2</sub> flux based on  
4394 climatological surface ocean pCO<sub>2</sub>, and seasonal biological and temperature effects.  
4395 *Deep-Sea Res. Part II: Topical Studies in Oceanography, Vol. 49* (Issues 9-10), pp.1601-  
4396 1622.
- 4397 [Takahashi et al., 2009] Takahashi, T., S. C. Sutherland, R. Wanninkhof, C. Sweeney, R. A.  
4398 Feely, D. W. Chipman, B. Hales, ... and N. R. Bates. (2009). Climatological mean and  
4399 decadal changes in surface ocean pCO<sub>2</sub>, and net sea-air CO<sub>2</sub> flux over the global oceans,  
4400 *Deep Sea Res., Part II, Vol. 56*, pp. 554–577. Retrieved from:  
4401 [http://cdiac.ornl.gov/oceans/LDEO\\_Underway\\_Database/air\\_sea\\_flux\\_2010.html](http://cdiac.ornl.gov/oceans/LDEO_Underway_Database/air_sea_flux_2010.html). DOI:  
4402 10.1016/j.dsr2.2008.12.009
- 4403 [Tans and Keeling, n.d.] Tans, P., and R. Keeling. (n. d.). Trends in Atmospheric Carbon Dioxide.  
4404 *National Oceanic & Atmosphere Administration, Earth System Research Laboratory*  
4405 *(NOAA/ESRL)*. Retrieved from: <http://www.esrl.noaa.gov/gmd/ccgg/trends/>
- 4406 [Tans et al., 1990] Tans, P. P., I. Y. Fung, and T. Takahashi. (1990), Observational Constraints on  
4407 the Global Atmospheric CO<sub>2</sub> Budget. *Science, Vol. 247*, pp.1431-1438.
- 4408 [Tarnocai et al., 2009] Tarnocai, C., J.G. Canadell, E.A.G. Schuur, P. Kuhry, G. Mazhitova and  
4409 S. Zimov. (2009). Soil organic carbon pools in the northern circumpolar permafrost  
4410 region. *Global Biogeochemical Cycles, Vol 23* (Issue 2), GB2023. DOI: 10.1029/  
4411 2008GB003327
- 4412 [Tippett et al., 2003] Tippett, M. K., J. L. Anderson, C. H. Bishop, T. M. Hamill, T. M. and J. S.  
4413 Whitaker. (2003, July). Ensemble Square Root Filters\*. *Monthly Weather Review, Vol.*  
4414 *131* (Issue 7), pp.1485-1490.
- 4415 [Tran et al., 2006] Tran, H., C. Boulet, and J.-M. Hartmann. (2006, August). Line mixing and  
4416 collision-induced absorption by oxygen in the A band: Laboratory measurements, model,  
4417 and tools for atmospheric spectra computations. *J. of Geophysical Res., Vol. 111* (Issue  
4418 *D15*), pp. 16. D15210, 2006. DOI: 10.1029/2005JD006869
- 4419 [Uliasz, 1994] Uliasz, M. (1994), Lagrangian particle dispersion modeling in mesoscale  
4420 applications. *Environmental Modeling, Vol. II*, pp. 71-102.
- 4421 [UN, 2013] UN. (2013). United Nations Statistics Division. Retrieved from:  
4422 <http://unstats.un.org/unsd/default.htm>
- 4423 [U.S. DOC/NOAA, 2005] U.S. DOC/NOAA OFCM, Washington, D.C. (2005, September).  
4424 *Federal Meteorological Handbook No. 1 - Surface Weather Observations and Reports*.  
4425 Retrieved from: <http://www.ofcm.gov/fmh-1/fmh1.htm>
- 4426 [Vay et al., 2003] Vay, S. A., J. H. Woo, B. E. Anderson, K. L. Thornhill, D. R. Blake, D. J.  
4427 Westberg, C. M. Kiley, ... and S. R. Nolf. (2003, October). Influence of regional-scale  
4428 anthropogenic emissions on CO<sub>2</sub> distributions over the western North Pacific. *J. Geophys.*  
4429 *Res. Atmospheres, Vol. 108* (Issue D20), pp. 8801. DOI: 10.1029/2002JD003094
- 4430 [Wang et al., 2014] Wang, J. S., S. R. Kawa, J. Eluszkiewicz, D. F. Baker, M. Mountain, J.  
4431 Henderson, T. Nehrkorn, and T. S. Zaccheo. (2014). A Regional CO<sub>2</sub> Observing System  
4432 Simulation Experiment for the ASCENDS Satellite Mission.

- 4433 [Wennberg et al., 2012] Wennberg, P. O., W. Mui, D. Wunch, E. A. Kort, D. R. Blake, E. L.  
4434 Atlas, G. W. Santoni, ... and M. L. Fischer. (2012). On the Sources of Methane to the Los  
4435 Angeles Atmosphere. *Environmental Science & Technology*, Vol. 46 (Issue 17), pp. 9282-  
4436 9289. DOI: 10.1021/es301138y
- 4437 [Werle et al., 1993] Werle, P., R. Mucke, and F. Slemr. (1993). The limits of signal averaging in  
4438 atmospheric trace-gas monitoring by tunable diode-laser absorption spectroscopy  
4439 (TDLAS). *Applied Physics B Photophysics and Laser Chemistry*, Volume 57 (Issue 2), pp.  
4440 131-139. DOI: 10.1007/BF00425997
- 4441 [Werle et al., 2004] Werle P. W., P. Mazinghi, F. D'Amato, M. De Rosa, K. Maurer, F. Slemr.  
4442 (2004). Signal processing and calibration procedures for in situ diode-laser absorption  
4443 spectroscopy. *Spectrochimica Acta Part A: Molecular and Biomolecular Spectroscopy*,  
4444 Volume 60 (Issue 8), pp. 1685-1705. DOI: 10.1016/j.saa.2003.10.013
- 4445 [Wilson et al., 2007] Wilson E.L., E. M. Georgieva, and W. S. Heaps. (2007). Development of a  
4446 Fabry-Perot interferometer for ultra-precise measurements of column CO<sub>2</sub>. *Meas. Sci.*  
4447 *Technology*, Vol. 18 (Issue 5), pp. 1495-1502, 2007
- 4448 [Wunch et al., 2011] Wunch, D., P. O. Wennberg, G. C. Toon, B. J. Connor, B. Fisher, G. B.  
4449 Osterman, C. Frankenberg, ... and S. C. Wofsy. (2011). A method for evaluating bias in  
4450 global measurements of CO<sub>2</sub> total columns from space. *Atmospheric Chemistry and*  
4451 *Physics*, Vol. 11 (Issue 23), pp.12317-12337. DOI: 10.5194/acp-11-12317-2011
- 4452 [Wunch et al., 2013] Wunch, D., P. O. Wennberg, J. Messerschmidt, N. C. Parazoo, G. C. Toon,  
4453 N. M. Deutscher, G. Keppel-Aleks, ... and J. Notholt. (2013). The covariation of Northern  
4454 Hemisphere summertime CO<sub>2</sub> with surface temperature in boreal regions. *Atmospheric*  
4455 *Chemistry and Physics*, Vol. 13, pp. 9447-9459. DOI: 10.5194/acp-13-9447-2013
- 4456 [Wysocki et al., 2006] Wysocki, P., T. Wood, A. Grant, D. Holcomb, K. Chang, M. Santo, L.  
4457 Braun, and G. Johnson. (2006, March 5). High Reliability 49 dB Gain, 13 W PM Fiber  
4458 Amplifier at 1550 nm with 30 dB PER and Record Efficiency. Optical Society of America  
4459 / Optical Fiber Communication Conference, Anaheim. ISBN: 1-55752-802-0
- 4460 [Yang et al., 2006] Yang, F. et al. (2006). Evaluation of the NCEP Global Forecast System at the  
4461 ARM SGP Site. *Monthly Weather Review*, Vol. 134 (Issue 12), pp.3668-90. Retrieved  
4462 from: <http://journals.ametsoc.org/doi/abs/10.1175/MWR3264.1>
- 4463 [Yoshida et al., 2012] Yoshida, Y., N. Kikuchi, I. Morino, O. Uchino, S. Oshchepkov, A. Bril, T.  
4464 Saeki, ... and T. Yokota. (2013). Improvement of the retrieval algorithm for GOSAT  
4465 SWIR XC02 and XCH4 and their validation using TCCON data. *Atmospheric*  
4466 *Measurement Techniques*, Vol. 6 (Issue 6), pp. 1533-1547. DOI: 10.5194/amt-6-1533-2013
- 4467 [Yu et al., 2003] Yu J., A. Braud, and M. Petros. (2003). 600-mJ, double-pulse 2- $\mu$ m laser. *Optics*  
4468 *Letters*, Vol. 28 (Issue 7), pp. 540-542. <http://dx.doi.org/10.1364/OL.28.000540>
- 4469 [Yu et al., 2012] Yu J., M. Petros, K. Reithmaier, Y. Bai, B. C. Trieu, T. F. Refaat, M. J. Kavaya,  
4470 and U. N. Singh. (2012). A 2-micron pulsed integrated path differential absorption lidar  
4471 development for atmospheric CO<sub>2</sub> concentration measurements. 26th International Laser  
4472 Radar Conference, June 25-29, 2012, Porto Heli, Greece.

- 4473 [Zhang et al., 1999] Zhang, T., R. G. Barry, K. Knowles, J. A. Heginbottom, and J. Brown.  
4474 (1999). Statistics and characteristics of permafrost and ground-ice distribution in the  
4475 Northern Hemisphere. *Polar Geography Vol. 23* (Issue 2), pp. 147–169.
- 4476 [Zhao and Tans, 2006] Zhao, C. L. and P.P. Tans. (2006). Estimating uncertainty of the WMO  
4477 mole fraction scale for carbon dioxide in air. *J. Geophys. Res. Vol. 111* (Issue D8),  
4478 D08S09. DOI: 10.1029/2005JD006003
- 4479 [Zimov et al., 1999] Zimov, S. A., S. P. Davidov, G. M. Zimova, A. I. Davidova, F. S Chapin III,  
4480 M. C. Chapin & J. F. Reynolds. (1999). Contribution of Disturbance to Increasing  
4481 Seasonal Amplitude of Atmospheric CO<sub>2</sub>, *Science, Vol. 284*, pp. 1973-1976.

4482 **B. Acronyms**

4483		
4484	4DVAR	4-Dimensional Variational
4485	ABL	Atmospheric Boundary Layer
4486	ACOS	Atmospheric CO <sub>2</sub> Observations from Space
4487	ACES	ASCENDS CarbonHawk Experiment Simulator
4488	ACS	Attitude Control Subsystem
4489	AD&CS	Attitude Determination and Control System
4490	AER	Atmospheric and Environmental Research
4491	AGCM	Atmospheric General Circulation Model
4492	AIRS	Atmospheric Infrared Sounder
4493	AOM	Acousto-Optic Modulator
4494	APD	Avalanche Photodiode Detector
4495	ASCENDS	Active Sensing of CO <sub>2</sub> Emissions over Nights, Days, and Seasons
4496	A-SCOPE	Advanced Space Carbon and Climate Observation of Planet Earth
4497	AVOCET	Atmospheric Vertical Observations of Carbon Dioxide in the Earth's Troposphere
4498	BBL	Broad Band Lidar
4499	CA	California
4500	CALIPSO	Cloud-Aerosol Lidar and Infrared Pathfinder Satellite Observations
4501	Caltech	California Institute of Technology
4502	CASA	Carnegie-Ames-Stanford-Approach
4503	CBE	Current Best Estimate
4504	CCGG	Carbon Cycle Greenhouse Gas
4505	CCSM	Community Climate System Model
4506	CDF	Cumulative Distribution Function
4507	CDIAC	Carbon Dioxide Information Analysis Center
4508	CFSR	Climate Forecast System Reanalysis
4509	CH <sub>4</sub>	Methane, Natural Gas
4510	CIRA	Cooperative Institute for Research in the Atmosphere
4511	CNES	Centre National d'Etudes Spatiales (French Space Agency)
4512	CO <sub>2</sub>	Carbon Dioxide
4513	CONUS	Contiguous United States, Continental United States
4514	CSU	Colorado State University

4515	CW	Continuous Wave
4516	DAOD	Differential Absorption Optical Depth
4517	DEM	Digital Elevation Model
4518	DFB	Distributed Feedback
4519	DFB-LD	Distributed Feedback Laser Diode
4520	DIAL	Differential Absorption Lidar
4521	DOD	Differential Optical Depth
4522	DOI	Digital Object Identifier
4523	DRS	DRS Technologies Sensors and Targeting Systems, Inc., in Dallas, TX.
4524	DSS	Dual Spacecraft System
4525	eAPD	electron initiated Avalanche Photodiode Detector
4526	ECMWF	European Centre for Medium-Range Weather Forecasts
4527	EDFA	Erbium Doped Fiber Amplifier
4528	EE8	Earth Explorer 8
4529	EELV	Evolved Expendable Launch Vehicle
4530	EMC	Electromagnetic Compatibility
4531	EMI	Electromagnetic Interference
4532	EnKF	Ensemble Kalman Filter
4533	ENSO	El Niño Southern Oscillation
4534	EnviSAT	Environmental SATellite
4535	EPA	Environmental Protection Agency
4536	ESA	European Space Agency
4537	ESD	Earth Science Division
4538	ESMPO	Earth Systematic Mission Program Office
4539	ESRL	Earth System Research Laboratory
4540	ESRL GMD	Earth System Research Laboratory Global Monitoring Division
4541	ESTO	Earth Science Technology Office
4542	EU	European Union
4543	FF	Fossil Fuel
4544	FFCO <sub>2</sub>	Fossil Fuel CO <sub>2</sub>
4545	FFT	Fast Fourier Transform
4546	FM/CW	Frequency-Modulated/Continuous Wave
4547	FOV	Field of View

4548	FP	Fabry-Perot
4549	FTS	Fourier Transform Spectrometer
4550	FWHM	Full Width at Half Maximum
4551	GAW	Global Atmospheric Watch
4552	GCM	General Circulation Model
4553	GEVS	General Environmental Verification Specification
4554	GFED	Global Fire Emissions Database
4555	GFS	Global Forecast System
4556	GIM	Geostatistical Inverse Modeling
4557	GHG	Green House Gas
4558	GLAS	Geoscience Laser Altimeter System
4559	GMAO	Global Modeling and Assimilation Office, Goddard Modeling and Assimilation
4560		Office
4561	GOSAT	Greenhouse gases Observing SATellite
4562	GPP	Gross Primary Production, Gross Primary Productivity
4563	GPS	Global Positioning System
4564	GSFC	Goddard Space Flight Center
4565	Gt	Gigatons
4566	GTOPO30	30-arc second resolution Digital Elevation Model developed by USGS
4567	HgCdTe	Mercury Cadmium Telluride
4568	HITRAN	High Resolution Transmission
4569	Hz	Hertz
4570	IASI	Infrared Atmospheric Sounding Interferometer
4571	IAV	InterAnnual Variability
4572	ICE/Sat	Ice, Cloud and land Elevation Satellite
4573	ICESAT	Ice, Cloud and land Elevation Satellite
4574	IF	Intermediate Frequency
4575	IIP	Instrument Incubator Program
4576	IM-CW	Intensity-Modulated Continuous-Wave
4577	INTEX	Intercontinental Chemical Transport Experiment
4578	INTEX-NA	Intercontinental Chemical Transport Experiment-North America
4579	IPCC	Intergovernmental Panel on Climate Change
4580	IPDA	Integrated Path Differential Absorption

4581	IR	Infrared
4582	ISD	Integrated Surface Database
4583	Exelis	ITT Exelis, Inc.
4584	JPL	Jet Propulsion Laboratory
4585	kHz	Kilohertz (1thousand Hertz)
4586	KTP	Potassium Titanyl Phosphate
4587	LAI	Leaf Area Index
4588	LaRC	Langley Research Center
4589	LAS	Laser Absorption Spectrometer
4590	LBLRTM	Line-By-Line Radiative Transfer Model
4591	LEO	Low Earth Orbit
4592	LGS	Lucent Government Solutions
4593	LIDAR	Light Detection and Ranging
4594	LO	Local Oscillator
4595	LPJ	Lund–Potsdam–Jena Dynamic Global Vegetation Model
4596	LPDM	Lagrangian Particle Dispersion Model
4597	MCR	Mission Confirmation Review
4598	MCT	Mercury Cadmium Telluride
4599	MERRA	Modern Era Retrospective-analysis for Research and Applications
4600	MFLI	Multifunctional Fiber Laser Lidar
4601	MHz	Megahertz (1 million Hertz)
4602	MOPA	Master Oscillator Power Amplifier
4603	NA	North America
4604	NAM	North American Mesoscale Model
4605	NASA	National Aeronautics and Space Administration
4606	NCAR	National Center for Atmospheric Research
4607	NCDC	National Climatic Data Center
4608	NDP	Numeric Data Package
4609	NEE	Net Ecosystem Carbon Exchange
4610	NEP	Noise-Equivalent Power
4611	NGA	Northrop Grumman Aerospace
4612	NOAA	National Oceanic and Atmospheric Administration
4613	NM	New Mexico

4614	NRC	National Research Council
4615	NWP	Numerical Weather Prediction
4616	O <sub>2</sub>	Oxygen
4617	OCO	Orbiting Carbon Observatory
4618	OCO-2	Orbiting Carbon Observatory-2
4619	OCO-3	Orbiting Carbon Observatory-3
4620	OD	Optical Depth
4621	ODIAC	Open-source Data Inventory of Anthropogenic CO <sub>2</sub> emission
4622	OFCM	Office of the Federal Coordinator for Meteorology
4623	OPA	Optical Parametric Amplifier
4624	ORNL	Oak Ridge National Laboratory
4625	OSSE	Observing Systems Simulation Experiment
4626	P	Pressure
4627	PCTM	Parameterized Chemistry and Transport Model
4628	PDR	Preliminary Design Review
4629	PIN	PIN diode (PIN corresponds to the diode construction)
4630	PN	Pseudorandom Noise
4631	ppm	Parts Per Million
4632	ppmv	Parts Per Million by Volume
4633	PWG	planar waveguide amplifier
4634	QE	Quantum Efficiency
4635	RAOB	RADiosonde OBservation
4636	RMS	Root Mean Square
4637	RMSE	Root Mean Square Error
4638	RRV	Railroad Valley, Nevada
4639	SCIAMACHY	SCanning Imaging Absorption Spectrometer for Atmospheric CartograpHY
4640	SH	Southern Hemisphere
4641	SiB3	Simple Biosphere model, version 3
4642	SiB-CASA	Simple Biosphere/Carnegie-Ames-Stanford Approach
4643	SLED	SuperLuminExcent Diode
4644	SNR	Signal to Noise Ratio
4645	SOCCR	State of the Carbon Cycle Report
4646	SPCM	Single Photon Counting Module

4647	SRTM	Shuttle Radar Topography Mission
4648	SSE	Scattering Surface Elevations
4649	STILT	Stochastic Time-Inverted Lagrangian Transport
4650	SZA	Solar Zenith Angle
4651	T	Temperature
4652	TANSO	Thermal And Near infrared Sensor for carbon Observation
4653	TBD	To Be Determined
4654	TBR	To Be Reviewed?
4655	TCCON	Total Carbon Column Observing Network
4656	TVAC	Thermal Vacuum
4657	US	United States
4658	USGS	United States Geological Survey
4659	UTC	Universal Time Coordinated
4660	WBI	West Branch Iowa
4661	WDCGG	World Data Centre for Greenhouse Gases
4662	WMO	World Meteorological Organization
4663	WRF	Weather Research and Forecasting
4664	WV	Water Vapor

4665 **C. Detailed Comparison of Modeling Approaches**

4666

4667

**Table C-1 Detailed Comparison of Modeling Approaches**

Modeling Approaches					
	4DVAR-TM5	4DVAR-PCTM	EnKF-GEOS-Chem	Bayesian	GIM
<b>Team</b>	OU/Melbourne	CSU-CIRA	CSU-CIRA	GSFC/AER	Stanford-Carnegie
<b>Inversion Method</b>	Four-dimensional variational data assimilation	Four-dimensional variational data assimilation	Ensemble Kalman filter	Batch Bayesian synthesis inversion	Batch geostatistical synthesis inversion
<b>Transport Model</b>	TM5 (Global Eulerian, 6°x4°, winds regridded from 1°x1.25° ECWMF)	PCTM (Global Eulerian, 6°x4.5°, winds regridded from 1°x1.25° MERRA)	GEOS-Chem (Global Eulerian, 2°x2.5°, winds regridded from 1°x1.25° MERRA)	WRF-STILT (Regional Lagrangian particle dispersion model, 40 km WRF meteorology)	WRF-STILT (Regional Lagrangian particle dispersion model, 40 km WRF meteorology)
<b>Domain and Flux Spatial Resolution</b>	Global 6°x4°, with North America nest at 1°x1°	Global 6°x4.5°	Global 2°x2.5° regularization via spatial covariance smoothing	North America 1°x1° (with spatial correlation)	North America 1°x1° (with spatial correlation and constrained by geostatistical model)
<b>Flux Temporal Resolution</b>	Monthly	Weekly	Two weeks	Weekly (with temporal correlation)	3-hourly (with temporal correlation)
<b><u>Truth Emissions:</u></b>					
Ocean	Takahashi et al. (2009)	NCAR Ocean Model (Doney et al., 2006; Najjar et al., 2007)	Prior + decreased seasonal cycle	--	--
Anthropogenic	CDIAC/Oak Ridge National Laboratory(ORNL) Numeric Data Package (NDP) 058 v2011	None	Same as Prior	--	VULCAN/ODIAC
Biosphere	CASA-GFED2	LPJ (Sitch et al., 2003)	Prior + enhanced sinks (Amazon, Europe, east Asia)	--	CASA-GFED2
<b><u>Prior Emissions:</u></b>					
Ocean	Perturbed Truth	Takahashi, et al. (1999)	Woods Hole Institute (Doney)	--	--
Anthropogenic	Perturbed Truth	None	ODIAC (Oda et al., 2009)	--	--

Modeling Approaches					
	4DVAR-TM5	4DVAR-PCTM	EnKF-GEOS-Chem	Bayesian	GIM
Biosphere	Perturbed Truth	CASA land model (Randerson et al., 1997)	SiB3 (Baker et al., 2008)	--	--
<b><u>Prior Uncertainties:</u></b>					
Variations	Prior - Truth	Prior - Truth	Estimated by EnKF	Variability of CASA-GFED v3 NEE, scaled up to CSU/NOAA overall magnitudes	Monthly varying (See Shiga et al., 2014.)
Spatial Correlation	0km	0km	800km (land), 1600km (ocean)	Monthly varying (300-650km, Gourjji et al. (2012))	Monthly varying (See Shiga et al., 2014.)
Temporal Correlation	none	None	none	Monthly varying (2-17 days, Gourjji et al. (2012))	Monthly varying (See Shiga et al., 2014.)

4668

4669 ***EnKF Inversion Detail***

4670 NEE is optimized by estimating scaling factors to a priori GPP and respiration. As opposed to  
 4671 4DVAR techniques that provide a simultaneous flux estimate across time, the EnKF proceeds  
 4672 sequentially, thus the prior flux (first guess) evolves through time. The initial guess for mean flux  
 4673 is the unperturbed flux case (annual net zero NEE SiB3 fluxes described above) while the ‘truth’  
 4674 consists of the initial guess plus the tested perturbations. The initial uncertainty consists of an  
 4675 independent 15% standard deviation on both GPP and total respiration, Gaussian distributed. Due  
 4676 to the independent errors, this allows for the uncertainty on the difference (NEE) to be even larger  
 4677 than 15%. The correlation structure *within* GPP (and respiration) is then formed from an isotropic  
 4678 exponential covariance model which effectively constrains the solution to be smooth in  
 4679 geographic space (Table C-1 in Appendix C). This “initial guess” then evolves through time by  
 4680 weighting incremental adjustments to the state estimate over time with the original prior flux  
 4681 guess at time zero, as well as a small multiplicative inflation factor (5%). With this setup, there is  
 4682 an implicit assumption made regarding where we think flux corrections should occur, i.e. in  
 4683 locations of strong a priori flux but otherwise there are no a priori assumptions made on where the  
 4684 correction will be made. The strength of the EnKF is providing explicit uncertainty estimates, as  
 4685 shown in Figure 3-14, however we note that these are heavily dependent upon the nature of the  
 4686 propagation of the covariance between assimilation cycles, which often requires extensive testing  
 4687 and tuning.

4688

4689 **Box C-1** Calculation of Model-Data Mismatch Errors

4690 The Bayesian and GIM OSSEs carried out by teams at GSFC and Carnegie-Stanford use only  
 4691 observation locations that fall within the domain used in the WRF meteorological runs (excluding  
 4692 those within 400 km of the boundaries to provide adequate WRF coverage to simulate back  
 4693 trajectory calculations inside the domain). Soundings with total column cloud-plus-aerosol OD >  
 4694 0.7 are rejected. The errors for each 5 km (0.74 s) individual CALIPSO observation point are  
 4695 aggregated over 10-s intervals to increase signal-to-noise for the pseudo-data, using the formula

$$\sigma(10s) = \sqrt{\frac{\sum_{i=1}^N \sigma(5km)_i^2}{N^2}} \quad (C-1)$$

4696 where N is the number of valid 5 km observations across the 10-s span. The uncertainties in the  
 4697 series of 10-s pseudo-data are assumed to be uncorrelated.

4698 The 4D-VAR-TM5 and EnKF OSSEs led by the teams at OU and CSU first identify ‘n’  
 4699 continuous (along track) soundings that fall within a single grid cell of their model. Soundings  
 4700 with total column OD > 0.3 are rejected. Equation 3-1 is used to calculate the monthly scale  
 4701 factors for each observation. Finally, a variance weighted mean across all the observations in the  
 4702 grid cell is calculated.

4703 In the 4D-VAR-PCTM OSSEs a single measurement is applied per orbit for each model grid box  
 4704 that the satellite views. This measurement characterizes the information content of all the  
 4705 individual measurements taken along-track inside the box. Furthermore, the same measurement  
 4706 uncertainty value is assumed for all satellite crossings in a single month per grid box, whatever  
 4707 the optical depth conditions happen to be during each overpass: the applied uncertainty in  
 4708 increased statistically to account for climatological optical depth conditions at that grid box  
 4709 during that month. If a grid box has an optical depth of zero half the time and infinity the other  
 4710 half, the uncertainty applied will be  $\sqrt{2}$  times the clear-sky value. Using the monthly scale factors  
 4711 from Equation 3-1, the measurement uncertainties applied for any grid box crossing in the  
 4712 assimilation are given by

$$\sigma = f\sigma_{RRV} \sqrt{P_o/P} \quad (C-2)$$

4713 where P is the time that the satellite FOV falls within the grid box in [sec], and  $P_o = 10$  sec is the  
 4714 base time that the uncertainties are referenced to.